# 2 MHz ELECTRICAL RESISTANCE TOMOGRAPHY FOR STATICLIQUID-SOLID PROFILE MEASUREMENT

YASMIN BINTI ABDUL WAHAB

UNIVERSITI TEKNOLOGI MALAYSIA

**UNIVERSITI TEKNOLOGI MALAYSIA**

**DECLARATION OF THESIS / ~~UNDERGRADUATE~~ PROJECT REPORT AND COPYRIGHT**

Author's full name : YASMIN BINTI ABDUL WAHAB

Date of Birth : 12 DECEMBER 1985

Title : 2 MHz ELECTRICAL RESISTANCE TOMOGRAPHY FOR STATIC LIQUID-SOLID PROFILE MEASUREMENT

Academic Session : **2016/2017-II**

I declare that this thesis is classified as:

| | | |
|---|---|---|
| ☐ | **CONFIDENTIAL** | (Contains confidential information under the Official Secret Act 1972)* |
| ☐ | **RESTRICTED** | (Contains restricted information as specified by the organization where research was done)* |
| ✓ | **OPEN ACCESS** | I agree that my thesis to be published as online open access (full text) |

I acknowledged that Universiti Teknologi Malaysia reserves the right as follows:

1. The thesis is the property of Universiti Teknologi Malaysia
2. The Library of Universiti Teknologi Malaysia has the right to make copies for the purpose of research only.
3. The Library has the right to make copies of the thesis for academic exchange.

Certified by:

| | |
|---|---|
| SIGNATURE | SIGNATURE OF SUPERVISOR |
| 851212-03-5340 | PROFESOR DR RUZAIRI ABDUL RAHIM<br>Pensyarah<br>Fakulti Kejuruteraan Elektrik<br>Universiti Teknologi Malaysia<br>81310 UTM Skudai, Johor, Malaysia |
| (NEW IC NO/PASSPORT) | NAME OF SUPERVISOR |
| Date: 2/5/17 | Date: 2/5/17 |

**NOTES:** * If the thesis is CONFIDENTAL or RESTRICTED, please attach with the letter from the organization with period and reasons for confidentiality or restriction.

"We hereby declare that we have read this thesis and in our opinion this thesis is sufficient in terms of scope and quality for the award of the degree of Doctor of Philosophy (Electrical Engineering)"

| | | |
|---|---|---|
| Signature | : | ........................................ |
| Name of Supervisor | : | Prof. Dr. Ruzairi Bin Abdul Rahim |
| Date | : | 2/5/17 |
| Signature | : | ........................................ |
| Name of Co-Supervisor | : | Assoc. Prof. Dr. Herlina Binti Abdul Rahim |
| Date | : | 2/5/17 |
| Signature | : | ........................................ |
| Name of Co-Supervisor | : | Dr. Leow Pei Ling |
| Date | : | 2/5/2017 |
| Signature | : | ........................................ |
| Name of Co-Supervisor | : | Dr. Mohd Hafiz Bin Fazalul Rahiman |
| Date | : | 2/5/17 |

**BAHAGIAN A – Pengesahan Kerjasama***

Adalah disahkan bahawa projek penyelidikan tesis ini telah dilaksanakan melalui kerjasama antara ________________________ dengan ________________________

Disahkan oleh:

Tandatangan : ……………………………….. Tarikh : ……………………..
Nama : ……………………………………….
Jawatan : ……………………………………..
(Cop rasmi)

** Jika penyediaan tesis/projek melibatkan kerjasama.*

=:=:=:=:=:=:=:=:=:=:=:=:=:=:=:=:=:=:=:=:=:=:=:=:=:=:=:=:=:=:=:=:=:=:=:=:=:=:=:=:=:=:=:=:=:=

**BAHAGIAN B – Untuk Kegunaan Pejabat Sekolah Pengajian Siswazah**

Tesis ini telah diperiksa dan diakui oleh:

Nama dan Alamat Pemeriksa Luar : **Prof. Dr. M. Iqbal Saripan**
**Department of Computer &**
**Communication Systems Engineering**
**Faculty of Engineering**
**Universiti Putra Malaysia**
**43400 Serdang, Selangor**

Nama dan Alamat Pemeriksa Dalam : **Prof. Madya Dr. Sallehuddin bin Ibrahim**
**Fakulti Kejuruteraan Elektrik,**
**Universiti Teknologi Malaysia,**
**81310 UTM Johor Bharu.**
**UTM Johor Bharu**

Disahkan oleh Timbalan Pendaftar di SPS:

Tandatangan : ……………………………………… Tarikh : …………………
Nama : **ENCIK AZRI BIN HOHAD** ………………………………………

# 2 MHz ELECTRICAL RESISTANCE TOMOGRAPHY FOR STATIC LIQUID-SOLID PROFILE MEASUREMENT

YASMIN BINTI ABDUL WAHAB

A thesis submitted in fulfilment of the
requirements for the award of the degree of
Doctor of Philosophy (Electrical Engineering)

Faculty of Electrical Engineering
Universiti Teknologi Malaysia

MAY 2017

I declare that this thesis entitled "*2 MHz Electrical Resistance Tomography for Static Liquid-Solid Profile Measurement*" is the result of my own research except as cited in the references. The thesis has not been accepted for any degree and is not concurrently submitted in candidature of any other degree.

Signature : ..................................................

Name : YASMIN BINTI ABDUL WAHAB

Date : 2/5/17

*In the name of Allah, the most Gracious and the most Merciful.*

*To my beloved and supportive parents,*

*husband,brothers, sisters*

*and*

*my lovely children*

# ACKNOWLEDGEMENT

I would like to dedicate my deepest gratitude to my supervisor Prof. Dr. Ruzairi Abdul Rahim for his outstanding support and excellent supervisions. This research would not have been successful without his valuable guidance, enthusiastic help as well as constructive criticisms throughout the research. I would also like to give my sincere thanks to Dr. Mohd Hafiz Fazalul Rahiman, Dr. Leow Pei Ling, and Assoc. Prof. Dr. Herlina Abdul Rahim as my co-supervisors for their valuable suggestions and constructive criticisms.

My whole appreciation to PROTOM-*i* research group members at Faculty of Electrical Engineering, Universiti Teknologi Malaysia especially Suzanna Ridzuan Aw, Fazlul Rahman Mohd Yunus, Bro Jaysuman, Juliza Jamaludin, Helen Goh, Nor Muzakkir, Naizatul shima, Mohd Fadzli, Saiful Badri, my friend Dr. Nurul Adila and process control laboratory technician Mr. Md Fadzli Bin Sahril for your helps and supports during my research. Also, thanks to my friends and all those whom had helped me in one-way or other during my research.

Special thanks to my parents for sharing their wisdoms and continued guidance during my study. To my lovely husband, Ahmad Syamrim, you are my better half, thank you for your constant encouragement and infinitive support from the beginning of my research. For my beloved daughters Iffah Humaira and Izzah Humaira, thank you for always cheering up for me.

I would like to thank Universiti Malaysia Pahang and Ministry of Higher Education for granting my scholarship. Last but not least, to Universiti Teknologi Malaysia for allowing me to use the facilities during my research is greatly appreciated and without it, this research could not have been carried out.

.

# ABSTRACT

Tomography is a technique used to reconstruct cross-sectional image of a pipeline for flow monitoring applications. There are several types of tomography system such as X-ray tomography, ultrasonic tomography, and electrical resistance tomography (ERT). ERT has many advantages compared to other types of tomography such as low cost, robust and no radiation. Thus, it becomes particularly suitable for industrial applications. However, it has been observed that the conventional practice of ERT through invasive sensing technique has exposed the ERT metal sensor to corrosion and limited its application because of inaccurate measurement of the data. Consequently, non-invasive ERT has also been introduced in low frequency (in kHz) applied to the ERT system. The low frequency ERT makes use of the phase-sensitive demodulation (PSD) approach and is a complicated technique to implement. Hence, the goal of this research is to design and develop a non-invasive ERT system with a high frequency (2 MHz) source. A total impedance of coupling capacitances (between metal electrode and conductive medium) series with resistance (conductive medium) for each pair of electrodes was assumed in the research. Based on the mathematical equation of the total impedance, a real part that is the resistance (conductive medium) must be larger than an imaginary part (capacitances), so that it easily to detect the concentration profile of the conductive medium. Therefore, the minimum frequency to ensure the real part is bigger than the imaginary one is 2 MHz. Simultaneously, the independent and flexible sixteen ERT electrodes designed for the system make it easier to replace and troubleshoot any problems with the sensor. In addition, the system carried out an experimental two-phase static liquid–solid regime for a linear back-projection algorithm using online configuration, with MATLAB as a software platform. It was also able to detect and visualize the non-homogenous system of the two-phase regime. Later, the reconstructed image was improved using a global threshold technique through offline configuration. The experiment results indicate that it could detect obstacles in a vertical pipe with minimum 12 mm in diameter and 4.5 cm in height, and above.

## ABSTRAK

Tomograpfi merupakan satu teknik yang digunakan untuk menggambarkan keratan rentas bagi saluran paip dalam aplikasi-aplikasi pemantaun aliran. Terdapat beberapa jenis sistem tomografi seperti tomografi X-ray, tomografi ultasonik, dan tomografi rintangan elektrik (ERT). ERT mempunyai banyak kelebihan jika dibandingkan dengan jenis-jenis tomografi yang lain seperti kos yang rendah, kukuh dan tiada radiasi. Maka, ia sangat sesuai untuk aplikasi-aplikasi industri. Tetapi, konvensional ERT melalui teknik penderia invasif menyebabkan penderia logam ERT terdedah kepada kesan kakisan dan ia menghadkan penggunaannya kerana pengukuran data yang tidak tepat. Maka, teknik penderia bukan invasif juga telah diperkenalkan dengan menggunakan frekuensi yang rendah (dalam kHz). Frekuensi rendah memerlukan kaedah penyahmodulatan peralihan fasa (PSD) dan ianya merupakan teknik yang rumit untuk dilaksanakan. Oleh itu, matlamat kajian ini adalah untuk mereka bentuk dan membangunkan sistem ERT tidak invasif dengan menggunakan sumber frekuensi yang tinggi (2 MHz). Anggapan jumlah galangan bagi setiap pasangan elektrod dengan mengambil kira gandingan kemuatan (antara elektrod logam dan bahan konduktif) sesiri dengan rintangan (bahan konduktif) digunakan dalam kajian ini. Berdasarkan persamaan matematik bagi jumlah galangan tersebut, bahagian sebenar mesti lebih besar daripada bahagian khayalan supaya lebih mudah untuk mengesan profil kepekatan bahan konduktif. Maka, frekuensi minimum bagi membolehkan bahagian sebenar lebih besar daripada bahagian khayalan ialah 2 MHz. Pada masa yang sama, enam belas elektrod ERT yang telah direka secara individu dan fleksibel membolehkan penderia lebih mudah diperiksa dan ditukar. Sebagai tambahan, sistem ERT telah dapat memantau eksperimen secara konfigurasi terus untuk linear kembali unjuran algoritma bagi dua fasa cecair-pepejal rejim yang statik; dengan MATLAB sebagai platform perisian. Ia juga telah dapat mengesan dan memberi gambaran bagi sistem dua fasa yang bukan homogen. Kemudiannya, kaedah ambang global melalui konfigurasi tidak terus untuk penambahbaikan gambaran tersebut telah digunakan. Keputusan eksperimen juga telah menunjukkan sistem ini boleh mengesan objek dalam paip menegak dengan ukuran diameter minimum ialah 12 mm dan tinggi sekurang-kurangnya 4.5 cm.

# TABLE OF CONTENTS

# LIST OF TABLES

# LIST OF FIGURES

## LIST OF ABBREVIATIONS

| | | |
|---|---|---|
| ERT | — | Electrical resistance tomography |
| ECT | — | Electrical capacitance tomography |
| kHz | — | Kilo hertz |
| PSD | — | Phase-sensitive demodulation |
| MHz | — | Mega hertz |
| PT | — | Process tomography |
| DAS | — | Data acquisition system |
| EIT | — | Electrical impedance tomography |
| UT | — | Ultrasonic tomography |
| LBP | — | Linear back-projection |
| FEM | — | Finite element model |
| PVC | — | Plasticized polyvinyl chloride |
| OT | — | Optical tomography |
| EQS | — | Electro quasi-static |
| MQS | — | Magneto quasi-static |
| 2D | — | Two-dimensional |
| PDE | — | Partial differential equation |
| kΩ | — | Kilo ohm |
| pF | — | Pico farad |
| mA | — | Mili ampere |
| 3D | — | Three-dimensional |
| MSSIM | — | Multi scale structural similarity |
| AE | — | Area error |
| $P_{Th}$ | — | Threshold pre-set value |
| I-to-V | — | Current-to-voltage |
| DDS | — | Direct digital synthesizer |

| | | |
|---|---|---|
| AC | — | Alternate-Current |
| DC | — | Direct Current |
| GBP | — | Gain Bandwidth Product |
| ADC | — | Analogue-To-Digital Conversion |
| PCB | — | Printed Circuit Board |
| GUI | — | Graphical User Interface |
| ANOVA | — | Analysis Of Variance |
| $V_{pp}$ | — | Peak-to-peak voltage |

# LIST OF SYMBOLS

| | | |
|---|---|---|
| $R$ | — | Resistance |
| $V$ | — | Voltage |
| $I$ | — | Current |
| $\sigma$ | — | Electrical conductivity |
| $L$ | — | Outer diameter pipe |
| $A$ | — | Area of electrode |
| $G$ | — | Conductance |
| $D$ | — | Electric flux density |
| $E$ | — | Electric field intensity |
| $J$ | — | Current density |
| $\rho$ | — | Free charge density |
| $B$ | — | Magnetic flux density |
| $H$ | — | Magnetic field intensity |
| $\omega$ | — | Angular frequency |
| $\varepsilon$ | — | Permittivity |
| $\mu$ | — | Permeability |
| $Z$ | — | Impedance |
| $C$ | — | Capacitance |
| $f$ | — | Frequency |
| $IM$ | — | Independent measurement |
| $N$ | — | Total sensors |
| m | — | Mili |
| $d$ | — | Thickness of non-conducting pipe |
| d | — | Outer plane thickness |
| $M$ | — | Sensitivity map |
| $G_T$ | — | Threshold image |

| | | |
|---|---|---|
| $\times$ | — | multiplication |
| $\cdot$ | — | Scalar multiplication |
| $\pi$ | — | Pi (3.142) |
| +/- | — | Plus or minus sign |

# LIST OF APPENDICES

# CHAPTER 1

# INTRODUCTION

## 1.1 Introduction

The word ‘tomography’ comes from the Greek: the term *tomos* means to slice, and *graphein* means to write [1]. The *Oxford English Dictionary* [2] defines tomography as:

> *Radiography in which an image of a predetermined plane in the body or other object is obtained by rotating the detector and the source of radiation in such a way that points outside the plane give a blurred image. Also in extended use, any analogous technique using other forms of radiation.*

Tomography’s introduction into the medical field started in the 1950s and led to the possibility of scanning the human body for diagnostic purposes. In medical fields, X-ray tomography was implemented firstly to image the internal human structure (bones) based on the attenuation of X-ray. This radiation-based method allows the medical staff to investigate the internal human structure or the object of interest non-invasively. As a result of this concept of tomography, the technique has become a pioneer for subsequent industrial applications.

Nevertheless, tomography used in the medical field is different from that used in industry, due to the different aims of the applications. Normally, medical tomography is used to determine a specific object in the space, whereas industrial tomography focuses on measuring phase proportions; for instance, the concentration of mediums and the velocity of movement. The development of tomography for industrial applications evolved in the 1980s. Process Industrial Tomography (PIT), known simply as Process Tomography (PT), is a term used for industrial applications. Process tomography has become a promising technique for visualizing and analysing the internal characteristics of process plants in industry applications, such as for two-phase/multiphase flow in pipelines. This PT consists of has many advantages: low cost, non-invasive, non-intrusive, no radiation hazards, and it is suitable for different sized vessels. Thus, process tomography is one of the most important techniques in industrial processes nowadays.

There are three main parts of process tomography: the sensing system; interfacing; and an image reconstruction algorithm for displaying the tomogram, as shown in Figure 1.1. The sensing system includes the sensor, measurement circuits for transmitting and receiving a signal, and signal conditioning circuits to amplify and filter the signal before they are used for the interfacing part. The interfacing part refers to the data acquisition system (DAS). Then, the information from the sensing system about the medium of interest will be used via the DAS in the image reconstruction algorithm for getting and analysing the image of interest, or the 'tomogram'. As a result, the different types of process tomography work based on the different principles of the sensors involved and implemented in the applications.

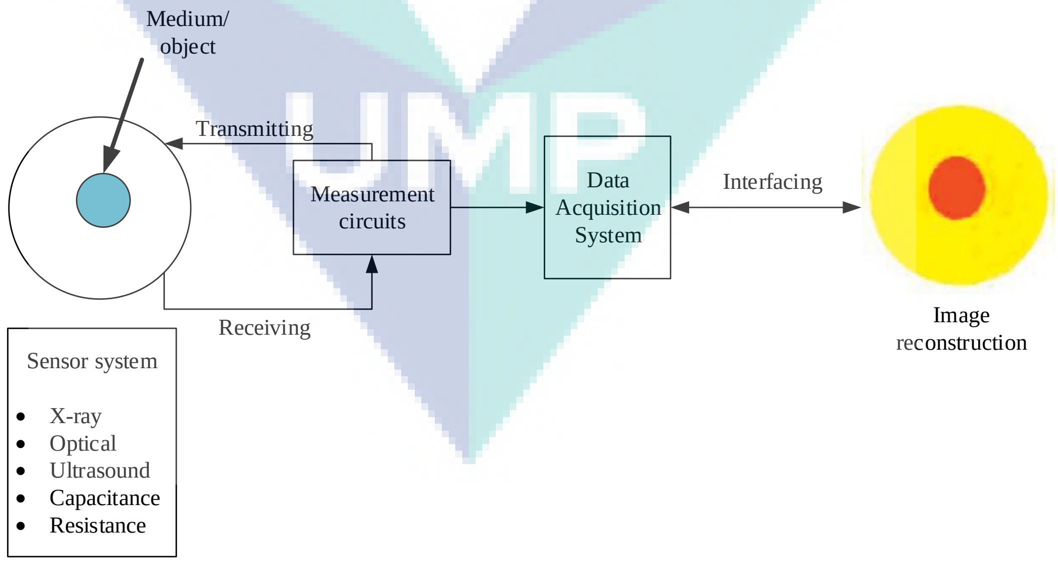


**Figure 1.1:** General system configuration of process tomography

Tomography can be divided into two fields: hard-field tomography; and soft-field tomography [3]. These classifications of tomography are referred to as the natural behaviour of sensors. Hard-field tomography refers to a condition where the sensitivity of the medium imaged is independent of the distribution of the measured parameters in its whole volume [4]. X-ray tomography, optical tomography, and ultrasonic tomography are examples of hard-field tomography. Soft-field tomography means that the sensitivity of the medium imaged depends on the distribution of the measured parameters in its whole volume [5]. Alternatively, this will cause a challenge in solving the inverse problem of the medium of interest. Electrical tomography can be categorized as a soft-field tomography that includes Electrical Capacitance Tomography (ECT), Electrical Impedance Tomography (EIT) and Electrical Resistance Tomography (ERT).

## 1.2 Sensing Technique of Process Tomography

Process tomography offers a unique opportunity to reveal the complexities of the internal structure of an object without the need to invade it. There are four types of sensing techniques for tomography: intrusive, non-intrusive, invasive, and non-invasive. The word ‘intrusive’ is related to how the sensor protrudes into the medium of interest, and ‘invasive’ means the sensor is applied to the inner surface of the wall of the pipeline. Additionally, the sensing techniques can be combined so that they can be intrusive and invasive, intrusive and non-invasive, non-intrusive and invasive, and non-intrusive and non-invasive as in [6,7]. These concepts are represented in detail in Figure 1.2. However, the non-intrusive and non-invasive is a well-known method applied in industry as it has several advantages. For example, it can avoid the contamination of pure or sterile materials, minimizing the hazards of working with poisonous, radioactive, explosive, flammable or corrosive materials, and decreasing safety and accountancy difficulties with valuable process materials. For this reason, the non-invasive and non-intrusive method is one of the favourite methods applied in process plants compared to other sensing techniques.

| Sensing Technique | Invasive | Non-Invasive |
|---|---|---|
| Intrusive | 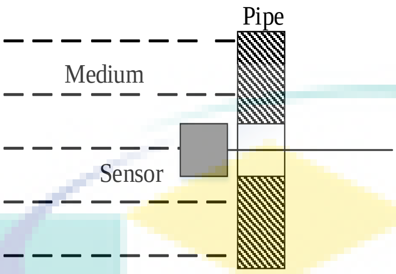 | 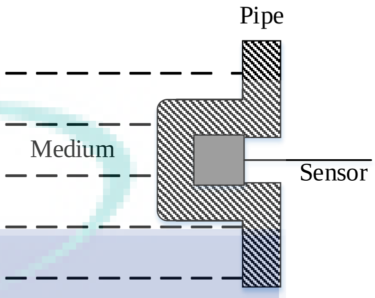 |
| Non-Intrusive | 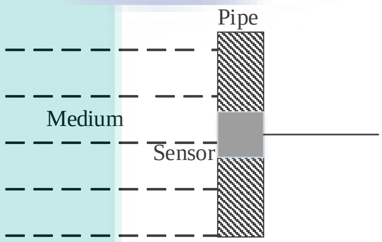 | 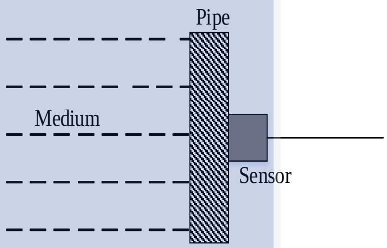 |

**Figure 1.2:** Types of sensing techniques

## 1.3 Research Background

A mixture such as liquid–liquid, liquid–solid and liquid–gas two-phase regime is the main concern in process industry applications. The industrial applications involving mixtures, for example, are bubble column, fluidized bed reactor, stirred tank reactor and vertical or horizontal vessel. Visualization of the mixture at an early stage in an industry application may promise good performance and prevent any unwanted conditions during the process. One of the methods that can do this prior visualization is process tomography. Process tomography is used to reconstruct the cross-sectional image of the medium of interest. As it is a non-destructive technique, process tomography has gained wide interest amongst researchers.

Electrical resistance tomography (ERT) is one of the most extensive modalities of process tomography being applied, and has been used in many applications such as in geological surface [8–11], agriculture processes [12,13] and also in industrial processes [14]. The advantages of the ERT application are that it is relatively safe to use and it provides fast response for online and real-time monitoring of the process plant. There are many examples of ERT systems that have been studied, focusing on imaging technique of the liquid–gas, liquid–liquid or liquid–solid mixtures. However, only a few researchers have considered ERT with a non-invasive sensing technique [15–21]. At present, non-invasive process tomography has become a promising imaging technique for monitoring, with potentially enormous applications for mixtures analysis. Therefore, the non-invasive ERT system for measuring and imaging mixtures of a static two-phase regime in a pipeline is proposed for this research.

## 1.4 Problem Statements

The following are the problems that need to be considered in the design of a non-invasive electrical resistance tomography system for liquid–solid profile measurement.

i. The conventional technique of ERT is applied invasively to the pipeline and causes the metal electrodes to have direct contact with the conductive liquid. The contact between the electrodes and the conductive liquid, such as electrolyte, causes an oxidation to the electrode, also known as an electrochemical erosion effect. This situation leads to electrode corrosion [16].

ii. The current researches into ERT systems produces inconsistency in measurements with unpredictable error [21]. Improper, invasive installation of the electrodes enables the electrodes to produce small bubbles around it when energized by the current signal. Thus, the signal cannot be transmitted and received appropriately.

iii. The use of an invasive ERT system in industrial applications is limited [19]. Limitation of conventional ERT is because the electrodes might affect the nature of the process flow, because the contact between metal electrode and conductive liquid can produce a chemical reaction.

Consequently, the solution to these problems is to use a non-invasive approach, whereby the sensor is clamped to the outside of the pipe wall.

## 1.5 Aim and Research Objectives

The aim of this research is to design and develop a non-invasive ERT system for a liquid–solid two–phase regime. The objectives of this research are as follows:

i. To design and develop a suitable ERT measurement section using a non-invasive sensing technique, including proposing the suitable excitation frequency and its electronic measurement systems.

ii. To interface the hardware and software for system validation. This validation is demonstrated by the concentration profile computations using online configuration.

iii. To reconstruct the image of a phantom position, using non-invasive ERT system.

## 1.6 Research Scopes

In developing the non-invasive electrical resistance tomography system to monitor the two-phase regimes of liquid–solid; the scopes of the research will comprise of:

i. The sensor consists of sixteen electrodes that perform as transceiver-sensing operation and clamped on an experimental pipe non-invasively.

ii. Non-invasive ERT development and analysis is conducted on a vertical non-conducting (acrylic) pipe with 100 mm outer diameter and 2 mm wall thickness. The specification of the pipe used in this research does not reflect a vessel applied in industrial applications.

iii. The experimental will be only tested for static flow with tap water and a wooden rod as the conductive liquid and phantom, respectively.

iv. Only one set of measurement data is collected for every experiment conducted in the research. The collection of data is through online configuration.

v. The image reconstruction application is based on existing back-projection algorithms, with no new derivation of an image reconstruction algorithm in this research. The tomogram is reconstructed based on a linear back-projection algorithm through online configuration, and improved using a global thresholding technique through offline configuration.

## 1.7 Motivation and Contribution

The development of ERT systems in existing studies indicates that most studies have focused on the invasive ERT system. Only several papers have studied the non-invasive ERT system technique [15–21]. However, the presented papers did not particularly discuss hardware designation and development. Therefore, the work in this thesis has thus designed and developed a non-invasive ERT system using 2 MHz frequency that can produce an analysis for multiphase mixtures.

In addition, most of the presented works in the cited literature for ECT and ERT develop the system with a frequency in kHz. At this point, a phase-sensitive demodulation (PSD) method using sophisticated circuit design also needs to be developed in conjunction with the ECT or ERT system, to measure the internal permittivity or internal conductivity. Thus, in this work, it is proven that by developing the non-invasive ERT system with a high frequency level, the PSD technique is not required. The utilization of a high frequency level enables the system to detect the concentration profile of the medium of interest.

Furthermore, corrosion-free electrodes and no contact with the flow in the medium in the non-invasive ERT system introduced a non-invasive conductivity conductor for industry. Thus, it can provide the system with better sensing accuracy.

Moreover, any damage of the sensor occurring in the system can easily be replaced and dealt with in non-invasive ERT. The independent and flexible design of the research enables it to reduce the duration of the troubleshooting process.

## 1.8 Structure of Thesis

The thesis consists of seven chapters as summarized below:

i. Chapter 1 briefly describes the background of tomography, types of sensing techniques, research background, problem statement, the aim and research objectives, scopes and the study's contribution.
ii. Chapter 2 is the literature review of non-invasive process tomography, current works related the electrical resistance tomography (ERT), the basic principles of non-invasive ERT and also image reconstruction applied in industrial tomography.
iii. Chapter 3 presents the modelling of the non-invasive ERT system that focuses on the optimum frequency source and optimum electrode dimension using COMSOL software.
iv. Chapter 4 discusses solving the forward problem of the system, back-projection algorithm for image reconstruction, the image quality assessment and improving the tomogram using a thresholding technique.
v. Chapter 5 provides details of the hardware and measurement systems, such as the design of electronic measurement circuits, hardware jig and metal sensor, together with the software part of the developed system.
vi. Chapter 6 presents the experiments, results and discussion and compares these with the simulation results. It involves two parts; sensor performance analysis and image reconstructed analysis.
vii. Chapter 7 provides the conclusion to the study and suggestions for future work.

# CHAPTER 2

# LITERATURE REVIEW

## 2.1 Introduction

The aim of this chapter is to review the current research on the non-invasive process tomography approach that has been conducted in previous works. This chapter also presents previous studies on conventional and non-invasive electrical resistance tomography. Also, the basic principles regarding non-invasive ERT, including resistance and conductivity, quasi-static electric field and measurement strategy, are explained. Lastly, this chapter reviews image reconstruction in the process tomography.

## 2.2 Current Research on Types of Non-Invasive Industrial Tomography

Two-phase regimes of non-invasive industrial tomography are reviewed, from 2004 till the present. The types of non-invasive tomography delineated in the following sub-sections are X-ray tomography, Ultrasonic tomography, Optical tomography and Electrical Capacitance tomography.

### 2.2.1 X-ray Tomography

X-ray tomography was the first type of tomography introduced in medical applications during the 1970s. This then expanded into industrial processes, where it is now established. X-ray tomography reconstructs the image based on attenuation of the X-rays. X-ray tomography is used widely in chemical mixtures for detecting liquid–gas phase flow compared to other types of two-phase flow. An investigation of liquid–gas in a large bubble column (approximately 32 cm in diameter ) has been reported by [22, 23]. Hubers *et al.* [22], for instance, presented an investigation of X-ray tomography for a bubble column with diameter 32 cm and length of almost 4 m. Tubes of different sizes and materials were applied for the study, such as acrylic tubes (6.35 mm, 9.53 mm, 12.27 mm, and 12.6 mm), Teflon (6.35 mm) and PVC tubes (8.99 mm and 12.7 mm). Based on the filtered back-projection, by comparing the real position of the tubes in the column with the image obtained, it is observed that the system is capable of visualizing the water–gas in a large bubble column.

In addition, the research on X-ray tomography also focuses on improving the quality of the reconstructed image just as in the applied cross-correlation method [24] and algebraic reconstruction technique (ART) [25]. Moreover, X-ray tomography is also compared with a wire mesh sensor as two high-speed imaging modalities. The wire mesh sensor can provide a phase fraction distribution in the cross-section of the flow. However, the wire mesh sensor uses the intrusive and invasive technique. Thus, modality X-ray tomography with wire mesh is not a non-invasive technique. However, dual-modality with the combination of X-ray tomography and wire mesh sensor was found to produce a better-reconstructed image compared to a single modality X-ray tomography, as in [26, 27]. The study concerned measured the water–gas flow in a vertical pipeline. Boden *et al.* [28] presented the implementation of X-ray cone beam tomography (CBCT) in chemicals in a stirred tank reactor. The dimension of the stirred tank reactor in the research was 0.008 m thick with an inner diameter of 0.08 m. The material of the stirred tank reactor was borosilicate glass. It showed a different image when the gas velocity increased from 1000 min$^{-1}$ to 1200 min$^{-1}$.

Even though X-ray tomography is useful for producing a high resolution for the images reconstructed, the subject of hardware development is not discussed in detail. In addition, the technique needs a specialist to operate the system and the main disadvantages of X-ray tomography are its expense and the need for major safety precautions related to radiation issues.

### 2.2.2 Ultrasonic Tomography

Ultrasonic tomography (UT) works based on the interaction between the ultrasonic wave and the measured medium. The capability of ultrasonic sensors depends on the frequency of interest and also the beam angle of the sensors. High frequency and a large beam angle influence the result of the reconstructed image of UT because the acoustic impedance of the UT is increased, and the area covered by each of the sensors is high enough to cover the projected area. In addition, the number of sensors used also affects the reconstructed image. If the number of sensors around the pipeline is increased, the image will be more accurate because the projection signal covers most of the area inside the pipeline. In ultrasonic tomography, the voltage received by the ultrasonic receiver is processed to reconstruct the image of the medium of interest. Recently, UT has also been applied in chemical application to detect chemical mixtures such as liquid–liquid, liquid–solid, and liquid–gas.

Abdul Rahim *et al.* [29] presented a principle study on transmission ultrasonic tomography for oil–water phase flow using four pairs of ultrasonic sensors in a horizontal pipeline. The initial results of the average output voltage for each of receivers were plotted, and it was concluded that the average voltage dropped when the percentage of oil in the pipeline rose. Correspondingly, an experiment with 16 pairs of ultrasonic sensors and parallel projection with different kinds of oil such as corn oil, soybean oil and palm oil in water flow was discussed by Fazalul Rahiman *et al.* [30]. The linear back-projection (LBP) algorithm was used for the purpose of getting the tomogram. The paper also explained in detail the implementation of a LBP algorithm to the system, including the calculation of the percentage error between the real condition and the measurement sensor values for each of the water and oil compositions. Thus, the accuracy of the tomogram can be obtained based on that percentage measurement. In addition, Steiner *et al.* [31] applied UT for detecting oil–water. Parallel projection with 16 pairs of ultrasonic sensors was used in the study, which focused on the time-of-flight method applied in UT system. It is reported that the method was able to determine the oil-water interfaces in the oil production.

Additionally, the work by Wockel *et al.* [32] proposed the detection of interfaces between a phase flow of solid acryl and liquid kernel layers. 2D ultrasonic propagation in the vessel was modelled by using a finite element model (FEM) in COMSOL Multiphysics software. The research implemented a fast estimation algorithm for the reconstructed image, and it was observed that the system produced a high-quality tomogram of the liquid–solid phase flow. Moreover, the detection of water particles in a vertical PVC pipe was then investigated in [33]. Different sizes of PVC plastic rod assumed as particles (12 mm, 26 mm, and 60 mm) were used in the study to work out the smallest sizes of particles that could be detected by the UT system.The result showed that the detection of the smallest sizes of particles dropped depending on the ultrasonic wavelength; if the object could block the wavelength, information on the sensing area could be determined. Muhamad *et al.* [34] employed UT in investigating the water–solid flow regime in a vertical pipeline. By using four pairs of ultrasonic sensors in fan beam geometry, the UT system could be used to detect the solid medium in the vessel.

In the work by Zakaria *et al.* [35], the competence of different numbers of sensors in the projection for water–gas phase flow in a horizontal pipe was discussed in detail. A transceiver type of the ultrasonic sensor which can function as a transmitter or receiver was used in the study. The advantage of using a transceiver in the UT system is that fewer sensors are needed to produce the same quality as separate ultrasonic sensors. Simulations using 8, 16 and 32 transceivers at 40 kHz were compared, and it was concluded that the 32-transceiver set-up was the optimum number of sensors to produce a good reconstructed image of the water–gas. Supardan *et al.* [36] described the pattern of gas hold-up distribution in a bubble column. In the research, the column applied was a methyl- methacrylate material, 16 cm in diameter and 200 cm in height. The research deployed three parallel ultrasonic transducer arrays, and each array had six pairs of ultrasonic sensors in parallel geometry. Simultaneously, each array was arranged non-symmetrically and rotated at 20º. The gas sensed by the UT system was between 5.8 mm and 6.1 mm in mean diameter for 2 MHz frequency. The photograph of the bubble column was captured to validate the tomogram of gas hold-up in the column.

The reflection mode of ultrasonic tomography system applied to liquid–gas detection in an insulating pipe with fan beam geometry was investigated by Steinar *et al.* [7, 31]. Furthermore, ultrasonic tomography based on 32 transceivers at high frequency (333 kHz, 125° beam angles) for detecting gas hold-up in a bubble column progressively was studied by Fazalul Rahiman *et al.* [37–40]. The novelty of the adjacent criterion method in the inverse problem was proposed in the study, and it proved that the smallest size of bubble that could be sensed by the bubble column was 2.84 mm. However, Nor Ayob *et al.* [41–43] improved the study for detecting the gas size in the bubble column. The minimum size of gas detected in the bubble column was smaller than that in the research by Fazalul Rahiman *et al.*, namely, 2.5 mm. Otherwise, the UT system used 333 kHz and 16 pairs of ultrasonic sensors but in a dual plane by using the cross-correlation method.

UT has advantages for detecting chemical mixtures, and the sensors for ultrasonic tomography are readily available from manufacturers. However, it is very expensive if the number of ultrasonic sensors used increases ( i.e., 32 pairs and above) for a high resolution reconstructed image.

### 2.2.3 Optical Tomography

Optical tomography (OT) is applied mostly to the chemical mixtures application for investigating two-phase liquid–gas flow measurements compared to the liquid-liquid and liquid-solid two-phase flow measurements. Optical tomography reconstructs the image based on optical radiation [44], transmitting a beam of light from one boundary and receiving the beam of light from another boundary. Optical radiation can be obtained by using different kinds of optical sensor, such as laser, linear CCD, and LED. Schleicher *et al.* [45] proposed bubble flow detection in a low gas fraction in a bubble column (acrylic pipe with an outer diameter 280 mm and inner diameter 50 mm). The system implements LED as the optical transmitter and optical fibre as the receiver. The minimum size of the bubble detected in this paper was 0.1 mm, and the maximum size was 10.3 mm. It is observed that, based on the back-projection algorithm, the system can improve the quality of the image of the bubble flow in the bubble column.

Similarly, Md Yunos *et al.* [46] implemented a linear CCD sensor as an optical sensor for measuring bubble flow in a vertical pipeline. The linear CCD sensor applied was ILX503A, which contains 2048 sensors (effective pixels). It was observed that the ILX503A limits the bubble velocity up to 0.04 m/s when the sampling is at 1 MHz. Moreover, research on improving the reconstructed image of the liquid–gas phase flow was introduced by using a hybrid back-projection algorithm in [47]. The authors in [47] used four dichroic halogen bulbs acting as light projectors for two planes of optical-fibre receivers. Every plane consists of 8 × 8 arrays of orthogonal and 11 × 11 array of rectilinear projections. Here, the minimum size of gas that could be detected by the system was 20 mm. However, in 2013, Mohd Fadzil *et al.* [48] proposed optical tomography for a vertical bubble column (130 mm in outer diameter and 1.2 m in length). Here, sixteen laser pointers and sixteen photodiode model EPD-660-5 were chosen as transmitters and receivers, respectively. The study discussed the detail of the hardware development needed to ensure that the OT system is capable of detecting the bubble flow in the bubble column.

However, the limitation of optical tomography relates to the limitation of its optical surface. The sensors cannot be placed too close to each other so as to avoid reflection, and can only detect the image in between the area of the optical sensors.

### 2.2.4 Electrical Capacitance Tomography

Electrical capacitance tomography (ECT) is the first type of tomography that evolved in industry from the 1980s. ECT reconstructs the image based on the permittivity distribution of the medium of interest [49]. In other words, ECT is also known as a dielectric system. Essentially, ECT is applied non-invasively to the system. The conductive electrodes are mounted on the periphery of the pipeline or vessel, and shielding is necessary to eliminate the external electrical interferences and also to protect the electrodes from damage [50]. The permittivity of the medium can be investigated, and the capacitance value between adjacent electrodes in terms of different potential units can be measured. Later, the image is reconstructed based on the capacitance data and the algorithm applied.

ECT is used in chemical mixtures for detecting liquid–liquid, liquid–solid and liquid–gas. For example, Chen and Han [51] discussed in detail the improvement of high-speed, high-image resolution, with little measurement error for oil–water two-phase flow in ECT. Here, the authors focused on the development of the image data-capture system (IDCS) for better ECT system performance. However, application of ECT in detecting liquid–liquid flow in chemical mixtures was not investigated greatly by the researchers. Cao *et al.* [52] presented the development of ECT for liquid–solid two-phase flow. Water and polyethylene particles were placed in different types of flow in the pipeline, such as annular flow, core flow and laminar flow. The paper detailed the hardware development for liquid–solid flow in a vertical insulating pipeline with a frequency of 500 kHz and implemented digital signal processing (DSP). As a result, the system was capable of getting a good image of the medium of interest using linear back-projection (LBP), the Landweber method and the Newton algorithm. The image colour from red to blue indicates that the permittivity of the material is increasing; blue and red denoted for minimum and maximum permittivity, respectively. However, it can be observed that the image reconstructed by LBP was closer to the real image in the pipeline compared to the iterative algorithms such as the Landweber and Newton algorithms. In addition, the multiple trickle system with different positiona of different numbera of organic glass roda in the pipeline was also tested in [52] for the purpose of comparing the effectiveness of the algorithms. Thus, it can be concluded that an LBP algorithm is more suitable for a simple system whereas an iterative algorithm is suitable for the multiple trickle system.

In 2013, research on ECT was improved for measuring the capacitance of micro-particles in deionized water for a micro-channel with different particle diameters used, such as 1.3 mm, 1.5 mm, and 2.1 mm, as in [53]. A quartz glass-diamond-shaped micro-channel of 800 μm (height), and 700 μm (width) was used for the purpose of the study. Also, the size of every twelve platinum electrodes applied to the system was 200 μm (length) × 0.25 μm (height). In micro-channel research, owing to the small sizes of particles, the frequency for the ECT system is 12.5 MHz. More importantly, the frequency used in a large diameter pipeline is low compared to a small diameter pipeline. Thus, the size of the pipeline and the medium of interest will influence the frequency used in the ECT system.

In reviewing the application of ECT for chemical mixtures, liquid–gas two-phase flow emerged as a primary concern for researchers compared to liquid–liquid and liquid–solid two-phase flow. Different approaches and improvements have been proposed by researchers for detecting water–gas flow in chemical applications, such as Yang *et al.* [54] and Yu & Deyun [55]. In addition, Teixeira and Fan [56], Al-Masry *et al.* [57], and Banasiak *et al.* [58] presented 3D ECT for detecting liquid–gas flow in the pipeline. In particular, glycol–gas detection in horizontal and vertical pipelines in 3D was compared, for instance, with the equivalent image from a CCD camcorder view. In [58], owing to the high density of the mesh used in 3D ECT, which is around 111 k tetrahedrons for forward problem and 80 k tetrahedrons for the inverse problem, the 3D images were made using GPU NVidia CUDA acceleration (CUDA technology). This is a promising and useful method of detecting liquid–gas two-phase flow in chemical usage, because it produces precise and more accurate conditions for the medium in the pipeline compared to a 2D image.

Instead of water–gas detection, researchers were also concerned about oil–gas detection using the ECT system, especially for the oil and gas industry. Gamio *et al.* [59] presented an oil–gas detection method for a pressurized pipeline. An insulating pipe with 12 electrodes mounted on the periphery of a 7.62 cm diameter horizontal pipeline was used for that purpose. Here, the gas velocity was from 0 to 16.5 m/s, and linear back-projection was used as a reconstruction algorithm. Despite not focuing on the hardware development, some researchers also focused on improvement of the ECT image based on the inverse problem, such as a hybrid algorithm [60], simulated annealing for non-metallic pipes [61] and fuzzy logic [62]. Xie *et al.* [62] applied the diesel fuel flow rate (0–15 $m^3$/h) and air flow rate (0–30 $m^3$/h) to a horizontal pipe.

Mohamad *et al.* [63] proposed a new design of an ECT sensor system that is segmented and portable for two-phase flow such as water–gas, palm oil–gas and water–palm oil detection. The ECT system offers industry a more flexible measurement for two-phase flow. Zhao *et al.* investigated oil–gas detection in a small diameter (26 mm) pipeline. [64]. They focused on the high viscosity effect on the characteristics of oil–gas with the oil velocities (0.06–0.5 m/s) and gas velocity (0.3–12.0 m/s). In addition, Zhang *et al.* [65] investigated dual-modality tomography (ECT-gamma source) for a horizontal acrylic pipe in measuring the oil–gas phase flow. The different size of gases tested at different locations in the pipeline in the research were 8 mm, 12 mm, 16 mm, 22 mm, and 29 mm. It was observed that the combination of dual-modality tomography could improve the image reconstructed for the system.

However, ECT systems have many advantages when analysing the chemical mixtures if the main concern of the study is an insulating medium rather than a conductive medium such as oil, gas and particles. On the other hand, if the main concern is a conductive medium such as water, another type of process tomography could be used.

## 2.3 Recent Works Related to Electrical Resistance Tomography

Conventional Electrical Resistance Tomography (ERT) uses an invasive but non-intrusive sensing approach. The invasive technique is used to make sure that there is continuous contact between the electrodes and main fluids so that the current can be conducted through the medium of interest [14]. Later, the resistance of the medium can be determined, and the electrical conductivity distribution of the medium interest can be reconstructed. Table 2.1 is a summary of recent research on conventional ERT systems [66–89] in the last ten years, applied to two-phase regimes with different types of mixtures.

**Table 2.1:** Summary of conventional ERT for two-phase mixtures

| Types of chemical mixtures | Authors | Application |
|---|---|---|
| Liquid–liquid | [66] | Water–oil flow in horizontal pipe |
| | [67] | Water–oil drop for wet logging |
| | [68] | Water–200 ml brine of concentration 10 g/l in stirred vessel |
| | [69] | Dichloride methane – water and toluene – water in plant reactor |
| Liquid–solid | [70] | Particle distribution in the micro-channel |
| | [71], [72] | Percentage of total solid-content milk for milk-powder production |
| | [73], [74] | Percentage of total solid-content milk for milk-powder production but in 3D |
| | [75] | Particle size glass beads (210–1500mm)- solid concentration tap water (5–30 wt%) in an agitated tank |
| | [76] | Liquid–solid circulating fluidized beds (LSCFB) [glass beads particles (spherical shape, 2500 kg/m$^3$ & irregular shape, 2210 kg/m$^3$)] |
| | [77] | Solid–liquid in wet particulate processing |
| | [78] | Pulverized kaolin clay and water |
| Liquid–gas | [79] | Gas dispersion performance of an aerofoil impeller and a standard Rushton turbine (pure water–8 L/min gas flow rate) |
| | [80] | Characterization of high concentration ionic bubble column<br><br>(homogeneous regime at 0.85 cm/s, heterogeneous regime at 2.5 cm/s slug flow regime at 4.2 cm/s) |

| | | |
|---|---|---|
| | [81] | Mixing in air–water flow (air-suspension flow: 3.0 m/s, 0.11 m/s, 5.0 m/s ) |
| | [82] | Bubble distribution in bubble column for volume fraction<br><br>(gas flow rate: 0.04 m/s, 0.07 m/s, 0.09 m/s, 0.11 m/s, 0.13 m/s, 0.16 m/s, 0.18 m/s) |
| | [83] | Gas–liquid slug vertical pipe flow with data fusion from electromagnetic flow meter |
| | [84] | 3D gas holdup in the flotation cell (gas flow rate: 0.20 cm/s, 0.67 cm/s) |
| | [85] | Performance of a counter-current bubble column<br><br>(gas flow rate: 0.28 cm/s, 0.56 cm/s, 0.84 cm/s, 1.12 cm/s) |
| | [86] | Slug flow of horizontal pipe validated with CCD |
| | [87] | Flow-rate measurement of air–water |
| | [88] | Bubble velocity in swirling the flow<br><br>(water–gas velocity:0.63 m/s/, 0.065 m/s,0.037 m/s, 0.41 m/s/ 0.068 m/s) |
| | [89] | Liquid–gas velocity in vertical upward pipe by using cross-correlation |

A conventional ERT electrode has direct contact with a fluid. In this case, it causes the electrochemical erosion and polarization effects to the sensor and may cause unpredictable measurement error to the system. This limitation of a conventional ERT system limits the practical application in industrial plant. It follows that in 2010, a group from Tianjin University proposed a non-invasive ERT system for chemical mixtures. This means that the new approach for an ERT system does not have direct contact with the fluid. The researchers Cao *et al.* [15] started with sixteen electrodes applied on the horizontal acrylic pipeline, and the image between water–gas with a stratified flow gave a good result (as shown in Figure 2.1). Also, the sensor configuration was similar to an ECT system. This means that the image reconstruction for non-invasive ERT was similar to that achieved with a reconstruction algorithm in ECT. The image reconstructed was compared between back-projection and Lavrentiev regularization. However, the first non-invasive ERT just applied an impedance analyser (Agilent 4294A) as a source for the exciting electrode and signal-conditioning process with a frequency of 1 MHz. No detail was given regarding the development of the hardware part of the system.

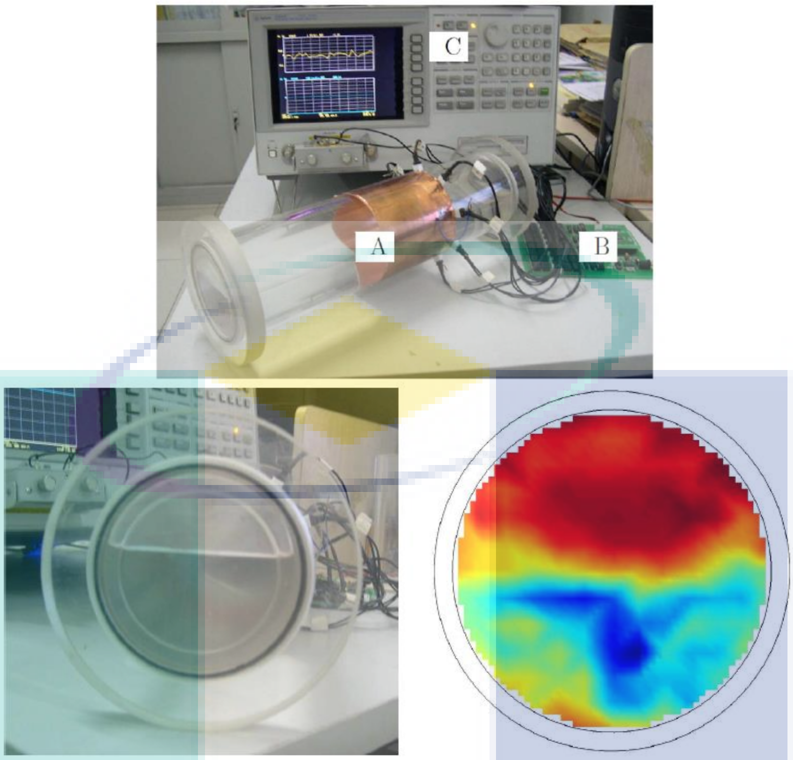


**Figure 2.1:** ERT system using ECT sensor [15]; A. ECT sensor, B. Switching unit, C. Impedance analyser (Agilent 4294A )

Similar research had been carried out in [18] by implementing the ECT sensors to reconstruct the conductivity material at a high frequency but with a different principle applied, based on dielectric spectroscopy. The medium was assumed to be like the complex capacitance and the conductive material became like the dielectric medium at high frequency. The linear back-projection algorithm was applied to generate the tomogram. That aside, the research of the non-invasive ERT only used the impedance analyser (HP4192A) for the data acquisition for 200 kHz and 2 MHz source frequencies. Again no hardware development was focused on in the research.

Later, a group from Zhejiang University, Wang *et al.* [16,17], [19–21], improved the research by designing and developing twelve segmented electrodes for non-invasive ERT. The study was based on capacitively coupled contactless conductivity detection ($C^4D$). Phase-sensitive demodulation (PSD) was a main component of the AC circuit used for the study. A voltage signal was used as the excitation source and the current signal was measured on the detection electrodes. Figure 2.2 illustrates the sensor configuration and the image reconstructed in annular flow. The optimum sensor configuration was modelled based on a finite element model (FEM) in COMSOL Multiphysics software. The latest study shows that it was implemented for detecting liquid–solid (water–plastic rod as a solid medium) in a vertical insulating pipeline. A frequency of 100 kHz applied in the non-invasive ERT system was much lower than in the first and second non-invasive ERT system. In this case, ERT can be known as one type of process tomography that offers advantages to the system when the primary medium is a conductive medium rather than an insulating medium.

Based on the review of invasive versus non-invasive ERT systems from previous works, it is observed that the non-invasive approach provided benefits for measuring concentration profile of the medium of interest; for example, it was easy to handle and troubleshoot the sensor, and the lifespan of the sensor increased as well. However, the limitations regarding the lack of discussion about the hardware part, such as the electronic measurement circuit designation and development which only tested using impedance analyser, and designs which only use phase-sensitive demodulation (PSD), have resulted in the aims of this particular study.

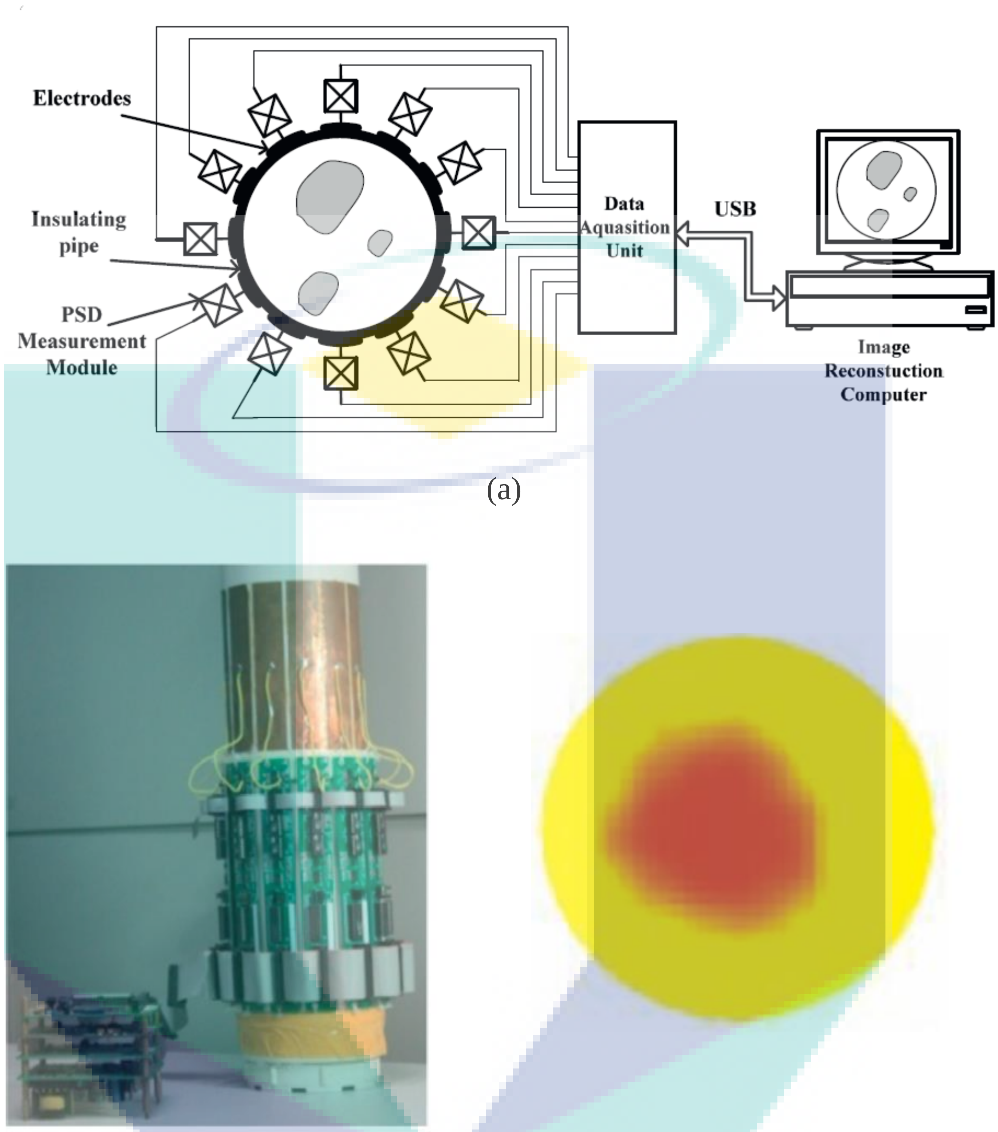


(b) (c)

**Figure 2.2:** (a–b) Segmented non-invasive ERT system; (c) example of reconstructed image for annular flow [20]

## 2.4 Basic Principles of Non-Invasive ERT System

In this sub-section, an overview of basic principles and the measurement strategy on the insulating pipe wall for non-invasive ERT is presented. This review is important in conducting research on non-invasive ERT systems.

### 2.4.1 Resistance and Conductivity

Electrical resistance tomography is used to reconstruct the image based on the resistance distribution, or the conductivity distribution of the medium of interest. Thus, it is important to know the basic principle of resistance and conductivity. Resistance is an element that indicates its capability to oppose the flow of electric current. Ohm's law states that the voltage, $V$ across a resistor is directly proportional to the current, $I$ flowing through the resistor, $R$ [90]. This law is expressed in Equation (2.1).

$$R = \frac{V}{I}\ (\Omega) \tag{2.1}$$

In process tomography applications, the resistance can be measured by exciting voltage (or current) and detecting current (or voltage) via sensors mounted on the circumference of the pipe walls [75]. In addition, conductivity of the medium is a measurement of electron flow in a medium under the influence of an external electric field. It is a criteria used to classify the medium as a conductor or insulator.

A conductor has many free electrons that can move with random direction and velocity. If the external electric field were applied, this free electron would move from one atom to another atom. In addition, the movement of the electron is in the reverse direction to the external electric field and has an average velocity. Thus, it will conduct an electric current through this medium. However, an insulator does not have a free electron, hence, it will not allow the electric current to flow through the medium, even though an external electric field is applied. A perfect insulator has a zero value of conductivity whereas a perfect conductor has an infinite value of conductivity. The electrical conductivity, $\sigma$, can be described based on Equation (2.2) [91, 92].

$$\sigma = \frac{L}{RA}\ (\Omega\text{m}) \tag{2.2}$$

For a non-invasive ERT system, $R$ is the resistance of the medium of interest, $L$ is the outer diameter of the pipe, and $A$ is the area of the electrode. It is observed that, the $\sigma$ is inversely proportional to the $R$. Thus, the conductance, $G$ can be defined as in Equation (2.3) [93].

$$G = \frac{\sigma A}{L} = \frac{I}{V} = \frac{1}{R} \tag{2.3}$$

However, most researchers use an insulating pipe as a vessel, with the non-invasive ERT sensor mounted on the periphery of the non-conducting pipe wall. Hence, the current signal cannot be applied as a source because it will prevent the electricity from penetrating the non-conducting pipe. Therefore, the non-invasive ERT system applies a voltage as a source and measures the current as a received signal. The dimension of the electrode of the non-invasive ERT also is very important in order to make sure that the signal can be transmitted and received appropriately. For this reason, if the rectangular electrode is the main concern, the area of the electrode in terms of the width and height will play a vital role in influencing the output current of the non-invasive ERT system. The large size of the electrode is needed to reduce the spatial resolution of the inverse problem of the reconstruction part in tomography [94]. In an ideal case, based on Equation (2.3), the excitation electrode of a non-invasive ERT system should be as small as possible and the detection electrode should be as large as possible. However, it is difficult to implement them practically because the same electrode is used alternately as the excitation and detection electrode. So, it is very important to design and optimize the best dimension of the size of the electrode to be implemented in the real system of a non-invasive ERT system.

### 2.4.2 Quasi-Static Electric Field

The electrical tomography technique applies knowledge of electromagnetic field theory. In electromagnetic field theory, Maxwell’s equations are key to describing the electromagnetic phenomena. Based on Maxwell’s equation, it will cause the field of the electrical tomography system to be an electrostatic field, a magnetostatic field, an electromagnetic field or a quasi-static field, depending on the field of interest and the medium considered.

The quasi-static approximation can be divided into two conditions: electro quasi-static (EQS) and magneto quasi-static (MQS) [95]. In EQS, the magnetic induction is neglected, and results in the system are influenced by the capacitive effect. In addition, the MQS is only influenced by the inductive effect, and the displacement current is neglected. Since the non-invasive ERT only considers conductivity distribution, the EQS was applied for the system. Hence, the Maxwell equations for EQS [95] are represented as follows:

$$\nabla.\boldsymbol{D} = \rho \text{ (Gauss law)} \tag{2.4}$$

$$\nabla.\boldsymbol{B} = 0 \text{ (Gauss law)} \tag{2.5}$$

$$\nabla \times \boldsymbol{H} = \boldsymbol{J} + j\omega\boldsymbol{D} \text{ (Ampere's Law)} \tag{2.6}$$

$$\nabla \times \boldsymbol{E} = 0 \tag{2.7}$$

***D*** is the electric flux density, ***E*** is the electric field intensity, ***J*** is the current density and $\rho$ is the free charge density. ***B*** is the magnetic flux density, ***H*** is the magnetic field intensity and ω is the angular frequency. Also, the relationship between ***D*** and ***E***, ***J*** and ***E***, and ***B*** and ***H*** can be represented in Equations (2.8)–(2.10).

$$\boldsymbol{D} = \varepsilon\boldsymbol{E} \tag{2.8}$$

$$\boldsymbol{J} = \sigma\boldsymbol{E} \tag{2.9}$$

$$\boldsymbol{B} = \mu\boldsymbol{H} \tag{2.10}$$

where ε, σ, and μ are the permittivity, conductivity and permeability, respectively.

Non-invasive ERT considers the voltage as the excitation signal and current as the detection signal. So, it is important to know the sensing field principle in the system and also how the current signal propagates and can be measured at the detection electrode. Based on Equation (2.6) if we multiply the equation with divergence of each side, we get:

$$\nabla \cdot (\nabla \times \boldsymbol{H}) = \nabla \cdot (\boldsymbol{J} + j\omega\boldsymbol{D}) \tag{2.11}$$

Since, the divergence of the curl is identically zero, the equation of continuity [96] is given by,

$$0 = \nabla \cdot \boldsymbol{J} + \nabla \cdot j\omega\boldsymbol{D} \tag{2.12}$$

Knowing that, the potential gradient is $\boldsymbol{E} = -\nabla V$ [97], where $V$ is the potential distribution. Substituting Equation (2.8), Equation (2.9), and ***E*** into Equation (2.12), the EQS equation of sensing field in the non-invasive ERT system can be shown in Equation (2.13).

$$\nabla \cdot (\sigma + j\omega\varepsilon)\nabla V = 0 \quad \textbf{(2.13)}$$

Based on Equation (2.13), it is clearly seen that the non-invasive ERT is based on the $\sigma$ and relative permittivity, $\varepsilon$, which is due to the conductive medium, and non-conducting pipe implemented. $\omega$ represents the angular frequency of the excitation source. Likewise, Equation (2.13) is also known as Poisson-type differential equation. The main reason why EQS plays important role in the sensing field is a result of the need for current flow through two different mediums: the non-conducting pipe and the conductive medium. The specific boundary condition of the sensing field of a non-invasive ERT system in two dimensions is determined by Equation (2.14) [20].

$$\text{Quasi-static electric field } (x,y) = \begin{cases} \nabla \cdot (\sigma(x,y) + j\omega\varepsilon(x,y))\nabla V(x,y) = 0 & (x,y) \subseteq \Omega \\ V_i(x,y) = V_0 & (x,y) \subseteq \Gamma_i \\ V_j(x,y) = 0 & (x,y) \subseteq \Gamma_j \\ \dfrac{dV(x,y)}{dn} = 0 & (x,y) \subseteq \Gamma_k, (k \neq i, j) \end{cases} \quad \textbf{(2.14)}$$

$\Gamma_i$ and $\Gamma_j$ represent the spatial locations of n electrodes; i and j are the indexes of excitation and detection electrodes respectively, and $V_o$ is the voltage applied to the system.

The modeling to prove the concept can be done and analysed by using Finite Element Model (FEM) simulation software, COMSOL Multiphysics. Based on the simulation, the author felt that the current value between every pair of electrodes can be obtained from Ampere’s law in the Maxwell’s equation of EQS that is totally different when compared to Ref. [20]. Based on Ampere’s law, if considering the integral form, we get the total current equation on the surface of the sensing field [98] as in Equation (2.15):

$$\oint_c \boldsymbol{H}\, dl = \oint_s \boldsymbol{J}\, ds + \oint_s \frac{d}{dt}\boldsymbol{D}\, ds = I_c + I_d = I \quad \textbf{(2.15)}$$

where $I$ is a total current on the surface, $I_c$ is a conduction current, and $I_d$ is a displacement current. $s$ is the surface of the electrode, and $ds$ is the discrete element of the electrode.

### 2.4.3 Measurement Strategy

A measurement strategy is necessary for electrical tomography, especially in ERT, to make sure that the experiment can be done correctly. In ERT, quantitative data that describes the state of the conductivity distribution inside the vessel is obtained. Good data-collection strategies are very important because distorted images can be rebuilt if a full set of independent measurements is not collected [99]. For this reason, selecting the strategy that has a good distinguished ability and high sensitivity to conductivity changes in the process is necessary for ERT. For conventional ERT, the current signal is used as the excitation source and the voltage is determined at the detection electrodes. Thus, the three common current measurement strategies that can be applied are adjacent strategy, opposite strategy, or conducting boundary strategy [100]. Details of the three main current measurement strategies applied in a conventional ERT system for sixteen electrodes is given in Tables 2.2 and 2.3. Based on description, advantages and disadvantages listed in Tables 2.2 and 2.3, the type of current measurement strategy can be chosen by the user, depending on their concern and application.

However, the common current measurement strategies cannot be applied to the non-invasive ERT because the electrodes are mounted on the periphery of the non-conducting pipe wall, voltage is used as the excitation source, and current is also determined at the detection electrodes. Therefore, based on [20], the measurement strategy that can be applied to non-invasive ERT is similar to the ECT measurement strategy. In ECT, the number of independent measurement, IM strategy is expressed by Equation (2.16) [20], [100–103]:

$$IM = \frac{N(N-1)}{2} \tag{2.16}$$

where $N$ is the total number of electrodes.

Additionally, a complete measurement cycle for a non-invasive ERT system starts with the first electrode as the excitation electrode and all the other electrodes as detecting electrodes, connected to the ground. Thus, the internal resistance is measured between the first electrode and the adjacent electrodes. The process is repeated for all other electrodes until each of the electrodes has become a source electrode, and a complete measurement cycle is done. Thus, according to Equation (2.16), if sixteen electrodes are utilized; the maximum amount of independent measurement for one complete measurement cycle is 120. Each complete measurement cycle also gives a single frame for the reconstructed image.

**Table 2.2:** Current measurement strategy applied in conventional ERT system [100], [104–107]

| **Types of current measurement strategy** | **Adjacent method** | **Opposite method** | **Conducting Boundary method** |
|---|---|---|---|
| Illustration (for each figure, dotted line denotes current stream lines and solid line denotes equal potential lines) | 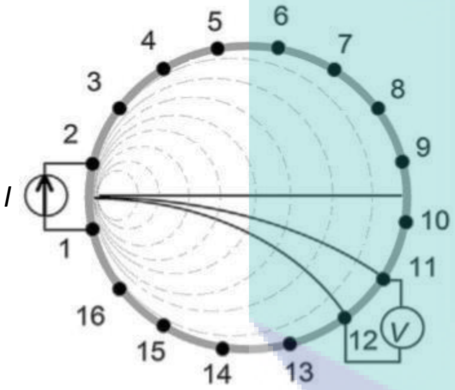 | 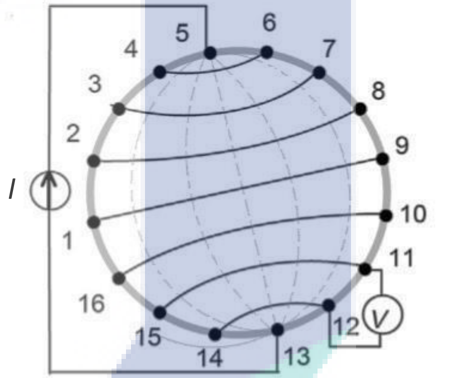 | 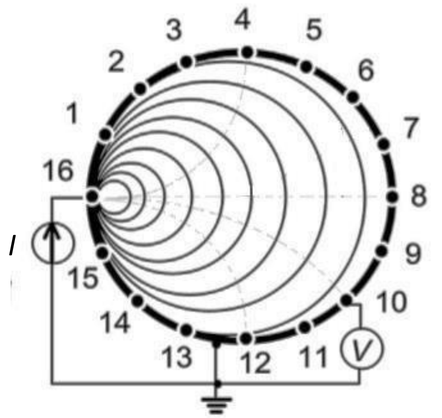 |
| Description | Current is applied between adjacent electrode pairs and voltages are measured between every other pair of adjacent electrode except the current injection ones. | Current is injected through a pair of two diametrically opposite electrodes and the voltages are measured with respect to the reference (electrode adjacent to the current injection electrode) except the current injection ones. | Current is injected from one electrode and the metal wall is set as ground. All the voltage measurements are referred at the same ground. |

**Table 2.3:** Current measurement strategy applied in conventional ERT system [100], [104–107] (continued)

| Types of current measurement strategy | Adjacent method | Opposite method | Conducting Boundary method |
|---|---|---|---|
| Equation for independent measurement (N= number of electrodes, i.e. N=16) | $\frac{N(N-3)}{2} = 104$ | $\frac{N}{4}\left(\frac{3N}{2} - 1\right) = 92$ | $\frac{N(N-1)}{2} = 120$ |
| Advantage | Simple design | Sensibility is more distributed within the sensing area | Higher number of independent measurements compared to adjacent and opposite strategies |
| Disadvantage | Sensibility at the centre is low compared to the boundary | Image quality is reduced | Sensibility at the centre is low compared at the boundary |

## 2.5 Image Reconstruction in Process Tomography

The image reconstruction of process tomography, can be divided into two parts: forward problem and inverse problem [108]. The forward problem is solved first in order to know the theoretical value of each of the sensors output based on the signal projection, whereas the algorithm is solved later in the inverse problem of getting the tomogram.

### 2.5.1 Forward problem

The forward problem also known as the sensitivity map of the system and can be divided into three solutions: linearization solution, numerical solution and analytical solution. The linearization solution is applied when the linear approximation to the relationship of the signal projection of sensors output is made for the system [109]. In addition, the numerical solution – for example, the finite element method (FEM) – is normally used for complex geometry, and the analytical method is used for simple geometry [108]. Most researchers applied numerical solution to solve the forward problem in industrial applications owing to the complex geometry. Also, the availability of FEM software in the market such as COMSOL Multiphysics software, ANSYS software, and EIDORS software help researchers to apply a numerical solution for solving the sensitivity map.

The sensitivity map as a part of sensitivity matrix of electrical tomography for ERT and ECT in two-dimensional can be solved as expressed in Equations (2.17) and (2.18) [67], [107], [110–113].

ERT :
$$M_{i,j}(x,y) = \int_{A(x,y)} \frac{\boldsymbol{E}_i(x,y)}{I_i} \cdot \frac{\boldsymbol{E}_j(x,y)}{I_j} dxdy \tag{2.17}$$

ECT:
$$M_{i,j}(x,y) = \int_{A(x,y)} \frac{\boldsymbol{E}_i(x,y)}{V_i} \cdot \frac{\boldsymbol{E}_j(x,y)}{V_j} dxdy \tag{2.18}$$

where $M_{i,j}(x,y)$ is defined as the sensitivity map between pair electrode i and j at position $(x,y)$ within area $A(x,y)$. Electric field, $\boldsymbol{E}_i$ , is due to the current or voltage driven owing to electrode i, and electric field, $\boldsymbol{E}_j$, is due to the current or voltage driven owing to electrode j. Differentiation between ERT and ECT is only a result of the type of excitation source applied at the source electrode. But it is observed that a concern in electrical tomography is still the electric field propagation inside the medium of interest. The dot-multiplication between $E_i$ and $E_j$ produces a pair projection for each i–j electrode. In addition, electrical tomography produces a curved line for each of sensitivity map of pair electrodes owing to its soft-field nature [19], [67], [114, 115]. Meanwhile, a straight line of sensitivity map occurs in hard-field tomography [116–118]. In addition, the soft-field nature produces a poor condition for sensitivity distribution in electrical tomography, which becomes gradually poorer when it moves towards the centre of the vessel region [119]. In other words, the sensitivity distribution for electrical tomography is more sensitive near to the electrodes. The electrical field distribution in soft-field tomography also depends on the material characteristic inside the pipe region and it is inhomogeneous [119] .

### 2.5.2 Inverse problem

After the sensitivity map of the system has been solved, the tomogram is obtained by using either a non-iterative or an iterative algorithm in the inverse problem part [120].

A non-iterative algorithm is a direct method of image reconstruction and a back-projection algorithm is categorized as a non-iterative algorithm [121]. It is a famous technique in tomography application consisting of a linear back-projection (LBP) algorithm and a filtered back-projection (FBP) algorithm. LBP is applied in many tomography processes, such as in ultrasonic tomography [35], [122–124], optical tomography [47], [118], [125, 126], electrical resistance tomography [21], [111], [127, 128] and electrical capacitance tomography [129–133]. The advantages of the LBP algorithm is its low computational complexity, and it can generate an image at high speed [134]. In reconstructing the image using LBP, each sensitivity matrix is multiplied with its corresponding sensor reading [135]. The back-projected data values are smeared back across the unknown density function (image) and overlap each other to increase the projection data density [35]. Hence, the main disadvantage of LBP algorithm is that it produces a blurred image, also known as the smearing effect [136].

The FBP algorithm is used to sharpen the reconstructed image obtained from the LBP algorithm [137]. It is applied mostly in hard-field tomography compared to soft-field tomography such as in ultrasonic tomography [116], [138, 139], X-ray tomography [140–142] and optical tomography [125], [143, 144], but was only discussed in electrical impedance tomography in 1992 [145]. For example, a filter matrix was implemented by M. H. Fazalul Rahiman [116] in FBP for ultrasonic tomography applications. This filter matrix has the same dimension as the sensitivity matrix so that it produces a weighting for the individual pixel. Hence, it can produce a uniform concentration profile for equal sensor output. The filter matrix, $F$, is expressed by Equation (2.19) [116].

$$F = \frac{P_m}{W} \tag{2.19}$$

where $P_m$ is the maximum pixel magnitude in total matrix, $W$. This filter matrix eliminates the non-uniform of concentration profile obtained in LBP algorithm. Therefore, the FBP algorithm can be solved by multiplying the filter matrix by the LBP result (see Equation (2.20)) [116].

$$G_{FBP}(x, y) = F(x, y) \times G_{LBP}(x, y) \tag{2.20}$$

where $G_{FBP}$ is the FBP concentration profile and $G_{LBP}$ is the LBP concentration profile.

Nevertheless, if comparison is made between those sensitivity distributions for hard-field tomography and soft-field tomography (see Table 2.4); the distribution for soft-field tomography using FBP produces an inverse curve surface, while a flat surface of sensitivity distribution occurs in hard-field tomography. This example of sensitivity distributions for hard-field tomography and soft-field tomography are based on Ref. [116] and conducted research, respectively. This is due to the nature of soft-field behaviour that produces a curve line of each pair projections of the sensitivity map. Thus, it makes the sensitivity distribution becomes a curve surface instead of a flat surface. Observation of the same pixel gives a higher pixel value resulting in colour scale ratio changes. This give the colour scale in FBP shifted. As an example, when image is reconstructed using COMSOL Multyphysic (see Figure 2.3), the tomogram obtained for FBP is not accurate. The colour scale ratio that changes in FBP influences the reconstructed image. It is believed that when every pixel from the curved filter matrix is multiplied with the LBP result, the colour scale in FBP shifted. Consequently, the FBP is not the concern on this research.

**Table 2.4:** Comparison sensitivity distribution between hard-field and soft-field tomography

| Sensitivity Distribution | Hard-field [116] | Soft-field (non-invasive ERT) |
|---|---|---|
| LBP | 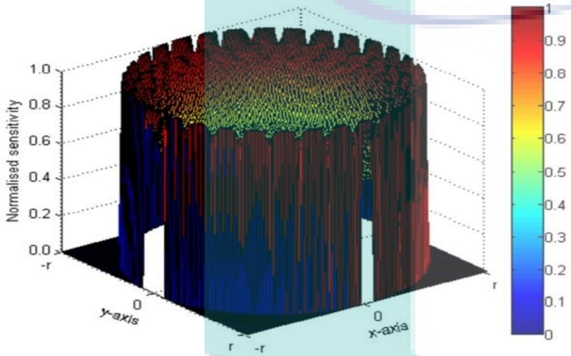 | 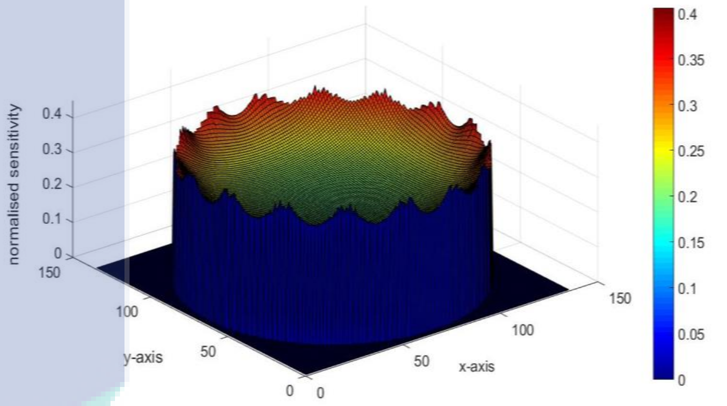 |
| FBP | 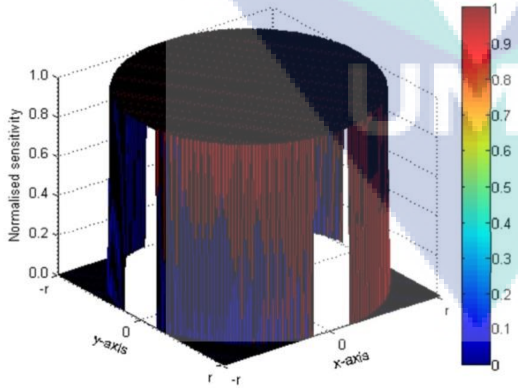 | 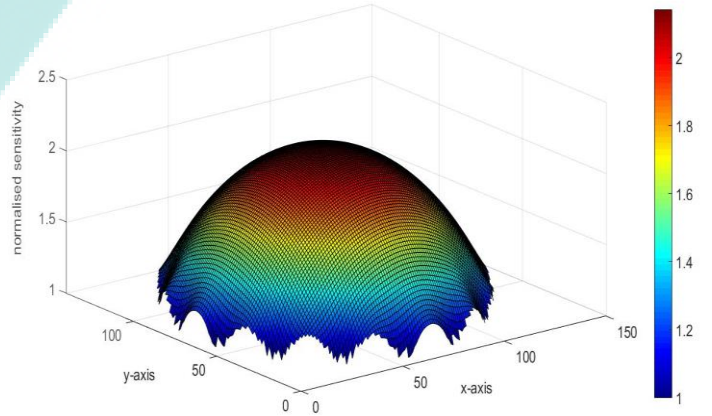 |

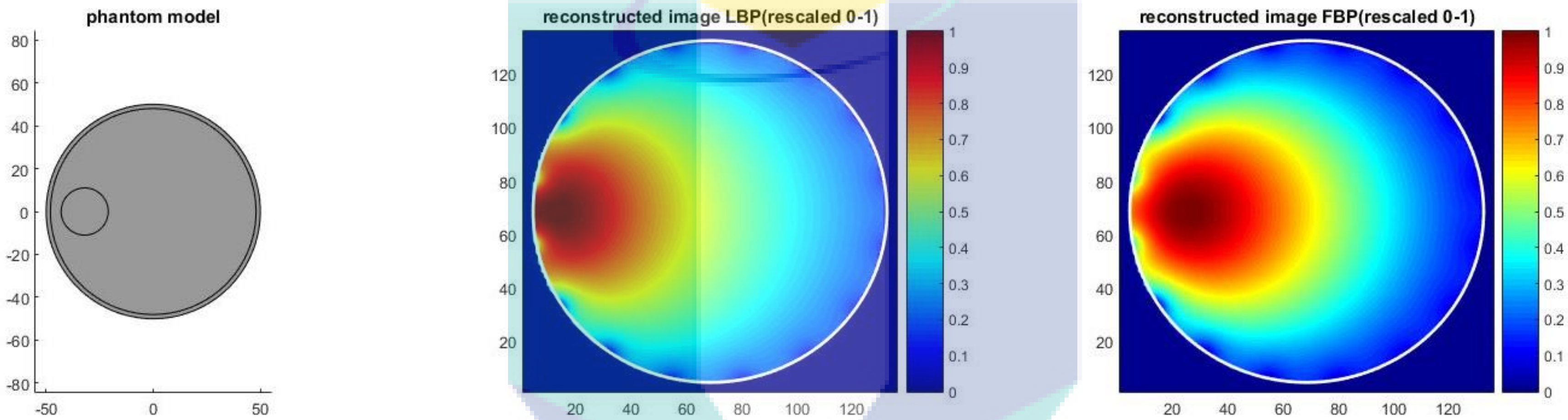


**Figure 2.3:** Example of comparison between reconstructed image using LBP versus FBP

In contrast, the iterative algorithm can produce a better resolution image than the LBP algorithm but at low speed because the inverse problem is solved iteratively until a sufficient result can be obtained [115]. The examples of the iterative algorithm are applied in electrical tomography such as the Landweber [146, 147], and Gauss-Newton algorithm [148, 149]. Subsequently, there will be a trade-off between the speed and resolution in solving the image-reconstruction part of process tomography.

In online and real-time monitoring system, the capture time must be fast relative to the transport dynamic, and it is also essential that the data-processing time is fast relative to the control dynamic [150]. For this reason, the LBP is widely used because it is the simplest and fastest method to produce an image compared to other methods. Knowing that, the tomogram obtained by the LBP algorithm is not so clear, but is still sufficient to identify the medium of interest. Nevertheless, the high-resolution image involves a complex algorithm and of course takes a long time to process the data and hence, slows down the system. Consequently, most researchers implemented LBP compared to the iterative algorithm in online and real-time monitoring processes, so it is also a concern in this research.

## 2.6 Summary

This chapter reviewed some related works in non-invasive process tomography in industrial applications. Non-invasive tomography sensors for two-phase mixtures applications were reviewed, and included X-ray tomography, ultrasonic tomography, optical tomography, electrical capacitance tomography and non-invasive electrical resistance tomography. Finally, some principles related to non-invasive electrical resistance tomography and image reconstruction in industrial tomography were discussed.

In addition, two-phase medium tested in the research of conventional ERT is summarized in Table 2.5, whereas a summary of the research on non-invasive process tomography is presented in Table 2.6.

**Table 2.5:** Summary of medium tested for research on conventional ERT

| Two-phase regime | Authors | Medium |
|---|---|---|
| Liquid/liquid | [66–69] | Water/oil/chemical (brine solution, dichloride- methane, toluene) |
| Liquid/solid | [70–78] | Water/milk powder/glass beads/kaolin clay |
| Liquid/gas | [79–89] | Water/bubble (gas flow rate: 0.2 cm/s-5.0 m/s) |

**Table 2.6:** Summary research on non-invasive industrial tomography

| Types | Authors | Source | Two-phase regime | Limitations |
|---|---|---|---|---|
| X-ray Tomography or Computed Tomography | [22–28] | Attenuation of the X-rays | -Mostly applied for Liquid/gas.<br>i.e: water/air in bubble column and vertical pipeline | -Radiation issues<br>-needs a specialist to operate the system |
| Ultrasonic Tomography (UT) | [29–43] | Attenuation of acoustic impedance | -Liquid/liquid. i.e: water/oil<br>-Liquid/gas. i.e: water/air<br>-Liquid/solid.<br>i.e: liquid kernel layers/solid acryl , Water/particle flow | -Is expensive if the number of ultrasonic sensors used increases |
| Optical Tomography (OT) | [44–48] | Optical radiation | -Mostly applied for Liquid/gas.<br>i.e: water/air in bubble column and vertical pipeline | -Limitation on optical surface, where the sensors cannot be placed too close to each other to avoid reflection |
| Electrical Capacitance Tomography (ECT) | [49–65] | Permittivity distribution | -Liquid/liquid. i.e: oil/water<br>-Liquid/gas. i.e: oil/gas (commonly applied)<br>-Liquid/solid.<br>i.e: Water/polyethylene particle | -Cannot work properly if we concentrate more on conductivity medium compared to permittivity medium |

# CHAPTER 3

# MODELLING AND SIMULATION

## 3.1 Introduction

The aim of this chapter is to explain the modelling and simulation of the non-invasive ERT system. COMSOL Multiphysics software was implemented as the software tool for the simulation purpose. Firstly, the system was modelled and analysed for the utilizing frequency compatibility for use in the hardware circuit design. Secondly, the modelling of the sensor size was studied. These studies are to ensure the feasibility that the electrodes work correctly in the system. Lastly, the simulated frequency and electrode size were tested with a phantom inside the pipe, to test the capability of the system to detect any change in the conductivity distribution inside the column.

## 3.2 General Set-up of Model in COMSOL Multipyhsics Software

A 2D space dimension of Electric Current (ec) under the branch of AC/DC with a stationary study was selected for the purpose of COMSOL simulation. There are several steps to be followed before the result can be obtained and analysed. They are:

1. **Create a physical model using available geometries**: A 2D dimension model was developed to mimic the real system. The lines representing the width of the sixteen electrodes (E1 – E16) were drawn on the boundary of the

pipe surface. The reason for drawing the lines was because the main concern of modelling using COMSOL Multiphysics was the sensor sensitivity. This means that if we give the voltage signal to the electrode, it will allow the electricity to penetrate through the non-conducting pipe, no matter how thick the electrode is. In addition, it is also to avoid a complexity simulation in COMSOL. The 2D geometry of the non-invasive ERT system with sixteen electrodes is shown in Figure 3.1. The dotted line represents the vertical non-conducting pipe implemented in the real hardware.

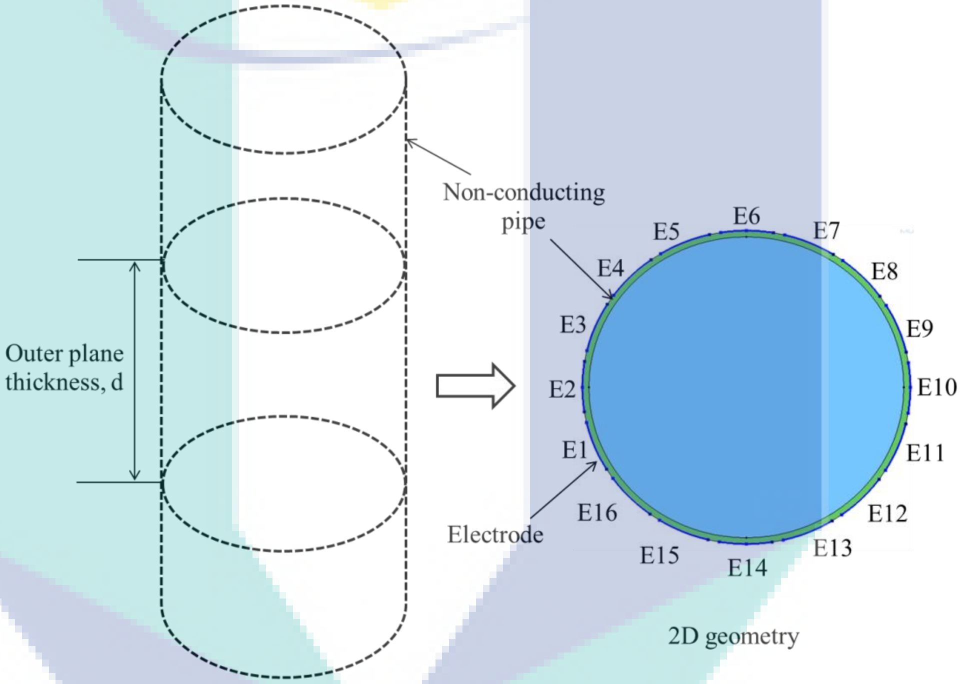


**Figure 3.1:** Circle drawing for non-invasive ERT system in COMSOL Multiphysics

2. **Define materials for each domain created**: The material for each related domain in the designed model was defined so that it resembled the real system. The pipe itself was defined as an acrylic medium, whereas the main medium was tap water. The details of parameters of all materials set in COMSOL Multiphysics are shown in Table 3.1. The value of electrical conductivity of tap water was reflected with measured real tap water used in the real hardware, using a conductor meter and other materials, based on [151].

**Table 3.1:** Parameters material defined in COMSOL Multiphysics

| Material | Electrical conductivity, S/m | Electrical permittivity |
|---|---|---|
| Acrylic | $3.0 \times 10^{-14}$ | 3.45 |
| Water | $7.0 \times 10^{-3}$ | 80 |
| Wood | 0 | 2.75 |

3. **Set the electric current equation for the model:** Since the system was in a quasi-static electric field, the frequency domain with frequency user defined had to be set such that it represented the quasi-static electric field distribution. By setting the value of applied frequency, it assumed that the model works in the AC system. Also, the outer plane thickness, d was defined to have the same height of the implemented electrode. If the value of d is not defined, by default the COMSOL simulator will set the thickness of the 2D space to be 1 meter.
4. **Set the boundary condition for each of the electrodes:** The boundary condition is very important to ensure that the electric field can propagate correctly like the real system. The boundary condition for the voltage source was set at the boundary between the electrode and the non-conducting pipe. Therefore, the terminal types under the ec branch were applied. Sixteen voltage terminals type were set with the transmitter at 10 V and receivers at 0 V (ground). Only DC amplitude was needed for the source because the frequency was applied in step 3.
5. **Mesh the model:** In the simulation process, meshing the model can be crucial in obtaining the best result in a faster way. Thus, extra fine meshing (see Figure 3.2) under physically-controlled mesh was chosen since denser meshing would provide a more reliable finite element method (FEM) simulation.

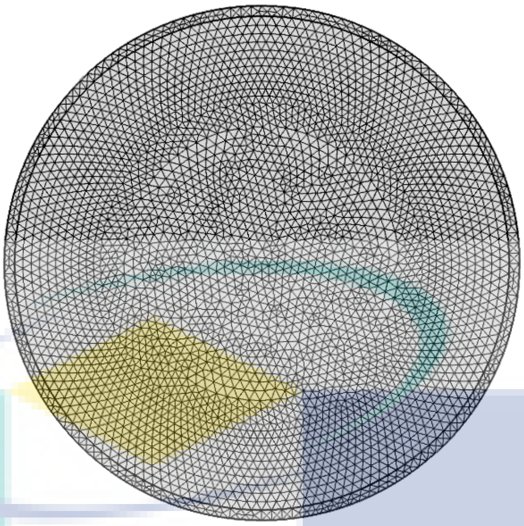

**Figure 3.2:** Extra fine meshing model

6. **Run the study:** The model was computed with default stationary study. The implementation of stationary solver assumed that the load and deformation do not vary in time. Besides, the physics model chosen solves the partial differential equation (PDE) and boundary condition numerically.
7. **Analyse the 2D result:** Lastly, the 2D performance of the result obtained was selected according to the user. The analysis of the model was done by observing the surface plot, contour plot, streamline plot and other numerical post processing methods. The contour plot for instance represents the current distribution line and the electric field line distribution was by the streamline plot of the non-invasive ERT system.

## 3.3 Determination of Compatible Frequency

Based on [16, 17], [19–21], since the non-conducting pipe was implemented as a part of the sensing field for the non-invasive ERT system, the coupling capacitance of the non-conducting pipe was also generally considered for the sensing field, as in Figure 3.3.

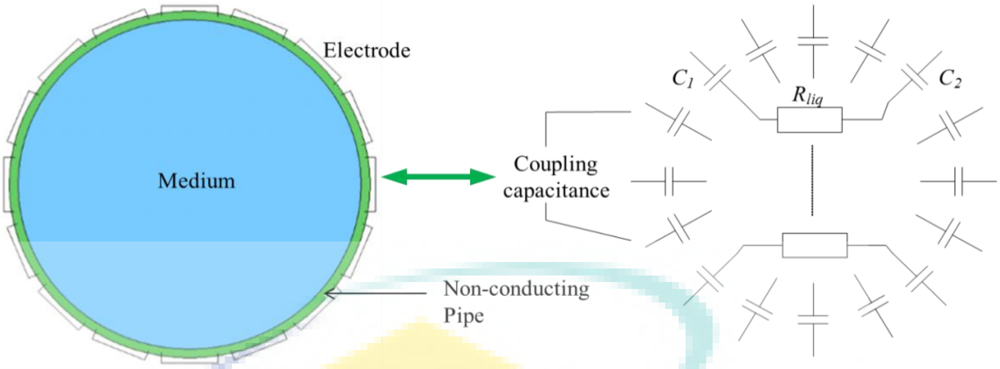


**Figure 3.3:** Non-invasive ERT sensor and its equivalent circuit

The coupling capacitance refers to the capacitance between the electrodes mounted on the non-conducting pipe wall and the conductive liquid. Thus, it will have two coupling capacitances for one pair of the measurement electrodes. It is very different if compared to the conventional ERT system, which only considers the resistance between each pair of the measurement electrodes. In that case, the non-invasive ERT system will have total impedance, $Z_{total}$ of resistance in series with the coupling capacitances as in Equation (3.1).

$$Z_{total} = R_{liq} - j\frac{1}{2\pi f\left(\frac{C_1C_2}{C_1+C_2}\right)} \quad \textbf{(3.1)}$$

Nevertheless, the non-invasive ERT system is not exactly an electrical impedance tomography (EIT) system. The EIT system consists of the complex impedance model whereby the equivalent resistor and capacitor are in parallel in the measuring circuit, as studied in [152]. Simultaneously, the EIT system reconstructs the image based on both electrical conductivity and permittivity distribution of the medium interest [153].

Later, by implementing a certain frequency to the system that is high enough to optimize the reactance part of the impedance, Ohm's law can determine the impedance that is only equivalent to the resistance between any pairs of electrodes. $R_{i,j}$, $V_o$ and $I_{i,j}$ in Equation (3.2) refer to the value of the resistance, voltage and current for every pair of electrodes, respectively. The value of the resistance will be used later for the image reconstruction part to relate with the conductivity distribution of the medium of interest.

$$Z_{total} \approx R_{i,j} \approx real\frac{V_0}{I_{i,j}} \tag{3.2}$$

Accordingly, the conductance in Equation (2.3) in section 2.4.1 for non-invasive ERT inside the medium of interest can be defined as [95]:

$$G_{i,j} = \frac{1}{R_{i,j}} = \frac{I_{i,j}}{V_0} = \frac{1}{V_0}\oint_S \sigma \cdot \boldsymbol{E}ds \tag{3.3}$$

In which $I_{i,j}$ is the measured current between *i-j* and $V_0$ is the source voltage. Equation (2.15) in section 2.4.2 was applied to determine $I_{i,j}$. When a high frequency was applied to the system as discussed before, the conduction current inside the conductive medium was larger than the displacement current because the reactance part of the total impedance could be ignored. Hence, $I_{i,j}$ is assumed based only on the conduction current, $I_c$.

Since all the pairings of electrodes are similar, only one pair of electrodes (see Figure 3.4) is used to make a simple calculation and prove a compatible frequency for the non-invasive ERT system. A simple calculation can be obtained based on Equation (3.1). In addition, the resistance, $R$ and the capacitance, $C$ values can be measured by using Equation (2.2) section 2.4.1, and the formula $C = \frac{\varepsilon_o \varepsilon_r A}{d}$ [154]. $\varepsilon_o$ is the permittivity of free space, $\varepsilon_r$ is the relative permittivity of non-conducting pipe, $A$ is the area of the electrode, and $d$ is the thickness of the non-conducting pipe.

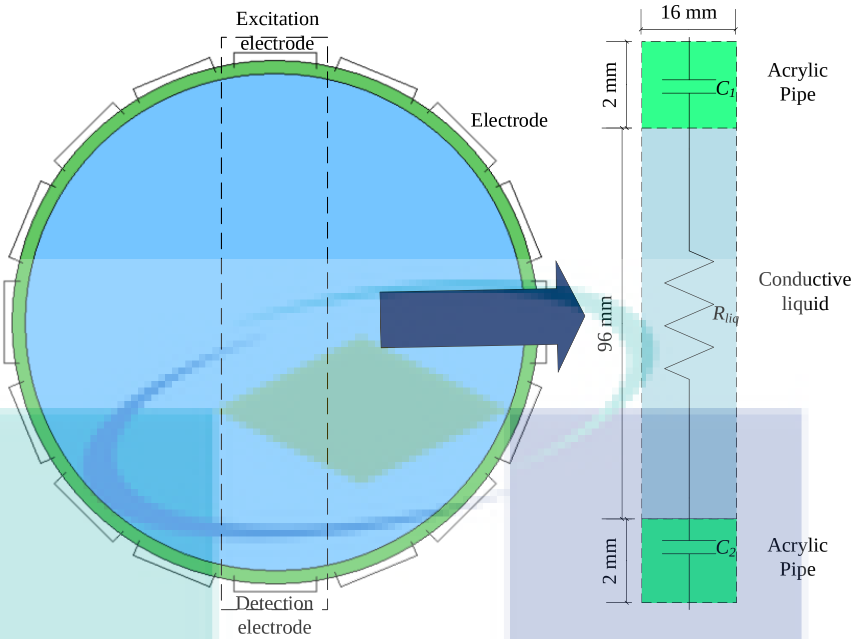


**Figure 3.4:** One pair of the measurement electrodes for non-invasive ERT

For instance, 16 rectangular metal electrodes each with an electrode area of $3.2\times10^{-3}$ m$^2$, acrylic pipe with thickness 2 mm and inner diameter 96 mm, $\sigma$ is $7\times10^{-3}$ S/m, and $\varepsilon_r$ is 3.45. By using Equation (2.2) and the formula of capacitance, the resistance value of the conductive liquid and the capacitance value for each of the coupling capacitance yields 4.29 kΩ and 48.85 pF, respectively. Hence, based on Equation (3.1), a minimum frequency that could be applied is 2 MHz to ensure the real part of the total impedance is dominant and also to optimise the reactance part of the total impedance of the non-invasive ERT system. It means that if the frequency is below 2 MHz, the conductivity of the non-invasive ERT system cannot be determined because the reactance part is dominant compared to the real part. Later, the value of the current flow through the medium can be measured. A simple schematic diagram of the circuits for one pair of electrode can be shown in Figure 3.5.

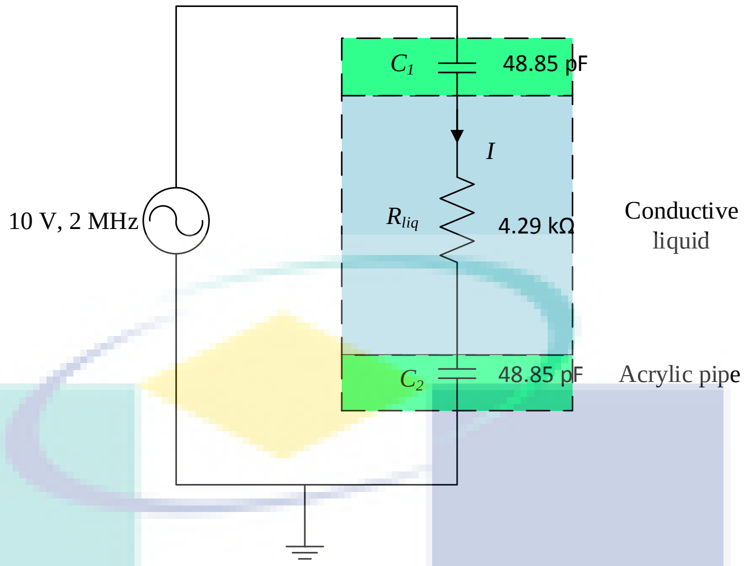


**Figure 3.5:** Schematic diagram for one pair of electrode measurements

The value of current can be calculated based on Ohm's law. If the voltage applied to the excitation electrode is 10 V, with frequency 2 MHz, and assuming the reactance part is neglected as expressed in Equation (3.2), the value of current at the detection electrode is around 1.8 mA. The concept is later proven numerically to study the electricity penetration and distribution profiles within the acrylic pipe with a conductive and non-conductive liquid. The top of the rectangle was set as the exciting electrode and the bottom part as the ground. The material of the electrode was not defined in the simulation because the main consideration is the setting of the electrical signal of the boundary condition. Thus, only a single line represents the electrode.

### 3.3.1 Optimizing a Suitable Frequency for Non-Invasive ERT

The simulation is performed in order to investigate the feasibility of the electricity penetration by the excited electrodes through the acrylic pipe. As calculated in section 3.3, if the applied frequency is sufficiently high, the voltage signal should penetrate the acrylic pipe and decrease gradually when it reaches the detection electrode. As the detection electrode is connected to the ground, later the current can be measured at the detection electrode. As the system is assumed to be a RC series circuit, the current flow from excitation electrode to the detection electrode should be the same. As the frequency increases, the current that flows from the top electrode to the bottom electrode remains the same at the applied frequency as shown in Figure 3.6.

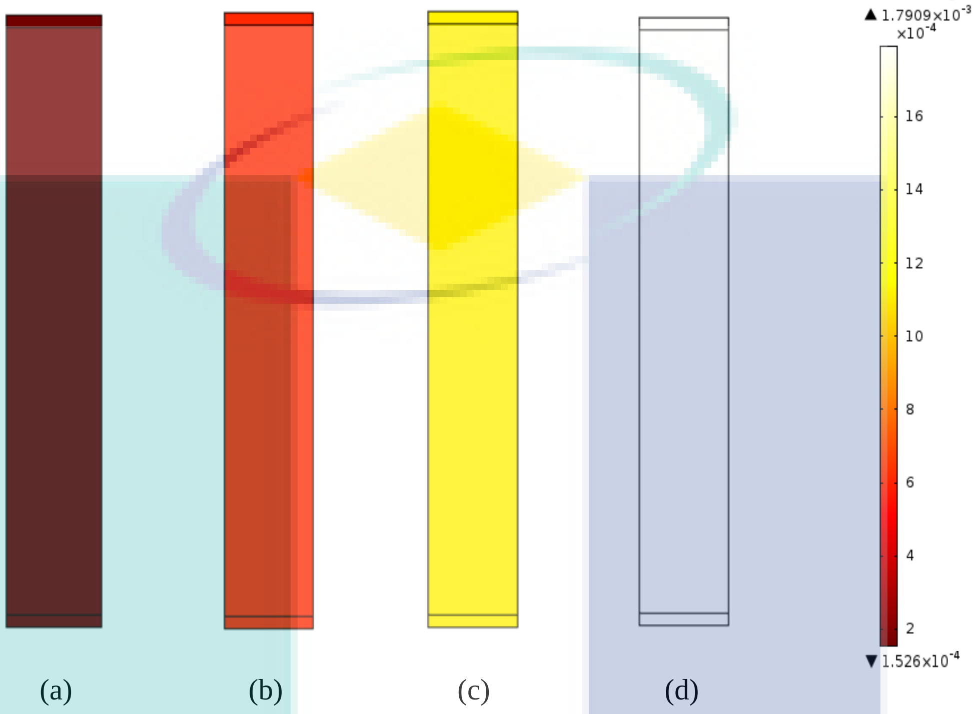


**Figure 3.6:** Current distribution with different frequencies for: (a) 100 kHz; (b) 500 kHz; (c) 1 MHz; and (d) 2 MHz

Thus, the best method to investigate signal propagation is based on voltage distribution, as voltage is directly proportional to current. Therefore, it is not an issue to use voltage distribution to identify the suitable utilizing frequency for the non-invasive ERT system, even though the main concern for non-invasive ERT is the value of the current. As a result, the voltage distribution decreases significantly from top to the ground with frequency 2 MHz, as illustrated in Figure 3.7. This value is significant for the calculated value. Correspondingly, there is very poor voltage distribution in Figure 3.7(a), which decreased sharply from 10 V to around 5 V, and remained constant in the conductive liquid. Similar to Figures 3.7(b) and (c), even the voltage signal propagation is improved, and it is observed that the signal does not drop significantly compared to Figure 3.7(d).

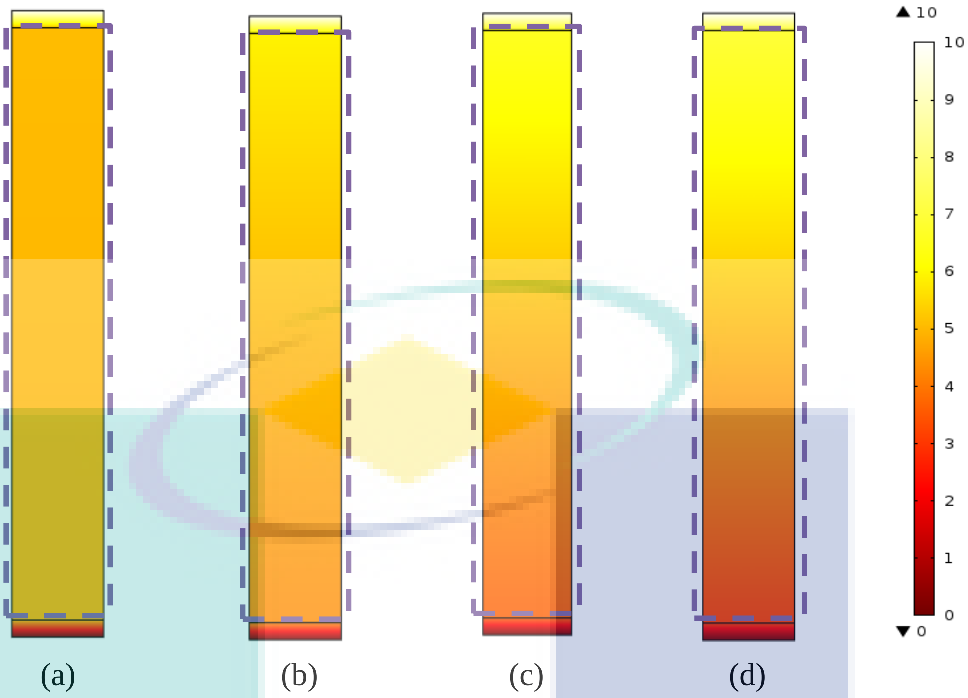


**Figure 3.7:** Voltage distribution with different frequencies for: (a) 100 kHz; (b) 500 kHz; (c) 1 MHz; and (d) 2 MHz

In addition, the voltage distribution in the medium is also analysed in the line graph by taking 15 points from the top to the bottom part, as shown in Figure 3.8. Points 1 and 15 are the locations between the excitation electrode and the detection electrode, respectively; points 2 and 14 are in the acrylic pipe, and points 3–13 are the points in the conductive liquid. There was a noticeable drop in the voltage distribution for all frequencies applied. The absolute voltage at point 3 to point 7 shows a proportional trend with respect to the utilizing frequency. However, from point 9 to point 13 it shows that as the utilizing frequency increases, the voltage decreases. Thus, from Figure 3.8, the minimum frequency to be applied for the signal to penetrate through the acrylic pipe for the non-invasive ERT system work properly is 2 MHz.

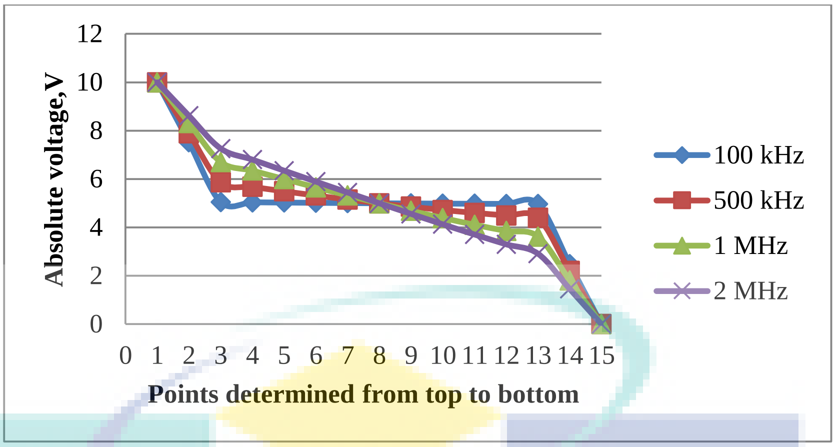


**Figure 3.8:** Absolute voltage versus location of fifteen points measured from excitation electrode (point 1) to the detection electrode (point 15)

However, this is only in an ideal case. In practice, the cross-section of the non-conducting pipe used is a circle and all the detection electrodes are connected to the ground. For this reason, there is a possibility that the current values are not exactly the same, but it is still believed that it can be applied as a guideline for getting the optimum frequency for the non-invasive ERT system. The details of the normalized current values obtained for the increment of frequencies is shown in Figure 3.9. The maximum value of current obtained was only around 0.8 mA which was totally different compared to the single pair of the system measured. However, it can be observed that 100 kHz only achieved a very small current which was smaller than 0.1 mA, and the current values kept increasing when the frequency increased. The curve pattern of the current distribution at the detection electrodes could only be seen clearly when the frequency applied was 2 MHz.

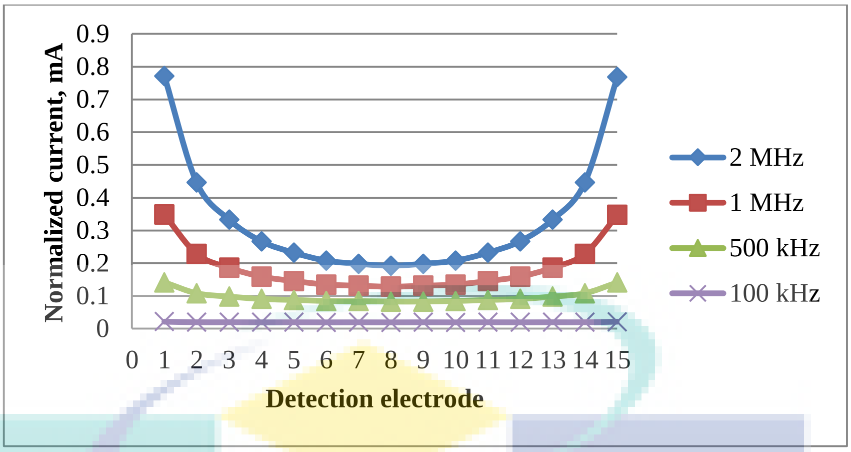


**Figure 3.9:** Normalized current distribution for the increment of frequencies

The simulation in 2D of a circle representing a real non-invasive ERT system was also done. As a result, the current distribution increased when the frequency applied increased. Also, it can be seen in Figure 3.10 that the sensor is only sensitive when the frequency applied was 2 MHz (see Figure 3.10(d)). That frequency was able to allow the electricity to penetrate through the pipe significantly compared to the low frequencies. The electric field distribution representing one of the soft-field tomography processes was also clearly seen in the 2 MHz frequency. Also, the 100 kHz frequency implemented to the system only gave a very small current that affected the sensitivity of the sensor, and the electric field distribution for 100 kHz was not evenly distributed as a soft-field tomography compared to 500 kHz afterwards. For this reason, 2 MHz is the significant and compatible frequency that can be applied to the research project.

Based on mathematical equations made from the total impedance and simulation, it is indicated that the minimum frequency was 2 MHz that can be applied to ensure that the real part reflects that the conductive medium is bigger than imaginary part. This means that the higher the frequency source implemented, the better the result that can be obtained. However, a minimum of 2 MHz was chosen in this research to prove the principle made. In addition, specifications of electronic components in hardware part are also considered. For example, mostly high bandwidth (20 MHz and above) operational amplifiers from available manufacturers are limited in-term of small +/- supply voltage range and slew rate. Consequently, the excitation frequency applied is limited to be suitable for all components chosen from the available manufacturer and hence, 2 MHz was applied for this research.

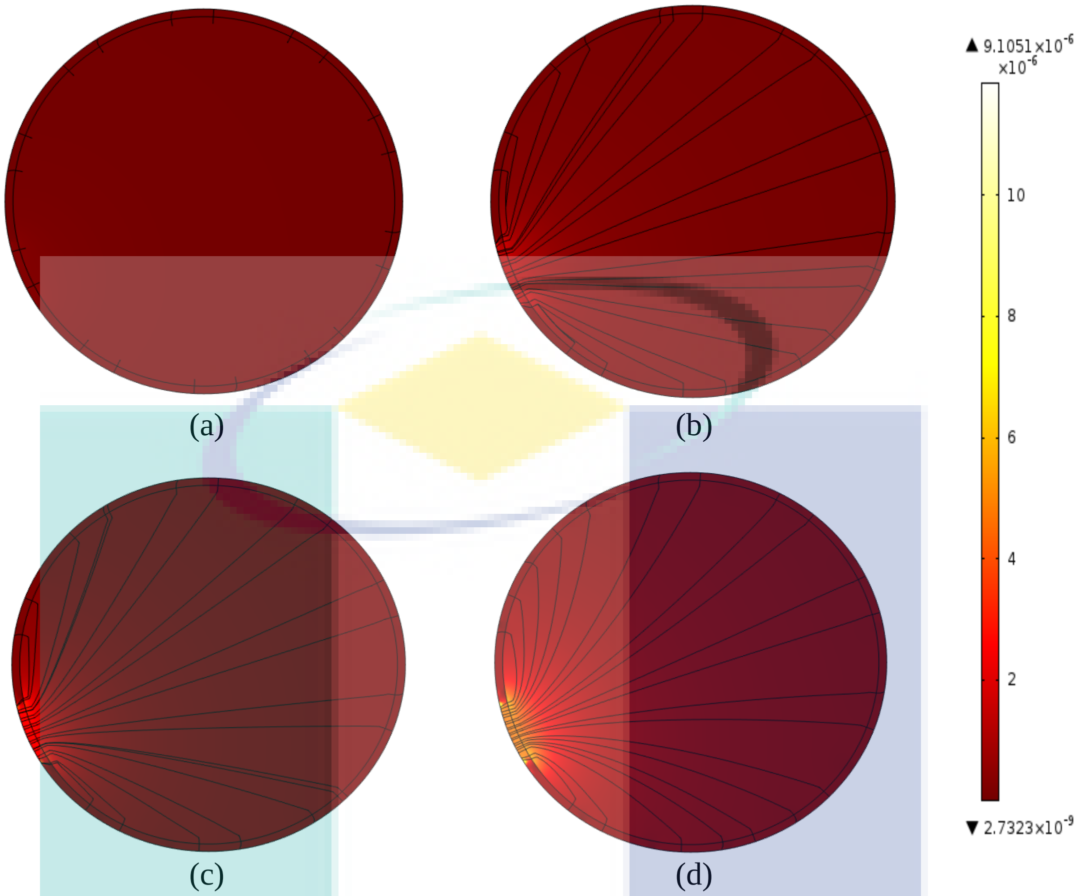


**Figure 3.10:** Surface current distribution and electric field distribution with different frequencies for: (a) 100 kHz; (b) 500 kHz; (c) 1 MHz; and (d) 2 MHz

### 3.3.2 Limitation of Main Medium Applied with the 2 MHz Frequency

The conductive liquid (tap water in the study) utilized in the non-invasive ERT system as the primary medium in the column will vary slowly all the time, owing to the factors of the surroundings, such as temperature and source of the liquid itself [155]. Therefore, the range of conductive liquid applied is crucial so that the system works effectively with the 2 MHz frequency to produce good results. Generally, the range of tap water is in between $5 \times 10^{-3}$ S/m and $80 \times 10^{-3}$ S/m [155]. According to Equations (2.2) and (3.1), the appropriate resistance value due to the changes of conductive liquid ensures that the resistance is bigger than the reactance (see Table 3.2). 3.26 kΩ of total reactance, $X_{Ctotal}$, was obtained with the applied 2 MHz frequency as the total coupling capacitance between the acrylic pipe and conductive liquid is 48.85 pF. It is observed that the appropriate tap water can be tested with the source frequency and is between $5\times10^{-3}$ S/m and $8\times10^{-3}$ S/m. If the electrical conductivity of the water is larger than that, the applied frequency is no longer suitable for the system.

**Table 3.2:** Range of conductivity of tap water to fix with real part bigger than imaginary part

| Conductivity tap water (S/m) | Resistance value, $R_{liquid}$ (kΩ) | $Z_{total}$ (kΩ) = $R_{liquid}$ $-jX_{Ctotal}$ |
|---|---|---|
| $5 \times 10^{-3}$ | 6 | 6 -j3.26 |
| $6 \times 10^{-3}$ | 5 | 5 -j3.26 |
| $7 \times 10^{-3}$ | 4.29 | 4.29 -j3.26 |
| $8 \times 10^{-3}$ | 3.75 | 3.75 -j3.26 |
| $9 \times 10^{-3}$ | 3.3 | 3.3 -j3.26 |
| $10 \times 10^{-3}$ | 3 | 3 -j3.26 |

## 3.4 Modelling for Electrode Dimension

The formula of 360°/N, with N as the number of electrodes, is used as the primary method for choosing the dimension of the width. Thus, the width for each of sixteen electrodes for 50 mm outer radius pipe, $r$ is approximately 20 mm or 22.5˚. But, this dimension of the width cannot be implemented because a stray capacitance exist between adjacent electrodes that are too close [156]. Therefore, the dimension of width, $W$, is calculated based on formula of arc length for sector of circle, as expressed in Equation (3.4).

$$W = \frac{\theta}{360°} \times 2\pi r \qquad \textbf{(3.4)}$$

By default, COMSOL will run the simulation in 3D even if a 2D study is chosen. So, as for the study of electrode height, the user just enters the required height in the out-of-plane thickness column under frequency domain solver in the Electric Current branch in COMSOL. As a result, the user does not need to run the

3D simulation to investigate the height of the electrode. The specific dimensions and parameters in Table 3.3 are used for modelling the non-invasive ERT system.

**Table 3.3:** Properties and specific dimension

| Num. | Item | Dimension |
|---|---|---|
| 1 | Electrode width | 9 mm – 16 mm |
| 2 | Electrode height | 90 mm – 500 mm |
| 3 | Thickness of pipe | 2 mm |
| 4 | Inner diameter of pipe | 96 mm |
| 5 | Voltage source | 10 V, frequency is 2 MHz |

### 3.4.1 Optimizing the Electrode Dimension of Non-Invasive ERT Electrode

It can be clearly seen in Figures 3.11 and 3.12 that there were steady rise in normalized current values for the nearest and furthest pair of measurement electrodes at each of the different widths and heights of the electrodes simulated. Furthermore, referring to Figures 3.11(a) and 3.12(a), when the width and the height of electrode increased from 9 mm (46.67%) to 16 mm (82.22%), and 90 mm to 130 mm, respectively, the value of normalized current for the nearest pair of measurement electrodes with the source also rose from around 0.16 mA (90 mm) to around 0.5 mA (130 mm). Despite this, there was just a small increase (around 0.07 mA up to 0.13 mA) for the farthest pair of measurement electrodes in Figures 3.11(b) and 3.12(b). Also, referring to Equation (2.3) in subsection 2.4.1, the current value is proportional to the area. Hence, the width and the height of the electrode are proportional to the output normalized current signal of a non-invasive ERT system. The clear visualization of the example surface current distribution with the increment of width at 130 mm height is shown in Table 3.4. Consequently, the optimum size of the width of the electrode chosen is 16 mm.

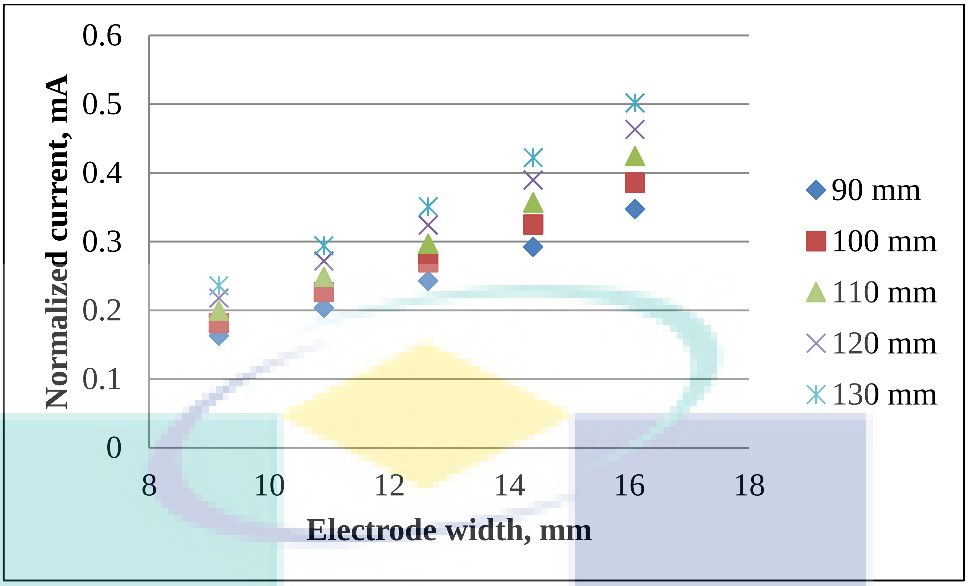


(a)

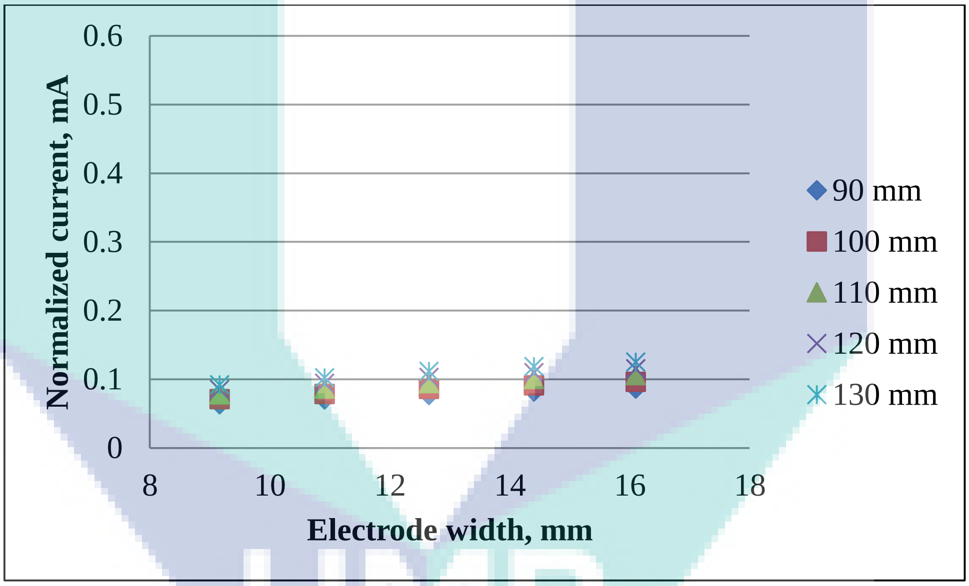


(b)

**Figure 3.11:** Normalized current distribution for a different width at a different height (90 mm to 130 mm): (a) E1-E2; (b) E1-E9

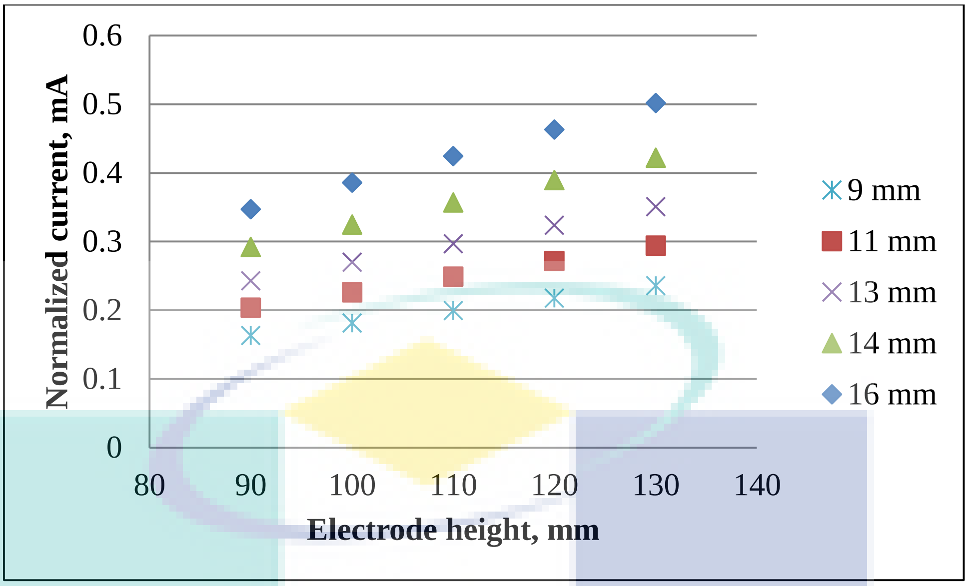


(a)

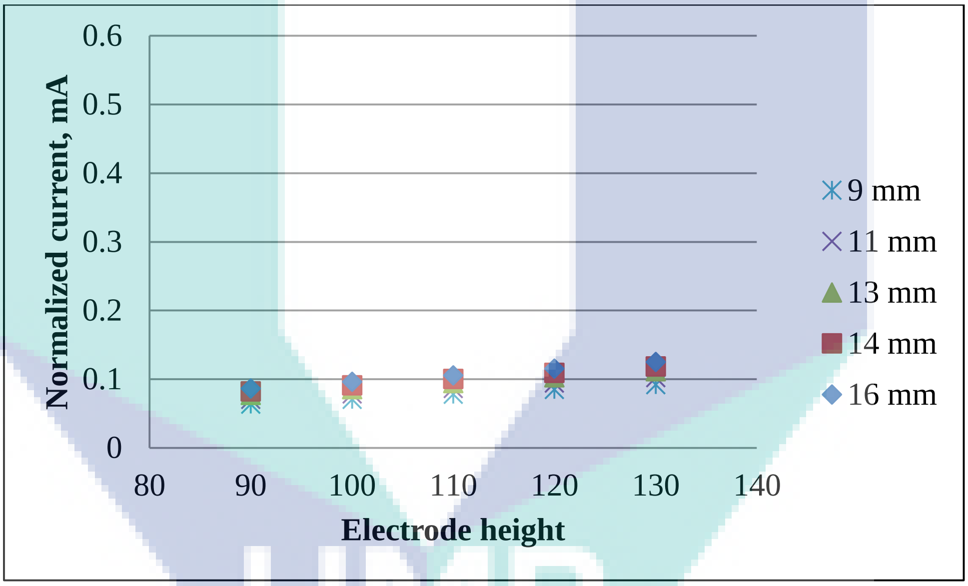


(b)

**Figure 3.12:** Normalized current distribution for a different height at a different width (9 mm to 16 mm): (a) E1-E2; (b) E1-E9

**Table 3.4:** Example of surface current distribution at height 130 mm with increment of width

| Width (mm) | Surface current distribution | Width ( mm) | Surface current distribution |
|---|---|---|---|
| 9 mm | 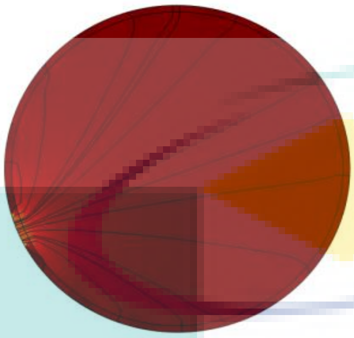 | 13 mm | 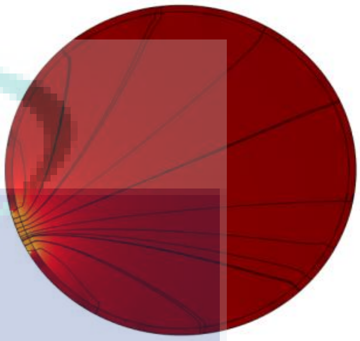 |
| 11 mm | 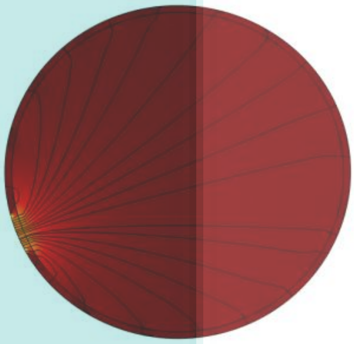 | 14 mm | 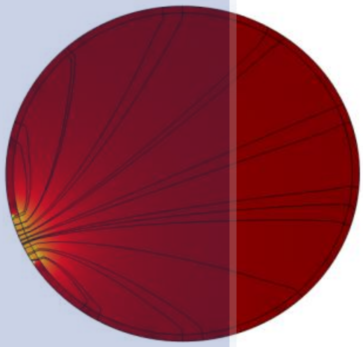 |
| 16 mm | 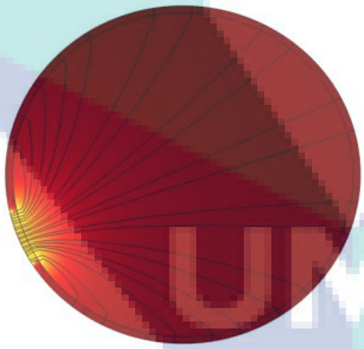 | | |

However, 130 mm in height for the electrode was still not chosen as the optimum height. Thus, the simulation proceeded for 100 mm up to 500 mm in height by intervals of 100 mm, for a width of 16 mm to observe the maximum output normalized current, as shown in Figures 3.13(a) and (b). It was found that the normalized current value kept increasing when the height of the pipe increased up to 500 mm. Therefore, it was assumed that the value would rise if the height increased by more than 500 mm.

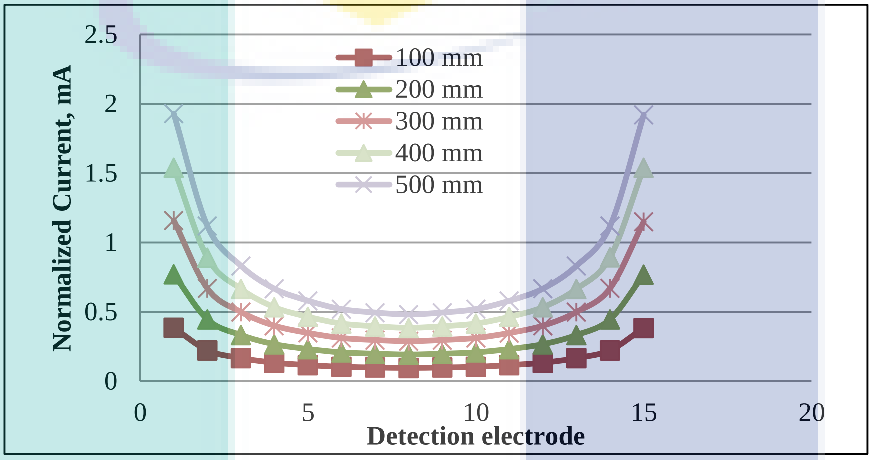


(a)

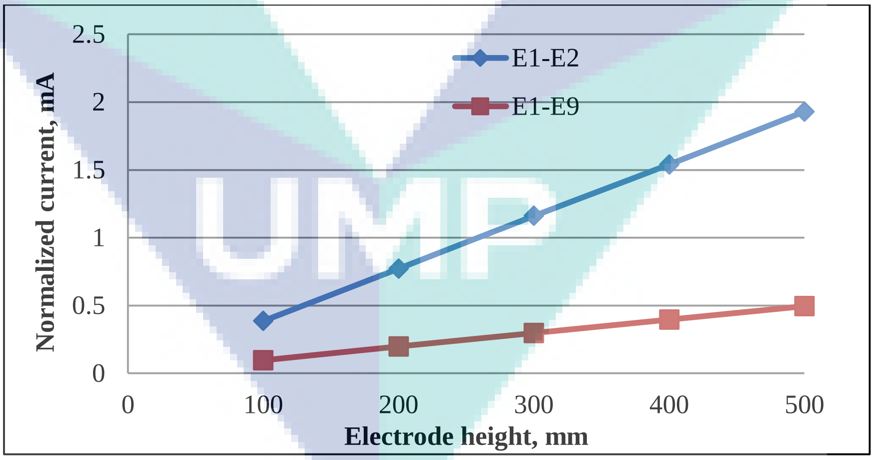


(b)

**Figure 3.13:** (a) Normalized current distribution versus detection electrode; (b) Normalized current distribution for the nearest and the furthest pair of measurement electrodes. For width 16 mm at different height (100–500 mm)

Correspondingly, if a height of 500 mm or higher is applied, some factors must be taken into account, such as high sensor fabrication cost and component availability in the market. Thus, a different size of the object as a non-homogenous system is analysed to determine the minimum height of the electrode that can detect the minimum obstacle size at origin, since this is the main problem of the soft-field sensor.

Figures 3.14(a)–(c) compare the normalized current value for a homogenous and non-homogenous system at the nearest (upper graph) and the farthest (bottom graph) pair of measurement electrodes with varying electrode height. Generally, the normalized current value for the electrode near the source was bigger than the farthest electrode when the size of the object becomes larger. However, it is clearly seen that the nearest and the farthest pair of measurement electrodes in Figure 3.14(a) did not give a clear differentiation between homogenous and non-homogenous systems if the obstacle at the centre of the pipe was 10 mm in diameter. Equally important, Figure 3.14(b) shows that a height below 150 mm was not the best height of the electrode since there was still no differentiation between a homogenous and non-homogenous system. Despite that, there was a little increment of normalized current value between 150 mm and 200 mm in height for a 20 mm object. This means that if the larger height of the electrode is chosen, the possibility of detecting a small sized obstacle could be achieved. Also, the normalized current value at the nearest and the farthest electrode falls compared to the homogenous system when the electrode height rises, as in Figures 3.14(b) and (c). This is due to the effect of the current density that becomes smaller when there is an increasing obstacle in the pipe because the small current value will travel across the pipe before being received by the receiver. Conversely, there was clearly a different value of normalized current between the homogenous and non-homogenous system for the measurement electrode when the obstacle was 30 mm (see Figure 3.14(c)). Simultaneously, it seems like the sensor was unable to detect the small size of the obstacle (10 mm) at the centre. The different value of normalized current between a homogenous and non-homogenous system indicated that the non-invasive ERT sensor is able to work in a non-homogenous system. As a result, it is suggested that a height of 200 mm for the non-invasive ERT system should be chosen as the optimum height of the electrode since it was sufficient to detect a 20 mm obstacle at the centre of the vessel.

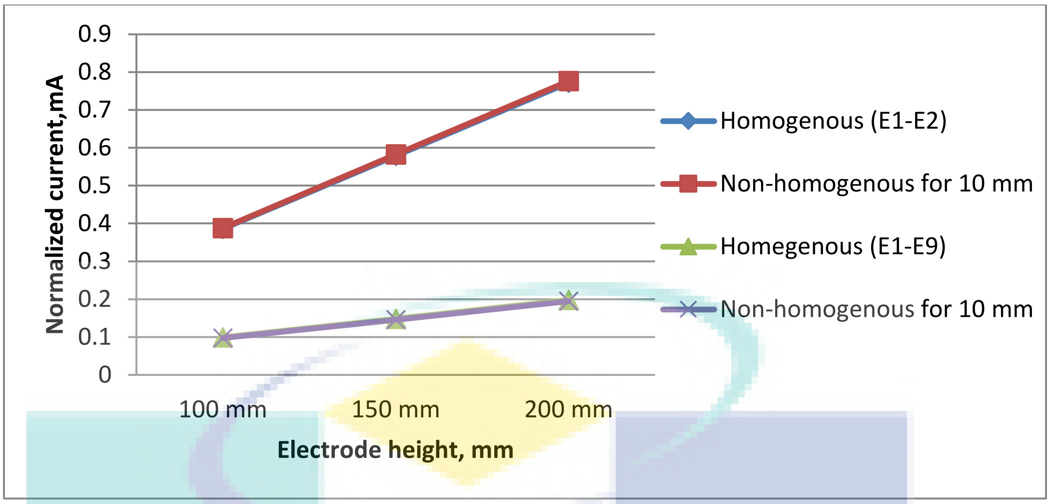


(a)

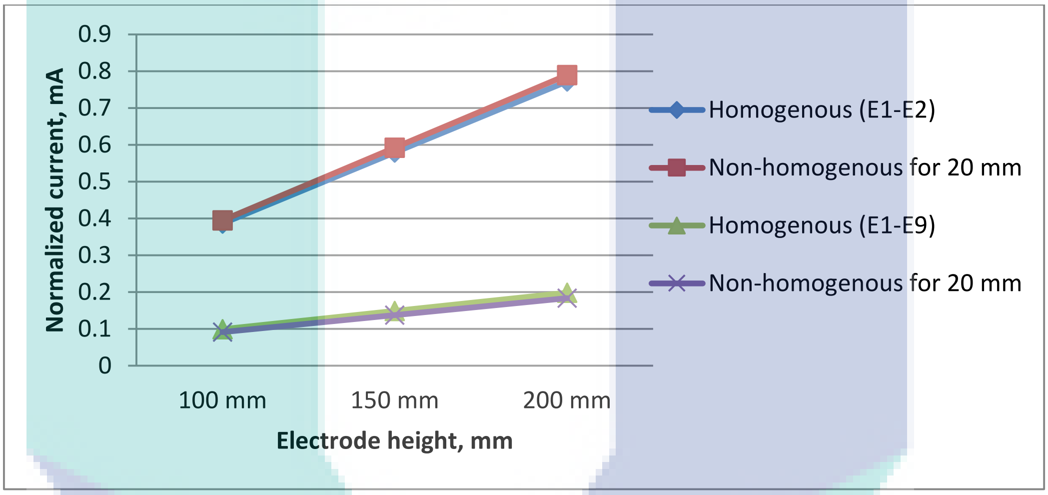


(b)

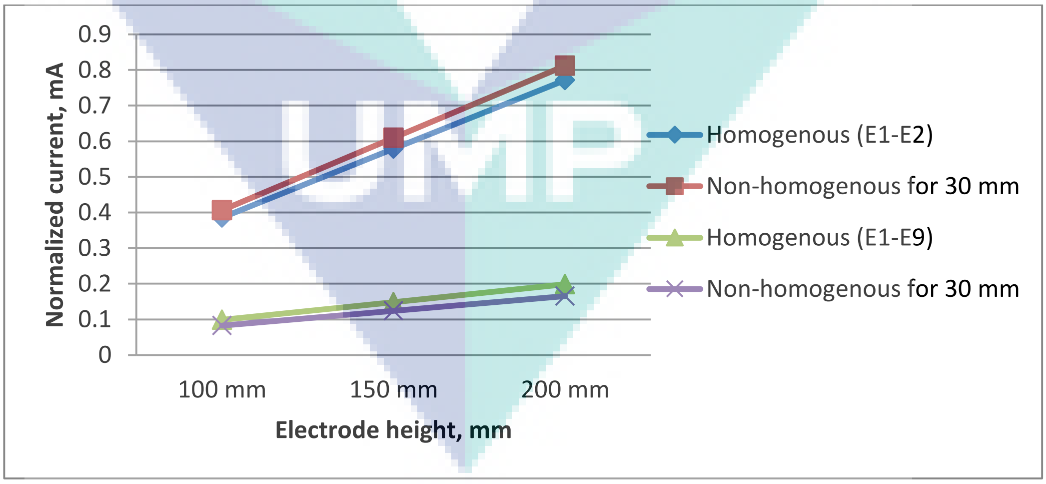


(c)

**Figure 3.14:** Normalized current distribution between homogenous and non-homogenous system for varying electrode height at different phantom placed at origin: (a) 10 mm; (b) 20 mm; (c) 30 mm

Tables 3.5 and 3.6 give an example of surface current distribution with electric field distribution between homogenous and non-homogenous systems at different heights (100 mm, 150 mm, and 200 mm). It can be clearly seen that the increment of height and size of an obstacle enabled the sensor to be more sensitive in allowing the current signal to penetrate through the pipe and detect the obstacle at the centre of the pipe. Simultaneously, the electric field that represented the soft-field behaviour could also be seen when the system was placed with the phantom. It became a more curved line with an increment of object inside the pipe region.

**Table 3.5:** Comparison of homogenous and non-homogenous systems

| Height | Homogenous | Non-homogenous | | |
|---|---|---|---|---|
| | | 10 mm | 20 mm | 30 mm |
| 100 mm | 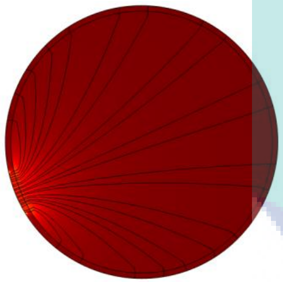 | 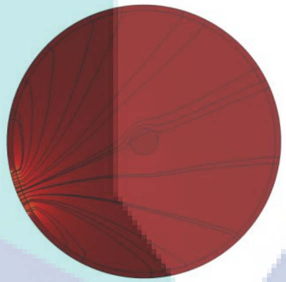 | 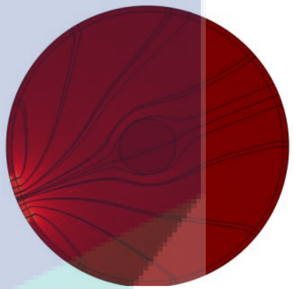 | 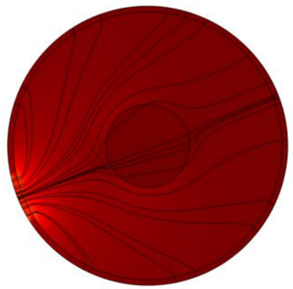 |
| 150 mm | 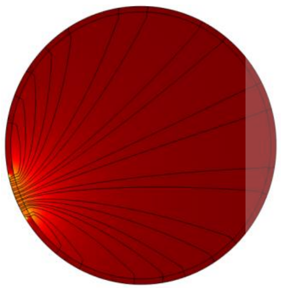 |  | 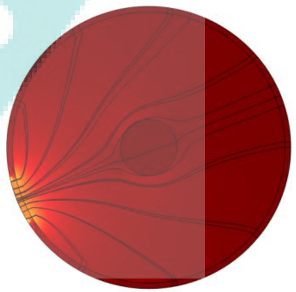 | 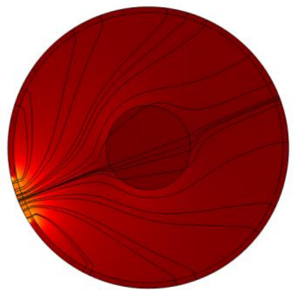 |

**Table 3.6:** Comparison of homogenous and non-homogenous systems (continued)

| Height | Homogenous | Non-homogenous | | |
|---|---|---|---|---|
| | | 10 mm | 20 mm | 30 mm |
| 200 mm | 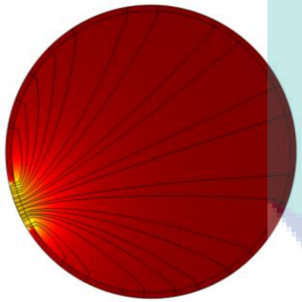 | 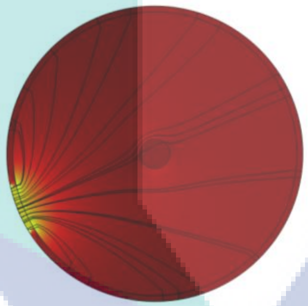 | 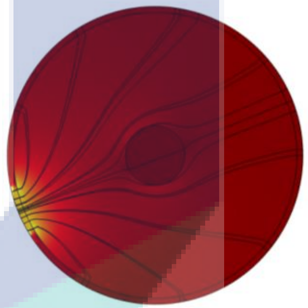 | 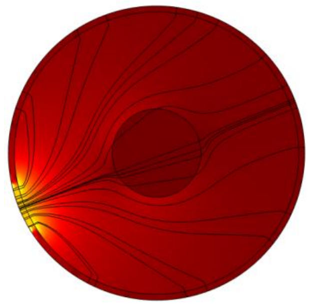 |

The size of electrode chosen was 16 mm (width) and 200 mm (height); the sensitivity of that size was analysed for several non-homogenous systems up to 50 mm. The sensor sensitivity indicates how much the sensor output changed when the measured quantity changed. A good sensor will have a high sensitivity value when it can measure very small changes in the system. Figure 3.15 illustrates the sensitivity of the size of electrode chosen when there is a different size of obstacle at origin in the vessel. Sensitivity, $\Delta I/I_h$, with respect to the normalized current value changes in a homogenous system induced by the obstacle inclusion. The sensitivity distribution was positive at electrode E1 to E3 and E13 to E15 owing to the high value of current near the source, and became negative starting with E4 to E15 because the current value depreciated as it travelled across the vessel. Overall, the sensitivity of the electrode size chosen rose steadily when the size of the obstacle increased. The visualization of the system also can be seen in Table 3.7. Here again, it is clear that the significant minimum size of the object that can be detected by the electrode was 20 mm since it was exactly equal to zero when the size of phantom was 10 mm at origin.

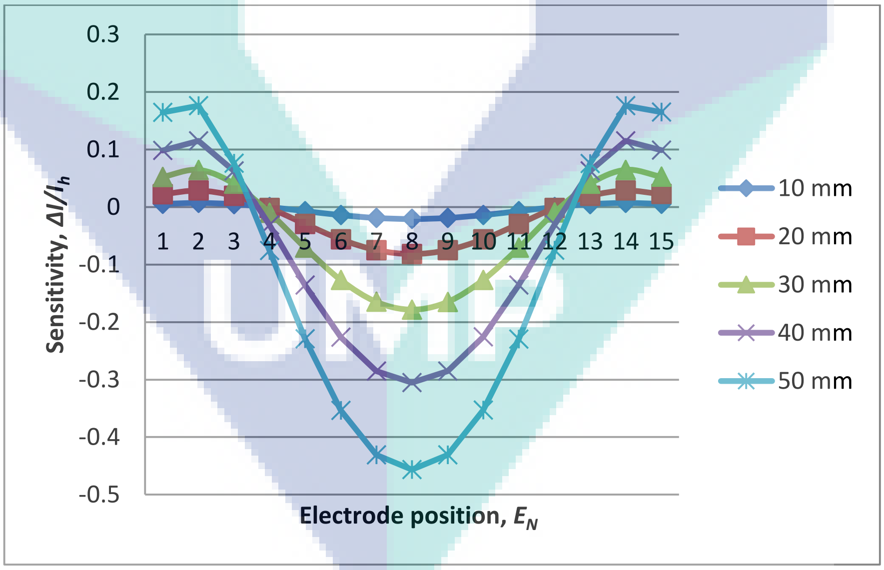


**Figure 3.15:** Sensitivity distribution at detection electrode position with varying obstacle size at origin

**Table 3.7:** Surface current distribution for the increment of obstacle at the centre of the pipe

| Obstacle size | Surface current distribution | Obstacle size | Surface current distribution |
|---|---|---|---|
| 10 mm | 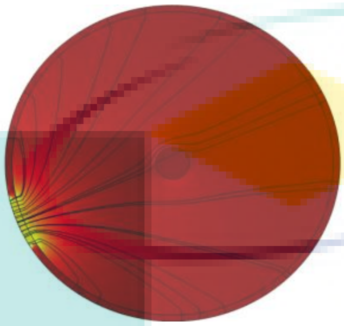 | 40 mm | 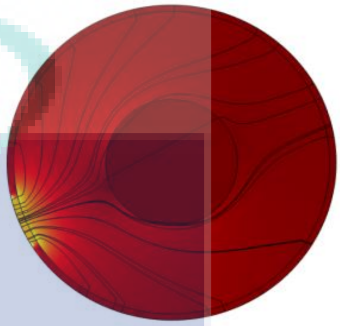 |
| 20 mm | 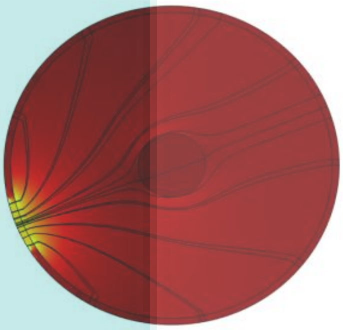 | 50 mm | 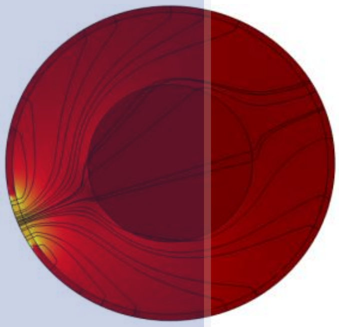 |
| 30 mm | 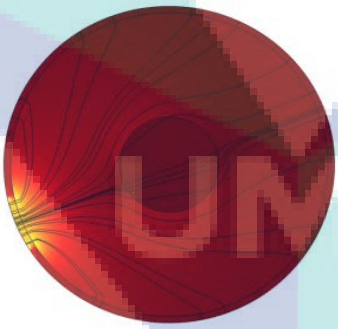 | | |

## 3.5 Summary

This chapter detailed the modelling of the non-invasive ERT system using COMSOL Multiphysics software. The modelling focuses on the determination of a suitable frequency and electrode dimension. The impedance equation is used as the basis for determining the suitable frequency. Then, it was tested in the COMSOL software to observe and analyse the result. It was shown that the compatible frequency that could be applied to the system was 2 MHz. However, there is a limitation on the frequency used, as it must correspond with the conductive liquid being used which has a conductivity range of $5 \times 10^{-3}$ S/m to $8 \times 10^{-3}$ S/m. Later, the optimum width and height of the electrode applied were also modelled. Since the system is the soft-field tomography; the centre of the pipe is involved. Consequently, the 16 mm (width) and 200 mm (height) were chosen as the dimensions of the sensor.

# CHAPTER 4

# IMAGE RECONSTRUCTION

## 4.1 Introduction

Two main aspects are discussed in this chapter. Firstly, the forward problem is explained so that the sensitivity map of the system can be obtained. COMSOL Multiphysics software was applied as the tool to generate the sensitivity map for each channel, followed by MATLAB software for manipulation purposes. Secondly, the inverse problem was solved to get the tomogram of the medium of interest. In this study, the algorithm was based on the back-projection technique. Next, the quality of the image assessment is briefly discussed. Lastly, the thresholding technique is explained briefly as the means to improve the quality of the image.

## 4.2 Forward Problem Solving

The forward problem is solved in order to know the theoretical value of each of the sensors' output based on the signal projection. For the electrical tomography system, the forward problem is solved by representing the electrical field distribution of the internal system [147]. Moreover, the ERT, ECT and non-invasive ERT electrodes are governed by Poisson's equations with only different coefficient values and boundary conditions. Thus, it should be solved depending on the types of electrical tomography system as in described by Sun and Yang [111] for ERT and Lei *et al.* [112] for ECT. As a result, based on relationship between conductance in

Equation (3.3) and references by Lionheart [104], and Sun and Yang [157], the sensitivity coefficient of a two-dimensional electrode pair for non-invasive ERT is based on Equation (4.1).

$$M_{i,j}(x,y) = \frac{\Delta G}{\Delta \sigma} = \int_{A(x,y)} \frac{\boldsymbol{E}_i}{V_i} \cdot \frac{\boldsymbol{E}_j}{V_j} dxdy \qquad \textbf{(4.1)}$$

According to Equation (4.1), the sensitivity coefficient for pair electrode ***i-j*** , $M_{i,j}(x,y)$ to the conductivity change of the pixel at position $(x,y)$ within the area $A(x,y)$ is solved by using dot-multiplying between the $i$-electric field, $\boldsymbol{E}_i$, and $j$-electric field, $\boldsymbol{E}_j$, when $V_i$ and $V_j$ are applied, respectively. Later on, based on the sensitivity map equation, the next sub-section will discuss in detail how to generate the sensitivity map using finite element model software.

### 4.2.1 Generating Map from COMSOL Multiphysics Software

A numerical approach using the finite element model (FEM) was utilized to obtain the sensitivity map distribution. For simplicity, the sensitivity map through the FEM was applied by using commercial software COMSOL Multiphysics. The electric field projection inside the pipe was exported according to how many pixels are involved. For this research, 128 × 128 pixels are the pixels concerned. The parameters of acrylic pipe and water were set as in Table 4.1.

**Table 4.1:** Parameters for system

| Item | Dimension |
|---|---|
| Thickness of pipe | 2 mm |
| Inner diameter of pipe | 96 mm |
| Electrical Permittivity | $\varepsilon_r = 3.45$ (acrylic), $\varepsilon_r = 80$ (water) |
| Electrical Conductivity | $\sigma = 3\times10^{-14}$ S/m (acrylic), $\sigma = 7\times10^{-3}$ S/m (water) |

The general steps for COMSOL simulation was same as in Chapter 3.2 except in the data analysis. A specific step for generating the map can be done manually under the results branch in COMSOL, by exporting how many regular grid data of x axis and y axis points are involved. The x and y points represent the pixels of the model. Similarly, the user also can use coding in MATLAB that is linked to COMSOL. In this research, this forward problem was solved in COMSOL via a live link with MATLAB software.

Firstly, the user must open COMSOL with MATLAB. This will open MATLAB which then links to the COMSOL software. Then, the coding for generating map was developed in MATLAB. The idea for writing the coding is as follows:

1. The single projection of each electrode out of sixteen was obtained. The 136 × 136 pixels data consisting of an electric field in the export function in COMSOL was generated. In this case, there are sixteen data each representing sixteen single projections.
2. Next, the pair projection electrode as in Equation (4.1) was determined by multiplying each single projection in step 1. Moreover, it would have 256 data representing each pair projection of sixteen sensors such as $E_{1,2}$, $E_{1,3}$, $E_{1,4}$,…till...$E_{16,16}$. The multiplication of pair projection was done until all pair projections had been completed. Hence, the map for each pair projections that contains the concerned pixels was achieved.

### 4.2.2 Masking Data for Better Sensitivity Map

As illustrated in Figure 4.1 the pipe drawing consists of the thickness of the pipe. The thickness of the pipe is needed in COMSOL software because the electrodes were applied to the periphery of the pipe wall. However, the sensitivity map is only the map inside the column excluding the thickness of the pipe. Hence, the 136 × 136 data representing the pixel values of the overall drawing were reduced to 128 × 128 pixels to enhance the quality of the sensitivity projection of each of the electrodes.

The idea is illustrated in Figure 4.1. The circle frame coloured by yellow was eliminated to get the affected 128 × 128 pixels. Accordingly, MATLAB software is used to remove the thickness of the pipe by using the masking approach. If the resolution used was 136 × 136 pixels, the radius of the circle was 68 pixels. However, it was interested in a radius of 64 pixels to get 128 × 128 pixels. Roughly, 4 pixels were assumed to be eliminated for each side (left, right, top and bottom) of the circle. However, at the curve side, it was difficult to assume how many pixels should be eliminated. Therefore, to ensure that the radius was consistent with 64 pixels; the approach was done based on Pythagorean Theorem as in [158] and coded in MATLAB, as shown in Figure 4.2.

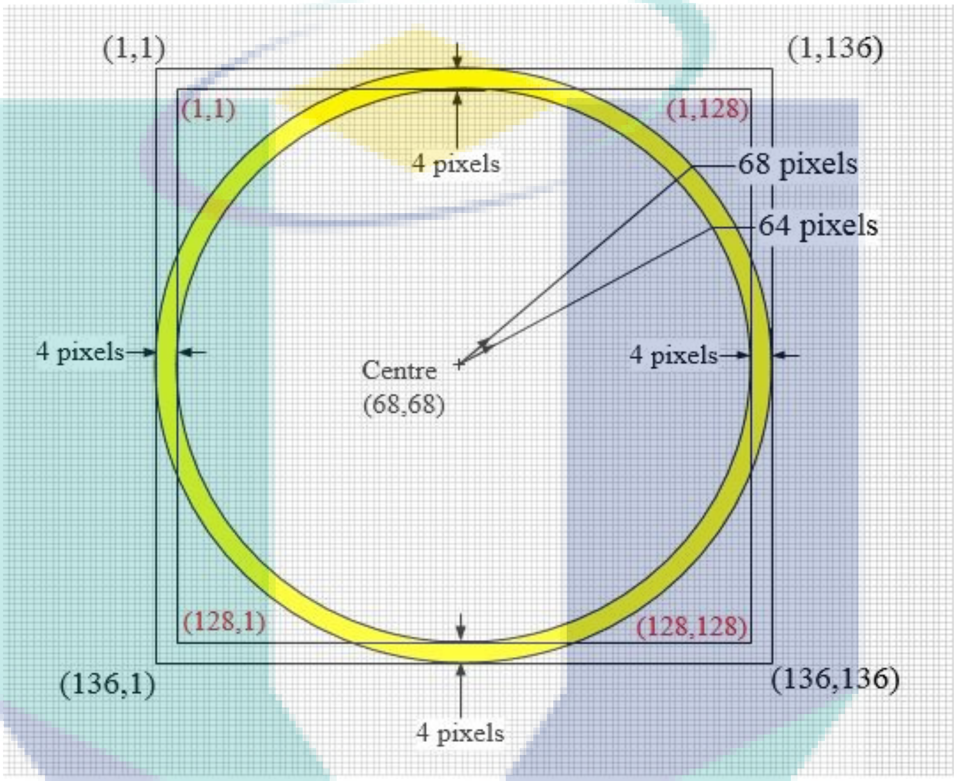


**Figure 4.1:** Basic drawing of 136 × 136 pixels to 128 × 128 pixels

```
%% eliminate the thickness of pipe
pixel= 136; %diameter of pipe in pixel

r=pixel/2; %radius of pipe in pixel

for x=1:pixel
 for y=1:pixel
%if pixel distance (between (x,y) and centre) bigger than 64
pixels, set value to 0
   if
   sqrt((x-pixel/2)^2+(y-pixel/2)^2)>= r-4
   EachProj{i}(x,y)=0; %EachProj{i} is the file of single map
   end
 end
end
```

**Figure 4.2:** Coding for eliminating thickness of pipe written in MATLAB

For each point of pixel ($x, y$); the distance between every point of the pixels and the centre (68,68) was compared. If the distance was bigger than 64 pixels, then, the value at the current point becomes zero. If not, the value will remain and therefore only the thickness of the pipe will be eliminated. The example of how it works is illustrated in Figure 4.3 and Equations (4.2) and (4.3).

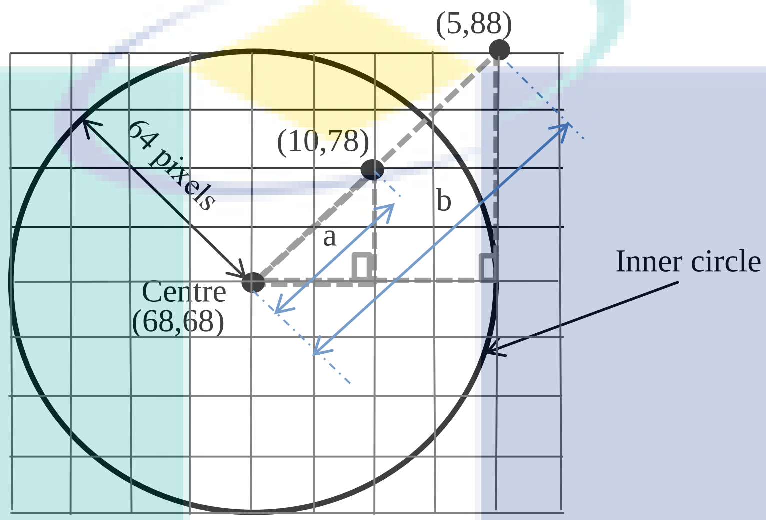


**Figure 4.3:** Example of illustration to eliminate pipe thickness

Based on Figure 4.3, let's say at point (x,y) = (10,78), distance a is

$$\sqrt{\left(10-\frac{136}{2}\right)^2+\left(78-\frac{136}{2}\right)^2}=59 \quad \textbf{(4.2)}$$

$$\therefore a=59<64$$

Thus, the value at point (10, 78) has not changed. But let's say at point (x,y) = (5,88), distance b is

$$\sqrt{\left(5-\frac{136}{2}\right)^2+\left(88-\frac{136}{2}\right)^2}=66 \quad \textbf{(4.3)}$$

$$\therefore b=66>64$$

Hence, the value at point (5, 88) was set to zero. Consequently, the array data of 128 × 128 pixels representing the inner area of the circle for each single projection can be obtained and applied for getting the sensitivity map. Figure 4.4 shows the comparison of the sensitivity distribution for electrode 1 and electrode 9 between, before and after eliminating the thickness of the pipe. From Figure 4.4, it can be seen that the sensitivity distribution of electrode 1 and 9, $E_{1,9}$ has increased.

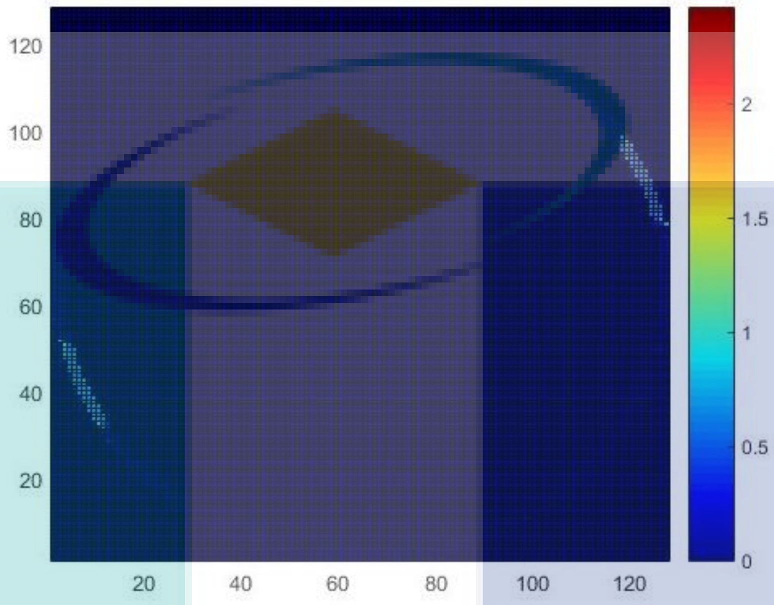


(a)

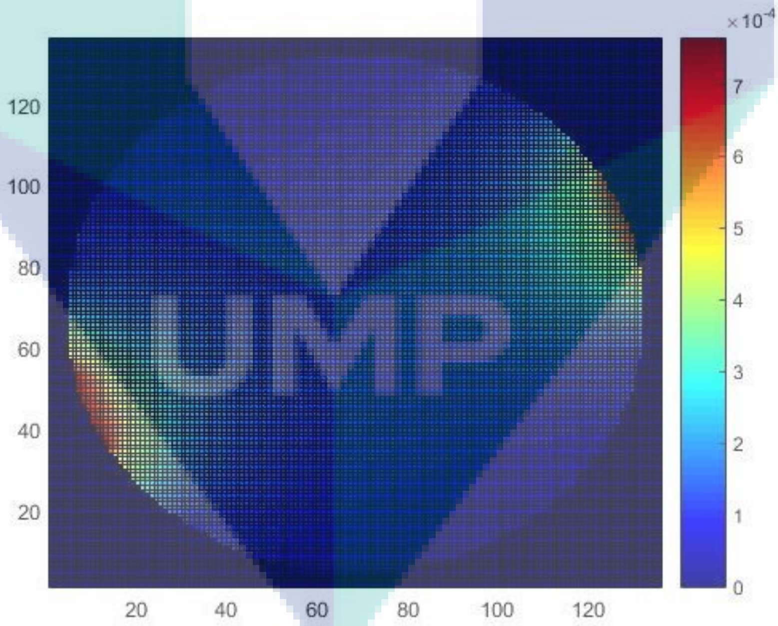


(b)

**Figure 4.4:** Example pairing projection between $E_1$ and $E_9$: (a) before; and (b) after eliminating the thickness of the pipe

If the direct data are applied without being manipulated, the map projection almost cannot be seen compared with after manipulation. Thus, by manipulating the data exported from COMSOL, the sensitivity screening for all pairing of electrodes rose. Also, the total map of the sensitivity distribution between before manipulated and after manipulated is shown in Figure 4.5.

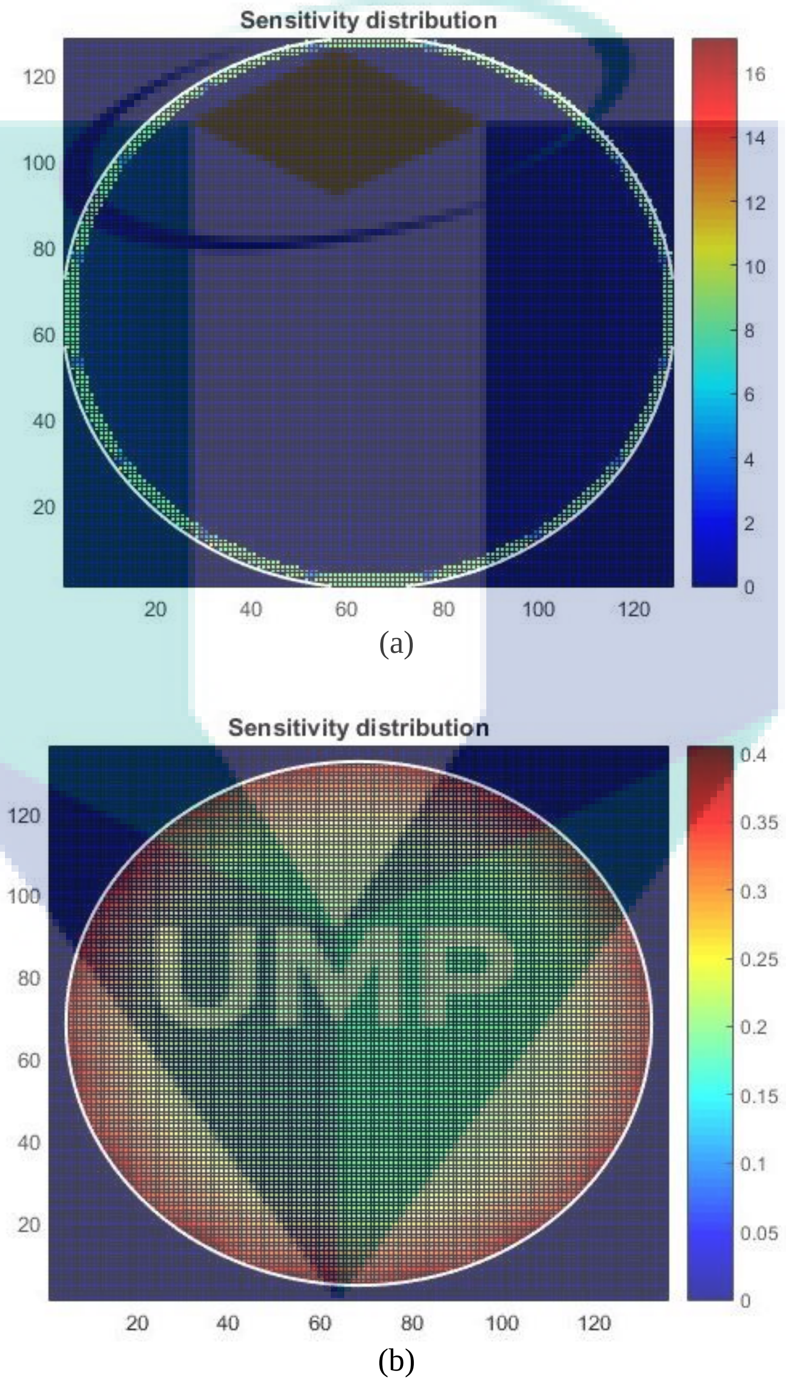


**Figure 4.5:** Total map of the system before and after eliminating the thickness of the pipe: (a) before; (b) after

It can be seen that the intensity of the sensitivity distribution of the overall electrodes was rose significantly particularly in the periphery and the centre of the pipe. Consequently, the manipulation data to eliminate pipe thickness approach was chosen in this research. Moreover, the sensitivity distribution for each of the pair projections is then normalized to get the standardized map. The normalization sensitivity distribution for each pair projection, $\overline{M_{i,j}}(x,y)$ was done by dividing each pair's sensitivity map by the sum of all pair projections, as in (4.4) [159, 160].

$$\overline{M_{i,j}}(x,y) = \frac{M_{i,j}(x,y)}{\sum_{i=1}^{16}\sum_{j=1}^{16} M_{i,j}(x,y)} \quad \textbf{(4.4)}$$

By implementing the manipulated data of the map distribution, this also raises the normalized pair projection. As sixteen electrodes act as transmitters and receivers, there are 256 sensitivity matrices overall in the system. Examples of normalized sensitivity distribution when channel one was set as the excitation electrode is shown in Figures 4.6 and 4.7. It can be seen that the projection for each pair of electrodes produces a curved line. The curved line occurred owing to the soft-field behaviour of the electrical tomography, as discussed in section 2.5.1. Also, the projection value of adjacent electrodes pairs (E1E2 and E1E16) are larger compared to the opposite electrode pair, which indicates that it failed to give a uniform and even sensitivity distribution. This is because of distinctive soft-field sensing characteristics [114]. The normalized sensitivity map obtained for each of the pair projections is later implemented in the inverse problem part.

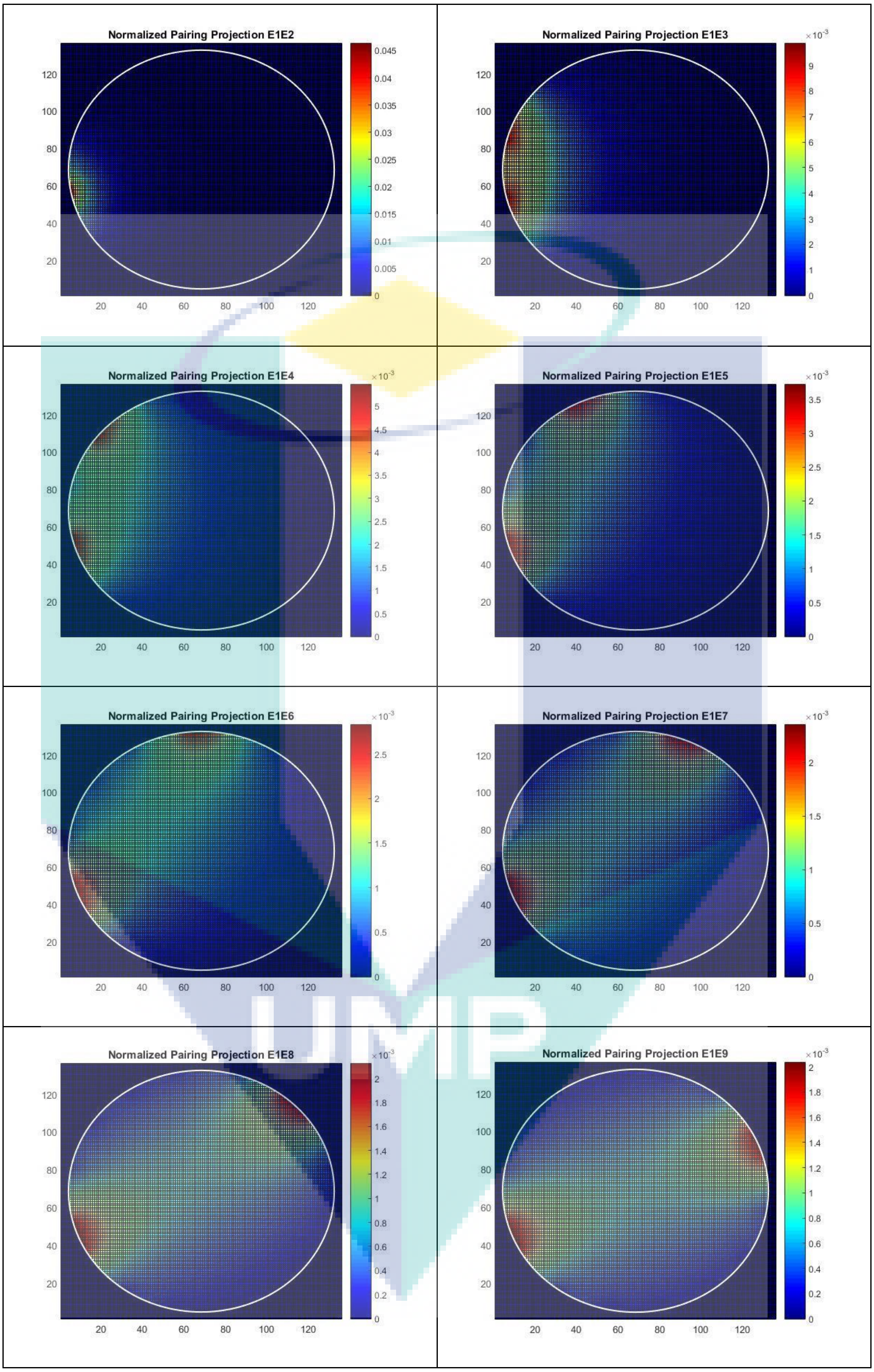


**Figure 4.6:** Sensitivity distribution for transmitter 1 with receiver 2 to receiver 9

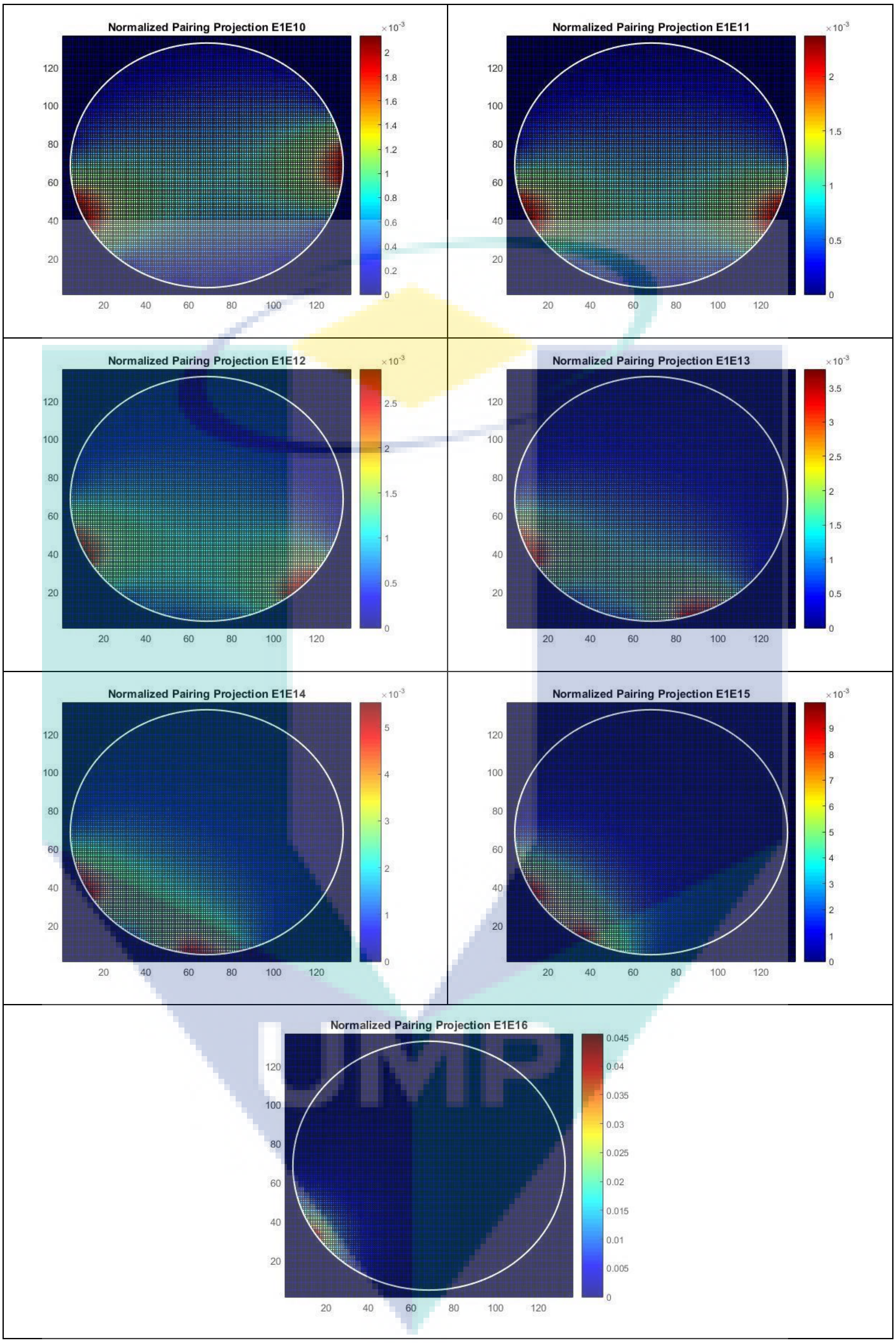


**Figure 4.7:** Sensitivity distribution for transmitter 1 with receiver 10 to receiver 16

## 4.3 Inverse Problem Solving

The inverse problem is applied to obtain the unknown component distribution in the system of interest, also known as the tomogram [161]. Alternatively, the inverse problem in the non-invasive ERT system is to determine the conductivity distribution from the current measurement data. In this study, the algorithm to reconstruct the image was based on the back-projection algorithm. There are several types of back-projection algorithm such as linear back-projection algorithm (LBP), filtered back-projection algorithm (FBP) and convolution back-projection algorithm (CBP). However, the LBP was implemented in this research project as the basis for the thresholding technique.

### 4.3.1 Linear Back-Projection Algorithm (LBP)

The LBP involves the matrix multiplication between the normalizing sensitivity map, $\overline{M}_{i,j}(x, y)$ and the signal loss amplitude of receiver *j*-th for projection *i*-th, $S_{i,j}$ [135], [162]. Then the same element of the arrays will be summed to get the back-projected conductivity distribution, also known as the concentration profile. Consequently, the concentration profile will be displayed in colour pixels. The mathematical equation of LBP can be expressed as follows:

$$P_{LBP}(x, y) = \sum_{i=1}^{16}\sum_{j=1}^{16}\overline{M}_{i,j}(x, y)\cdot S_{i,j} \tag{4.5}$$

In this study, the tomogram obtained by the LBP algorithm will be standardized from 0 to 1 by using Equation (4.6) for easy comparison and analysis.

$$P_{LBPnorm}(x,y) = \frac{P_{LBP(m,n)}(x,y) - P_{LBP\min}(x,y)}{P_{LBP\max}(x,y) - P_{LBP\min}(x,y)} \tag{4.6}$$

where

$P_{LBP}(x, y)$ is the conductivity distribution obtained using LBP algorithm or the concentration profile,

m and n are the specified location of 136 × 136 pixels of the concentration profile,

$P_{LBPnorm}(x,y)$ is the normalized concentration profile,

$P_{LBP(m,n)}(x,y)$ is the pixel value at m and n of the concentration profile,

$P_{LBP\min}(x,y)$ is the minimum value of pixel in the concentration profile, and

$P_{LBP\max}(x,y)$ is the maximum value of pixel in the concentration profile.

## 4.4 Image Quality Assessment

There are varieties methods of evaluating the quality of the reconstructed image. Basically, the reconstructed image (tomogram) can be compared with the referenced image (binary image). In this thesis, the multi scale structural similarity (MSSIM), percentage area error (AE) and solid concentration are utilized.

### 4.4.1 Multi Scale Structural Similarity (MSSIM)

MSSIM is a technique that compares the similarity between the resulted image and the reference image [163,164]. Zhou Wang *et al.* introduced the MSSIM to improve the old-style methods of image-quality assessment, such as mean square error (MSE) and peak signal to noise ratio (PSNR), which have the problem of inconsistency of human eye perception. Based on Wang *et al.* [163],[165], the MSSIM has proved to be more powerful compared to the MSE and PSNR.

The MSSIM results in the output between the indexes 0 to 1. A larger value of the MSSIM index will indicates that the reconstructed image closer to the reference image. The mathematical equation for MSSIM is illustrated in Equations (4.7) and (4.8). A detailed explanation of MSSIM can be found in Ref. [163–165].

$$\mathrm{MSSIM}(X, Y) = \frac{1}{M}\sum_{j=1}^{M}\mathrm{SSIM}(x_j, y_j) \qquad \textbf{(4.7)}$$

$$\mathrm{SSIM}(x, y) = [l(x, y)]^{\alpha}.[c(x, y)]^{\beta}.[s(x, y)]^{\gamma} \qquad \textbf{(4.8)}$$

where

X is the reference image.

Y is the distorted image.

*M* is the number of local windows of the image.

$x_j$ and $y_j$ are the image contents at the $j^{th}$ local window.

$l$(x,y) is the luminance comparison function .

$c$(x,y) is the contrast comparison function.

$s$(x,y) is the structure comparison function, and

$\alpha$, $\beta$, and $\gamma$ are parameters used to adjust the relative importance of the three components.

### 4.4.2 Area Error, AE

Area error can be obtained to get the error information of the tomogram as defined in [166]. In the tomography system, the reconstructed image, $G_R(p)$ was compared to the standard image, $G_s(p)$. The reconstructed image of M pixels was converted into binary image, $G_b(p)$ , to ensure that it was in the same range as the standard image utilized. In the study, 0 pixels were assumed to be the liquid component whereas others were the phantom element.

$$G_s(p) = \begin{cases} 0 & \text{for pixel occupied by liquid component} \\ G_M & \text{for pixel occupied by phantom component} \end{cases} \tag{4.9}$$

$$G_b(p) = \begin{cases} 0 & G_R(p) = 0 \\ G_M & G_R(p) > 0 \end{cases} (p = 1,2,....,M) \tag{4.10}$$

Thus, the percentage AE is defined as [166]:

$$AE(\%) = \frac{\sum_{p=1}^{M} G_b(p) - \sum_{p=1}^{M} G_s(p)}{\sum_{p=1}^{M} G_s(p)} \times 100 = \frac{N_R - N_s}{N_s} \times 100 \tag{4.11}$$

where

$G_s(p)$ = standard (reference) model pixels

$G_M(p)$ = colour level assigned to the phantom component

$G_b(p)$ = binary reconstruction image pixels

$N_R$ = number of pixels with non-zero colour level in the binary reconstructed image

$N_s$ = number of pixel with non-zero colour level in the standard image

The percentage of AE could be a positive or negative value. If the AE is positive, it means that the reconstructed image obtained is always larger than the standard image and vice versa [167].

### 4.4.3 Solid Concentration

The percentage concentration of the affected component of the reconstructed image was applied by using Equation (4.12) [166]. The number of non-zero pixels from the reconstructed image or standard image was divided by the effective area. The effective area, $EA_{area}$ of the cross-section of the inner pipe used, was determined by the M square image pixels. Based on sub-section 4.2.2, the 136 ×136 pixels image was chosen to display the tomogram. Hence, M= 12853 pixels where another 5643 pixels lie outside the pipe boundary. The information of this concentration gives the user the percentages of phantom or liquid covering the area in the pipe.

$$Phantom(\%) = \frac{N_R}{EA_{area}} \times 100 \tag{4.12}$$

## 4.5 Thresholding technique

The thresholding technique can be used to extract objects from the background [168]. In the tomography application, it can improve the quality of the reconstructed image by removing the unwanted pixels in the cross-section image, and the minor medium, such as gas or solid concentration, can be identified. The basic thresholding technique involves the intensity of pixels in the concentration profile that are converted into a binary value depending on the threshold value, $P_{Th}$ [169]. This is also known as the global threshold [168]. If the pixel value is greater than the pre-set threshold, the final pixel is set to 1 or is otherwise 0. Equation (4.13) shows the mathematical model of the thresholding process for a given reconstructed image from the LBP algorithm. $G_T(x,y)$ is the resulting image after the thresholding process. In subsection 6.3, the results of the tomograms are presented in pseudo-colour, which is red and blue, for binary value 1 and 0, respectively. Pseudo-colour is a technique of converting grey levels of a black-and-white image into an assigned colour [170]. The reason for using pseudo-colour is because it is attractive for the visual identification of the liquid–solid profile.

$$G_T(x,y) = \begin{cases} 1, if \ P_{LBPnorm(m,n)}(x,y) > P_{Th} \\ 0, if \ P_{LBPnorm(m,n)}(x,y) \le P_{Th} \end{cases} \qquad \textbf{(4.13)}$$

However, the threshold value must be carefully selected to ensure that the improved reconstructed image is reasonable. For that reason, the method to choose the best threshold value was done by taking 100 steps (with interval 0.01) of the pixel value of the concentration profile. Accordingly, the AE was determined, and the optimum threshold value that gave AE value to be almost +/- 0 was selected. Then the mean of the optimum threshold value for all types of simulations or experiments conducted was calculated and implemented for the final thresholding process.

## 4.6 Summary

This chapter discussed the image reconstruction technique for the developed non-invasive ERT system. The sensitivity map was solved using COMSOL software. The manipulation technique had been applied to increase the projection of the map. Then, it was implemented in the linear back-projection (LBP) algorithm to reconstruct the image. The MSSIM, AE, and concentration were pointed out as the image quality assessment. The threshold technique was explained as the focus of the image reconstruction and improvement of the LBP algorithm. The AE was applied to get the optimal threshold value from the 100 steps of the pixel value of the concentration profile.

# CHAPTER 5

# HARDWARE AND SOFTWARE DEVELOPMENT

## 5.1 Introduction

In this chapter, the hardware and software developments are discussed. Section 5.2 explains the details of the hardware design of the developed non-invasive ERT system. The hardware discussion includes the design and development of the electrodes, the electronic measurement circuits and data acquisition system for interfacing between the hardware and software. The output signal from the hardware part is used for the software part to obtain and analyse the tomogram. Next, section 5.3 discusses the software design applied for the tomography image reconstruction.

## 5.2 Non-Invasive ERT System-An Overview

In this research, the mixtures of two-phase regime in a vessel were monitored using a non-invasive electrical resistance tomography system. The proposed experimental set-up is illustrated in Figure 5.1. There were a total of sixteen channels of metal electrodes which were applied and attached non-invasively to the vertical non-conducting pipe. The non-conducting pipe was an acrylic tube with an outer diameter of 100 mm, a thickness of 2 mm and a height of 500 mm. As shown in Figure 5.1, each of the sixteen channels was switched as a transmitter or a receiver by using an analogue switch integrated circuit. The circuit was controlled by microcontroller dsPIC30F6010A.

There were two main parts to the designed circuits: signal generator circuit and signal conditioning circuit. Firstly, a sinusoidal voltage signal was generated by the signal generator circuit. A direct digital synthesis (DDS) integrated component was chosen to produce the sinusoidal signal. It was programmed by the microcontroller PIC18F4580. Then the signal was switched according to the transmitter channel by using demultiplexer. The signal from the selected transmitter channel was then amplified up to 10 $V_{pp}$ by using an amplifier circuit and applied to the transmitter. Secondly, in the signal-conditioning circuits, the received signal at the receiver was fed into a current-to-voltage (I-to-V) converter amplifier circuit and filtered using a low-pass filter. As a result, the converted signal was in the range of 2 MHz and eliminated for all the possible noise. It was different when compared to the previous work [17], [19–21] as reviewed in subsection 2.5, whereby a low-frequency source with a PSD approach was implemented after the I-to-V converter amplifier circuit. However, since a high frequency was applied, it was a challenge to choose the best and simplest technique for converting the sinusoidal signal into the direct current (DC) signal so that it could easily be used for reconstructing it into an image. Thus, in this research, the peak-detector circuit was designed to convert the alternate current (AC) to a DC signal. Finally, the DC signal was sampled by dsPIC30F6010A so that it could be applied for getting the tomogram in the tomography image reconstruction. The reconstructed image was done for only one set of measurement data from the sensor reading in this research.

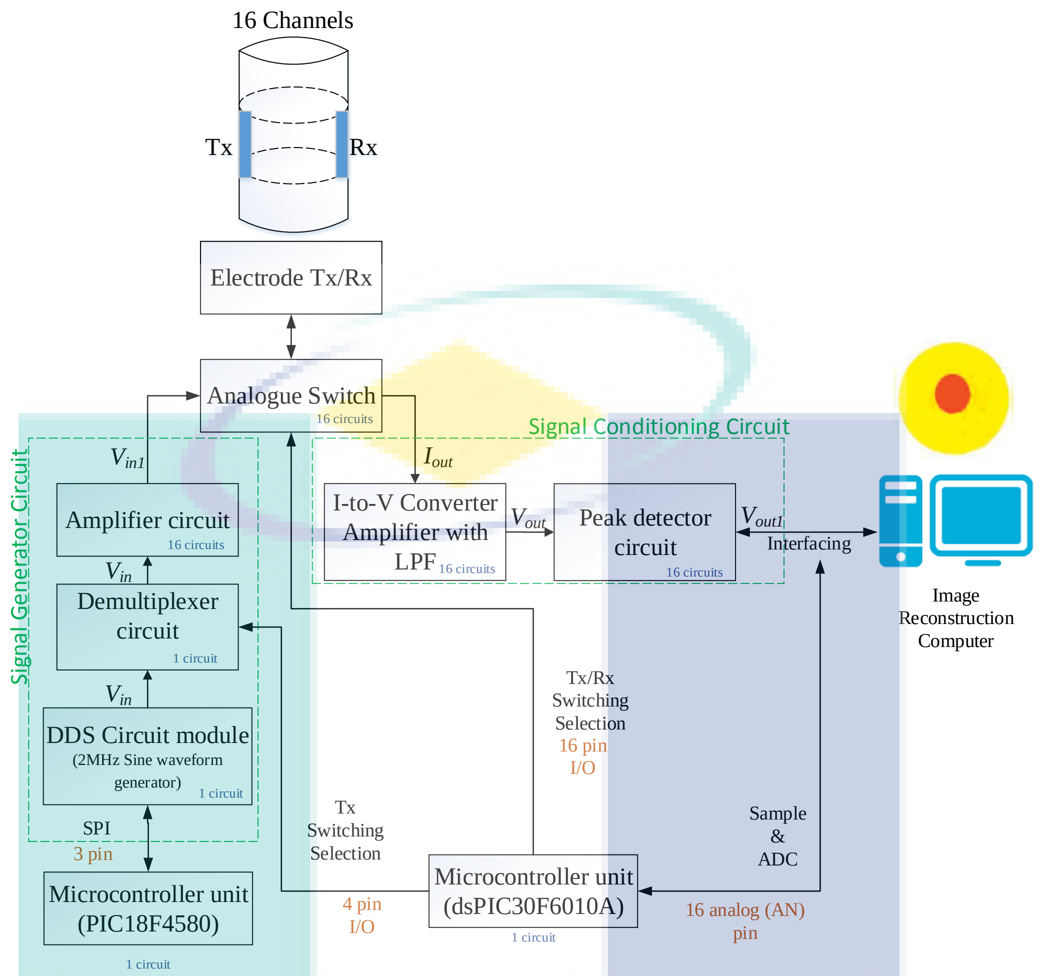


**Figure 5.1:** Experimental setup for non-invasive ERT system

### 5.2.1 Sensor Design

Based on simulation result of electrode dimension optimization (16 mm (width) × 200 mm (height)) in sub-section 3.4.1, each of the metal electrodes was made of a flexible printed circuit board because they could be easily bent. The bottom and upper details of the sensor design are illustrated in Figure 5.2. The area of the electrode other than the sensing area was shielded by connecting it to the ground to avoid the surrounding noise.

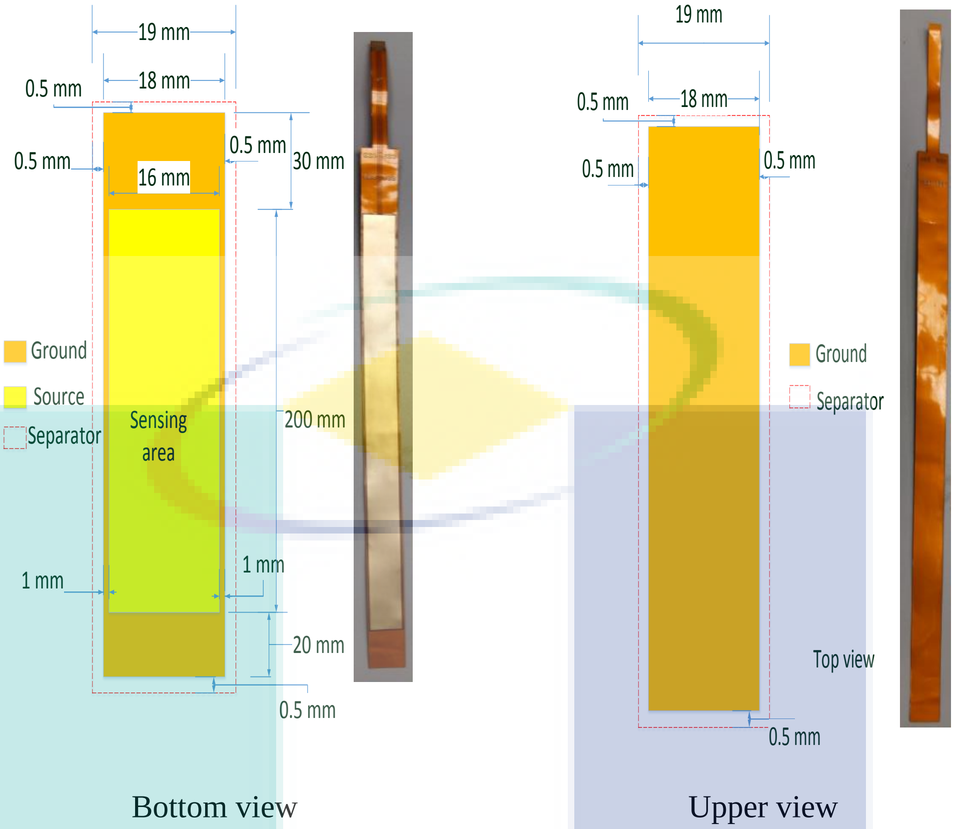


**Figure 5.2:** Designed non-invasive ERT sensor

Also, a sensor jig was designed to stick and hold each of the sixteen sensors independently, as illustrated in Figure 5.3. The design of the sensor jig was flexible to ensure that the jig could also be applied to other pipes if necessary. This means that the sensor jig for each the sixteen channels can be unscrewed independently. Simultaneously, a ring holder with two screw locks on the upper and lower sides of the pipe was also designed to hold the sensor jigs. Figure 5.4 shows the ring holder in which the sensor jigs were attached to the pipe.


(a) (b) (c)

**Figure 5.3:** (a) Ring holder with sensor jigs; (b) example of a sensor jig from the side; and (c) inner views

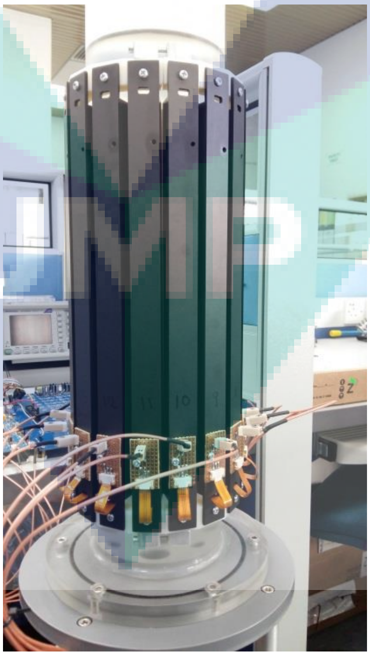

**Figure 5.4:** Sensor jig attached to the pipe (height of pipe is 500 mm)

### 5.2.2 Sensor Switching

Each of the sixteen non-invasive ERT sensors functioned either as a transmitter or a receiver. The analogue switch, MAX319 as shown in Figure 5.5 was chosen to turn each of the channels as a transmitter or a receiver. When the channel became a transmitter, the analogue switch circuit would connect to the signal generator circuit. The remaining sensors became receivers and were linked to the signal conditioning circuit. The switching sequences for the transmitter and receiver were controlled by the digital control from the microcontroller. Logic 1 turns on MAX319 as the excitation source, and logic 0 as the detection source.

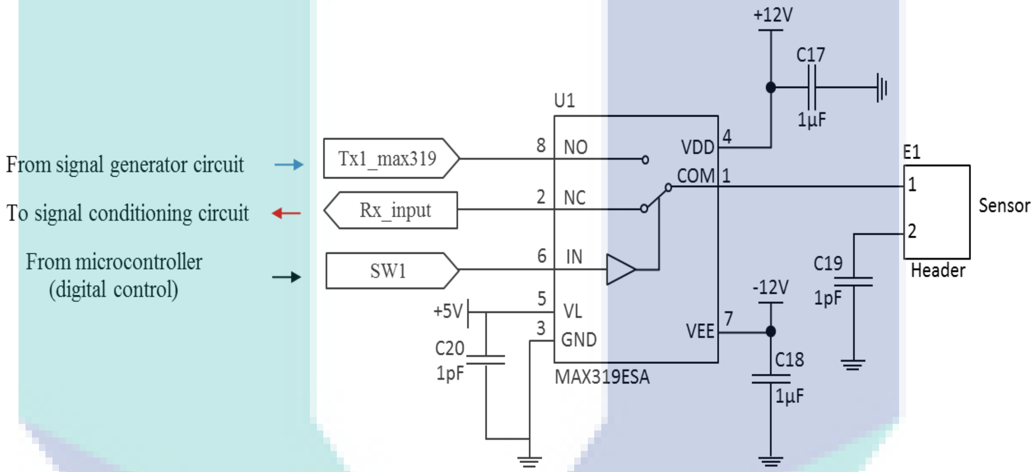


**Figure 5.5:** Analogue switch circuit

### 5.2.3 Selection of the Types of Source Signal

There are two possible conditions that affect the system when applying a high frequency source: (1) the potential for the amplitude of excitation source is reduced and (2) the circuit will not be able to offset the stray capacitance [18]. Therefore, in this research, the type of signal plays a significant role to ensure that the signal can be transmitted and received appropriately, and also achieves stability at high frequency. By using a function generator, two types of 10 $V_{pp}$ signals, square and sine waveforms, were tested. That signals were connected directly to the sensor without any circuitry. For this case, the function generator was assumed to be as the signal generator circuit.

Firstly, the square waveform was tested with a frequency less than 1 MHz, such as 500 kHz. It can be observed that the emitting signal in Figure 5.6 still retains the amplitude and square shape even though there is a slight curve at the top and bottom line of the graph. This was because the signal had enough time to charge and discharge at low frequency. However, due to the COMSOL simulation, the optimum rate to be applied to the system is 2 MHz. So, the low frequency was not used in the system.

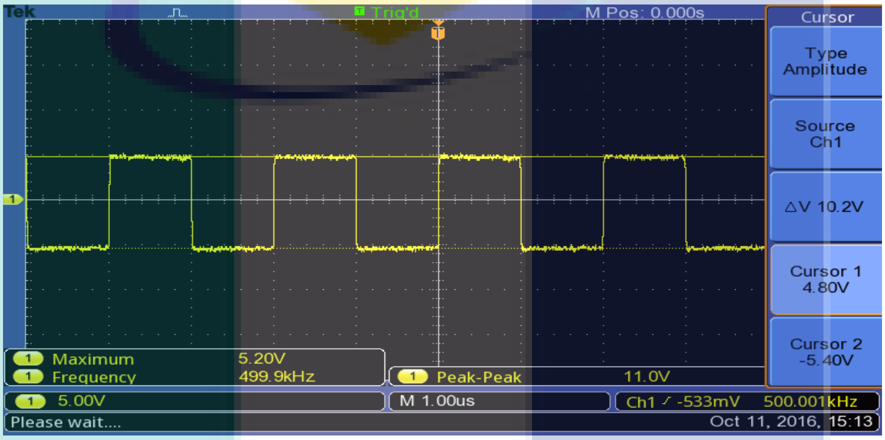


(a) Before being connected to the sensor

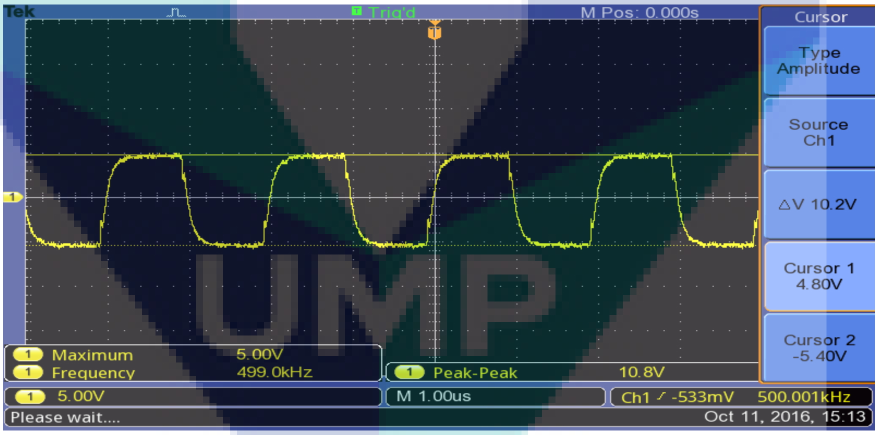


(b) After being connected to the sensor

**Figure 5.6:** Tested square waveform at 500 kHz

When the square waveform with 2 MHz was applied as the source, the transmitting signal itself was distorted, as shown in Figure 5.7. It can be seen that the transmitting signal was similar, but in triangular shapes which was due to the high frequency applied to the system. When the frequency was high, the capability of the signal to be charged and discharged was smaller. Hence, it affected the capability of the signal to retain the original shape generated. It also influenced the received signal owing to the affected transmitting signal. Therefore, it was difficult to maintain the square shape signal for the system if the square waveform was implemented.

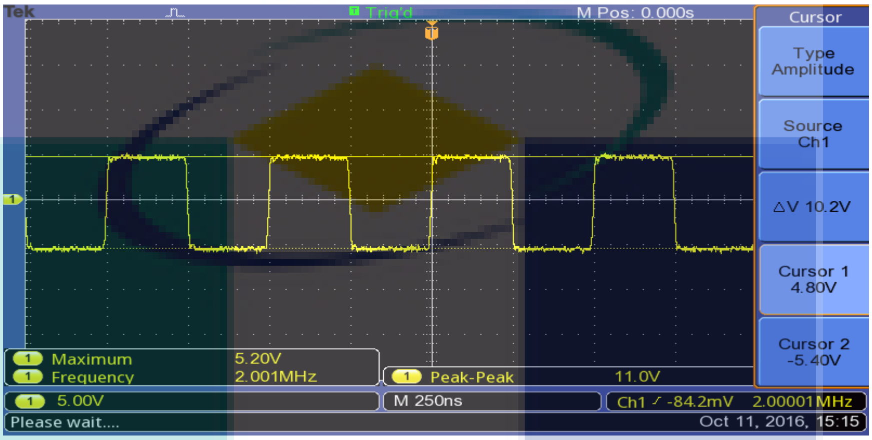


(a) Before being connected to the sensor

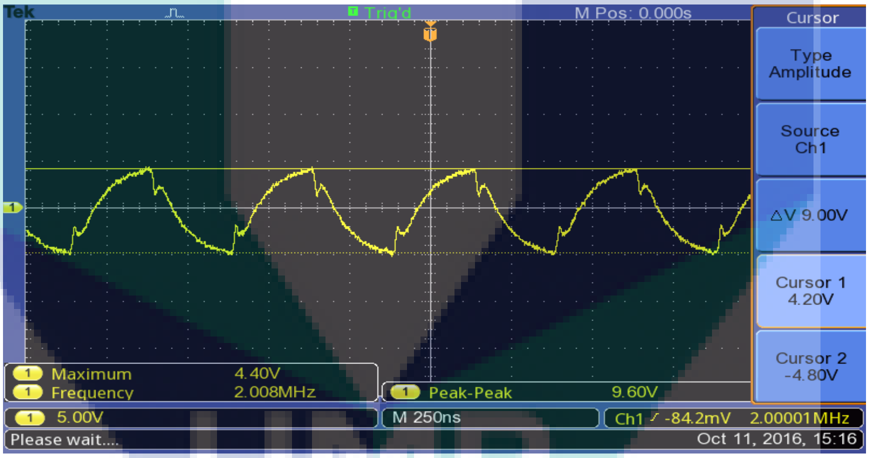


(b) After being connected to the sensor

**Figure 5.7:** Tested square waveform at 2MHz

Secondly, in contrast, when the sine waveform was applied in the system, it was found that the transmitting signal was maintained in the sinusoidal shape as illustrated in Figures 5.8 and 5.9. Equally important, the excitation amplitude must be as close as possible to the desired amplitude. Nevertheless, as shown in Figure 5.9, the peak-to-peak voltage of the source signal at the sensor was reduced around by 3.4 $V_{pp}$ as the frequency increased.

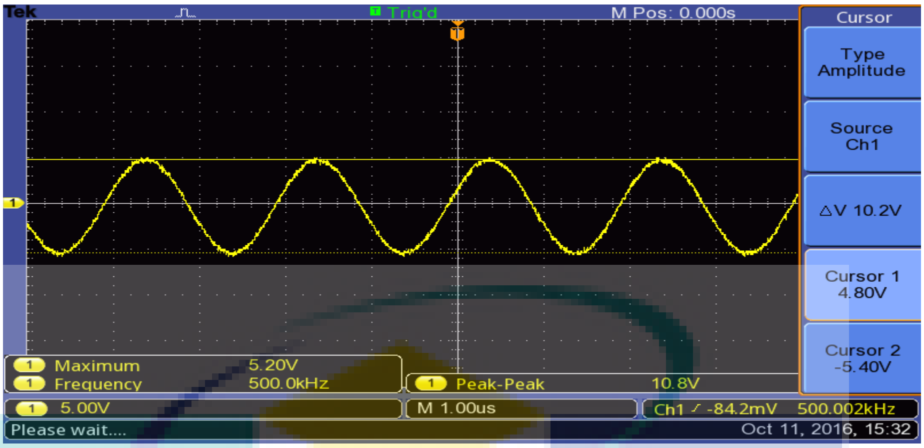


(a) Before being connected to the sensor

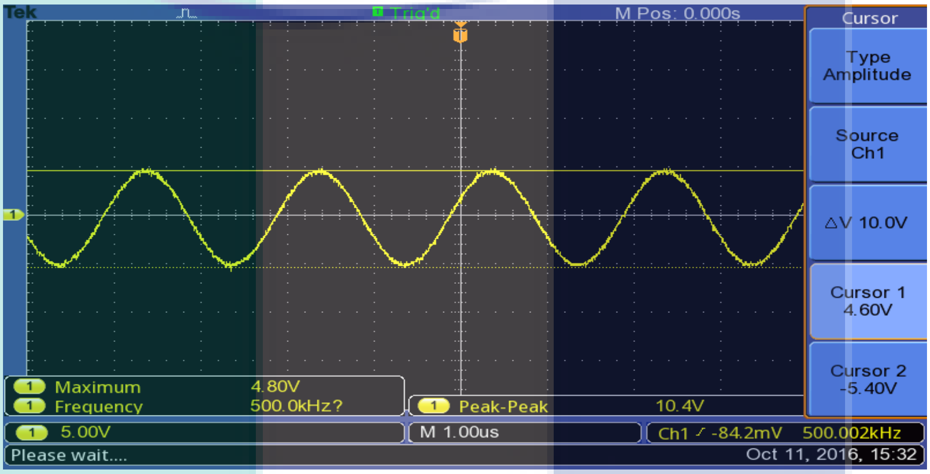


(b) After being connected to the sensor

**Figure 5.8:** Tested sinusoidal waveform at 500 kHz

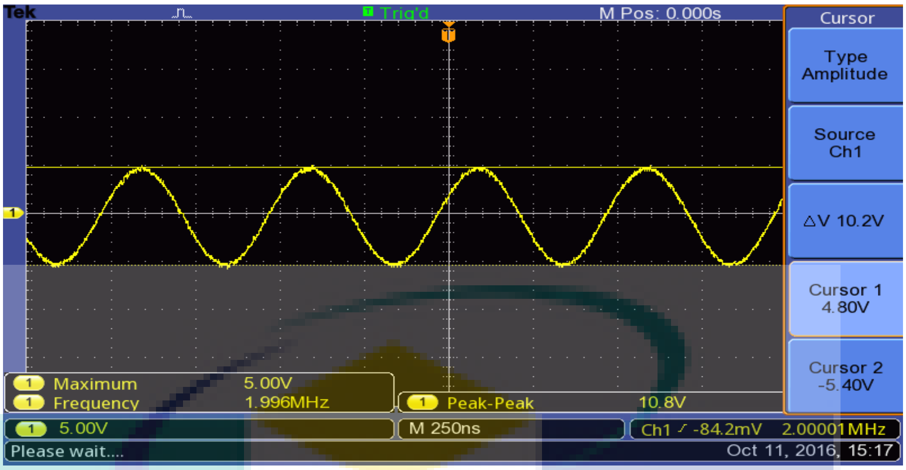


(c) Before connected to the sensor

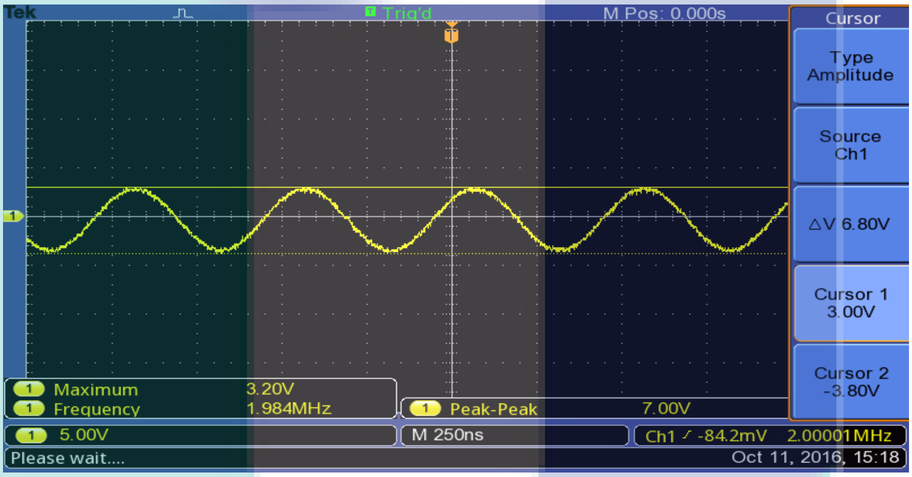


(d) After connected to the sensor

**Figure 5.9:** Tested sinusoidal waveform at 2MHz

Prior to this, the signal degradation is the main concern as it was not able to get the accurate receiving signal. Thus, to maintain the amplitude of the excitation signal at the sensor, a small capacitance around 1pF was placed at the shielded line connector at the analogue switch circuit to the ground as illustrated in Figure 5.10. Hence, by comparing the square and sine waveforms, the sine waveform was chosen as the source signal to be applied to the non-invasive ERT system.

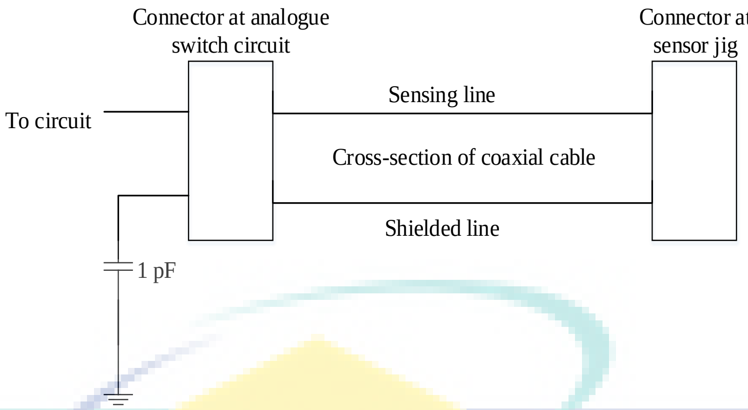


**Figure 5.10:** Connection of 1pF capacitor at the sensor connector

### 5.2.4 Signal Generator Circuit

There were three parts in the signal generator circuit: the DDS, the demultiplexer, and the amplifier circuits.

#### 5.2.4.1 DDS Circuit

As discussed in subsection 5.2.3, the signal chosen was the sinusoidal waveform. Therefore, the programmable waveform generator DDS circuit was applied to generate the sinusoidal waveform. The integrated circuit AD9833 was chosen to produce the sinusoidal waveform at 2 MHz frequency. The AD9833 is a digitalized programmable frequency and was programmed by using the serial peripheral interface (SPI) module in PIC18F4580. The following steps must be followed to program AD9833 to obtain a 2 MHz sinusoidal waveform:

1. Calculate the frequency register by using Equation (5.1).

$$\text{Frequency Register} = \frac{f_{out} \times 2^{28}}{f_{\text{MCLK}}} \tag{5.1}$$

where

$f_{out}$ is the desired output frequency.

$f_{MCLK}$ is the master clock frequency for AD9833 used.

Correspondingly, the desired frequency was 2 MHz and the master clock frequency applied was 20 MHz. Thus, the frequency register was 26843545 in decimal number.

2. The initialization sequence setting must be set as in Table 5.1.

**Table 5.1:** Initialization sequence setting

| Steps | Sequence | Hexadecimal |
|---|---|---|
| 1 | Control Register. Set the enable reset (D8=1), LSB & MSB written consecutively (D13=1) and sinusoidal signal mode (D1=0). | 0×2100 |
| 2 | Frequency Register 0 LSB. The bit D15 and D14 set to 0 and 1, respectively, which was the Frequency Register 0 address. Others bits were 1s. | 0×3FFF |
| 3 | Frequency Register 0 MSB. The bit D15 and D14 set to 0 and 1, respectively, which is the Frequency Register 0 address. Others bits were 0s. | 0×4000 |
| 4 | Write the value of 28 bits frequency register calculated for 2 MHz as in step 1. In this study, the microcontroller was programmed by comparing step 2 and 3 to do the maths to send the 28 bits automatically. Thus, the value was set in decimal. | 26843545 in decimal |
| 5 | Phase Register 0. The bit D15, D14, and D13 were set to 110. This setting would give the phase zero. | 0×C000 |
| 6 | Control Register. Set the disable reset (D8=0), LSB & MSB written consecutively (D13=1) and sinusoidal signal mode (D1=0). | 0×2000 |

The guidelines to program the AD9833 can be found in [171]. And the code for generating 2 MHz sinusoidal waveform using CCS compiler can be referred to in Appendix B.

The schematic diagram of the AD9833 to link with the PIC18F4580 is illustrated in Figure 5.11. The active low control input, FSYC pin was connected to the chip select, CS/RE2 pin. The serial clock input, SCLK pin was attached to the serial clock, SCK/RC3 pin. The serial data input, SDATA pin was linked to the serial data out, SDO/RC5 pin at PIC18F4580. Also, the MCLK pin from AD9833 was connected to the oscillator pin RA6 of PIC18F4580. The 51-ohm resistors at each of the SPI pin were applied to avoid the glitch signal.

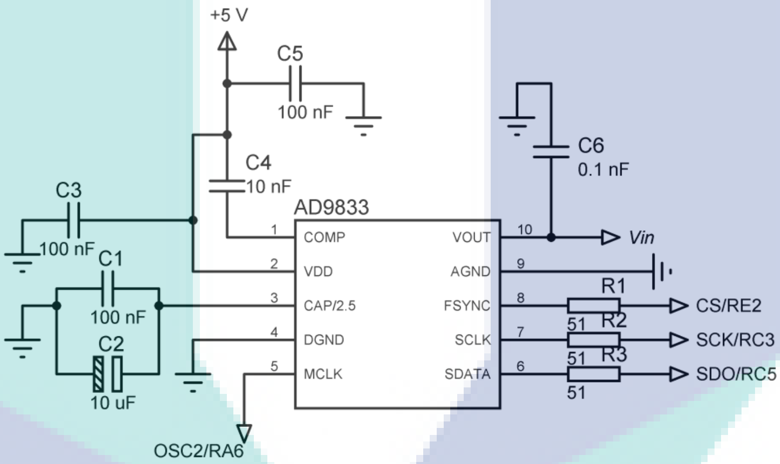


**Figure 5.11:** Connection pin of AD9833

Figure 5.12 shows the real output of AD9833 measured by the oscilloscope. The sinewave was at 2 MHz with the signal around 460 $mV_{pp}$. Thus, an amplifier circuit was needed to amplify it to 10 $V_{pp}$.

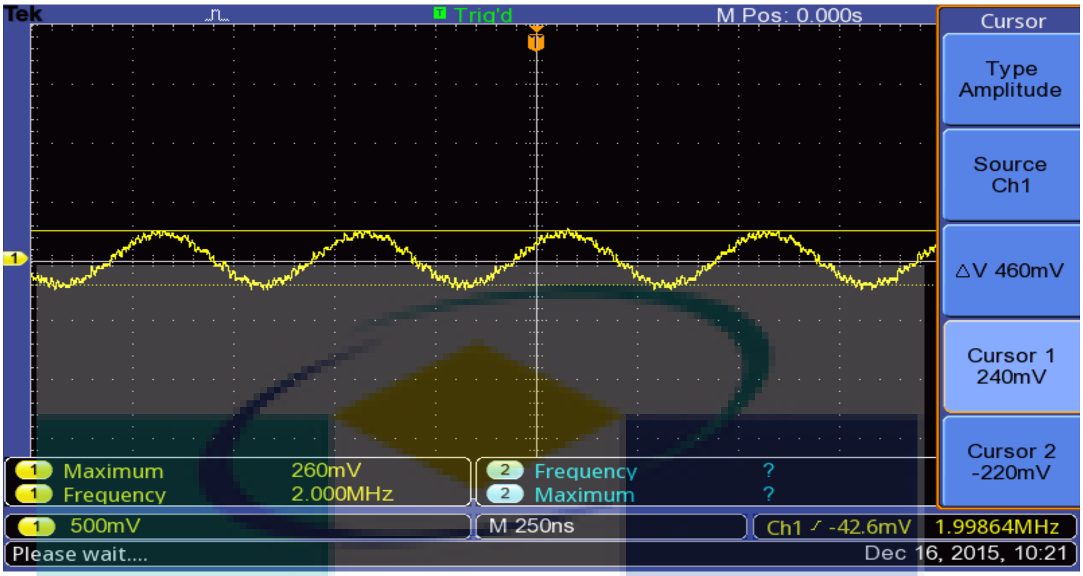


**Figure 5.12:** Output of 2 MHz sinusoidal waveform from AD9833

### 5.2.4.2 Demultiplexer

The demultiplexer was used as a switch for linking the sinusoidal waveform from AD9833 to the amplifier circuit when the channel was acting as the transmitter. DG406B was chosen as the demultiplexer because it allowed a current up to 30 mA for every terminal with a fast transition time of within 115 ns. The DG406B is a high-performance sixteen channel CMOS analogue multiplexer. It allows the current to conduct in both directions for each the active channels. The enable (EN) is to reset the chip, as it either functions as the multiplexer or the demultiplexer to all the stacking several devices. In addition, the switching of each channel was controlled digitally by setting the EN pin to logic ‘1’ and the control inputs, A0 till A3 pins, as the truth table in the data sheet. Figure 5.13 illustrates the basic connection of DG406B.

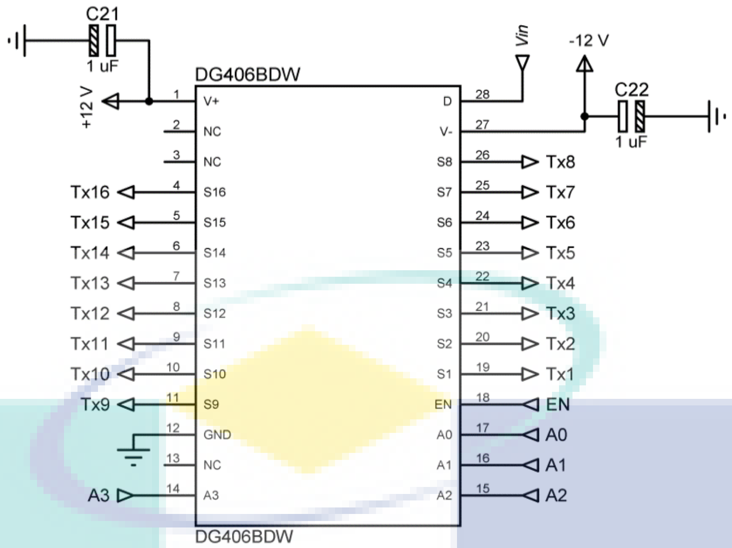


**Figure 5.13:** Connection of DG406B

### 5.2.4.3 Amplifier Circuit

Before the suitable operational amplifier is selected in the electronic measurement circuits, some important parameters must be considered from the data sheet. This were done to ensure that the component was suitable for the electronic measurement circuits, especially when it came to a high frequency (in the case of MHz) implementation. There were:

1. The slew rate of the component. The slew rate, *SR* was measured based on (5.2) [172].

$$SR = 2\pi \times frequency \times Amplitude \tag{5.2}$$

   Since the signal applied was 2 MHz frequency, with an amplitude 5 V, the minimum *SR* for the component was 62.83 V/us.

2. The gain bandwidth product (GBP) of the component. The gain depends on how much gain a system needs. For instance, if the gain is ten and the frequency is 2 MHz, the GBP will be 20 MHz (ten times of the frequency) [172]. However, if 20 MHz is chosen, it makes the component overwork, which gives a saturated signal. Thus, the suitable GBP is at least twenty times the frequency than the gain needed to give room for the component to work smoothly. The bigger the GBP, the better performance of the component.

3. The rise time, fall time and transition time of the component. This information is important because we applied the high frequency source. For a signal with 2 MHz frequency, the time was 500 ns for one cycle. Significantly, all the time stated above must be faster than 500 ns to allow a smooth signal of the 2 MHz frequency.

Therefore, LT1226, a low noise and high speed operational amplifier, was selected to amplify the output signal from AD9833 up to 10 $V_{pp}$. The 400 V/us *SR*, 1 GHz GBP and fast rise, fall and transition times made the LT1226 suitable to be used. The schematic diagram of the circuit is illustrated in Figure 5.14.

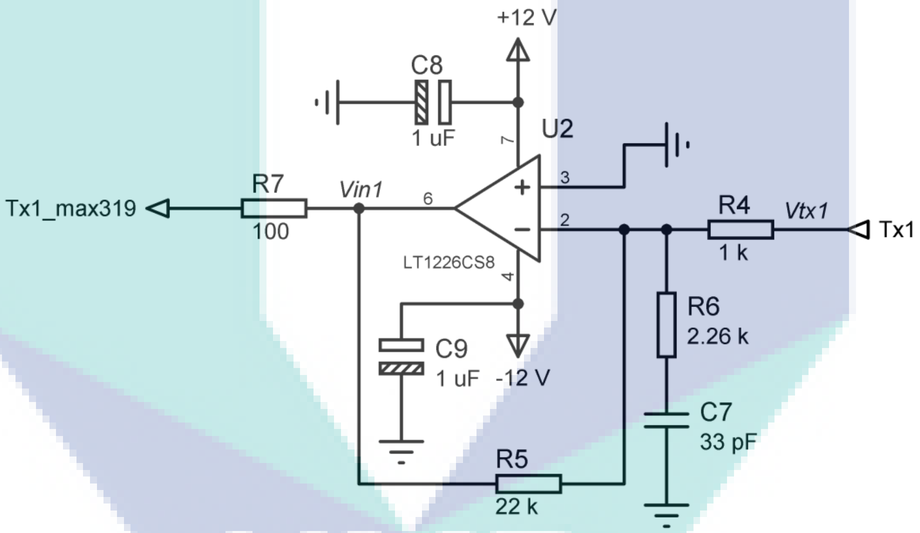


**Figure 5.14:** Schematic diagram of amplifier circuit

The inverting amplifier approach was applied and the gain was measured based on Equation (5.3). Since the output from AD9833 had around 460 $mV_{pp}$, by implementing a gain of -22 it gave the output of sine waveform at the transmitter of around 10 $V_{pp}$. The components R6, C7, and R7 were utilized to ensure that the signal through the circuit could be maintained at the desired value when connected to the sensor. Details of how to select that each the values of the components can be found in [173].

$$V_{\text{in1}} = -\frac{\text{R5}}{\text{R4}} \times V_{\text{t x1}} = -\frac{22\text{ k}}{1\text{ k}} \times 460\text{ m} = 10.12\text{ V}_{\text{pp}} \approx 10\text{ V}_{\text{pp}} \qquad \textbf{(5.3)}$$

Figure 5.15 shows the signal from the LT1226 circuit after amplification. The measured sinusoidal waveform was almost 10 $V_{pp}$ at 2 MHz.

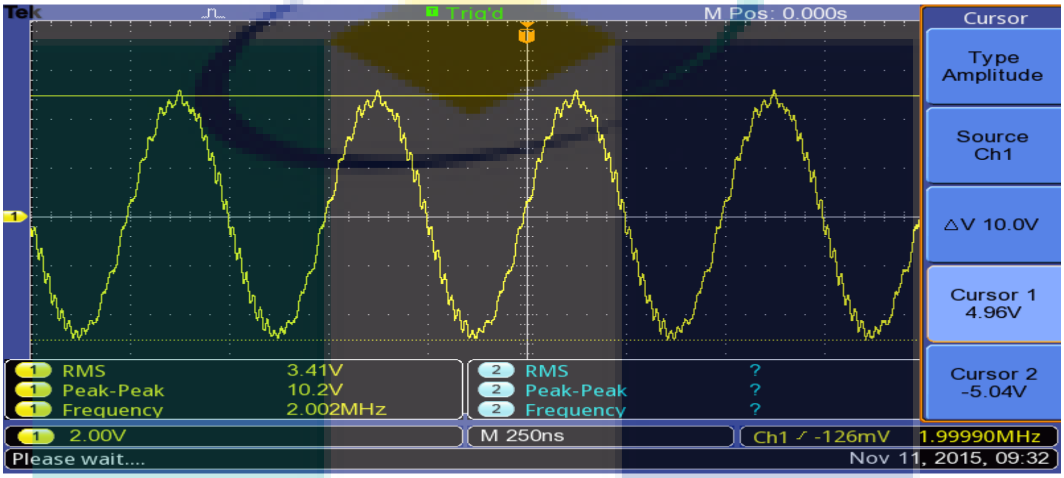


**Figure 5.15:** Signal of amplifier circuit

### 5.2.5 Signal Conditioning Circuit

The signal conditioning is necessary to process the received signal before it can be utilized for the image reconstruction. There are two primary designs: current-to-voltage amplifier circuit and peak detector circuit.

#### 5.2.5.1 Current-to-Voltage Amplifier Circuit

The current signal that is received at the detected electrode must be changed into a voltage level for easier next steps of signal processing before interfacing with the computer. Hence, the current-to-voltage, I-to-V converter amplifier was employed in the electronic measurement circuit.

The high speed and very high *SR* of the operational amplifier, LT1360 was chosen to perform the I-to-V converter amplifier. Figure 5.16 illustrates the schematic diagram of the I-to-V converter amplifier circuit.

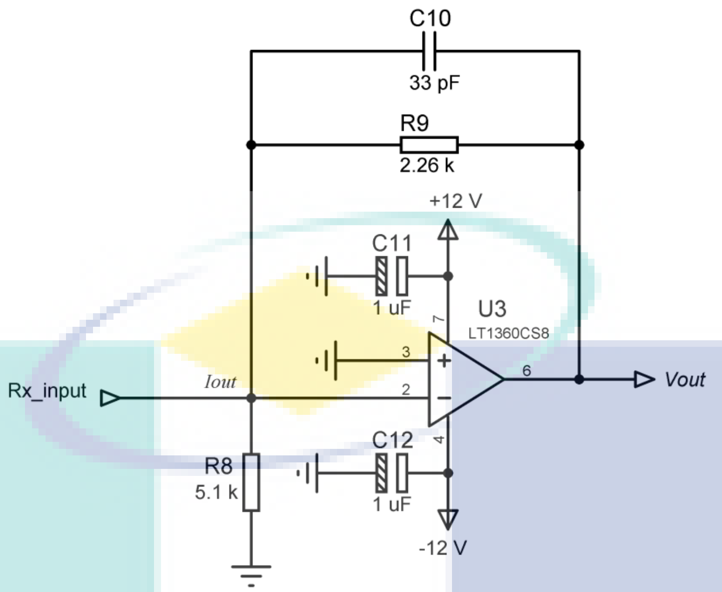


**Figure 5.16:** Schematic diagram of I-to-V converter amplifier circuit

Equation 5.4 shows the current-to-voltage conversion [174]. For instance, when the output current at receiver was 1.8 mA, then the converted output voltage would be around 4 $V_{pp}$. A resistor of 2.26 kΩ was chosen to ensure that the amplitude of the converted voltage did not exceed 5 V to simplify the next steps of designing and interfacing the circuit with the microcontroller unit. Each of the electrodes would give different values in current and these resulted in different values for the converted voltage levels.

$$V_{out} = -I_{out} \times \mathrm{R9} = -1.8\,\mathrm{mA} \times 2.26\,\mathrm{k} = 4.068\,\mathrm{V_{pp}} \approx 4\,\mathrm{V_{pp}} \qquad \textbf{(5.4)}$$

Also, to maintain the system at frequency 2 MHz, the parasitic capacitor, C10, was added to the circuit to combine with resistor, R9, to perform as a low-pass filter to stabilize the circuit [143]. The value of the capacitor was calculated using Equation (5.5). The resistor, R8, connected at the inverting input of the operational amplifier to the ground was to maintain the current flow from the pin of entry.

$$\mathrm{C10} = \frac{1}{2\pi \times \mathrm{R9} \times f_{cut-off}} = \frac{1}{2\pi \times 2.26\,\mathrm{k} \times 2.1\,\mathrm{M}} = 33.53\,\mathrm{pF} \approx 33\,\mathrm{pF} \qquad \textbf{(5.5)}$$

Figure 5.17 shows the example of I-to-V converter amplifier output. The output was maintained at frequency 2 MHz.

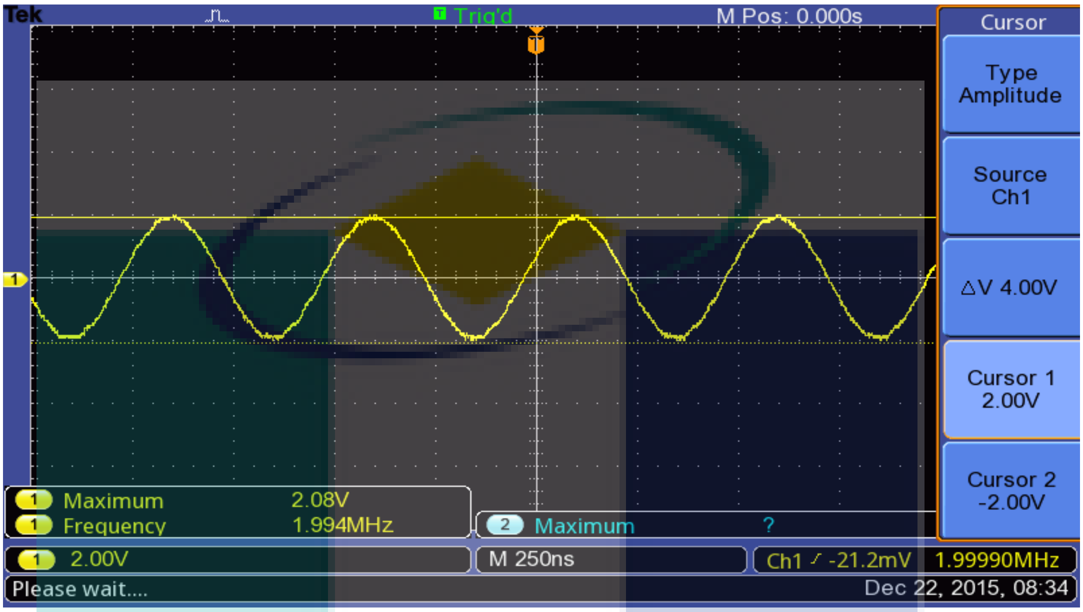


**Figure 5.17:** Example signal of the converted output voltage

### 5.2.5.2 Peak Detector Circuit

Figure 5.18 shows the peak detector circuit applied in the electronic circuit measurement. The peak detector circuit was to output the peak value of the input AC signal. It was constructed with a dual and quad high speed operational amplifier, LT1364 and a polyester capacitor, C13 to hold the peak value of the applied AC voltage from the previous circuit.

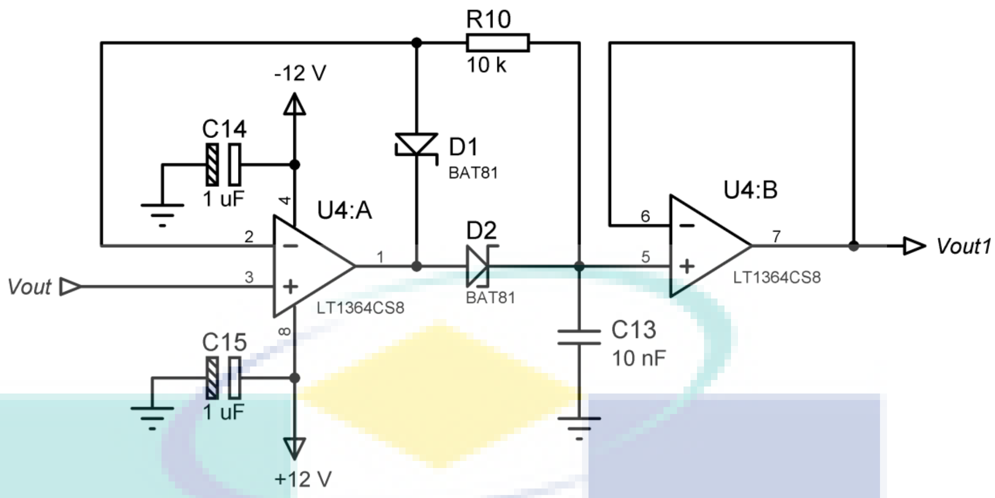


**Figure 5.18:** Schematic diagram of peak detector circuit

When the input voltage was rising, the capacitor would then be charged to a new peak value. Meanwhile, when the AC signal was falling, the Schottky diode (D1 and D2) would prevent the capacitor from discharging. Furthermore, the high frequency (2 MHz) system needed a fast switching action so the Schottky diode, BAT81 that has low forward voltage drop, could fulfil this requirement. In terms of being time consuming, a large value of capacitor will reduce the speed of the processing time to achieve the steady state signal, and vice versa. The resistor R10 was engaged to prevent current leakage through the entire circuit. Also, the second stage of operational amplifier was only used as a buffer.

The example signal of peak value from the peak circuit is shown in Figure 5.19. The yellow line is the AC signal from the previous circuit, and the blue line is the peak signal. The DC signal of the peak detector circuit could be easily applied to the interfacing part.

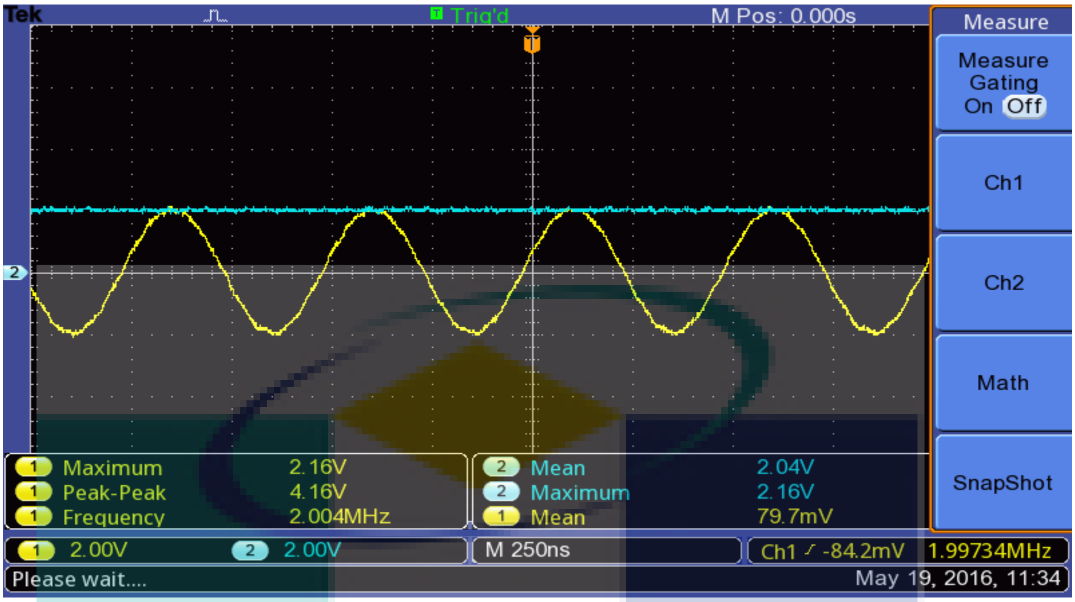


**Figure 5.19:** Example signal of peak value from the input AC signal

### 5.2.6 Microcontroller Unit (dsPIC30F6010A)

The microcontroller dsPIC30F6010A was utilized as the controller unit for controlling the sensors' switching, the analogue-to-digital conversion (ADC) and the data sampling. Firstly, channel 1 was set as the transmitter and the other channels as receivers. When channel 1 was the transmitter, the switching for triggering the sinusoidal waveform was set and the transmitted signal was applied at electrode 1. Simultaneously, all the received signals at electrodes 2 until 16 were converted from analogue to digital and sent to the computer through serial communication. Moreover, the ADC and data sampling were done for each channel by sequence until all sixteen channels had been processed. Later, the switching process would be repeated for channels 2 till 16. This process is shown in the form of a flowchart (see Figure 5.20).

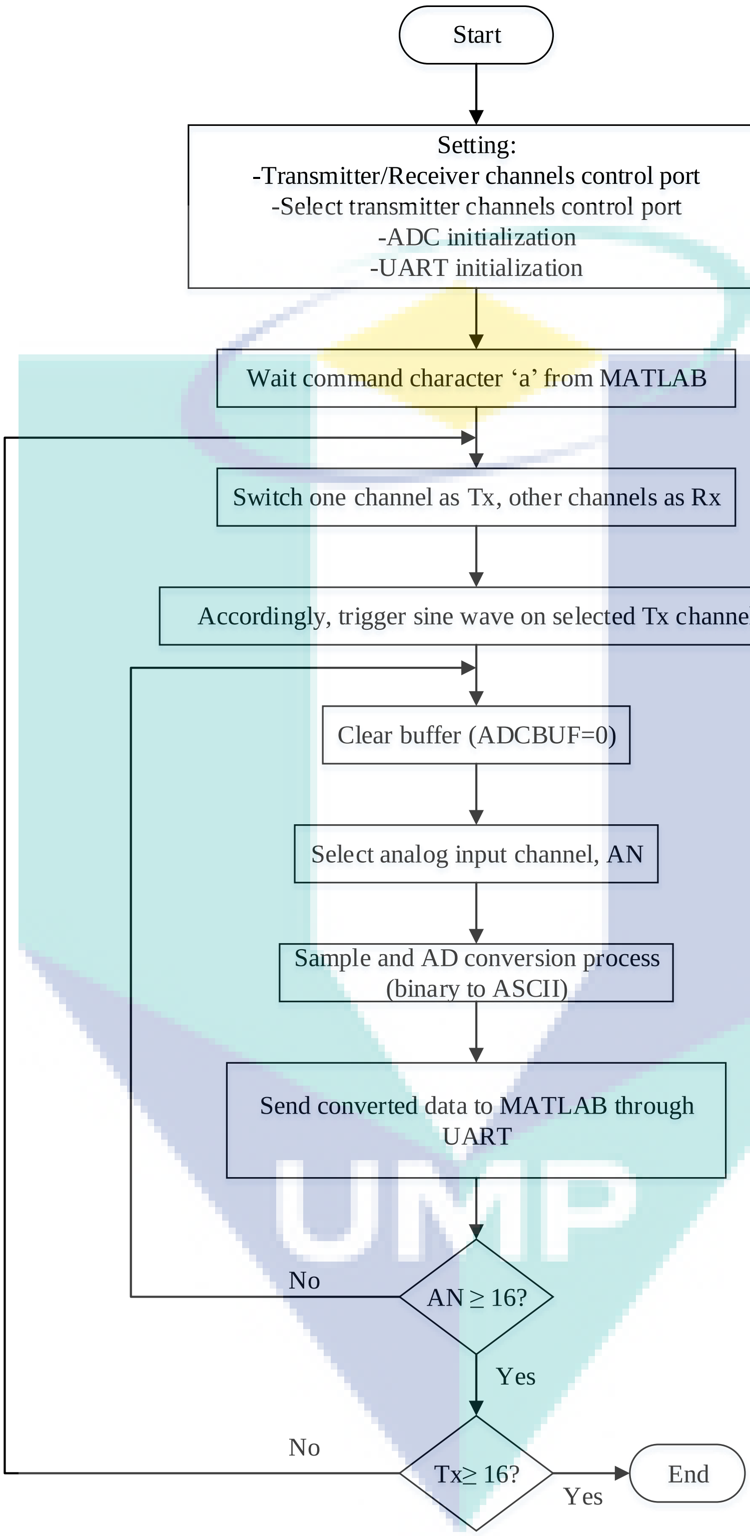


**Figure 5.20:** Flow chart for measurement process

#### 5.2.6.1 Analogue-to-Digital Conversion (ADC)

Figure 5.21 shows the timing diagram for one frame of the system. The MATLAB software sends the character 'a' to the mplab software. Then, the mplab receives character 'a' and then starts the switching, sampling, ADC and sending the serial data to the MATLAB. Before the ADC, a 100 us at every transmitting cycle was needed to stabilize the switch of the sensor switching. From the datasheet, an ADC clock requires 157 ns. Thus, the sampling and ADC process would be around 2.157 us because it requires a delay of 2 us to stabilize the process. For each channel, right after the ADC, the sensing data is sent to MATLAB through serial communication. Then the switching for transmitter 2 until 16 is repeated until the sequences are completed. 1 byte data was sent for every channel. The baud rate implemented for the system was 460800 bps. Therefore, to send every 8 bits, it would take an optimal period of around 17.36 us. Lastly, the tomogram would be plotted. The overall duration for both the hardware and the software were calculated using a start/stop watch timer in MATLAB. The hardware duration was around 60 ms and the software duration was around 190 ms. Thus, the total duration for the working system was 250 ms, and this gave the system speed of around 4 frames per second.

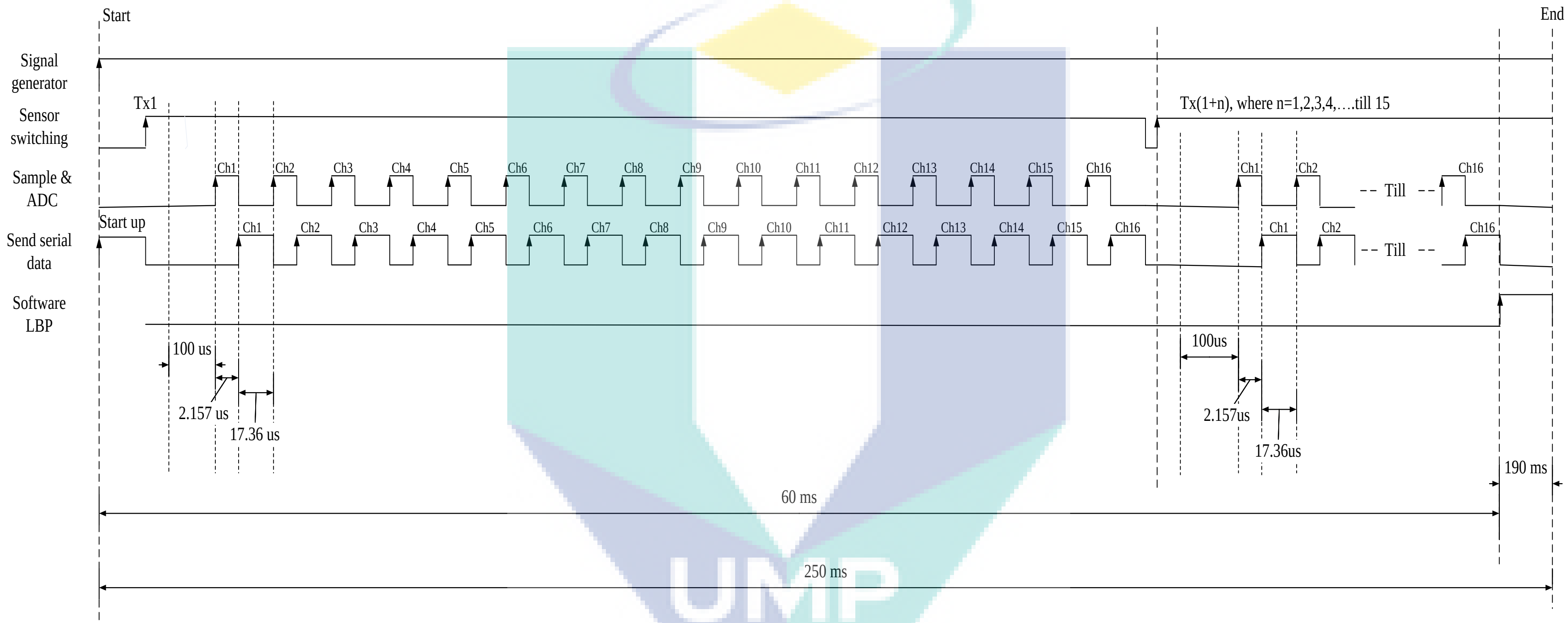


**Figure 5.21:** Timing diagram for one frame

### 5.2.7 Printed Circuit Board (PCB)

The PCB was fabricated for the non-invasive ERT system as the final stage of the prototype circuit. The single two layer PCB consists of a waveform generator circuit, a demultiplexer circuit, sixteen transmitter/receiver switching circuits, sixteen amplifier circuits for the transmitter, and sixteen signal conditioning circuits. The diagram of the PCB is shown in Figure 5.22. Besides, the microcontrollers (PIC18F4580 and dspic30f6010A) circuits were utilized from the available microcontroller kits from Cytron Technologies and the PROTOM research group.

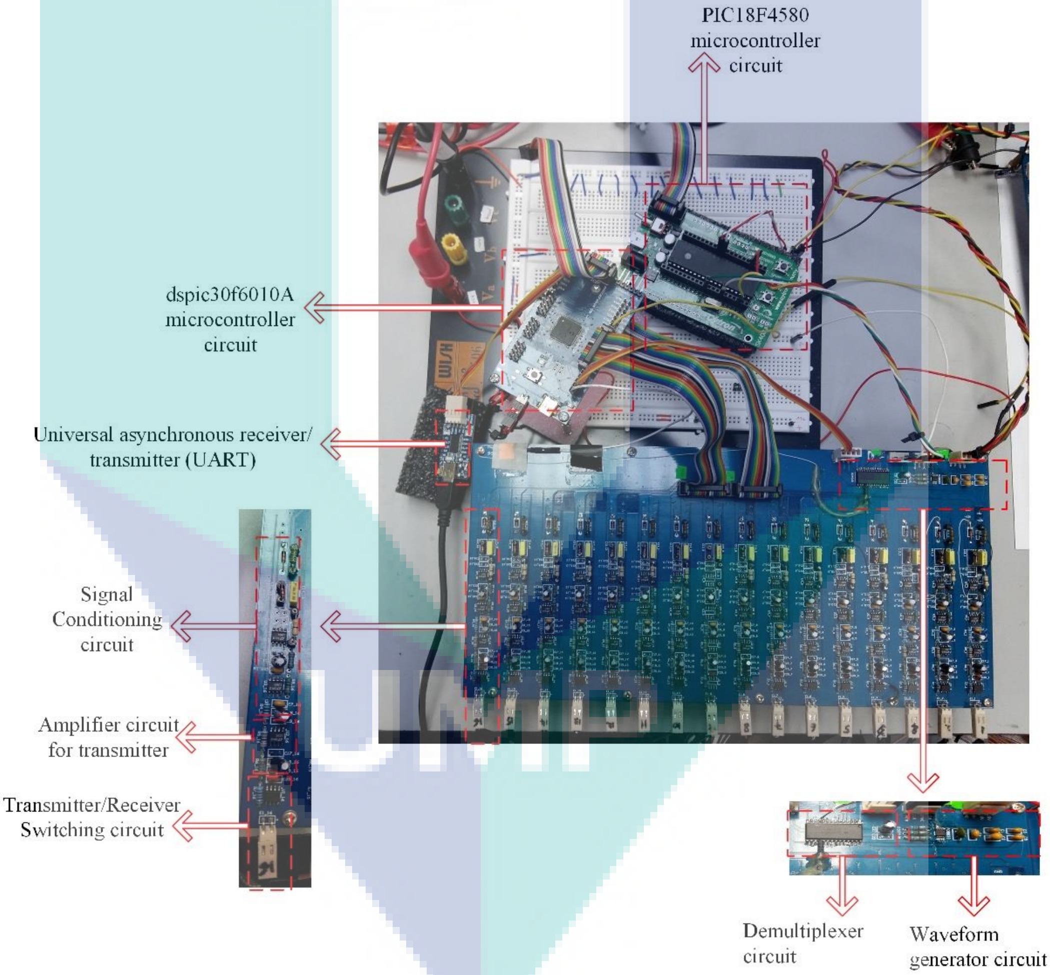


**Figure 5.22:** PCB for non-invasive ERT system

## 5.3 Software Development

In this research, the online and offline analysis programmes were developed using MATLAB software through a graphical user interface (GUI). MATLAB software was chosen as the GUI because MATLAB provides a user-friendly interface and the define function is ready to be used. Likewise, it only needs a small code to complete the tasks compared to the compiler language such as visual basic or C++.

Figure 5.23 shows the front panel of online non-invasive ERT GUI. The GUI consists of a main panel to display the reconstructed image and also the repeatability feature that provides the information of the sensor values. In addition, the user can also choose the value for the threshold approach using the slider bar. The main flowchart of the online system is illustrated in Figure 5.24. The serial communication was initialized at the beginning of the flowchart by clicking the 'Start' button on the online GUI panel. It was done before it could perform the system calibration. Then, the system continuously performed the data acquisition and reconstructed the tomogram. It was done when the 'LBP' button was clicked by the user. The process is continuous unless the user terminates the system by clicking the 'Stop' button on the online GUI panel.

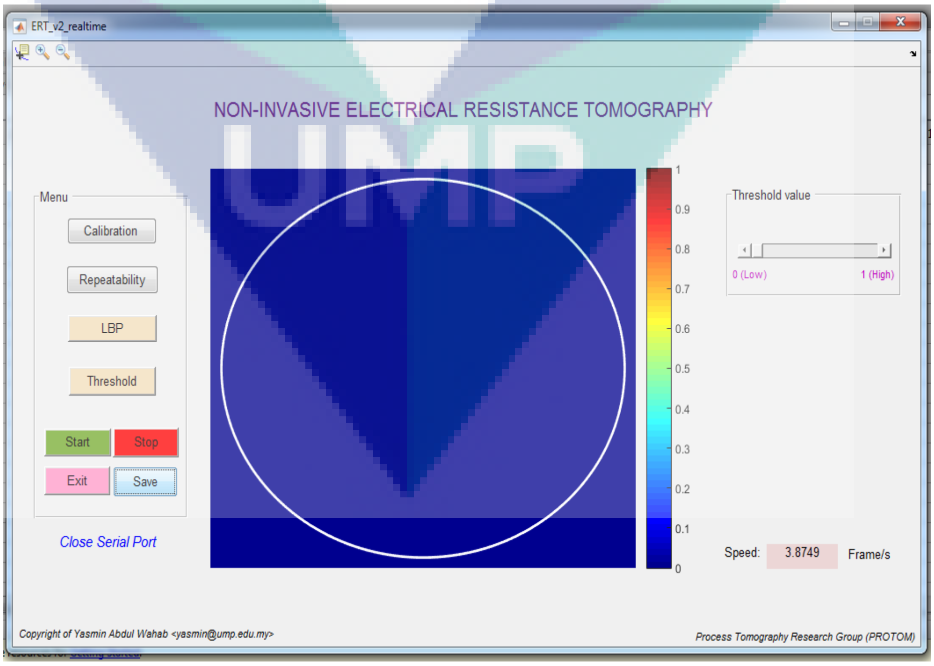


**Figure 5.23:** Front panel of online non-invasive ERT GUI using MATLAB software

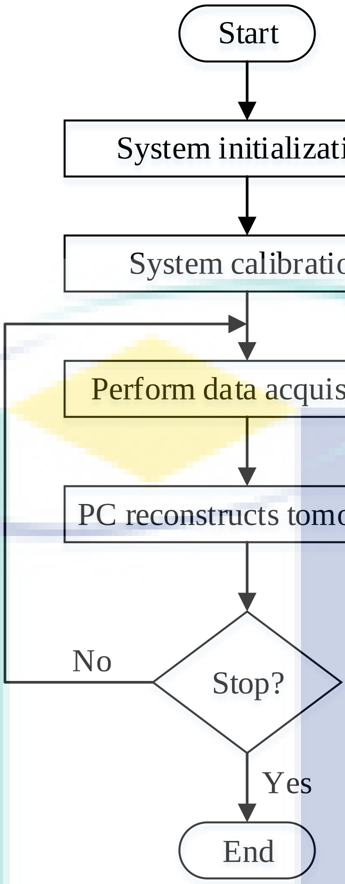


**Figure 5.24:** Online main program flowchart

The flowchart of the linear back-projection algorithm (LBP) is shown in Figure 5.25. The data for the normalized sensitivity map and sensor values were loaded first before reconstructing the image using LBP. Moreover, the data from transmitter, $i$=1 and receiver, $j$=1 were used as the initializations. Then, for each pair of $i$ and $j$, the LBP was applied. After the sixteen scans were completed, the tomogram was drawn. The system was ready for the measurement process unless the process was terminated.

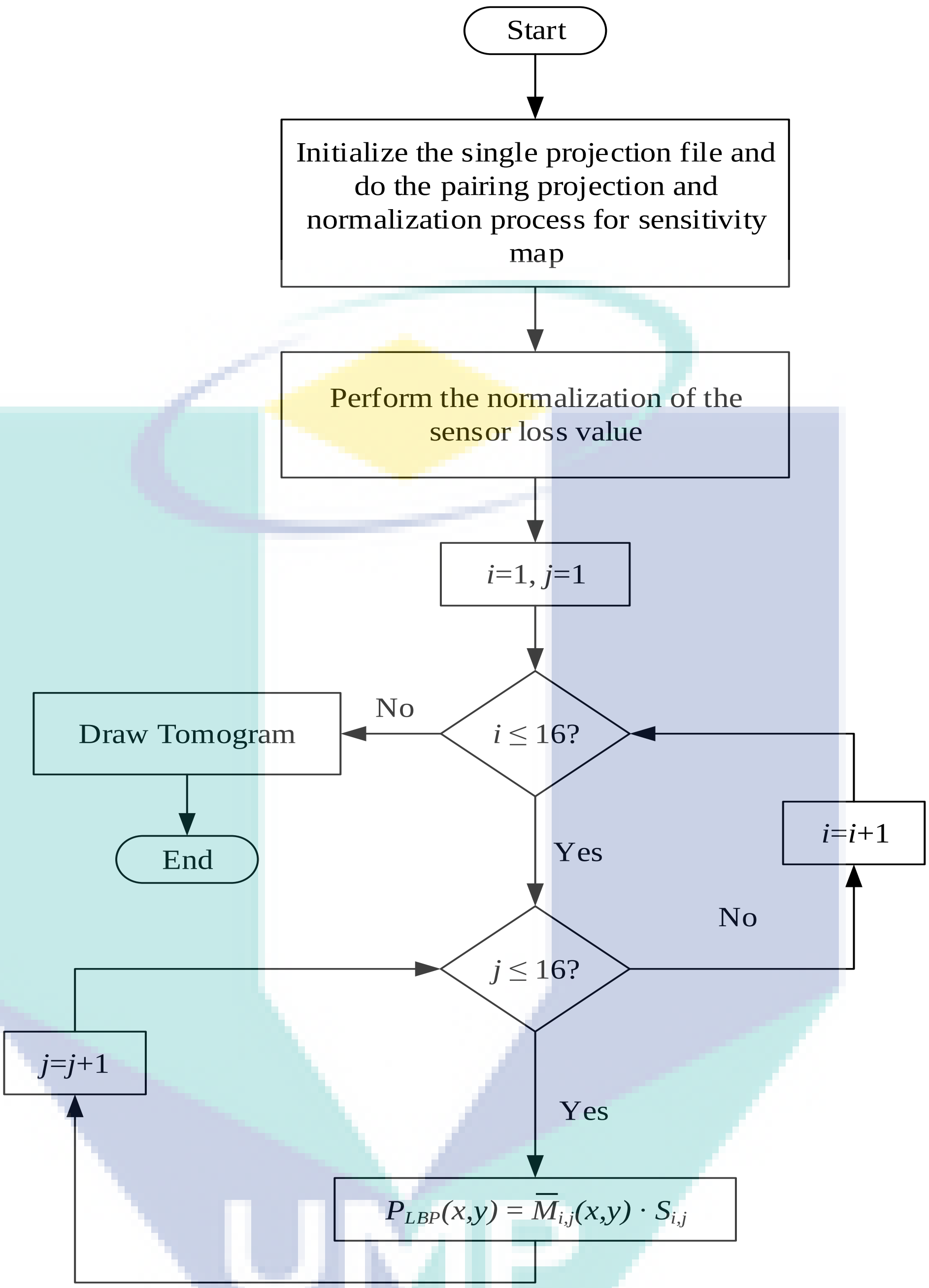


**Figure 5.25:** Linear Back-Projection Algorithm

In addition, all the data and tomogram obtained from the online system were saved for the offline analysis programme in the GUI. Specifically, offline analysis was performed to obtain the optimum values of threshold, MSSIM, AE percentage and phantom concentration percentage. It was also used for the easier comparison of experimental and simulative studies with respect to the reference image. Figure 5.26 shows the GUI for offline analysis.

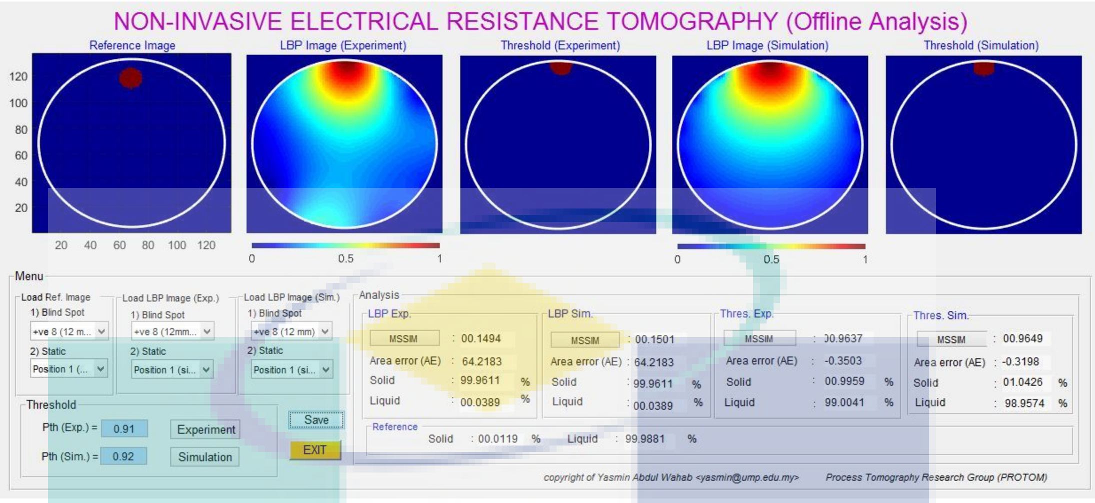


**Figure 5.26:** Front panel of offline analysis of non-invasive ERT GUI using MATLAB software

## 5.4 ANOVA for sensor validation

ANOVA works by comparing the variability difference between the groups with the variability difference within the groups [175]. In the research, the analysis focuses on the one-way ANOVA that compares the mean between the sensors data of experiment and simulation. According to the ANOVA test, a P-value larger than 0.05 means that the null hypothesis must be accepted and the alternative hypothesis, $H_1$ is rejected [176]. The hypothesis results will either validate that the experiment sensors reading are similar to the simulation sensors' reading statistically or not. The hypotheses are:

| |
|---|
| $H_0$: Sample mean for sensors reading experiment = Sample mean for sensors reading simulation.<br>$H_1$: Sample mean for sensors reading experiment $\neq$ Sample mean for sensors reading simulation. |

The analysis of the one set of sensor data obtained from both experimental and simulation is discussed detail in section 6.2.2.

## 5.5 Summary

The hardware and software development were discussed in detail. The preparations for the sensor design, including the materials and how it was attached to the pipe, were presented. The details of the signal generator circuits, signal conditioning circuits, sensor switching circuits, microcontroller unit and PCB circuits were also highlighted. For the software development, MATLAB software through GUIs was employed for online and offline analysis programmes. Lastly, a brief explanation on ANOVA for sensor validation was presented in this chapter.

# CHAPTER 6

# RESULTS AND DISCUSSION

## 6.1 Introduction

The experiment and simulation which were carried out to test and validate the capability of the ERT system are discussed. Firstly, the experimental sensors reading of sixteen electrodes at full conductive water were compared with the simulation results using statistical analysis. The data were divided into two groups; experimental group and simulation group. For each transmitter, all receivers were set as one group each. Thus, there were sixteen groups for each experiment and simulation. The Minitab 16 software was applied as the tool for statistically calculation and analysis. The homogenous test of variance was conducted to ensure that the data from each set had equal variance. Then, the one way analysis of variance (ANOVA) test was performed to prove statistically that the experimental sensors reading were similar to the simulation sensors' readings or not.

Secondly, the limitation of the image reconstructed, and the tomogram of the phantoms at different locations and sizes were executed and analysed. The linear back-projection algorithm was used as the basis for comparison with the thresholding technique. In the research, the experiments used tap water as the primary conductive liquid and a wooden rod as the non-conductive phantom. The non-conductive medium was chosen as the tested medium to get an as large as possible conductivity difference between the two mediums. Thus, it could give better differentiability and measurement accuracy [14]. Lastly, the summary of the results obtained is discussed at the end of the chapter.

## 6.2 Sensor Reading Analysis and Validation

This part details the sensors' reading performance for the receivers from each of the transmitter groups. The measurement data in sixteen transmitter groups from each simulation and experiment are illustrated in Figure 6.1. The voltage readings obtained from the experiment were converted into current values for comparison with the simulation values. Under the comparison, it can be highlighted that the U-shape pattern for each transmitter group remained significant. It is believed that the fluctuation that occurred mainly at the adjacent electrodes in Figure 6.1 (b) was a result of the fringe effect, the non-symmetrical sensors' position and a slight different in the real conductivity of the materials applied. Even the data from the online measurement were not distributed symmetrically, as well as the simulation data, so they can still be accepted. Essentially, the data were then employed in the statistical engineering analysis for the validation between the experiment and the simulation.

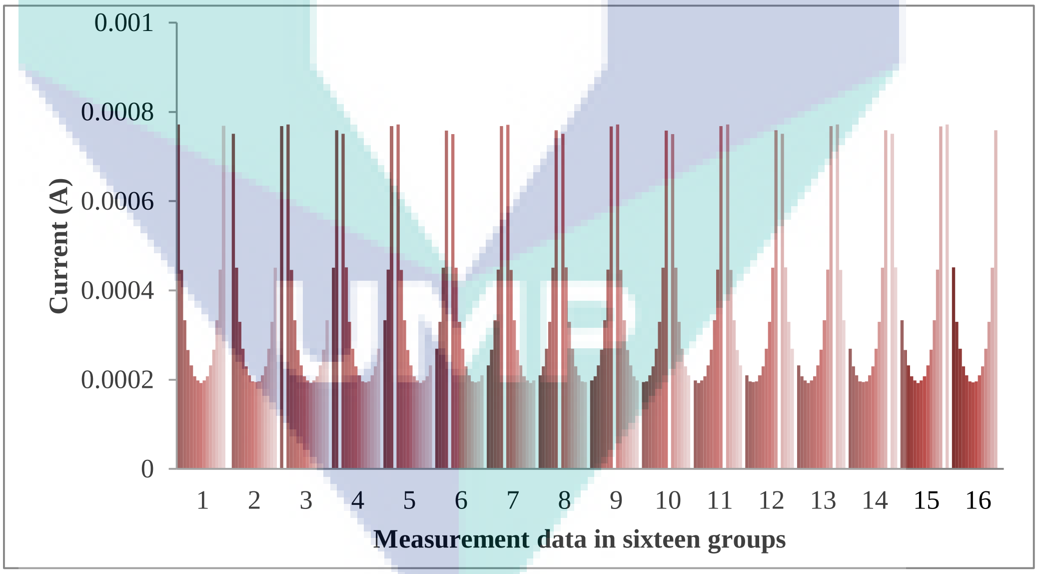


(a)

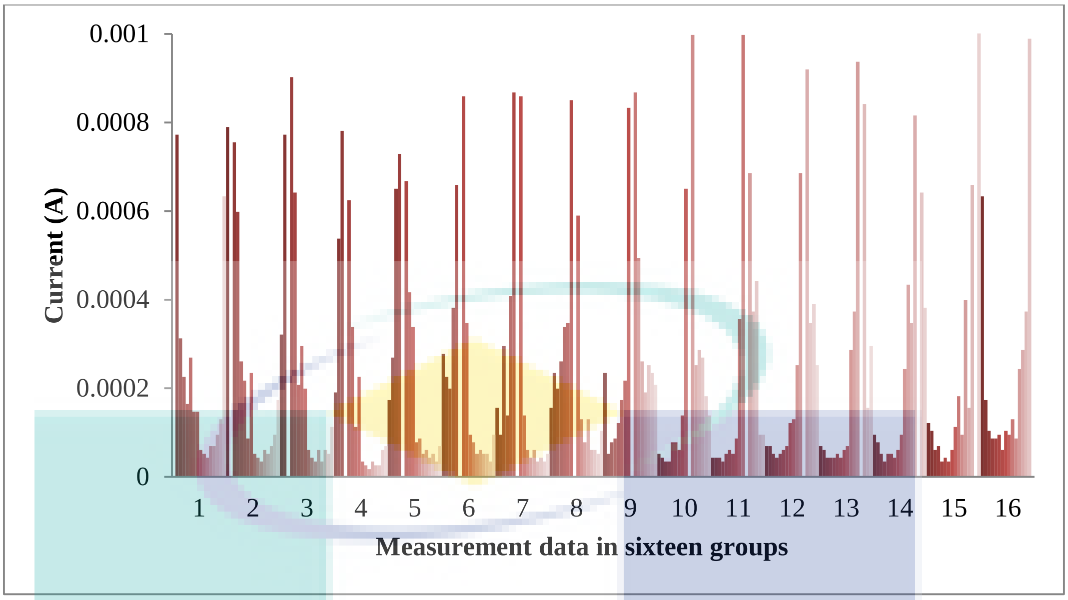


(b)

**Figure 6.1:** Measurement data in sixteen transmitter groups collected via a non-invasive ERT system in a homogenous field: (a) simulation versus (b) experiment

### 6.2.1 Homogeneity of Variance Test

The test for equal variance is needed before conducting an ANOVA. The purpose of this test is to observe whether the set of data has homogenous variance or not. If the test output is non-homogenous, then the cause of it needs to be verified, or another set of data is used instead. There are several types of homogeneity of variance test such as Bartlett's test, Levene's test and F-test [177]. The Bartlett's test is applied to compare more than two subgroups, and the data must come from the normal distributions. If they are only two subgroup data, the F-test is preferable. The Levene's test is used for two or more subgroups, and the data are not necessarily distributed normally.

In Minitab, the result is based on the P-value, which is a probability of obtaining a test statistic, where minimum Type 1 error rate (>0.05) will accept the null hypothesis [178]. In addition, the variance of the sample data from both subgroups also can be displayed in a 95 % interval (CI) graph and box plot graph. In the research, the F-test and Levene's test were applied to analyse the data. If the P-value from both tests was greater than 0.05, it would fail to reject the null hypothesis; that is, these data do not provide enough evidence to claim that both subgroups have unequal variance.

Figures 6.2 and 6.3 illustrate the homogeneity of variance test results obtained using Minitab software for each of the transmitter groups. From those figures, the important parameter that must be considered is the result of the P-value for both tests; F-test and Levene's test. The null hypothesis claimed that the sensors reading from the experiment and simulation give the same data of variance if the P-value is greater than 0.05. Therefore, Table 6.1 is the P-value results from those figures for easy observation and results interpretation. Under the observation, it is indicated that all the P-values for all transmitter groups were greater than 0.05. Consequently, it must accept the null hypothesis that both the experiment and the simulation have the same data of variance.

**Table 6.1:** P-Value of homogenous variance test for each set group of each transmitter

| Group | P-Value | | Group | P-Value | |
|---|---|---|---|---|---|
| | F-Test | Levene's Test | | F-Test | Levene's Test |
| Tx1 | 0.856 | 0.989 | Tx9 | 0.424 | 0.765 |
| Tx2 | 0.335 | 0.613 | Tx10 | 0.297 | 0.732 |
| Tx3 | 0.212 | 0.447 | Tx11 | 0.214 | 0.614 |
| Tx4 | 0.437 | 0.646 | Tx12 | 0.344 | 0.638 |
| Tx5 | 0.432 | 0.496 | Tx13 | 0.206 | 0.690 |
| Tx6 | 0.465 | 0.662 | Tx14 | 0.460 | 0.624 |
| Tx7 | 0.253 | 0.706 | Tx15 | 0.264 | 0.872 |
| Tx8 | 0.692 | 0.827 | Tx16 | 0.358 | 0.883 |

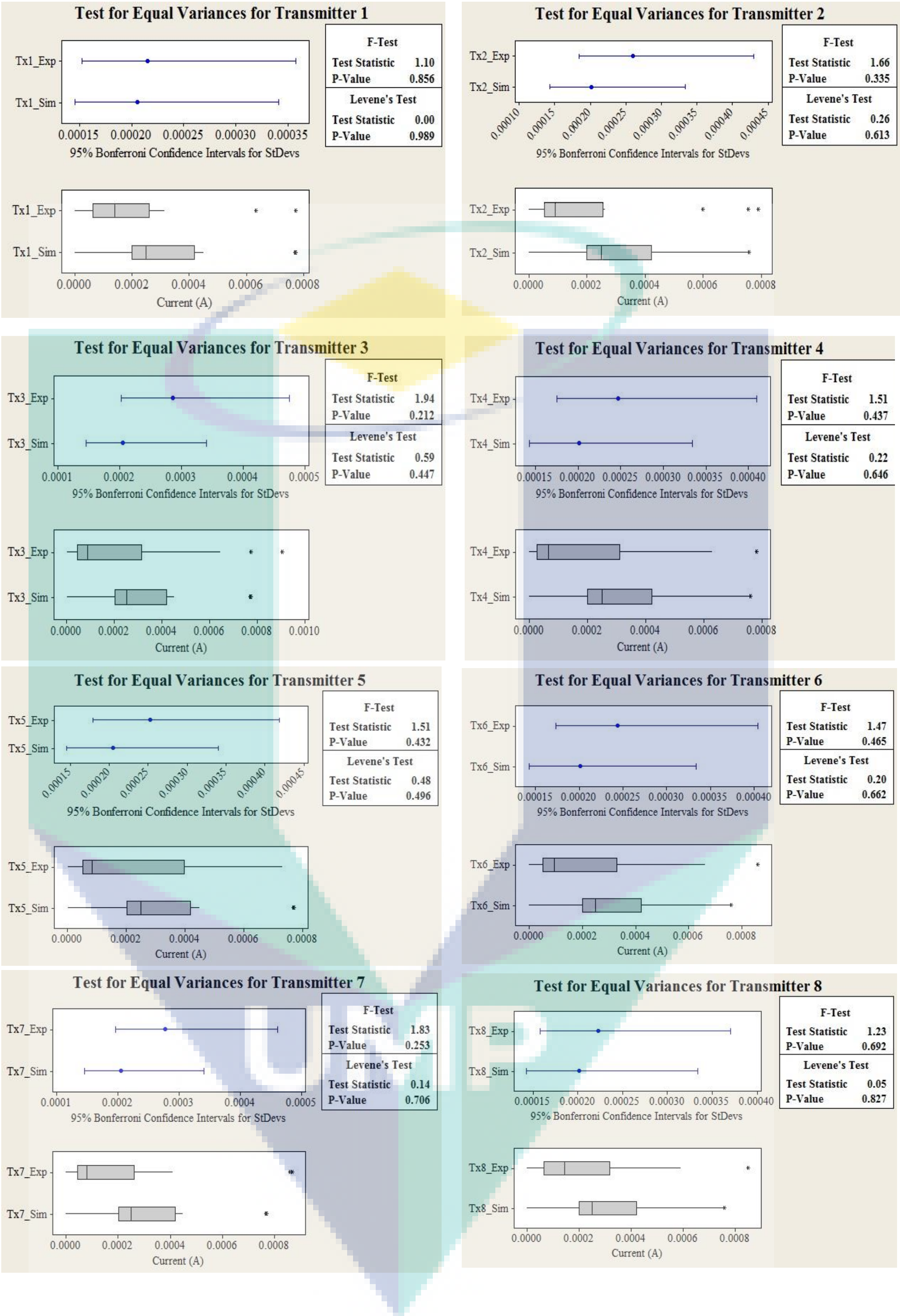


**Figure 6.2:** Homogeneity variance test results for each transmitter group (transmitter 1 until transmitter 8) between experiment and simulation

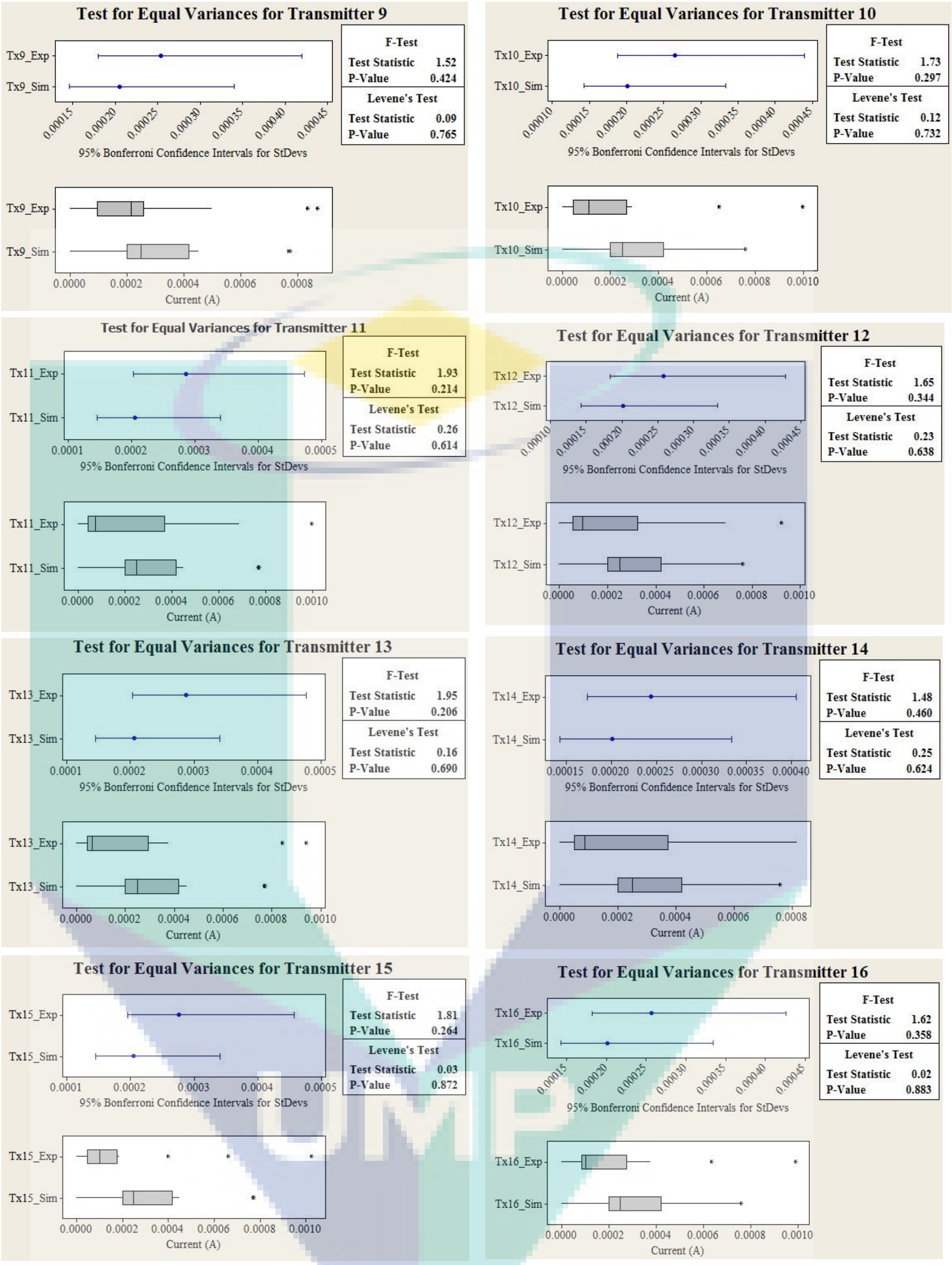


**Figure 6.3:** Homogeneity variance test results for each transmitter group (transmitter 9 till transmitter 16) between experiment and simulation

### 6.2.2 Analysis using ANOVA

Based on the hypotheses of ANOVA in section 5.4, one set data of sensor readings was analysed (see Figures 6.4–6.7). From the individual value plot, the position of the mean value for each group and the line between them can be observed. It can be perceived that the line between the experiment and the simulation group for all transmitter groups was slightly increasing. It is believed that this was due to the slight difference values obtained from the experiment and the simulation. In contrast, the P-value from all groups of the transmitter gave a value bigger than 0.05, which leads to the acceptance of the null hypotheses of the sensors' reading performance. Alternatively, the overlapping of the intervals from the 95 % CI graph also can give the result for whether it has a different significance or not. A statistical significant occurs when there is at least a 25 % interval overlap of the 95 % CI graph between the groups [179]. It can be seen that the intervals from both groups of the individual 95 % CI graph were overlapping each other and hence the difference was not significant. Therefore, it can be concluded that the sensors' reading from the hardware system gave similar results to the non-invasive ERT modelling.

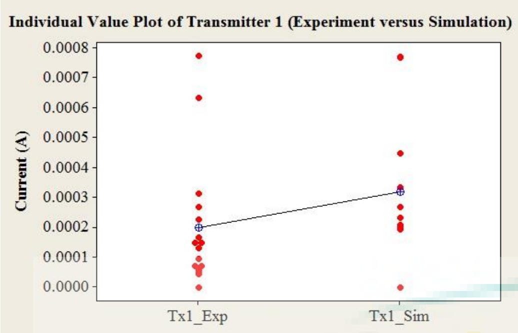


**One-way ANOVA: Transmitter 1 (Experiment versus Simulation)**

```
Source  DF         SS         MS     F      P
Value    1  0.0000001  0.0000001  2.57  0.119
Error   30  0.0000013  0.0000000
Total   31  0.0000014

S = 0.0002104   R-Sq = 7.90%   R-Sq(adj) = 4.83%

Level     N       Mean     StDev
Tx1_Exp  16  0.0001995  0.0002154
Tx1_Sim  16  0.0003189  0.0002053

                Individual 95% CIs For Mean Based on
Pooled StDev
Level     --+---------+---------+---------+--------
Tx1_Exp    (---------*----------)
Tx1_Sim                (----------*----------)
          --+---------+---------+---------+--------
          0.00010   0.00020   0.00030   0.00040
```

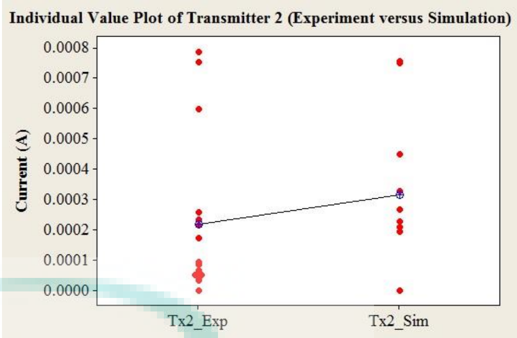


**One-way ANOVA: Transmitter 2 (Experiment versus Simulation)**

```
Source  DF         SS         MS     F      P
Value    1  0.0000001  0.0000001  1.40  0.246
Error   30  0.0000016  0.0000001
Total   31  0.0000017

S = 0.0002321   R-Sq = 4.46%   R-Sq(adj) = 1.27%

Level     N       Mean     StDev
Tx2_Exp  16  0.0002202  0.0002594
Tx2_Sim  16  0.0003173  0.0002012

                Individual 95% CIs For Mean Based on
Pooled StDev
Level     -+---------+---------+---------+---------
Tx2_Exp    (-----------*-----------)
Tx2_Sim               (-----------*----------)
          -+---------+---------+---------+---------
          0.00010   0.00020   0.00030   0.00040
```

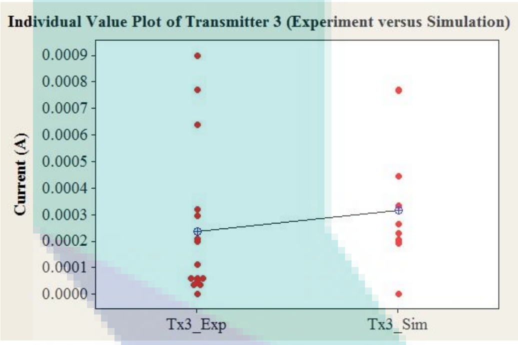


**One-way ANOVA: Transmitter 3 (Experiment versus Simulation)**

```
Source  DF         SS         MS     F      P
Value    1  0.0000001  0.0000001  0.86  0.362
Error   30  0.0000019  0.0000001
Total   31  0.0000019

S = 0.0002487   R-Sq = 2.77%   R-Sq(adj) = 0.00%

Level     N       Mean     StDev
Tx3_Exp  16  0.0002375  0.0002857
Tx3_Sim  16  0.0003189  0.0002052

                Individual 95% CIs For Mean Based on
Pooled StDev
Level     ---------+---------+---------+---------+
Tx3_Exp   (-----------*-----------)
Tx3_Sim           (-----------*-----------)
          ---------+---------+---------+---------+
                0.00020   0.00030   0.00040   0.00050
```

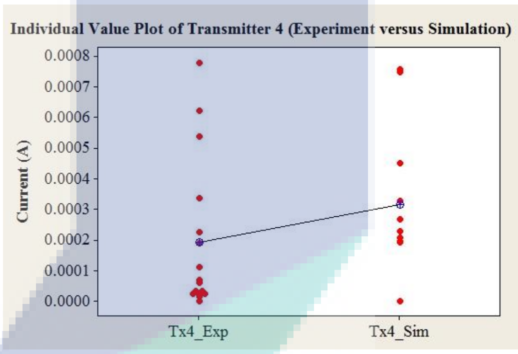


**One-way ANOVA: Transmitter 4 (Experiment versus Simulation)**

```
Source  DF         SS         MS     F      P
Value    1  0.0000001  0.0000001  2.39  0.132
Error   30  0.0000015  0.0000001
Total   31  0.0000016

S = 0.0002252   R-Sq = 7.39%   R-Sq(adj) = 4.30%

Level     N       Mean     StDev
Tx4_Exp  16  0.0001941  0.0002469
Tx4_Sim  16  0.0003173  0.0002012

                Individual 95% CIs For Mean Based on
Pooled StDev
Level     --+---------+---------+---------+-------
Tx4_Exp    (---------*-----------)
Tx4_Sim               (----------*----------)
          --+---------+---------+---------+-------
          0.00010   0.00020   0.00030   0.00040
```

**Figure 6.4:** One-way ANOVA test for each source of channel 1 till channel 4

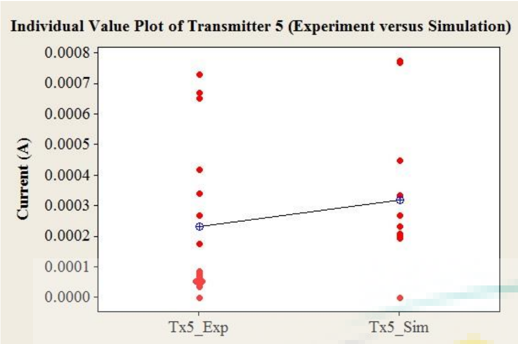


**One-way ANOVA: Transmitter 5 (Experiment versus Simulation)**

```
Source  DF         SS         MS     F      P
Value    1  0.0000001  0.0000001  1.12  0.298
Error   30  0.0000016  0.0000001
Total   31  0.0000016

S = 0.0002301   R-Sq = 3.61%   R-Sq(adj) = 0.40%

Level     N       Mean      StDev
Tx5_Exp  16  0.0002326  0.0002525
Tx5_Sim  16  0.0003188  0.0002052

           Individual 95% CIs For Mean Based on
Pooled StDev
Level     --------+---------+---------+---------+-
Tx5_Exp   (-----------*-----------)
Tx5_Sim          (-----------*-----------)
          --------+---------+---------+---------+-
              0.00020   0.00030   0.00040   0.00050
```

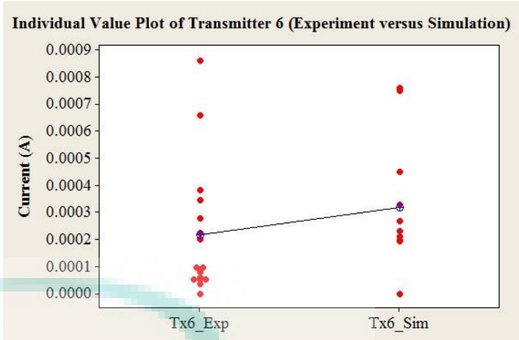


**One-way ANOVA: Transmitter 6 (Experiment versus Simulation)**

```
Source  DF         SS         MS     F      P
Value    1  0.0000001  0.0000001  1.61  0.214
Error   30  0.0000015  0.0000000
Total   31  0.0000016

S = 0.0002234   R-Sq = 5.10%   R-Sq(adj) = 1.94%

Level     N       Mean      StDev
Tx6_Exp  16  0.0002169  0.0002437
Tx6_Sim  16  0.0003172  0.0002011

          Individual 95% CIs For Mean Based on
Pooled StDev
Level     +---------+---------+---------+---------
Tx6_Exp    (-----------*----------)
Tx6_Sim              (-----------*-----------)
          +---------+---------+---------+---------
       0.00010   0.00020   0.00030   0.00040
```

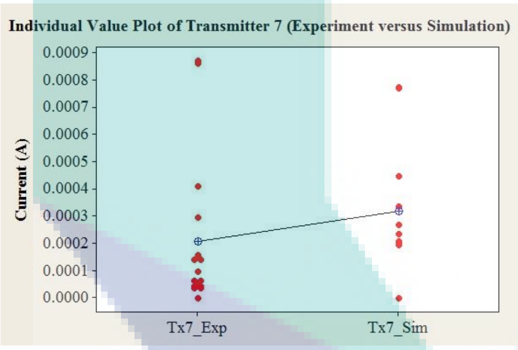


**One-way ANOVA: Transmitter 7 (Experiment versus Simulation)**

```
Source  DF         SS         MS     F      P
Value    1  0.0000001  0.0000001  1.72  0.199
Error   30  0.0000018  0.0000001
Total   31  0.0000019

S = 0.0002441   R-Sq = 5.43%   R-Sq(adj) = 2.28%

Level     N       Mean      StDev
Tx7_Exp  16  0.0002055  0.0002776
Tx7_Sim  16  0.0003188  0.0002052

          Individual 95% CIs For Mean Based on
Pooled StDev
Level     --+---------+---------+---------+-------
Tx7_Exp   (-----------*------------)
Tx7_Sim              (------------*-----------)
          --+---------+---------+---------+-------
        0.00010   0.00020   0.00030   0.00040
```

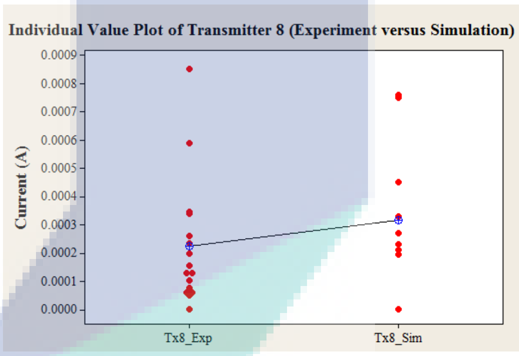


**One-way ANOVA: Transmitter 8 (Experiment versus Simulation)**

```
Source  DF         SS         MS     F      P
Value    1  0.0000001  0.0000001  1.53  0.226
Error   30  0.0000014  0.0000000
Total   31  0.0000014

S = 0.0002125   R-Sq = 4.84%   R-Sq(adj) = 1.67%

Level     N       Mean      StDev
Tx8_Exp  16  0.0002245  0.0002232
Tx8_Sim  16  0.0003173  0.0002011

          Individual 95% CIs For Mean Based on
Pooled StDev
Level     -----+---------+---------+---------+----
Tx8_Exp   (-----------*--------------)
Tx8_Sim             (--------------*-------------)
          -----+---------+---------+---------+----
       0.000160  0.000240  0.000320  0.000400
```

**Figure 6.5**: One-way ANOVA test for each source of channel 5 till channel 8

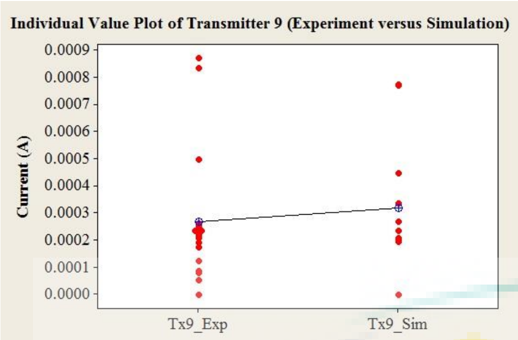


**One-way ANOVA: Transmitter 9 (Experiment versus Simulation)**

```
Source  DF         SS         MS     F      P
Value    1  0.0000000  0.0000000  0.37  0.545
Error   30  0.0000016  0.0000001
Total   31  0.0000016

S = 0.0002305   R-Sq = 1.23%   R-Sq(adj) = 0.00%

Level     N       Mean      StDev
Tx9_Exp  16  0.0002690  0.0002533
Tx9_Sim  16  0.0003188  0.0002052

         Individual 95% CIs For Mean Based on
Pooled StDev
Level    -+---------+---------+---------+--------
Tx9_Exp  (--------------*--------------)
Tx9_Sim        (--------------*--------------)
         -+---------+---------+---------+--------
       0.000160  0.000240  0.000320  0.000400
```

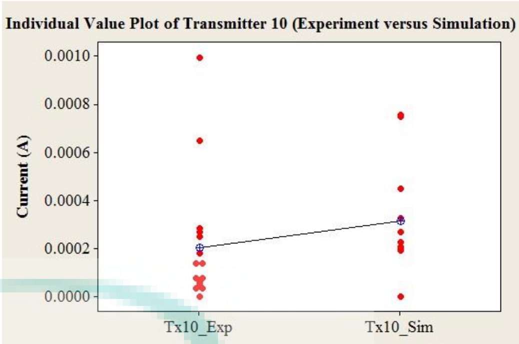


**One-way ANOVA: Transmitter 10 (Experiment versus Simulation)**

```
Source  DF         SS         MS     F      P
Value    1  0.0000001  0.0000001  1.79  0.191
Error   30  0.0000017  0.0000001
Total   31  0.0000018

S = 0.0002351   R-Sq = 5.63%   R-Sq(adj) = 2.48%

Level      N       Mean      StDev
Tx10_Exp  16  0.0002061  0.0002648
Tx10_Sim  16  0.0003172  0.0002011

          Individual 95% CIs For Mean Based on
Pooled StDev
Level     -+---------+---------+---------+--------
Tx10_Exp  (-----------*------------)
Tx10_Sim            (------------*------------)
          -+---------+---------+---------+--------
        0.00010   0.00020   0.00030   0.00040
```

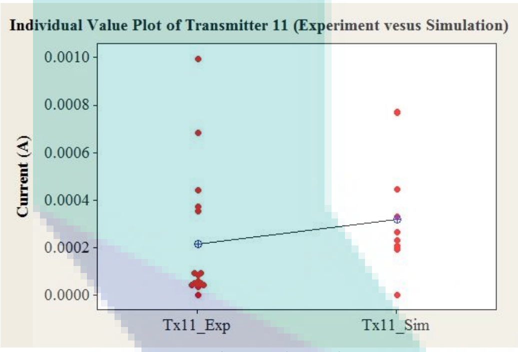


**One-way ANOVA: Transmitter 11 (Experiment versus Simulation)**

```
Source  DF         SS         MS     F      P
Value    1  0.0000001  0.0000001  1.36  0.253
Error   30  0.0000019  0.0000001
Total   31  0.0000019

S = 0.0002484   R-Sq = 4.34%   R-Sq(adj) = 1.15%

Level      N       Mean      StDev
Tx11_Exp  16  0.0002164  0.0002851
Tx11_Sim  16  0.0003188  0.0002052

          Individual 95% CIs For Mean Based on
Pooled StDev
Level     -+---------+---------+---------+--------
Tx11_Exp  (------------*------------)
Tx11_Sim            (------------*------------)
          -+---------+---------+---------+--------
        0.00010   0.00020   0.00030   0.00040
```

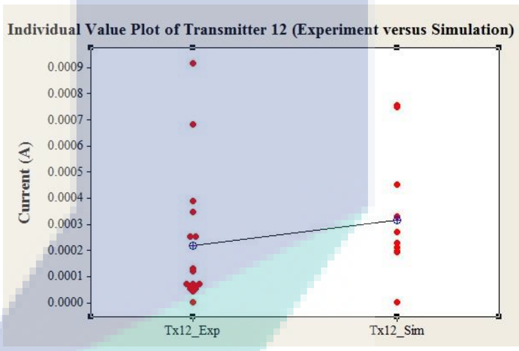


**One-way ANOVA: Transmitter 12 (Experiment versus Simulation)**

```
Source  DF         SS         MS     F      P
Value    1  0.0000001  0.0000001  1.43  0.242
Error   30  0.0000016  0.0000001
Total   31  0.0000017

S = 0.0002315   R-Sq = 4.53%   R-Sq(adj) = 1.35%

Level      N       Mean      StDev
Tx12_Exp  16  0.0002196  0.0002583
Tx12_Sim  16  0.0003173  0.0002012

          Individual 95% CIs For Mean Based on
Pooled StDev
Level     +---------+---------+---------+---------
Tx12_Exp  (-----------*-----------)
Tx12_Sim            (------------*------------)
          +---------+---------+---------+---------
        0.00010   0.00020   0.00030   0.00040
```

**Figure 6.6**: One-way ANOVA test for each source of channel 9 till channel 12

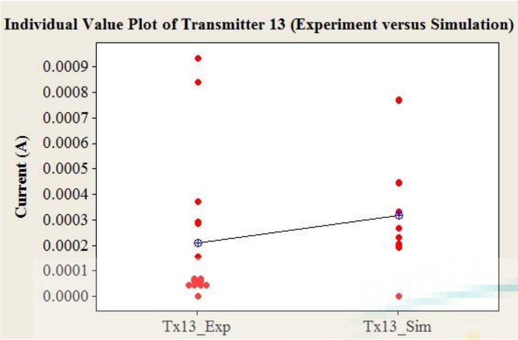


**One-way ANOVA: Transmitter 13 (Experiment versus Simulation)**

```
Source  DF         SS         MS     F      P
Value    1  0.0000001  0.0000001  1.50  0.231
Error   30  0.0000019  0.0000001
Total   31  0.0000020

S = 0.0002494   R-Sq = 4.75%   R-Sq(adj) = 1.58%

Level     N       Mean      StDev
Tx13_Exp  16  0.0002109  0.0002868
Tx13_Sim  16  0.0003188  0.0002052

            Individual 95% CIs For Mean Based on
Pooled StDev
Level     --+---------+---------+---------+-------
Tx13_Exp  (-----------*------------)
Tx13_Sim             (------------*-------------)
          --+---------+---------+---------+-------
          0.00010   0.00020   0.00030   0.00040
```

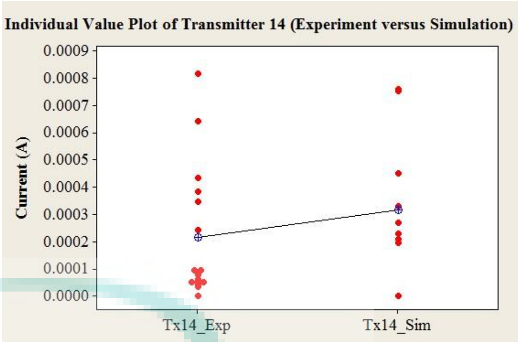


**One-way ANOVA: Transmitter 14 (Experiment versus Simulation)**

```
Source  DF         SS         MS     F      P
Value    1  0.0000001  0.0000001  1.70  0.203
Error   30  0.0000015  0.0000001
Total   31  0.0000016

S = 0.0002238   R-Sq = 5.35%   R-Sq(adj) = 2.20%

Level     N       Mean      StDev
Tx14_Exp  16  0.0002142  0.0002444
Tx14_Sim  16  0.0003173  0.0002012

          Individual 95% CIs For Mean Based on
Pooled StDev
Level     +---------+---------+---------+---------
Tx14_Exp    (-----------*-----------)
Tx14_Sim              (-----------*-----------)
          +---------+---------+---------+---------
          0.00010   0.00020   0.00030   0.00040
```

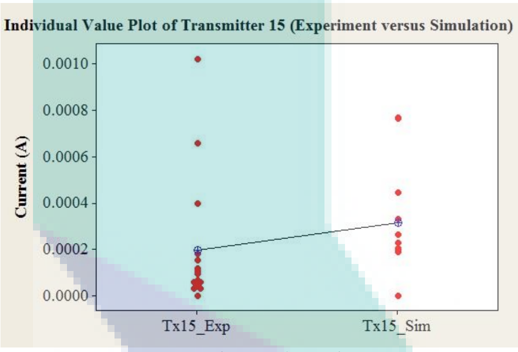


**One-way ANOVA: Transmitter 15 (Experiment versus Simulation)**

```
Source  DF         SS         MS     F      P
Value    1  0.0000001  0.0000001  2.00  0.168
Error   30  0.0000018  0.0000001
Total   31  0.0000019

S = 0.0002430   R-Sq = 6.24%   R-Sq(adj) = 3.12%

Level     N       Mean      StDev
Tx15_Exp  16  0.0001974  0.0002757
Tx15_Sim  16  0.0003188  0.0002052

             Individual 95% CIs For Mean Based on
Pooled StDev
Level     ---+---------+---------+---------+------
Tx15_Exp  (-----------*------------)
Tx15_Sim             (------------*-----------)
          ---+---------+---------+---------+------
          0.00010   0.00020   0.00030   0.00040
```

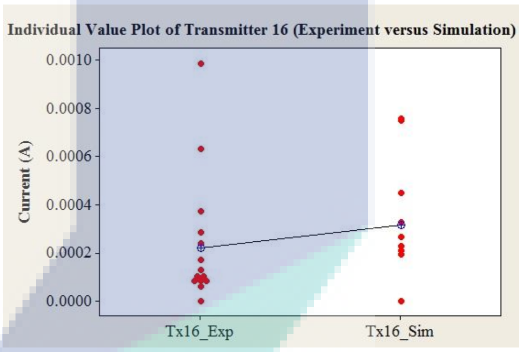


**One-way ANOVA: Transmitter 16 (Experiment versus Simulation)**

```
Source  DF         SS         MS     F      P
Value    1  0.0000001  0.0000001  1.37  0.250
Error   30  0.0000016  0.0000001
Total   31  0.0000017

S = 0.0002304   R-Sq = 4.38%   R-Sq(adj) = 1.19%

Level     N       Mean      StDev
Tx16_Exp  16  0.0002218  0.0002564
Tx16_Sim  16  0.0003172  0.0002011

          Individual 95% CIs For Mean Based on
Pooled StDev
Level     +---------+---------+---------+---------
Tx16_Exp    (----------*-----------)
Tx16_Sim              (-----------*-----------)
          +---------+---------+---------+---------
          0.00010   0.00020   0.00030   0.00040
```

**Figure 6.7**: One-way ANOVA test for each source of channel 13 till channel 16

## 6.3 Reconstruction Image Analysis and Validation

This section is divided into three parts; limitation of the image reconstructed; single phantom; and multiple phantoms. Before deciding to choose the solid rod as the phantom, several types of material were tested. For instance, a whole PVC pipe and a whole acrylic pipe as the gas phantom, oil in the plastic bag as the liquid phantom and plastic beads, as well as grains as particles in a plastic bag were tested. The tomograms were obtained. However, after considering the availability of the smallest size of the phantom on the market, the material of the phantom itself, and easy comparison, it was decided to choose a wooden rod as the phantom representing the liquid–solid two-phase regime instead of liquid–gas or liquid–liquid. The electrical conductivity and electrical permittivity of each of the materials was based on Ref. [151] and are stated in Table 6.2. It was also used in the simulation using COMSOL Multiphysics software. However, for the experiment, the electrical conductivity of water was based on the value measured using a conductor meter. The range of the electrical conductivity for water between $7.0 \times 10^{-3}$ S/m and $7.3 \times 10^{-3}$ S/m is stated by considering the source of the tap water taken every time the experiment was conducted. In addition, two diameter sizes of wooden rods were used in the experiments; 22 mm and 12 mm (see Figure 6.8). All tests were conducted using a vertical pipe.

**Table 6.2:** Parameter for material of phantom

| Material | Electrical conductivity, S/m | Electrical permittivity |
|---|---|---|
| Water | $7.0 \times 10^{-3}$-$7.3 \times 10^{-3}$ | 80 |
| Wood | 0 | 2.75 |

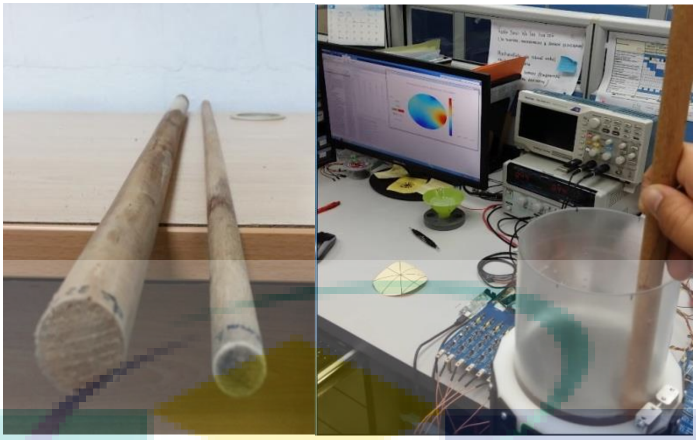

**Figure 6.8:** Sample of wooden rod used (left side); example tomogram obtained in online system (right side)

The electrical conductivity of the primary medium (tap water) was determined using the conductor meter (HI 991300) as shown in Figure 6.9. This measurement was performed every time the experiment was conducted to ensure that the conductivity value was in the range discussed in sub-section 3.3.2.

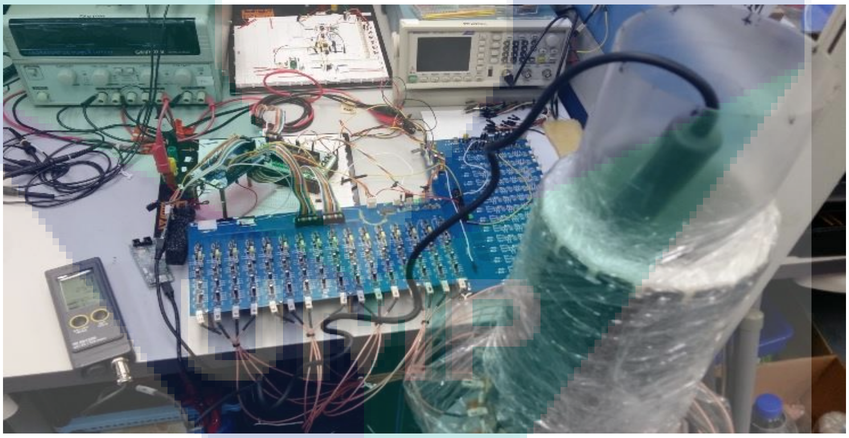

**Figure 6.9:** Tap water measured using a conductor meter

Additionally, cooking oil was also determined using the conductor meter and placed into the pipe. Then a solid rod was also placed into the pipe to know whether it could construct the image or not (see Figure 6.10), but no image was observed. Thus, this supported the theory that ERT needs a conductive medium as the main medium, as discussed in section 2.4. It was also a result of the behaviour of the non-conductive medium itself that cannot allow electricity in the field.

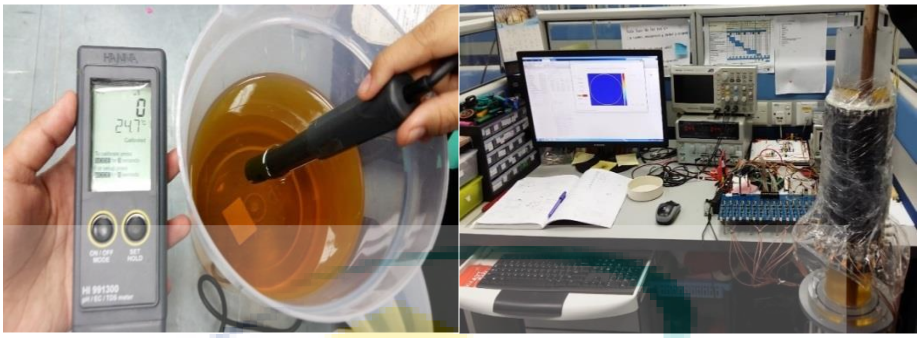

**Figure 6.10:** Measuring electrical conductivity of cooking oil using conductor meter and testing for image reconstruction

The research applied similar positions of the phantoms for the simulations and experiments so that they could be compared with each other. Figure 6.11 shows the jig used in the experiment, marked with different diameters, whereby the position (0, 0) is at the centre of the jig. The jig was applied to get the specific positions during the experiments.

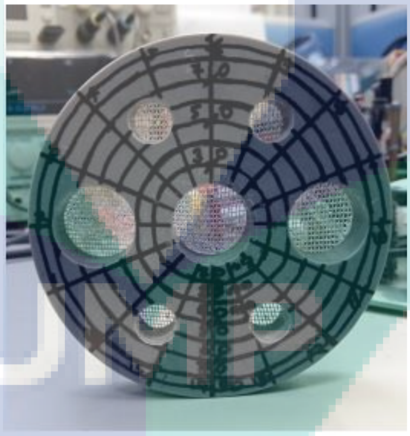

**Figure 6.11:** Jig for placing the phantom at the bottom of the pipe

After all the images were reconstructed using the LBP algorithm, the threshold pre-set value was determined based on sub-section 4.5. Lastly, the analysis and discussion of the reconstructed images were discussed.

### 6.3.1 Weakness of LBP Algorithm and Threshold Pre-Set Value Approach

As explained in sub-section 2.5, the smearing effect occurring around the boundary of the image cannot be avoided if the LBP algorithm is applied in the research. For example, as demonstrated in Figure 6.12, it is seen that the noise surrounding the interest phantom occurred owing to the LBP, and hence affects the accuracy of the image obtained. Also, it was proved by the values of MSSIM and AE that the values for both simulation and experiment gave only 0.15 and 64.2, respectively. In addition, the solid concentration of the reference image was only around 1.5 %, but not with the image obtained from the simulation and experiment. Consequently, as a result of the evidence presented, the threshold process is the focus of the rest of remaining sub-sections.

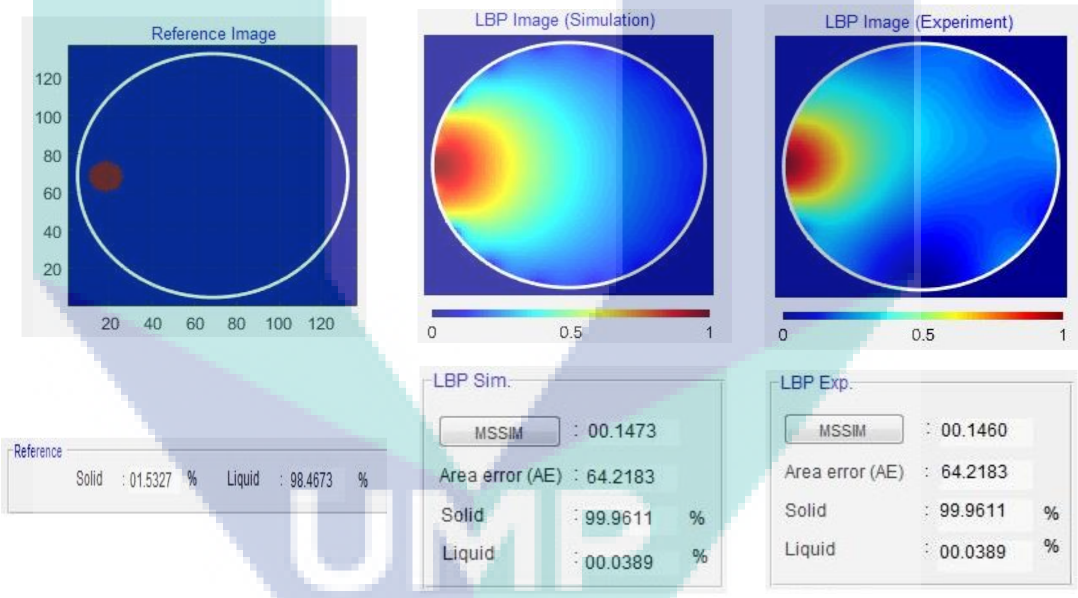


**Figure 6.12:** Example of tomogram reconstructed from simulation and experiment

The example of the threshold pre-set, $P_{th}$ value was determined as illustrated in Figure 6.13. The selection of the threshold value was based on the smallest AE nearest to +/-0. There was a significant decrease of AE when the value of the threshold increased. The same approach was made for all the simulations and experiments, and are summarized in Tables 6.3–6.5. Then, the mean for simulations and experiments were calculated. For this research, the average ratio of threshold value applied for image reconstruction was 0.91 (experiment) and 0.92 (simulation).

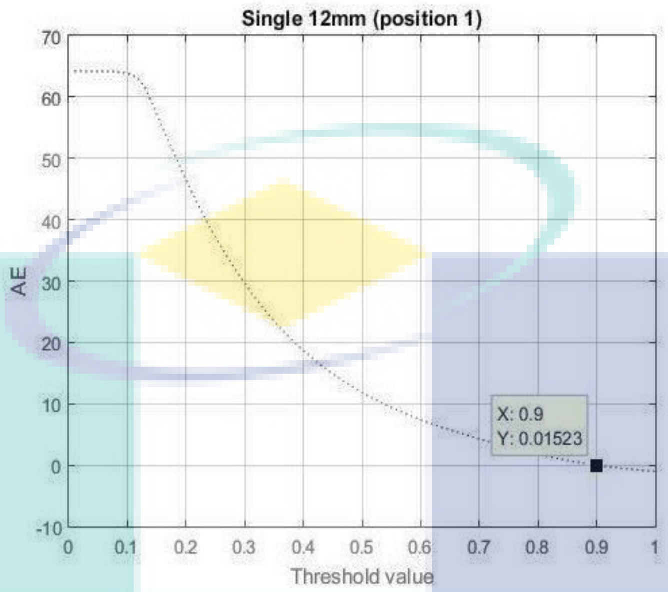


**Figure 6.13:** Example of getting threshold value from AE versus range of threshold value graph

**Table 6.3:** $P_{th}$ based on AE value for all simulations and experiments (single phantom)

| | Single 12mm | | | | Single 22mm | | | |
|---|---|---|---|---|---|---|---|---|
| | Simulation | | Experiment | | Simulation | | Experiment | |
| **Position** | $P_{th}$ | AE | $P_{th}$ | AE | $P_{th}$ | AE | $P_{th}$ | AE |
| **P1** | 0.90 | 0.01523 | 0.87 | 0.01015 | 0.88 | 0.00297 | 0.86 | -0.00594 |
| **P2** | 0.89 | 0.05076 | 0.88 | -0.00508 | 0.87 | -0.00594 | 0.89 | -0.00297 |
| **P3** | 0.90 | -0.03553 | 0.93 | -0.02538 | 0.87 | -0.00446 | 0.87 | 0.03863 |

**Table 6.4:** $P_{th}$ based on AE value for all simulations and experiments (double phantoms)

| | Double 12mm | | | | Double 22mm | | | |
|---|---|---|---|---|---|---|---|---|
| | Simulation | | Experiment | | Simulation | | Experiment | |
| **Position** | $P_{th}$ | AE | $P_{th}$ | AE | $P_{th}$ | AE | $P_{th}$ | AE |
| **P4** | 0.93 | -0.01523 | 0.85 | 0.05584 | 0.91 | -0.06984 | 0.88 | -0.01560 |
| **P5** | 0.90 | -0.07614 | 0.88 | 0.05838 | 0.91 | 0.00223 | 0.89 | 0.01560 |
| **P6** | 0.93 | 0.01269 | 0.94 | -0.01523 | 0.92 | -0.04012 | 0.89 | 0.01860 |

**Table 6.5:** $P_{th}$ based on AE value for all simulations and experiments (blind spot)

| | Blind Spot | | | | | | | |
|---|---|---|---|---|---|---|---|---|
| | 12mm | | | | 22mm | | | |
| | Simulation | | Experiment | | Simulation | | Experiment | |
| **Position** | $P_{th}$ | AE | $P_{th}$ | AE | $P_{th}$ | AE | $P_{th}$ | AE |
| **Pos8** | 0.90 | -0.06091 | 0.87 | 0.04569 | 0.87 | 0.00743 | 0.90 | 0.04012 |
| **Pos6** | Null | Null | Null | Null | 0.94 | 0.05795 | 0.94 | 0.06835 |
| **Pos4** | Null | Null | Null | Null | 0.97 | -0.11765 | 0.96 | -0.01912 |
| **Pos2** | Null | Null | Null | Null | 0.97 | 0.14870 | 0.96 | -0.02504 |
| **Zero** | Null | Null | Null | Null | 0.97 | 0.19470 | 0.96 | 0.11440 |
| **Neg2** | Null | Null | Null | Null | 0.97 | 0.16350 | 0.95 | 0.10160 |
| **Neg4** | Null | Null | Null | Null | 0.97 | -0.01765 | 0.95 | 0.06912 |
| **Neg6** | Null | Null | Null | Null | 0.95 | -0.04755 | 0.94 | -0.01040 |
| **Neg8** | 0.90 | -0.03553 | 0.89 | -0.03553 | 0.87 | 0.03566 | 0.88 | 0.00446 |

### 6.3.2 Limitation of the Image Reconstructed

Two types of experiment were conducted to know for sure what the limitations were of the system in reconstructing the image; blind spot experiment and minimum height of the phantom experiment.

#### 6.3.2.1 Blind Spot Experiment

Tables 6.6 and 6.7 show the results of the reconstructed image when the solid rod tested had a diameter of 22 mm. Every tomogram from simulations and experiments were compared with the reference image. The results show that the location of every tomogram from both simulations and experiments was similar to the reference image. However, the circle shape was only like the reference image when the phantom moved between positions Pos6 till Neg6, mainly from the simulation results. Furthermore, the exactly size of the reconstructed image was not similar to the reference image for both simulation and experiment.

**Table 6.6:** Tomograms for blind spot experiment at positions (22 mm)

| Position | Reference Image with its location (pixel) | Simulation | Experiment |
|---|---|---|---|
| Pos8 | 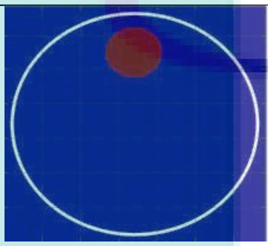 Coordinate=(68,110) | 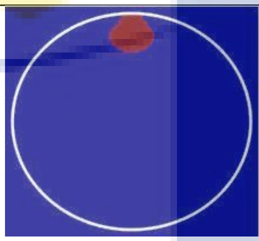 | 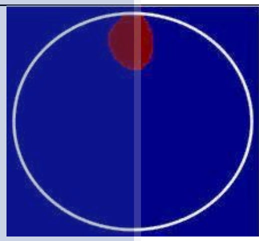 |
| Pos6 | 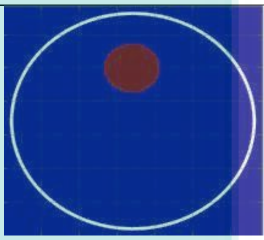 Coordinate=(68,100) | 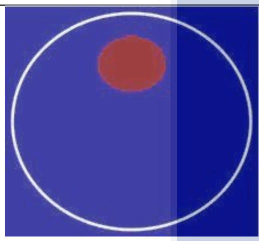 | 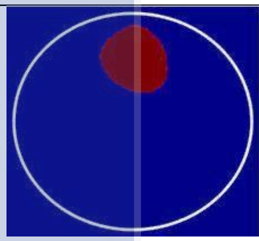 |
| Pos4 |  Coordinate=(68,86.67) | 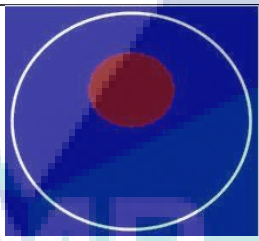 | 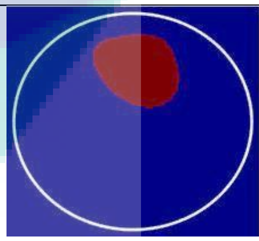 |
| Pos2 | 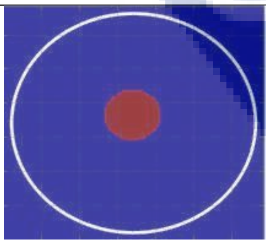 Coordinate=(68,73.33) | 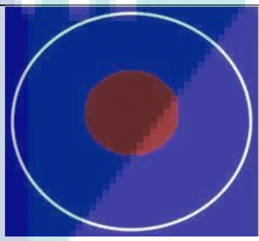 | 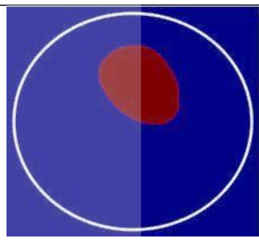 |
| Zero | 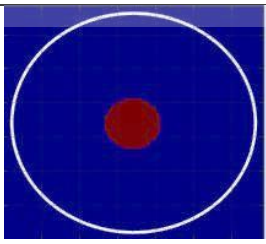 Coordinate=(68,68) | 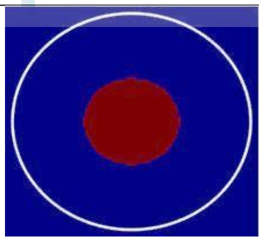 | 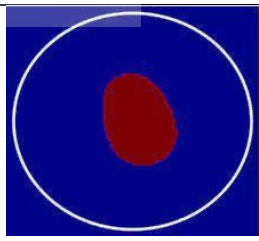 |

**Table 6.7:** Tomograms for blind spot experiment at different positions (22 mm) (continued)

| Position | Reference Image with its location (pixel) | Simulation | Experiment |
|---|---|---|---|
| Neg2 | 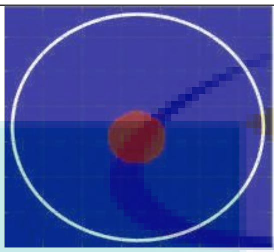 Coordinate=(68,62.67) | 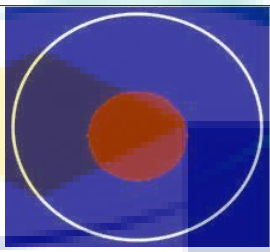 | 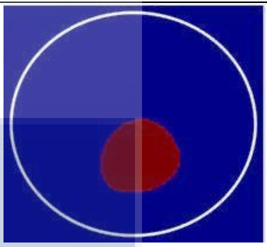 |
| Neg4 |  Coordinate=(68,49.33) | 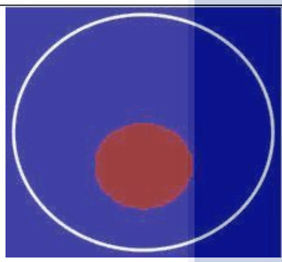 | 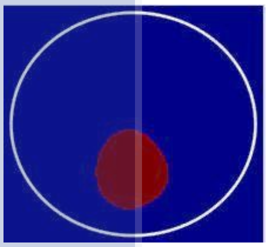 |
| Neg6 | 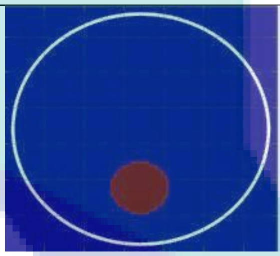 Coordinate=(68,36) | 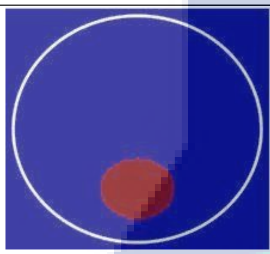 | 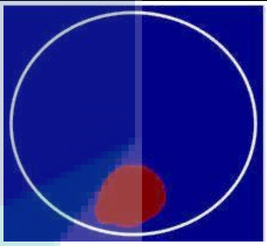 |
| Neg8 | 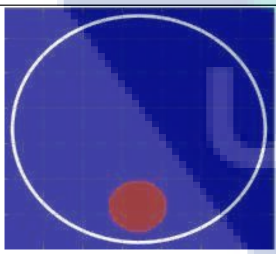 Coordinate=(68,25) |  | 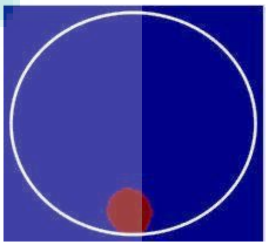 |

This contrasts the 12 mm solid rod tested, where the only sensitive position is near the sensors (Pos8 and Neg8), as shown in Table 6.8. Thus, images at position Pos6 till Neg6 are not shown in Table 6.8 because no image can be reconstructed at those positions in the pipe. This was because the electrical field still could propagate between locations Pos6 and Neg6, and it can be assumed that the small phantom could not affect the electric field inside the pipe with those positions. A detailed analysis is discussed in section 6.3.2.1.1.

**Table 6.8:** Tomograms for blind spot experiment at different positions (12 mm)

| Position | Reference Image with its location (pixel) | Simulation | Experiment |
|---|---|---|---|
| Pos8 | 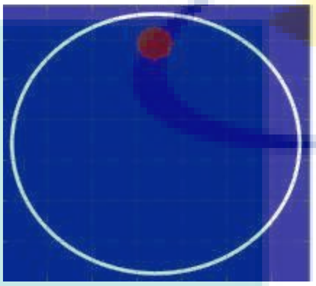 Coordinate=(68,118) | 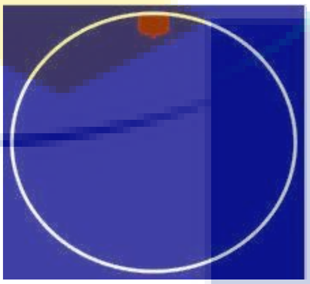 | 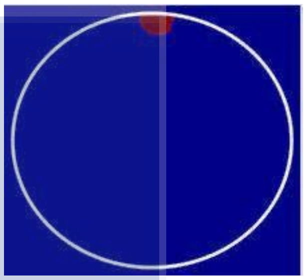 |
| Neg8 | 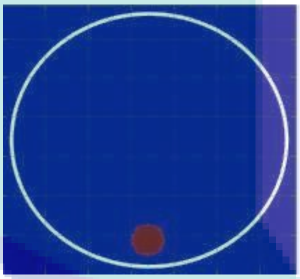 Coordinate=(68,18) | 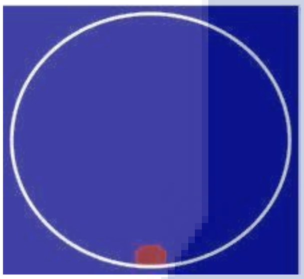 | 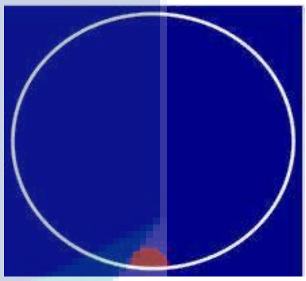 |

### 6.3.2.1.1 Analysis and discussion for Blind Spot Experiment

Figure 6.14 illustrates the percentage of AE for blind spot experiment. The percentage of AE increased when the phantom moved near to the centre of the pipe. Likewise, the negative of percentage AE of the phantom near the sensor for both sizes indicates that the reconstructed image was smaller than the reference image.


**Figure 6.14:** Percentage of AE of different positions for blind spot test (simulation versus experiment)

The MSSIM indexed for blind spot experiment is presented in Table 6.9, and Figure 6.15 shows it as a graph. The maximum MSSIM indexed was 0.9665 from simulation of a 12 mm solid rod, whereas the minimum score was 0.8428 from the experiment of a 22 mm solid rod. The MSSIM for a small phantom near the sensor was near to the indexed 1, and a small MSSIM indexed occurred as sensor closed at the centre of the pipe.

**Table 6.9:** MSSIM indexed measured on tomogram for blind spot

| | **Blind Spot** | | | |
|---|---|---|---|---|
| | **12mm** | | **22mm** | |
| **Position** | **Simulation** | **Experiment** | **Simulation** | **Experiment** |
| **Pos8** | 0.9649 | 0.9637 | 0.9264 | 0.9353 |
| **Pos6** | Null | Null | 0.9331 | 0.9132 |
| **Pos4** | Null | Null | 0.8742 | 0.8579 |
| **Pos2** | Null | Null | 0.8438 | 0.8428 |
| **Zero** | Null | Null | 0.8436 | 0.8708 |
| **Neg2** | Null | Null | 0.8420 | 0.8714 |
| **Neg4** | Null | Null | 0.8615 | 0.9040 |
| **Neg6** | Null | Null | 0.9193 | 0.9026 |
| **Neg8** | 0.9665 | 0.9648 | 0.9345 | 0.9340 |

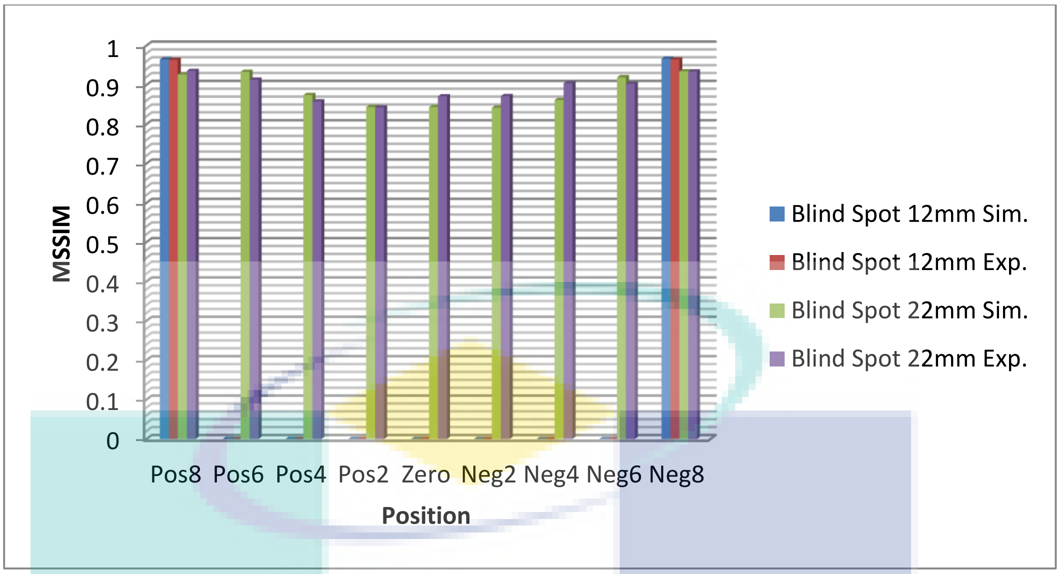


**Figure 6.15:** MSSIM indexed versus different positions of phantom for blind spot

The concentration of solid presented in Figure 6.16 specifies that the small size of phantom reduced by around 1.5 % concentration whereas there was around a 10 % increment in the solid concentration of 22 mm in diameter compared to the percentage of ideal concentration. Despite this, the solid concentrations of simulation and experiment were bigger than the ideal concentration when the 22 mm size of phantom located at point Pos6 till Neg6.

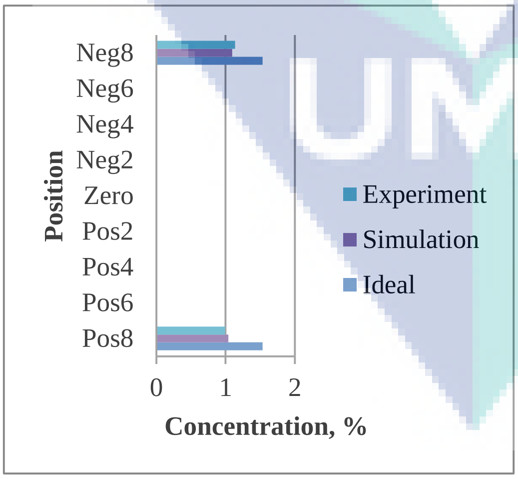


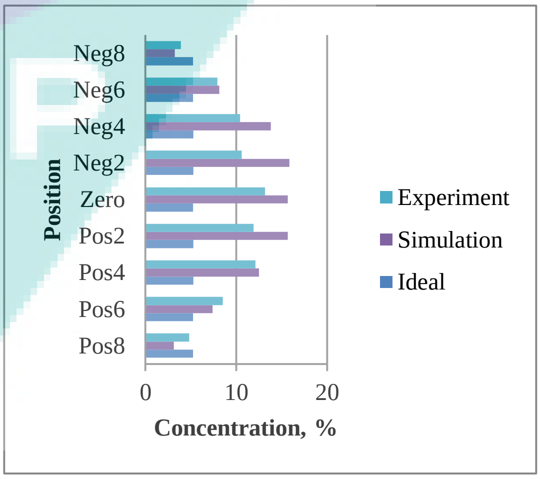


(a) (b)

**Figure 6.16:** Concentration of solid obtained from simulation and experiment (Blind Spot): (a) 12 mm; (b) 22 mm

It is believed that three factors affect the position, size and shape of the tomograms from both sizes of the tested phantom: soft-field nature of electrical tomography; LBP algorithm; and global threshold technique. Firstly, the soft-field nature in electrical tomography as stated in section 2.5.1, made the sensitivity of the reconstructed image poorer when it moved from the pipe wall to the centre of the pipe region. The electric field distribution especially at the central region produces a poor image for a large size of phantom and cannot be detected for a small size solid rod. Secondly, the disadvantage of the LBP algorithm, as mentioned in section 2.5.2, and even though the threshold technique was applied to improve the reconstructed image, is that the ideal size and shape of the phantom cannot be recognized because of the smearing effect. The back-projected data approach of sensor reading in LBP algorithm caused the image to be redundant and enlarged the size of the reconstructed image. Lastly, the fixed average ratio of the threshold pre-set value for the global threshold technique applied for all positions only gave a good reconstructed image for certain positions.

Consequently, the system was capable of detecting different sizes of phantom and was sensitive when the sensor was near to the inner wall surface of the pipeline. Additionally, a 12 mm diameter was considered the minimum size that could be detected by the system. Therefore, positions near the sensor were considered for conducting single phantom (section 6.3.3) and multiple phantom (section 6.3.4) experiments so that the comparison could be easily observed.

#### 6.3.2.2 Height Limitation of Phantoms

The experiment was conducted to investigate whether the height of the phantom affects the image reconstruction. Therefore, it was done by using a PVC pipe with a similar diameter to the solid rod; diameter 22 mm. The limit of detection is determined by using a series of phantoms (see Figure 6.17). The whole PVC pipe was filled with several small stones as ballast to avoid floating. The filling was also glue to prevent water coming through it, and was placed at the right-hand side of the pipe starting from the top to the bottom of the pipe. The solid rod was not applied because it floats in the water with the small height implemented.

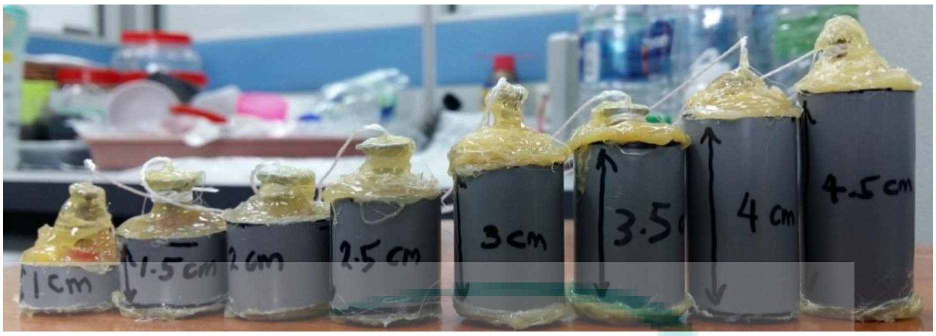


**Figure 6.17:** Different heights of phantoms applied. From left: 1 cm, 1.5 cm, 2 cm, 2.5 cm, 3 cm, 3.5 cm, 4 cm, and 4.5 cm.

Figure 6.18 demonstrates the results of the tomogram for the series of phantom that it detected at 4.5 cm in height. If the height of the phantom was smaller than that, no image could be reconstructed. The MSSIM value 0.9195 showed that it was close to the reference image. However, the negative value of AE means that the image was smaller compared to the reference image. The concentration of the reference image was 5.2361 %, and the differentiation was only around 0.87 %. In short, the minimum height of the phantom that could be identified by the system was around 22.5 % of the height of the electrode plate designed. Also, it can be concluded that the experiment cannot be performed for dynamic objects such as a plastic bead flow experiment through the column due to the limitation. This is because of the inconsistency of the height of the dynamic flow in the vertical pipe compared to a horizontal pipe. Also, it is noticed that the height of the wooden rod for experiment of single and double phantom in sections 6.3.3 and 6.3.4 were 600 mm, which is longer than the height of vertical pipe. This was chosen for easy handling during the experiments.

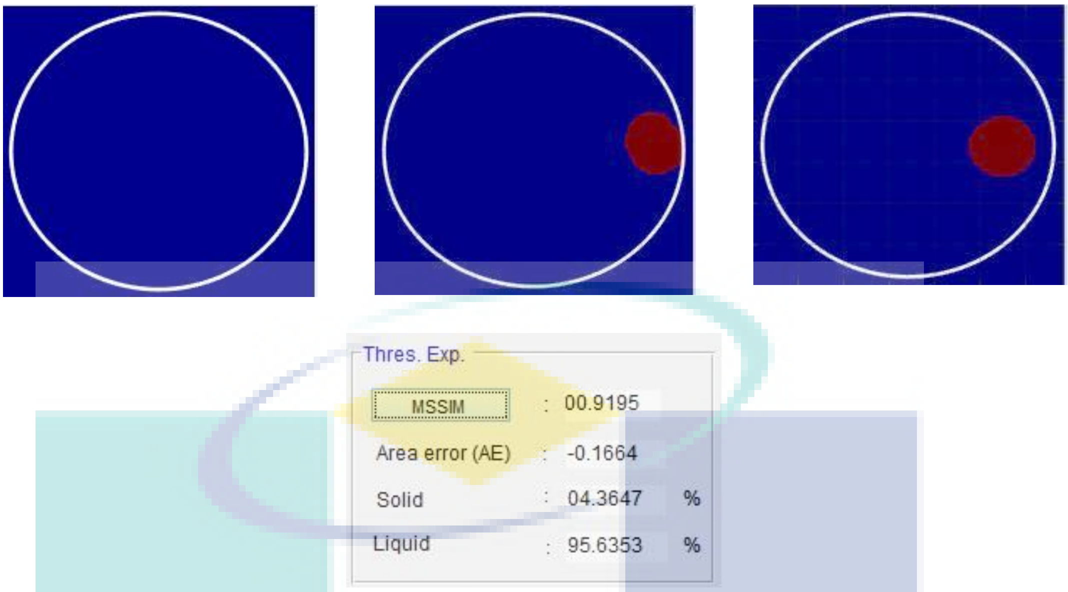


(a) (b) (c)

**Figure 6.18:** (a) No image detected for height 1 cm till 4 cm; (b) image detected when height was 4.5 cm; (c) reference image

### 6.3.3 Single Phantom

Three different positions of experiments were used for each size of the phantoms. And each of the experiments and simulations were compared with the reference image to evaluate the quality of the tomographic system.

#### 6.3.3.1 Experimental versus Simulation Results for Single Phantom

Tables 6.10 and 6.11 report the results of the single object for diameter 12 mm and 22 mm, respectively. The locations for all images reconstructed were similar to the reference images from both simulation and experiment studies. The sizes of the small and large objects were also differentiated. That aside, the circular shapes of the phantoms were not exactly identical to the reference image. The smearing effect from the LBP and the placement of the phantom near to the pipe wall caused the non-identical shape of the tomogram.

**Table 6.10:** Tomograms of single phantom for diameter 12 mm

| Position | Reference Image with its location (pixel) | Simulation | Experiment |
|---|---|---|---|
| P1 | 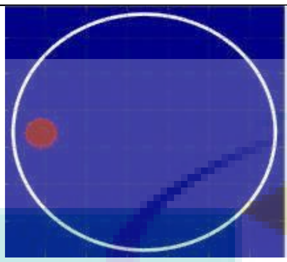 Coordinate=(18,68) | 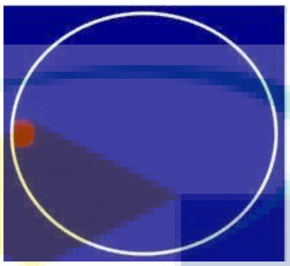 | 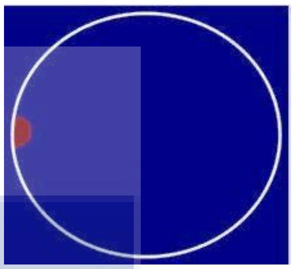 |
| P2 | 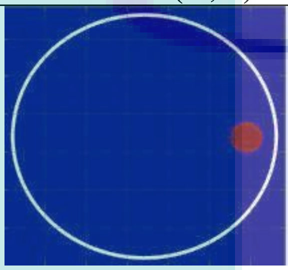 Coordinate=(118,68) | 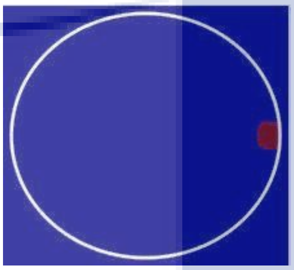 | 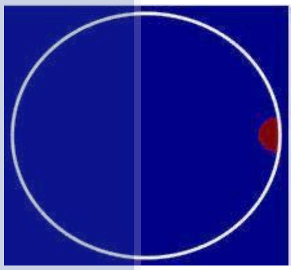 |
| P3 | 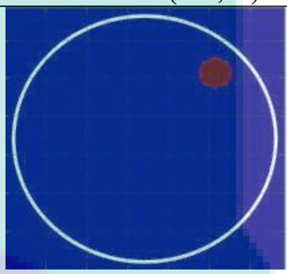 Coordinate=(103,103) | 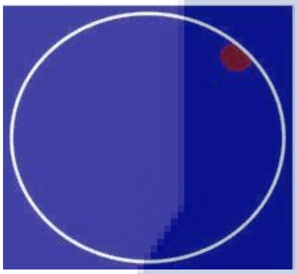 | 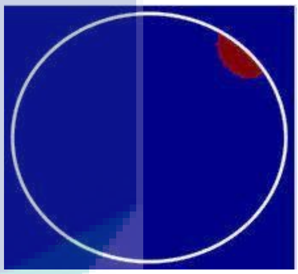 |

**Table 6.11:** Tomograms of single phantom for diameter 22 mm

| Position | Reference Image with its location (pixel) | Simulation | Experiment |
|---|---|---|---|
| P1 | 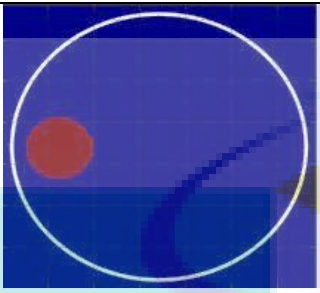 Coordinate=(25,68) | 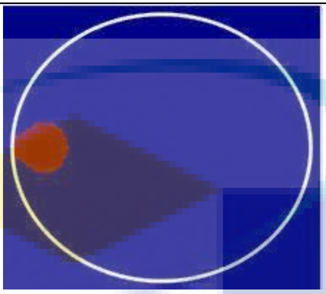 | 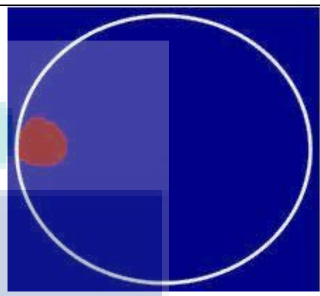 |
| P2 | 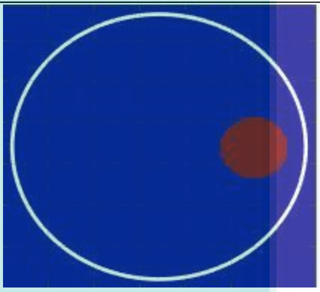 Coordinate=(110,68) | 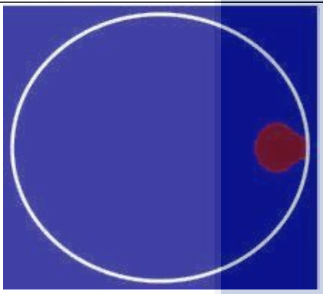 | 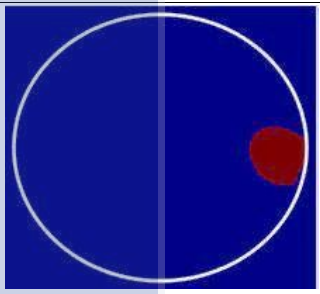 |
| P3 | 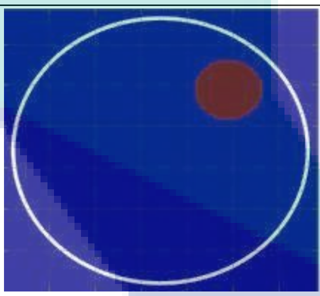 Coordinate=(98,98) | 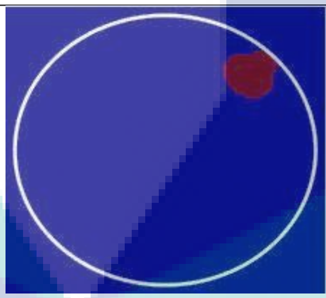 | 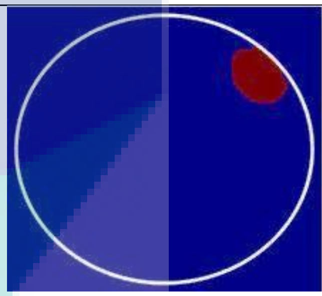 |

### 6.3.3.2 Analysis and Discussion for Single Phantom

The percentage of AE from both simulations and experiments for each of the size of phantoms is presented in Figure 6.19. There was a negative trend of the AE, and it means that the image was smaller than the real image. Also, the percentage of AE from both experiments and simulations were below -40% and only a slight increase occurred in the position P3 of the 22 mm object tested. Moreover, the lowest AE was obtained when the experiment for 22 mm was located at position P2. Correspondingly, a small phantom tested would provide a small percentage of AE.

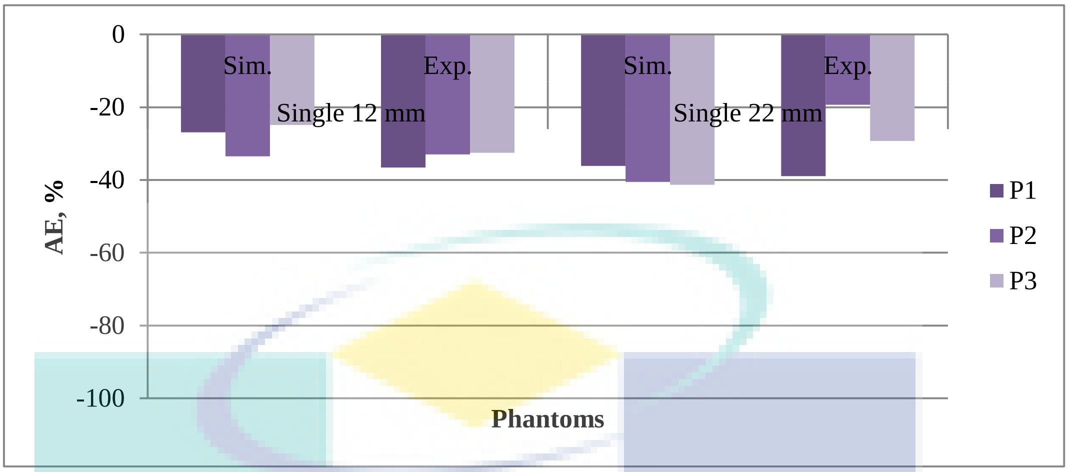


**Figure 6.19:** Percentage of AE for same sizes of single phantom at different positions (simulation versus experiment)

Another essential point is the MSSIM indexed as illustrated in Figure 6.20. The trends of MSSIM indexed from both groups (12 mm and 22 mm) were noticeably similar. Additionally, the MSSIM indexed for all experiments and simulations was above 0.9 and hence it can be claimed that the image only had a small differentiation from the real image. Furthermore, the MSSIM indexed became smaller when a large size of phantom was applied.

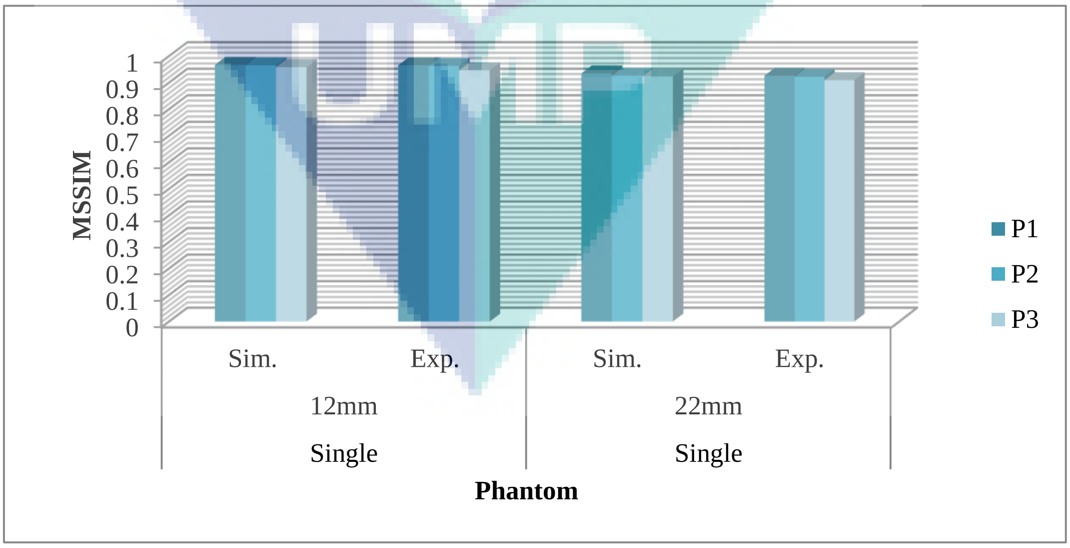


**Figure 6.20:** MSSIM versus different positions of phantom for single phantom

The concentration of both sizes and different locations was also determined, as shown in Figures 6.21 and 6.22. The ideal concentration for the small phantom was 1.5 %, and around 5 % for a large object tested. The simulations and experiments from a single object tested gave a decreased concentration of around 0.5 % and 2 % for 12 mm and 22 mm, respectively. But it also depended on the locations of the phantom inside the pipe. For example, the concentration of 12 mm positioning at the curve position of the pipe, P3, was larger than the theoretical concentration. Subsequently, the concentration from simulations was similar for all positions tested if compared to the experimental results.

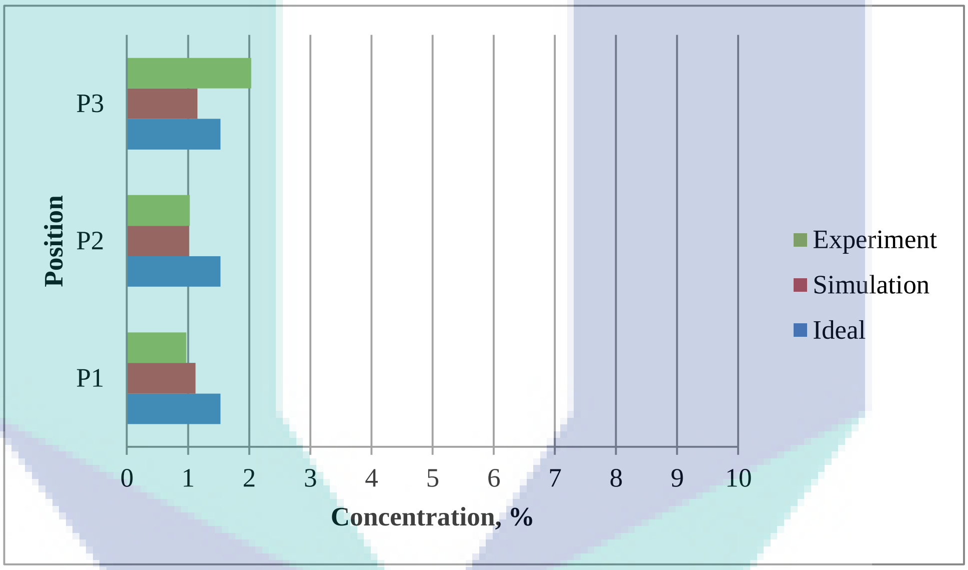


**Figure 6.21**: Concentration of solid obtained from simulation and experiment (single 12 mm)

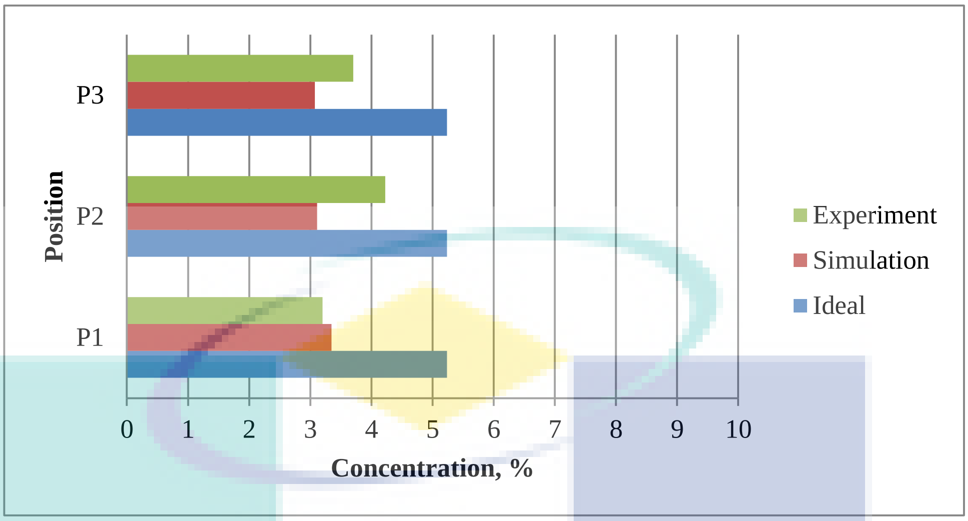


**Figure 6.22**: Concentration of solid obtained from simulation and experiment (single 22 mm)

Based on analysis of AE, MSSIM and solid concentration for a single solid rod, it was believed that the main failure of getting a good reconstructed image as clear as the reference image is because the image reconstruction was basically reconstructed from the LBP algorithm. The blurred image obtained from LBP and applied for the threshold technique influenced the reconstructed image. It affected a pre-set threshold value of threshold technique for each experiment, as well as the average ratio made of the pre-set threshold, and so produced non-ideal images. Another factor was owing to the slightly unstraight positioning of the tested phantom inside the pipe during the experiments. The unstraight position of the phantom gave a non-symmetrical image (like position P2 in Table 6.11), or a bigger size than the straight positioning of the phantom (like position P3 in Table 6.10).

To sum up, the system was capable of identifying a single object. The differentiation could be observed with the different positions and sizes of the phantoms, but not the shape of the phantom. However, it still gave sufficient information so that the system could detect a single object in the vertical column.

### 6.3.4 Multiple Phantoms

The experiments for multiple phantoms were done by using double solid rods. The same sizes of the different double solid rods were placed in the pipe. The results are discussed in sections 6.3.4.1 and 6.3.4.2.

#### 6.3.4.1 Experimental versus Simulation Results for Double Phantoms

The results for double phantoms are revealed in Tables 6.12 and 6.13. Like the single phantom tested, the locations and sizes of double objects could also be distinguished, but the shape was still not same as the reference image.

**Table 6.12:** Tomograms of double phantoms for diameter 12 mm

| Position | Reference Image with its location (pixel) | Simulation | Experiment |
|---|---|---|---|
| P4 | 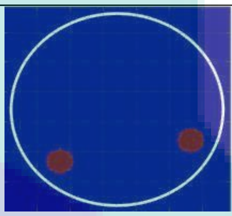 Coordinate=(34,34), (113,48) | 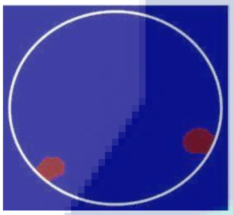 | 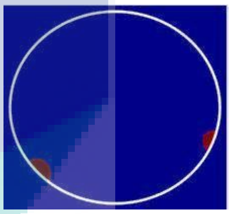 |
| P5 | 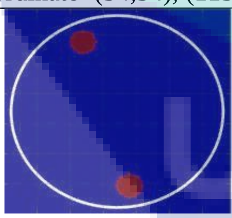 Coordinate=(48,115), (76,19) | 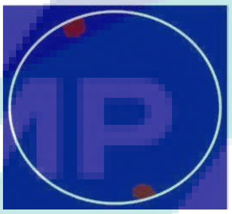 | 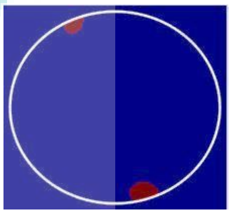 |
| P6 | 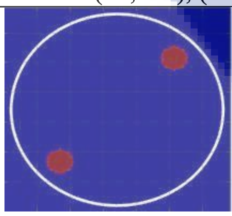 Coordinate=(34,34), (103,103) | 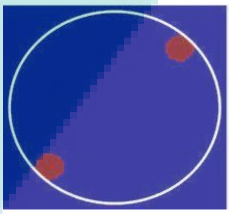 | 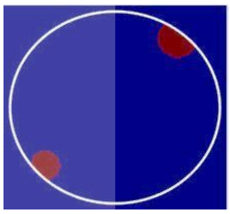 |

**Table 6.13:** Tomograms of double phantoms for diameter 22 mm

| Position | Reference Image with its location (pixel) | Simulation | Experiment |
|---|---|---|---|
| P4 | 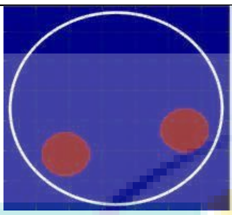 Coordinate=(38,38), (110,54) | 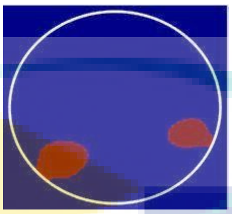 | 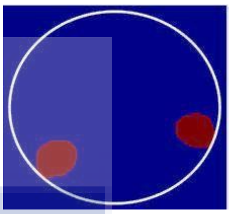 |
| P5 | 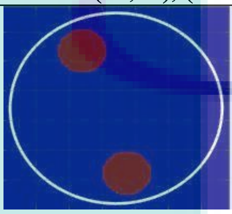 Coordinate=(48,107), (75,25) | 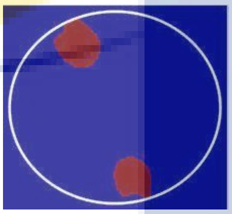 | 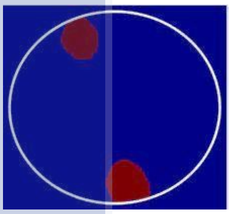 |
| P6 | 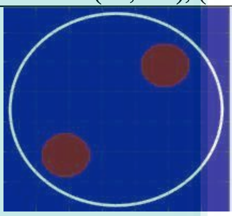 Coordinate=(38,38), (98,98) | 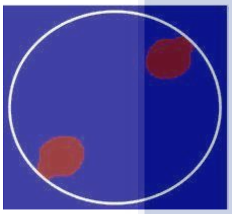 | 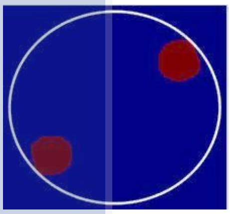 |

### 6.3.4.2 Analysis and Discussion for Double Phantoms

Figure 6.23 indicates the percentage of AE for double phantoms from both comparisons; the positive and negative values obtained from small double objects on the left-hand side of the graph. This means that the tomogram was bigger and smaller than the reference image. Complementary to this, the double 22 mm phantoms had same pattern on the negative side. Nevertheless, both the positive and negative percentages of AE were below 50 %. Also, it can be seen that there was a same noticeable pattern obtained between the simulation and the experiment for each of the locations, except for double 12 mm at position P4. This shows that the experimental results were good if the large multiple phantoms were applied because the pattern follows the simulation.

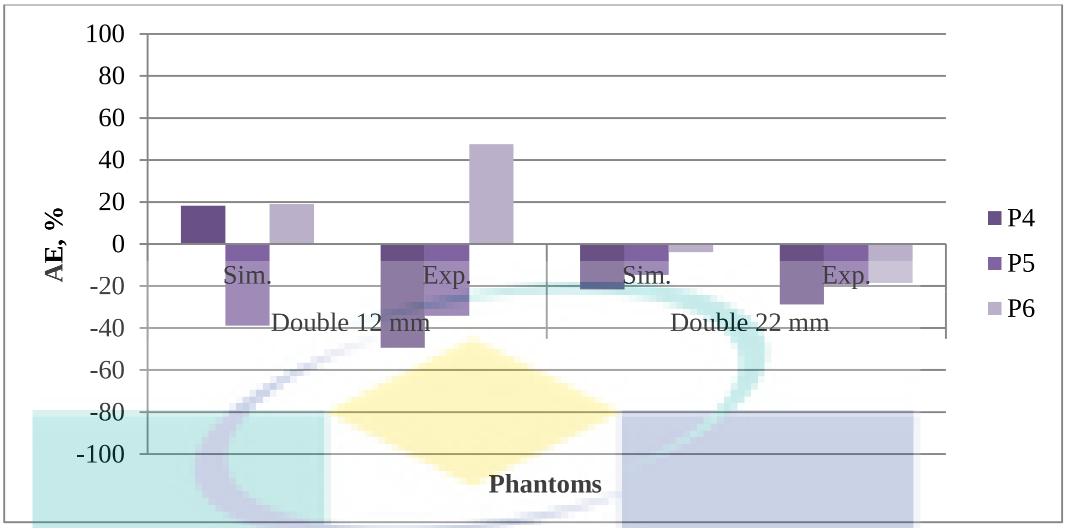


**Figure 6.23:** Percentage of AE for same sizes of double phantoms at different positions (simulation versus experiment)

Additionally, the differentiation of MSSIM indexed between small and large multiple objects group was only around 0.05 (see Figure 6.24). There was a consistent and steady trend of MSSIM indexed for all different positions for both groups. Moreover, it can be observed that the smallest MSSIM value occurred in the experimental results with 0.8 for bigger phantoms and 0.86 for smaller phantoms.

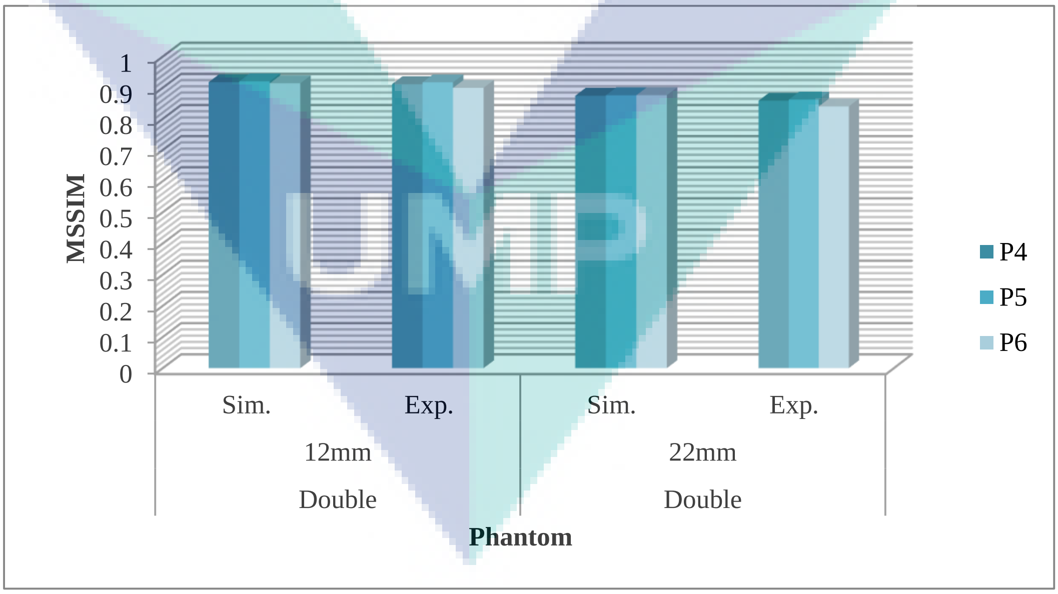


**Figure 6.24:** MSSIM versus different positions of phantom for double phantoms

The pattern for both comparisons (simulation and experiment) with respect to the ideal concentration fluctuated significantly (see Figure 6.25). Meanwhile, large double phantoms gave a small concentration values if compared to the ideal value (see Figure 6.26). The highest concentration values for small and big double phantoms were around 4.5 % (experiment) and 10 % (simulation), respectively. Simultaneously, that maximum value was obtained at the same location P6. Overall, errors for small double phantoms were 0.5–1 % and 1–1.5 % for simulation and experiment, respectively. However, the error range became bigger for large double phantoms compared to small double phantoms, which were around 0.5 %–2.5 % (simulation) and 2.5 %–3 % (experiment).

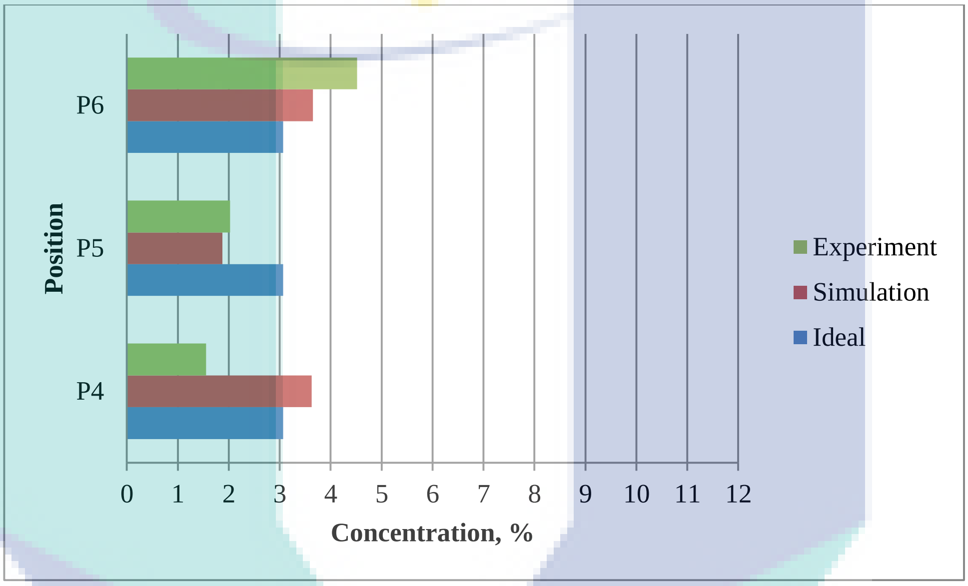


**Figure 6.25:** Concentration of solid (double 12 mm)

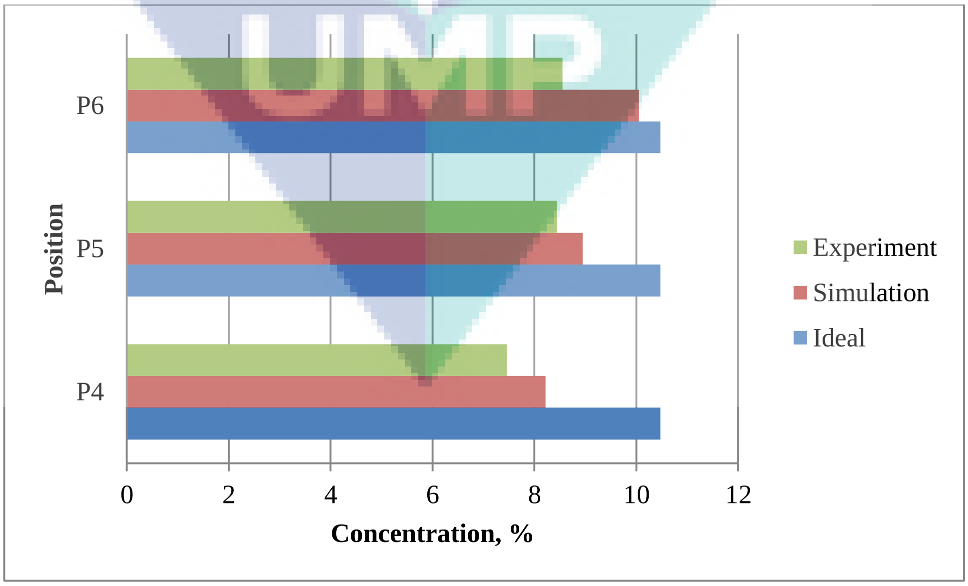


**Figure 6.26:** Concentration of solid (double 22 mm)

The reconstructed images and analysis done indicated that it was easier to recognize the non-homogenous part of the system with an increment in the size of the double phantom. The increment in size of double phantoms increased the non-uniform electrical distribution inside the pipe. Therefore, it gave a low value of MSSIM and a large value of solid concentration error if compared to the small double phantom. In addition, a smearing effect owing to the LBP influenced the reconstructed image. When the size of multiple phantoms in the pipe grew, the distance between both objects shortened. Simultaneously, each of the phantoms produced a smearing effect owing to the back-projected data of sensor reading, and hence, this noise became large when the number and size of phantoms were large. Thus, the tomograms from LBP affected the result of the threshold technique, as well as the pre-set threshold value for finding the best value of multiple phantoms if compared to the single phantom. A fixed average ratio of the pre-set threshold value also gave the results that only certain positions had a good image.

In short, the system was able to detect multiple objects, and the differentiation of sizes and locations could be performed. Some of the reconstructed images were also not similar to the reference images owing to a slight mistake during the experiments and the way the electric field propagated through the pipe. However, it still gave adequate information that the system could recognize the double objects in the vertical pipe.

## 6.4 Summary

The first part of this chapter showed that the sensors' reading from the hardware system had the same pattern as the simulation statistical reading. Therefore, the sensor modelling in Chapter 3 could be applied to the non-invasive ERT system. In addition, the weakness of the LBP algorithm was pointed out at the beginning of section 6.3 and became the reason for focusing on the threshold approach for image reconstruction. Thirdly, the results from the limitations experiment proved that the system could detect an object with a minimum of 12 % in diameter out of the outer pipe diameter, and 22.5 % in height out of the height of the electrode plate. If the dimensions were below than that no image could be obtained.

It was also demonstrated that the system was more sensitive if the objects were placed near the sensors. Lastly, the single and multiple objects tested verified that the system was also able to differentiate the sizes and positions of the objects. The analysis of MSSIM was able to give the information about the quality of a similar image. The AE and concentration could also be used to determine the quantity of the affected area in the pipe.

# CHAPTER 7

# CONCLUSIONS AND SUGGESTIONS FOR FUTURE WORK

## 7.1 Conclusions

The non-invasive ERT system was successfully developed, and its performance analysed and evaluated. In conclusion, all the research objectives were achieved successfully.

A total of sixteen electrode sensing plates were designed and modelled to function independently and flexibly. These sensors were embedded with shielding to reduce external interference and noise. The excitation electrode was injected with 2 MHz continuous sine waves to transmit signal, and this eliminated the phase-sensitive demodulation (PSD) approach of the measurement circuit. Compared to a low frequency signal, a high frequency signal was proved to be able to penetrate through the pipe wall into the region of interest.

The microcontroller which was implemented in the ERT system functioned as the interface between the hardware and software systems for system validation. It worked as a data acquisition system to transfer information from the hardware system to the software system. Therefore, there was no need for an external data-acquisition system. The developed software system used GUI which provided information about the reconstructed image using an LBP algorithm in online mode. Additionally, the offline mode GUI provided threshold approach results including analysis of the tomograms.

Moreover, the developed ERT system has successfully carried out measurement for liquid–solid two-phase regime thus its image results were reconstructed. It can detect obstacles with a minimum of 12 % in diameter of the outer pipe diameter and 22.5 % of the height of the electrode plate in the vertical pipeline. Furthermore, the forward problem was solved (as discussed in Chapter 4) and proved that the LBP algorithm successfully reconstructed the images of the liquid–solid regime. The LBP was used as the basis for the threshold process with a threshold value 0.91 for the experiment and 0.92 for the simulation. Thus, the single and multiple phantoms of simulations and experiments were carried out to validate the performance of the system.

## 7.2 Contribution of the Research

This research aimed to design and develop a tomographic imaging system based on non-invasive ERT for a two-phase regime. The outcome of the study demonstrates several improvements and achievements. The significant contributions are listed as follows:

i. The use of high frequency (2 MHz) in the non-invasive ERT.

By applying a high frequency to the system, the excitation signal can easily penetrate the pipe wall into the sensing region. This is proved by the modelling done in COMSOL and experiments carried out on the actual hardware.

ii. It introduces a non-invasive conductivity detector for industries that deal with two-phase regimes.

The developed ERT system is designed to be a non-invasive, non-intrusive and non-hazardous approach. Therefore, the system is much safer than invasive and intrusive approach, and causes no pollution effect on the environment, with no dangerous radiation or any hazardous substance. Hence, the electrode sensor is corrosion-free. The non-invasive and non-intrusive approach for ERT system keeps the electrodes sensors no contact with the flow medium, which leads to better sensing accuracy.

iii. Easy replacement and troubleshooting of the sensors.

In the case of any sensor faulty occur, the defected sensor can be easily removed and replaced since the sensors are design to be independent and flexible. Moreover, it can hasten up the duration of troubleshooting process.

## 7.3 Recommendations for Future Work

The recommendations for future works are listed as follows:

i. The increment of high frequency greater than 2 MHz is suggested to be applied in more conductive liquid mediums. Currently, 2 MHz frequency can only be implemented for conductive liquid between $5\times10^{-3}$ S/m and $8\times10^{-3}$ S/m.

ii. For faster serial communication between MATLAB and MPLAB, it is suggested that other coding methods are applied, such as using ‘interrupt function’ instead of using the ‘wait function’.

iii. Image reconstruction using local threshold like the adaptive threshold technique also can be implemented, which can increase the quality of the tomogram. If the image quality is more important than the speed of the system, the iterative algorithm is suggested as it could provide better spatial resolution of the image.

iv. Owing to the limitation of the height of the objects tested, it is also suggested that the experiment can be done in the horizontal position. By doing this, the system can be used to monitor the dynamic flow of the phase and the three-phase flow can also be identified.

# REFERENCES


[1] R. B. Northrop, *Noninvasive Instrumentation and Measurement in medical Diagnosis*. New York: CRC Press, 2002.

[2] R. A. Williams and M. S. Beck, *Process Tomography: Principles, Techniques and Applications*, 1 st. ed. Oxford: Butterworth-Heinemann, 1995.

[3] T. York, H. McCann, and K. Ozanyan, "Agile Sensing Systems for Tomography," *IEEE Sensors Journal*, vol. 11, no. 12, pp. 3086–3105, 2011.

[4] U. Z. Ijaz, J. Kim, A. K. Khambampati, M. Kim, S. Kim, and K. Kim, "Concentration Distribution Estimation of Fluid through Electrical Impedance Tomography based on Interacting Multiple Model Scheme," *Flow Measurement and Instrumentation*, vol. 18, no. 1, pp. 47–56, 2007.

[5] S. C. Murphy and T. A. York, "Electrical Impedance Tomography with Non-Stationary Electrodes," *Measurement Science and Technology*, vol. 17, no. 11, pp. 3042–3052, 2006.

[6] R. C. Asher, "Ultrasonic Sensors in the Chemical and Process Industries," *Journal of Physics E: Scientific Instruments*, vol. 16, no. 10, pp. 959–963, 1983.

[7] G. Steiner and F. Podd, "A Non-Invasive and Non-Intrusive Ultrasonic Transducer Array For Process Tomography," in *Proceedings of the XVIIII IMEKO World Congress Metrology for a Sustainable Development*, September 17-22, 2006, Rio de Janeiro, Brazil, 2006, pp. 17–22.

[8] E. Auken, J. Doetsch, G. Fiandaca, A. V. Christiansen, A. Gazoty, A. G. Cahill, and R. Jakobsen, "Imaging Subsurface Migration of Dissolved CO2 in A Shallow Aquifer using 3-D Time-Lapse Electrical Resistivity Tomography," *Journal of Applied Geophysics*, vol. 101, pp. 31–41, Feb. 2014.

[9] S. D. Carrière, K. Chalikakis, G. Sénéchal, C. Danquigny, and C. Emblanch,

"Combining Electrical Resistivity Tomography and Ground Penetrating Radar to study geological structuring of karst Unsaturated Zone," *Journal of Applied Geophysics*, vol. 94, pp. 31–41, Jul. 2013.

[10] J. Qiyun, H. Jishan, S. Ping, and P. Jing, "The Hardware Design of A Mine Resistivity Tomography Instrument," in *Proceedings of the 2009 IEEE International Workshop on Imaging Systems and Technique*, May 11-12, 2009, Shenzhen, China, 2009, pp. 235–238.

[11] R. L. Newmark, A. L. Ramirez, and W. D. Daily, "Monitoring Carbon Dioxide Sequestration using Electrical Resistance Tomography ( ERT ): A Minimally Invasive Method," *Greenhouse Gas Control Technologies*, vol. I, pp. 353–358, 2003.

[12] S. Garré, I. Coteur, C. Wongleecharoen, K. Hussain, W. Omsunrarn, T. Kongkaew, T. Hilger, J. Diels, and J. Vanderborght, "Can We Use Electrical Resistivity Tomography to Measure Root Zone Dynamics in Fields with Multiple Crops?," *Procedia Environmental Sciences*, vol. 19, pp. 403–410, 2013.

[13] J. Boaga, M. Rossi, and G. Cassiani, "Monitoring Soil-plant Interactions in an Apple Orchard Using 3D Electrical Resistivity Tomography," *Procedia Environmental Sciences*, vol. 19, pp. 394–402, 2013.

[14] M. Sharifi and B. Young, "Electrical Resistance Tomography (ERT) Applications to Chemical Engineering," *Chemical Engineering Research and Design*, vol. 91, pp. 1625–1645, 2013.

[15] Z. Cao, L. Xu, C. Xu, and H. Wang, "Electrical Resistance Tomography (ERT) by using An ECT Sensor," in *Proceedings of the 2010 IEEE International Conference on Imaging Systems and Techniques*, July 1-2, 2010, Thessaloniki, Greece, 2010, pp. 63–66.

[16] B. L. Wang, Z. Y. Huang, H. F. Ji, and H. Q. Li, "Towards Capacitively Coupled Electrical Resistance Tomography," in *Proceedings of the 6th World Congress on Industrial Process Tomography*, September 6-9, 2010, Beijing, China, 2010, pp. 1574–1577.

[17] B. Wang, Y. Hu, H. Ji, Z. Huang, and H. Li, "A Novel Electrical Resistance Tomography System Based on C4D Technique," in *Proceedings of the 2012 IEEE International Conference on Instrumentation and Measurement Technology*, May 13-16, 2012, Graz, Austria, 2012, pp. 1929–1932.

[18] Y. Li and M. Soleimani, "Imaging Conductive Materials with High Frequency Electrical Capacitance Tomography," *Measurement*, vol. 46, no. 9, pp. 3355–3361, 2013.

[19] B. Wang, Y. Hu, H. Ji, Z. Huang, and H. Li, "A Novel Electrical Resistance Tomography System Based on C4D Technique Technique," *IEEE Transactions on Instrumentation and Measurement*, vol. 62, no. 5, pp. 1017–1024, 2013.

[20] B. Wang, W. Zhang, Z. Huang, H. Ji, and H. Li, "Modeling and Optimal Design of Sensor for Capacitively Coupled Electrical Resistance Tomography System," *Flow Measurement and Instrumentation*, vol. 31, pp. 3–9, 2013.

[21] B. Wang, W. Tan, Z. Huang, H. Ji, and H. Li, "Image Reconstruction Algorithm for Capacitively Coupled Electrical Resistance Tomography," *Flow Measurement and Instrumentation*, vol. 40, pp. 216–222, 2014.

[22] J. L. Hubers, A. C. Striegel, T. J. Heindel, J. N. Gray, and T. C. Jensen, "X-Ray Computed Tomography in Large Bubble Columns," *Chemical Engineering Science*, vol. 60, pp. 6124–6133, 2005.

[23] T. J. Heindel, J. N. Gray, and T. C. Jensen, "An X-Ray System for Visualizing Fluid Flows," *Flow Measurement and Instrumentation*, vol. 19, pp. 67–78, 2008.

[24] A. Shaikh and M. Al-Dahhan, "Characterization of The Hydrodynamic Flow Regime in Bubble Columns via Computed Tomography," *Flow Measurement and Instrumentation*, vol. 16, pp. 91–98, 2005.

[25] C. Wu, Y. Cheng, Y. Ding, F. Wei, and Y. Jin, "A Novel X-Ray Computed Tomography Method for Fast Measurement of Multiphase Flow," *Chemical Engineering Science*, vol. 62, pp. 4325–4335, 2007.

[26] Z. Zhang, M. Bieberle, F. Barthel, L. Szalinski, and U. Hampel, "Investigation of Upward Cocurrent Gas–Liquid Pipe Flow using Ultrafast X-Ray Tomography and Wire-Mesh," *Flow Measurement and Instrumentation*, vol. 32, pp. 111–118, 2013.

[27] H. Prasser, M. Misawa, and I. Tiseanu, "Comparison Between Wire-Mesh Sensor and Ultra-Fast X-Ray Tomograph for An Air–Water Flow in A Vertical Pipe," *Flow Measurement and Instrumentation*, vol. 16, pp. 73–83, 2005.

[28] S. Boden, M. Bieberle, and U. Hampel, "Quantitative Measurement of Gas

Hold-Up Distribution in a Stirred Chemical Reactor using X-Ray Cone-Beam Computed Tomography," *Chemical Engineering Journal*, vol. 139, no. 2, pp. 351–362, 2008.

[29] R. Abdul Rahim, N. W. Nyap, M. H. Fazalul Rahiman, and C. K. San, "Determination of Water and Oil Flow Composition Using Ultrasonic Tomography," *Jurnal Teknologi*, vol. 9, no. 1, pp. 19–23, 2007.

[30] M. H. Fazalul Rahiman, Z. Zakaria, R. Abdul Rahim, and W. N. Ng, "Ultrasonic Tomography Imaging Simulation of Two-Phase Homogeneous Flow," *Sensor Review*, vol. 29, no. 3, pp. 266–276, 2009.

[31] G. Steiner and C. Deinhammer, "Ultrasonic Time-of-Flight Techniques for Monitoring Multi-Component Processes," *Elektrotechnik und Informationstechnik*, vol. 126, no. 5, pp. 200–205, 2009.

[32] S. Wöckel, U. Hempel, and J. Auge, "Phase Boundary Characterization in Liquids by Acoustic Waves," *Measurement Science and Technology*, vol. 20, no. 12, pp. 1–6, 2009.

[33] M. H. Fazalul Rahiman and R. Abdul Rahim, "Development of Ultrasonic Transmission-Mode Tomography for Water-Particles Flow," *Sensors & Transducer*, vol. 117, no. 6, pp. 99–105, 2010.

[34] I. R. Muhamad, Y. A. Wahab, and S. Saat, "Identification of Water/Solid Flow Regime Using Ultrasonic Tomography," in *Proceedings of the 2012 IEEE International Conference on System Engineering and Technology*, September 11-12, 2012, Bandung, Indonesia, 2012, pp. 1–5.

[35] Z. Zakaria, M. H. Fazalul Rahiman, and R. Abdul Rahim, "Simulation of the Two-Phase Liquid–Gas Flow through Ultrasonic Transceivers Application in Ultrasonic Tomography," *Sensors & Transducer*, vol. 112, no. 1, pp. 24–38, 2010.

[36] M. D. Supardan, Y. Masuda, A. Maezawa, and S. Uchida, "The Investigation of Gas Holdup Distribution in A Two-Phase Bubble Column using Ultrasonic Computed Tomography," *Chemical Engineering Journal*, vol. 130, no. 2–3, pp. 125–133, 2007.

[37] M. H. Fazalul Rahiman, Z. Zakaria, and R. Abdul Rahim, "Ultrasonic Process Tomographic Imaging Sensor: An Approach Utilising Transceivers Method," in *Proceedings of the 2008 IEEE International Conference on Computer and Communication Engineering*, May 13-15, 2008, Kuala Lumpur, Malaysia,

2008, pp. 1147–1150.

[38] M. H. Fazalul Rahiman, R. Abdul Rahim, H. Abdul Rahim, and N. M. Nor Ayob, “Novel Adjacent Criterion Method for Improving Ultrasonic Imaging Spatial Resolution,” *IEEE Sensors Journal*, vol. 12, no. 6, pp. 1746–1747, 2012.

[39] M. H. F. Rahiman, R. A. Rahim, H. A. Rahim, N. M. N. Ayob, E. J. Mohamad, and Z. Zakaria, “Modelling Ultrasonic Sensor for Gas Bubble Profiles Characterization of Chemical Column,” *Sensors and Actuators B: Chemical*, vol. 184, pp. 100–105, 2013.

[40] M. H. F. Rahiman, R. A. Rahim, H. A. Rahim, E. J. Mohamad, Z. Zakaria, and S. Z. M. Muji, “An Investigation on Chemical Bubble Column using Ultrasonic Tomography for Imaging of Gas Profiles,” *Sensors and Actuators B: Chemical*, vol. 202, pp. 46–52, 2014.

[41] N. M. Nor Ayob, S. Yaacob, Z. Zakaria, M. H. Fazalul Rahiman, R. Abdul Rahim, and M. R. Manan, “Improving Gas Component Detection of An Ultrasonic Tomography System for Monitoring Liquid/Gas Flow,” in *Proceedings of the 2010 6th IEEE International Colloquium on Signal Processing & Its Applications*, May 21-23, 2010, Melaka, Malaysia, 2010, pp. 278–282.

[42] N. M. Nor Ayob, M. J. Pusppanathan, R. Abdul Rahim, M. H. Fazalul Rahiman, F. R. Mohd Yunus, S. Buyamin, I. M. Abd Rahim, and Y. Md. Yunos, “Design Consideration for Front-End System in Ultrasonic Tomography,” *Jurnal Teknologi*, vol. 64, no. 5, pp. 53–58, 2013.

[43] N. M. Nor Ayob, M. H. Fazalul Rahiman, Z. Zakaria, S. Yaacob, R. Abdul Rahim, and M. R. Manan, “Simulative Study in Liquid/Gas Two-Phase Flow Measurement for Dual-Plane Ultrasonic Transmission-Mode Tomography,” *Jurnal Teknologi*, vol. 54, pp. 79–94, 2011.

[44] R. Abdul Rahim, J. F. Pang, and K. S. Chan, “Optical Tomography Sensor Configuration using Two Orthogonal and Two Rectilinear Projection Arrays,” *Flow Measurement and Instrumentation*, vol. 16, no. 5, pp. 327–340, 2005.

[45] E. Schleicher, M. J. Da Silva, S. Thiele, A. Li, E. Wollrab, and U. Hampel, “Design of An Optical Tomograph for the Investigation of Single- and Two-Phase Pipe Flows,” *Measurement Science and Technology*, vol. 19, no. 9, pp. 1–14, 2008.

[46] Y. Md. Yunos, R. Abdul Rahim, and R. G. Green, "Initial Result on Measurement of Gas Volumetric Flow Rate in Gas/Liquid Mixtures using Linear CCD," *Jurnal Teknologi*, vol. 48, no. D, pp. 1–12, 2008.

[47] S. Ibrahim, M. A. M. Yunus, R. G. Green, and K. Dutton, "Concentration Measurements of Bubbles in A Water Column using An Optical Tomography System," *ISA Transactions*, vol. 51, no. 6, pp. 821–826, 2012.

[48] N. S. Mohd Fadzil, R. Abdul Rahim, M. S. Karis, S. Z. Mohd Muji, M. F. Abdul Sahib, M. S. B. Mansor, N. M. Nor Ayob, M. F. Jumaah, and M. Z. Zawahir, "Hardware Design of Laser Optical Tomography System for Detection of Bubbles Column," *Jurnal Teknologi*, vol. 64, no. 5, pp. 69–73, 2013.

[49] W. Wang and H. Yang, "Imaging A Rectangular Fluidised Bed by Electrical Capacitance Tomography: Preliminary Results," *Sensor Review*, vol. 31, no. 4, pp. 315–320, 2011.

[50] W. Yang, "Key Issues in Designing Capacitance Tomography Sensors," in *Proceedings of the IEEE Sensors*, October 22-25, 2006, Daegu, Korea, 2006, pp. 497–505.

[51] D. Chen and Y. Han, "An Image Data Capture System for Electrical Capacitance Tomography of Oil/Water Two-Phase Flow," in *Proceedings of the 2006 IEEE International Conference on Information Acquisition*, August 20 - 23, 2006, Shandong, China, 2006, pp. 722–726.

[52] H. Y. Cao, X. M. Duan, and H. X. Wang, "Design of Electrical Capacitance Tomography Hardware System," *Advanced Materials Research*, vol. 753–755, pp. 2311–2315, 2013.

[53] N. T. Ali Othman, H. Obara, and M. Takei, "Cross-Sectional Capacitance Measurement of Particle Concentration in A Microchannel with Multi-Layered Electrodes," *Flow Measurement and Instrumentation*, vol. 31, pp. 47–54, 2013.

[54] W. Q. Yang, A. Chondronasios, S. Nattrass, V. T. Nguyen, M. Betting, I. Ismail, and H. McCann, "Adaptive Calibration of A Capacitance Tomography System for Imaging Water Droplet Distribution," *Flow Measurement and Instrumentation*, vol. 15, no. 5–6, pp. 249–258, 2004.

[55] C. Yu, Z. Jian, and C. Deyun, "Two-Phase Flow Parameters Measurement and Gauss-Newton Image Reconstruction Algorithm for Electrical Capacitance

Tomography," in *Proceedings of the 2009 IEEE International Conference on Industrial Mechatronics and Automation*, December 9-11, 2009, Christchurch, New Zealand, 2009, pp. 192–195.

[56] F. Teixeira and L. Fan, "Advances in Electrical Capacitance Tomography", Ph.D. Thesis, The Ohio State University, 2006.

[57] W. A. Al-Masry, E. M. Ali, S. A. Alshebeili, and F. M. Mousa, "Non-Invasive Imaging of Shallow Bubble Columns using Electrical Capacitance Tomography," *Journal of Saudi Chemical Society*, vol. 14, no. 3, pp. 269–280, 2010.

[58] R. Banasiak, R. Wajman, T. Jaworski, P. Fiderek, H. Fidos, J. Nowakowski, and D. Sankowski, "Study on Two-Phase Flow Regime Visualization and Identification using 3D Electrical Capacitance Tomography and Fuzzy-Logic Classification," *International Journal of Multiphase Flow*, vol. 58, pp. 1–14, 2014.

[59] J. C. Gamio, J. Castro, L. Rivera, J. Alamilla, F. Garcia-Nocetti, and L. Aguilar, "Visualisation of Gas–Oil Two-Phase Flows in Pressurised Pipes using Electrical Capacitance Tomography," *Flow Measurement and Instrumentation*, vol. 16, no. 2–3, pp. 129–134, 2005.

[60] Z. Huang, D. Xie, H. Zhang, and H. Li, "Gas–Oil Two-phase Flow Measurement using An Electrical Capacitance Tomography System and A Venturi Meter," *Flow Measurement and Instrumentation*, vol. 16, no. 2–3, pp. 177–182, 2005.

[61] C. Ortiz-Alemán and R. Martin, "Inversion of Electrical Capacitance Tomography Data By Simulated Annealing: Application to Real Two-Phase Gas–Oil Flow Imaging," *Flow Measurement and Instrumentation*, vol. 16, no. 2–3, pp. 157–162, 2005.

[62] D. Xie, Z. Huang, H. Ji, and H. Li, "An Online Flow Pattern Identification System for Gas–Oil Two-Phase Flow Using Electrical Capacitance Tomography," *IEEE Transactions on Instrumentation and Measurement*, vol. 55, no. 5, pp. 1833–1838, 2006.

[63] E. J. Mohamad, R. Abdul Rahim, L. P. Ling, M. H. Fazalul Rahiman, O. M. F. Marwah, and N. M. Nor Ayob, "Segmented Capacitance Tomography Electrodes : A Design and Experimental Verifications," *IEEE Sensors Journal*, vol. 12, no. 5, pp. 1589–1598, 2012.

[64] Y. Zhao, H. Yeung, E. E. Zorgani, A. E. Archibong, and L. Lao, “High Viscosity Effects on Characteristics of Oil and Gas Two-Phase Flow in Horizontal Pipes,” *Chemical Engineering Science*, vol. 95, pp. 343–352, 2013.

[65] R. Zhang, Q. Wang, H. Wang, M. Zhang, and H. Li, “Data Fusion in Dual-Mode Tomography for Imaging Oil–Gas Two-Phase Flow,” *Flow Measurement and Instrumentation*, vol. 37, pp. 1–11, 2014.

[66] F. Dong, C. Xu, Z. Zhang, and S. Ren, “Design of Parallel Electrical Resistance Tomography System for Measuring Multiphase Flow,” *Chinese Journal of Chemical Engineering*, vol. 20, no. 2, pp. 368–379, 2012.

[67] H. Zhou, L. Xu, Z. Cao, J. Hu, and X. Liu, “Image Reconstruction for Invasive ERT in Vertical Oil Well Logging,” *Chinese Journal of Chemical Engineering*, vol. 20, no. 2, pp. 319–328, 2012.

[68] S. Kim, A. N. Nkaya, and T. Dyakowski, “Measurement of Mixing of two Miscible Liquids in A Stirred Vessel with Electrical Resistance Tomography,” *International Communications in Heat and Mass Transfer*, vol. 33, no. 9, pp. 1088–1095, 2006.

[69] F. Ricard, C. Brechtelsbauer, X. Y. Xu, and C. J. Lawrence, “Monitoring of Multiphase Pharmaceutical Processes using Electrical Resistance Tomography,” *Chemical Engineering Research and Design*, vol. 83, no. 7, pp. 794–805, 2005.

[70] Y. H. Liu, N. Wang, H. Y. Sun, and W. Chen, “Solid-Liquid Two-Phase Flow Image Reconstruction in Microchannel Based on Tikhonov Regularization Method,” *Applied Mechanics and Materials*, vol. 333–335, pp. 1013–1019, 2013.

[71] M. Sharifi and B. Young, “Towards An Online Milk Concentration Sensor using ERT: Correlation of Conductivity, Temperature and Composition,” *Journal of Food Engineering*, vol. 116, no. 1, pp. 86–96, 2013.

[72] M. Sharifi and B. Young, “The Potential Utilisation of Electrical Resistance Tomography (ERT) in Milk Powder Processing for Monitoring and Control,” in *Proceedings of the 6th World Congress on Industrial Process Tomography*, September 6-9, 2010, Beijing, China, 2005, pp. 1–14.

[73] M. Sharifi and B. Young, “3-Dimensional Spatial Monitoring of Tanks for The Milk Processing Industry using Electrical Resistance Tomography,”

*Journal of Food Engineering*, vol. 105, no. 2, pp. 312–319, 2011.

[74] M. Sharifi and B. Young, "Qualitative Visualization and Quantitative Analysis of Milk Flow using Electrical Resistance Tomography," *Journal of Food Engineering*, vol. 112, no. 3, pp. 227–242, 2012.

[75] S. Hosseini, D. Patel, F. Ein-Mozaffari, and M. Mehrvar, "Study of Solid–Liquid Mixing in Agitated Tanks through Electrical Resistance Tomography," *Chemical Engineering Science*, vol. 65, no. 4, pp. 1374–1384, 2010.

[76] S. A. Razzak, S. Barghi, and J.-X. Zhu, "Application of Electrical Resistance Tomography on Liquid–Solid Two-Phase Flow Characterization in An LSCFB Riser," *Chemical Engineering Science*, vol. 64, no. 12, pp. 2851–2858, 2009.

[77] S. J. Stanley and G. T. Bolton, "A Review of Recent Electrical Resistance Tomography (ERT) Applications for Wet Particulate Processing," *Particle & Particle Systems Characterization*, vol. 25, no. 3, pp. 207–215, Sep. 2008.

[78] A. Madupu, A. Mazumdar, J. Zhang, D. Roelant, and R. Srivastava, "Electrical Resistance Tomography for Real-Time Mapping of The Solid-Liquid Interface in Tanks Containing Optically Opaque Fluids," in *Proceedings of the SPIE-IS&T Electronic Imaging - Computational Imaging III*, January 17-18, 2005, California, USA, 2005, vol. 5674, pp. 36–46.

[79] M. Sobri, A. Ahmad, M. Irwan, and S. Jantan, "ERT Visualization of Gas Dispersion Performance of Aerofoil and Radial Impellers in An Agitated Vessel," *Jurnal Teknologi*, vol. 64, no. 5, pp. 75–78, 2013.

[80] A. D. Okonkwo, M. Wang, and B. Azzopardi, "Characterisation of A High Concentration Ionic Bubble Column using Electrical Resistance Tomography," *Flow Measurement and Instrumentation*, vol. 31, pp. 69–76, 2013.

[81] W. Yenjaichon, J. R. Grace, C. Jim Lim, and C. P. J. Bennington, "Characterisation of Gas Mixing in Water and Pulp-Suspension Flow Based on Electrical Resistance Tomography," *Chemical Engineering Journal*, vol. 214, pp. 285–297, 2013.

[82] C. Yang, H. Wang, and Z. Cui, "Application of Electrical Resistance Tomography in Bubble Columns for Volume Fraction Measurement," in *Proceedings of the 2012 IEEE International Conference on Instrumentation and Measurement Technology*, May 13-16, 2012, Graz, Austria, 2012, pp.

1199–1203.

[83] X. Deng, G. Li, Z. Wei, Z. Yan, and W. Yang, “Theoretical Study of Vertical Slug Flow Measurement by Data Fusion from Electromagnetic Flowmeter and Electrical Resistance Tomography,” *Flow Measurement and Instrumentation*, vol. 22, no. 4, pp. 272–278, 2011.

[84] J. Kourunen, T. Niitti, and L. M. Heikkinen, “Application of Three-Dimensional Electrical Resistance Tomography to Characterize Gas Holdup Distribution in Laboratory Flotation Cell,” *Minerals Engineering*, vol. 24, pp. 1677–1686, 2011.

[85] H. Jin, S. Yang, G. He, M. Wang, and R. A. Williams, “The Effect of Gas-Liquid Counter-Current Operation on Gas Hold-Up in Bubble Columns using Electrical Resistance Tomography,” *Journal of Chemical Technology & Biotechnology*, vol. 85, no. 9, pp. 1278–1283, 2010.

[86] Y. Xu, H. Wang, Z. Cui, and F. Dong, “Application of Electrical Resistance Tomography for Slug Flow Measurement in Gas-Liquid Flow of Horizontal Pipe,” in *Proceedings of the 2009 IEEE International Workshop on Imaging Systems and Techniques*, May 11-12, 2009, Shenzhen, China, 2009, pp. 319–323.

[87] Z. Meng, Z. Huang, B. Wang, H. Ji, and H. Li, “Flowrate Measurement of Air-Water Two-Phase Flow using An Electrical Resistance Tomography Sensor and A Venturi Meter,” in *Proceedings of the 2009 IEEE International Conference on Instrumentation and Measurement Technology*, May 5-7, 2009, Singapore, 2009, pp. 118–121.

[88] M. Wang, G. Lucas, Y. Dai, N. Panayotopoulos, and R. A. Williams, “Visualisation of Bubbly Velocity Distribution in A Swirling Flow using Electrical Resistance Tomography,” *Particle & Particle Systems Characterization*, vol. 23, no. 3–4, pp. 321–329, 2006.

[89] F. Dong, Y. Xu, L. Hua, and H. Wang, “Two Methods for Measurement of Gas-Liquid Flows in Vertical Upward Pipe using ERT System,” *IEEE Transactions on Instrumentation and Measurement*, vol. 55, no. 5, pp. 1576–1586, 2006.

[90] C. K. Alexander and M. N. Sadiku, *Fundamentals of Electric Circuits*, 2nd. ed. New York: McGraw Hill, 2004.

[91] J. William H.Hayt and John A. Buck, “Current and Conductors,” in

*Engineering Electromagnetics*, 7th. ed., New York: Mc Graw Hill, 2006, p. 122.

[92] C. Kuo-Sheng, D. Isaacson, J. C. Newell, and D. G. Gisser, “Electrode Models for Electric Current Computed,” *IEEE Transactions on Biomedical Engineering*, vol. 36, no. 9, pp. 918–924, 1989.

[93] F. T. Ulaby, E. Michielssen, and U. Ravaioli, “Resistance,” in *Fundamentals of Applied Electromagnetics*, 6th ed., United State of America: Pearson, 2010, p. 196.

[94] F. R. M. Yunus, R. A. Rahim, S. R. Aw, N. M. N. Ayob, C. L. Goh, and M. J. Pusppanathan, “Simulation Study of Electrode Size in Air-Bubble Detection for Dual-Mode Integrated Electrical Resistance and Ultrasonic Transmission Tomography,” *Powder Technology*, vol. 256, pp. 224–232, 2014.

[95] D. K. Kalluri, “Quasistatic and Static Approximations,” in *Principles of Electromagnetic Waves and Materials*, Boca Raton: CRC Press, 2013, pp. 11–16.

[96] J. Larsson, “Electromagnetics from A Quasistatic Perspective,” *American Journal of Physics*, vol. 75, no. 3, p. 230, 2006.

[97] J. William H.Hayt and John A. Buck, “Energy and Potential,” in *Engineering Electromagnetics*, 7th. ed., New York: McGraw Hill, 2006, p. 99.

[98] F. T. Ulaby, E. Michielssen, and U. Ravaioli, “Displacement Current,” in *Fundamentals of Applied Electromagnetics*, 6th ed., United State of America: Pearson, 2010, pp. 299–300.

[99] L. Pakzad, F. Ein-Mozaffari, and P. Chan, “Measuring Mixing Time in the Agitation of Non-Newtonian Fluids through Electrical Resistance Tomography,” *Chemical Engineering & Technology*, vol. 31, no. 12, pp. 1838–1845, 2008.

[100] M. A. R. Frias, “Electrical Capacitance and Resistance Tomography with Voltage Excitation”, Master Thesis, University of Manchester, 2015.

[101] K. J. Alme and S. Mylvaganam, “Electrical Capacitance Tomography — Sensor Models , Design , Simulations , and Experimental Verification,” *IEEE Sensors Journal*, vol. 6, no. 5, pp. 1256–1266, 2006.

[102] Q. Marashdeh, F. L. Teixeira, and L.-S. Fan, “Electrical Capacitance Tomography,” in *Industrial Tomography: Systems and Applications*, Elsevier Ltd, 2015, pp. 3–21.

[103] D. Y. Chen, L. L. Wang, and Y. Chen, "Analysis and Simulation of Sensor Structure Parameters and Filling Materials Characteristics for Electrical Capacitance Tomography System," *Materials Science Forum*, vol. 575–578, pp. 1217–1221, 2008.

[104] S. Ridzuan Aw, R. Abdul Rahim, M. H. Fazalul Rahiman, F. R. Mohd Yunus, and C. L. G. Goh, "Electrical Resistance Tomography: A Review of The Application of Conducting Vessel Walls," *Powder Technology*, Jan. 2014.

[105] M. Wang, "Electrical Impedance Tomography," in *Industrial Tomography: Systems and Applications*, Elsevier Ltd, 2015, pp. 23–59.

[106] T. K. Bera and J. Nagaraju, "Studying the Resistivity Imaging of Chicken Tissue Phantoms With Different Current Patterns in Electrical Impedance Tomography (EIT)," *Measurement*, vol. 45, no. 4, pp. 663–682, 2012.

[107] F. Dickin and M. Wang, "Electrical Resistance Tomography for Process Applications," *Measurement Science and Technology*, vol. 7, no. 3, pp. 247–260, 1996.

[108] G. Dong, J. Zou, R. H. Bayford, X. Ma, S. Gao, W. Yan, M. Ge, and A. G. Equation, "The Comparison Between FVM and FEM for EIT Forward Problem," *IEEE Transactions on Magnetics*, vol. 41, no. 5, pp. 1468–1471, 2005.

[109] G. R. Shaw, Y. Goussard, and R. Guardo, "Linearization of The Forward Problem in Electrical Impedance Tomography," in *Proceedings of the IEEE International Conference on Engineering in Medicine and Biology Society*, October 28-31, 1993, San Diego, USA, 1993, no. 2, pp. 82–83.

[110] L. Peng, C. Mou, D. Yao, B. Zhang, and D. Xiao, "Determination of The Optimal Axial Length of The Electrode in An Electrical Capacitance Tomography Sensor," *Flow Measurement and Instrumentation*, vol. 16, no. 2–3, pp. 169–175, Apr. 2005.

[111] J. Sun and W. Yang, "Evaluation of Fringe Effect of Electrical Resistance Tomography Sensor," *Measurement*, vol. 53, pp. 145–160, 2014.

[112] J. Lei, S. Liu, X. Wang, and Q. Liu, "An Image Reconstruction Algorithm for Electrical Capacitance Tomography Based on Robust Principle Component Analysis," *Sensors*, vol. 13, no. 2, pp. 2076–92, 2013.

[113] L. Peng, J. Ye, G. Lu, W. Yang, and A. E. C. T. Sensor, "Evaluation of Effect of Number of Electrodes in ECT Sensors on Image Quality," *IEEE Sensors*

*Journal*, vol. 12, no. 5, pp. 1554–1565, 2012.

[114] E. J. Mohamad, “A Segmented Capacitance Tomography for Visualising Material Distributions in Pipeline Conveying Crude Plam Oil”, Ph.D. Thesis, Universiti Teknologi Malaysia, 2012.

[115] W. Q. Yang and L. Peng, “Image reconstruction algorithms for electrical capacitance tomography,” *Measurement Science and Technology*, vol. 14, no. 1, pp. R1–R13, 2003.

[116] M. H. Fazalul Rahiman, “Ultrasonic Tomography System for Liquid / Gas Bubble Column”, Ph.D. Thesis, Universiti Teknologi Malaysia, 2013.

[117] S. Zarina, M. Muji, R. Bin, A. Rahim, M. Hafiz, and F. Rahiman, “Sensitivity Map in Parallel and Fan Beam Mode in Optical Tomography,” in *Proceedings of the 6th World Congress on Industrial Process Tomography*, September 6-9, 2010, Beijing, China, 2010, pp. 762–771.

[118] J. Jamaludin, R. A. Rahim, H. A. Rahim, M. H. Fazalul Rahiman, S. Z. Mohd Muji, and J. M. Rohani, “Charge Coupled Device Based on Optical Tomography System in Detecting Air Bubbles in Crystal Clear Water,” *Flow Measurement and Instrumentation*, vol. 50, pp. 13–25, 2016.

[119] S. Mohammad, “Segmented Excitation for Electrical Capacitance Tomography”, Master Thesis, Universiti Teknologi Malaysia, 2012.

[120] Wael Abdelrahman Deabes, “Electrical Capacitance Tomography for Conductive Materials”, Ph.D. Thesis, Tennessee Technological University, 2010.

[121] Z. Zakaria, “Non-Invasive Imaging of Liquid/Gas Flow using Ultrasonic Transmission Mode Tomography”, Ph.D. Thesis, Universiti Teknologi Malaysia, 2007.

[122] N. M. N. Ayob, S. Yaacob, Z. Zakaria, M. H. F. Rahiman, R. A. Rahim, and M. R. Manan, “Improving Gas Component Detection of An Ultrasonic Tomography System for Monitoring Liquid / Gas Flow,” in *Proceedings of the 2010 6th IEEE International Colloquium on Signal Processing & Its Applications*, 2010, pp. 278–282.

[123] M. H. Fazalul Rahiman, R. Abdul Rahim, and J. Pusppanathan, “Two-Phase Flow Regime Identification by Ultrasonic,” *Sensors & Transducer*, vol. 116, no. 5, pp. 76–82, 2010.

[124] M. H. Fazalul Rahiman, R. Abdul Rahim, H. Abdul Rahim, and N. M. Nor

Ayob, "The Hardware Design Technique for Ultrasonic Process," *Sensors & Transducer*, vol. 141, no. 6, pp. 52–61, 2012.

[125] S. Z. Mohd Muji, R. Abdul Rahim, M. H. Fazalul Rahiman, Z. Tukiran, N. M. Nor Ayob, E. J. Mohamad, and M. J. Puspanathan, "Optical Tomography: Image Improvement Using Mixed Projection of Parallel and Fan Beam Modes," *Measurement*, vol. 46, no. 6, pp. 1970–1978, Jul. 2013.

[126] M. Wei, M. Tong, J. Hao, L. Cai, and J. Xu, "Detection of Coal Dust in A Mine Using Optical Tomography," *International Journal of Mining Science and Technology*, vol. 22, no. 4, pp. 523–527, 2012.

[127] T. Dyakowski, L. F. C. Jeanmeure, and A. J. Jaworski, "Applications of Electrical Tomography for Gas–Solids and Liquid–Solids Flows — A review," *Powder Technology*, vol. 112, no. 3, pp. 174–192, 2000.

[128] P. Wang, B. Guo, and N. Li, "Multi-Index Optimization Design for Electrical Resistance Tomography Sensor," *Measurement*, vol. 46, no. 8, pp. 2845–2853, 2013.

[129] Z. Cui, H. Wang, C. Yang, D. Zhang, and Y. Geng, "Development and Application of ECT Digital System for Online Flow Measurement," in *Proceedings of the 2012 IEEE International Conference on Imaging Systems and Techniques Proceedings*, July 16-17, 2012, Manchester, United Kingdom, 2012, pp. 599–604.

[130] E. J. Mohamad and R. Abdul Rahim, "Multiphase Flow Reconstruction in Oil Pipelines by Portable Capacitance Tomography," in *Proceedings of the 2010 IEEE SENSORS*, November 1-4, 2010, Kona, Hawaii, 2010, pp. 273–278.

[131] W. Q. Yang and L. Peng, "Image Reconstruction Algorithms for Electrical Capacitance Tomography," *Measurement Science and Technology*, vol. 14, pp. R1–R13, 2003.

[132] Y. Chen, L. Zhang, and D. Chen, "Two-Phase Flow Parameters Measurement and Image Reconstruction for Electrical Capacitance Tomography," in *Proceedings of the 2008 IEEE International Workshop on Education Technology and Training & International Workshop on Geoscience and Remote Sensing*, December 21-22, 2008, Shanghai, China, 2008, pp. 680–684.

[133] M. J. Pusppanathan, F. R. Yunus, N. M. Nor Ayob, R. Abdul Rahim, and F. A. Phang, "A Novel Electrical Capacitance Sensor Design For Dual

Modality," *Jurnal Teknologi*, vol. 5, pp. 45–47, 2013.

[134] J. Lei and S. Liu, "Dynamic Inversion Approach for Electrical Capacitance Tomography," *IEEE Transactions on Instrumentation and Measurement*, vol. 62, no. 11, pp. 3035–3049, 2013.

[135] S. Y. Nor Muzakkir Nor Ayob , Mohd Hafiz Fazalul Rahiman , Zulkarnay Zakaria , Ruzairi Abdul Rahim, "Eminent Pixel Reconstruction Algorithm for Ultrsonic Tomography," *Jurnal Teknologi*, vol. 55, no. 2, pp. 15–22, 2011.

[136] W. Warsito and L. Fan, "Measurement of Real-Time Flow Structures in Gas–Liquid and Gas-Liquid–Solid on Systems using Electrical Capacitance Tomography (ECT)," *Chemical Engineering Science*, vol. 56, pp. 6455–6462, 2001.

[137] G. L. Zeng, "Image Reconstruction - A tutorial," *Computerized Medical Imaging and Graphics*, vol. 25, pp. 97–103, 2001.

[138] T. R. Hay, R. L. Royer, H. Gao, X. Zhao, and J. L. Rose, "A Comparison of Embedded Sensor Lamb Wave Ultrasonic Tomography Approaches for Material Loss Detection," *Smart Materials and Structures*, vol. 15, no. 4, pp. 946–951, Aug. 2006.

[139] E. V Malyarenko, J. S. Heyman, H. H. Chen-Mayer, and R. E. Tosh, "Time-Resolved Radiation Beam Profiles in Water Obtained by Ultrasonic Tomography," *Metrologia*, vol. 47, no. 3, pp. 208–218, Jun. 2010.

[140] D. Sueseenak, T. Chanwimalueang, W. Narkbuekaew, K. Chitsakul, and C. Pintavirooj, "Cone-Beam X-Ray Tomography with Arbitrary-Orientation X-ray Tube," in *Proceedings of the 2006 1st IEEE Conference on Industrial Electronics and Applications*, May 24-26, 2006, Singapore, 2006, pp. 1–4.

[141] F. Meng, N. Zhang, and W. Wang, "Virtual Experimentation of Beam Hardening Effect in X-ray CT Measurement of Multiphase Flow," *Powder Technology*, vol. 194, no. 1–2, pp. 153–157, 2009.

[142] A. Contin and G. Schena, "3D Structural Analysis of Ground-Wall Insulation of ac Rotating Machines Using X-Ray Tomography," in *Proceedings of the IEEE International Conference on Solid Dielectrics*, June 30-July 4, 2013, Bologna, Italy, 2013, pp. 279–282.

[143] K. S. Chan, "Real Time Image Reconstruction for Fan Beam Optical Tomography System", Master Thesis, Universiti Teknologi Malaysia, 2002.

[144] M. Madec, J.-B. Fasquel, W. Uhring, and P. Joffre, "Optical Implementation

of The Filtered Backprojection Algorithm," *Optical Engineering*, vol. 46, no. 10, pp. 1–16, Oct. 2007.

[145] D. C. Barber, B. H. Brown, and N. J. Avis, "Image Reconstruction in Electrical Impedance Tomography Using Filtered Back - Projection," in *Proceedings of the Annual International Conference of the IEEE Engineering in Medicine and Biology Society*, October 29-November 1, 1992, Paris, France, 1992, pp. 1691–1692.

[146] R. Giguère, L. Fradette, D. Mignon, and P. A. Tanguy, "ERT Algorithms for Quantitative Concentration Measurement of Multiphase Flows," *Chemical Engineering Journal*, vol. 141, no. 1–3, pp. 305–317, 2008.

[147] W. R. B. Lionheart, "Reconstruction Algorithms for Permittivity and Conductivity Imaging," in *Proceedings of the 2001 World Congress on Industrial Process Tomography*, August 29-31, 2001, Hannover, Germany, 2001, pp. 4–11.

[148] Y. J. Zhang, Y. Chen, and D. Y. Chen, "Measurement of Two-Phase Flow Parameters and Image Reconstruction Based on Weighted SVD Truncated Conjugate Gradient Algorithm," *Key Engineering Materials*, vol. 439–440, pp. 1516–1521, Jun. 2010.

[149] X. Song, Y. Xu, and F. Dong, "An Improved Total Variation Regularization Method for Electrical Resistance Tomography," in *Proceedings of the 2013 Chinese Intelligent Automation Conference, , Lecture Notes in Electrical Engineering 255*, vol. 255, Z. Sun and Z. Deng, Eds. Berlin, Heidelberg: Springer Berlin Heidelberg, 2013, pp. 603–610.

[150] C. G. Xie, N. Reinecke, M. S. Beck, D. Mewes, and R. A. Williams, "Electrical Tomography Technique for Process Engineering Applications," *The Chemical Engineering Journal*, vol. 56, pp. 127–133, 1995.

[151] J. William H.Hayt and J. A. Buck, "Material Constants," in *Engineering Electromagnetics*, 7th. ed., New York: Mc Graw Hill, 2006, pp. 552–553.

[152] R. Thorn, G. A. Johansen, and B. T. Hjertaker, "Three-Phase Flow Measurement in The Petroleum Industry," *Measurement Science and Technology*, vol. 24, no. 1, p. 12003, 2013.

[153] M. Cheney and D. Isaacson, "Issues in Electrical Impedance Imaging," *IEEE Computational Science and Engineering*, vol. 2, no. 4, pp. 53–62, 1995.

[154] M. A. Zimam, E. J. Mohamad, R. Abdul Rahim, and L. P. Ling, "Sensor

Modeling for Electrical Capacitance Tomography System using COMSOL Multiphysics," *Jurnal Teknologi*, vol. 55, no. 2, pp. 33–47, 2011.

[155] Clean Water Team (CWT), "Electrical Conductivity / Salinity Fact Sheet, FS-3.1.3.0(EC)," in *The Clean Water Team Guidance Compendium for Watershed Monitoring and Assessment, Version 2.0. Division of Water Quality, California State Water Resources Control Board (SWRCB), Sacramento, CA*, 2004, pp. 1–5.

[156] P. R. Tortora, S. L. Ceccio, S. M. Trujillo, T. J. O'Hern, and K. a. Shollenberger, "Capacitance Measurements of Solid Concentration in Gas-Solid Flows," *Powder Technology*, vol. 148, no. 2–3, pp. 92–101, Nov. 2004.

[157] J. Sun and W. Yang, "A Dual-Modality Electrical Tomography Sensor for Measurement of Gas–Oil–Water Stratified Flows," *Measurement*, vol. 66, pp. 150–160, 2015.

[158] J. C. Sparks, *The Pythagorean Theorem: Crown Jewel of Mathematics*. Bloomington, Indiana: AuthorHouse, 2008.

[159] Y. S. Kim, S. H. Lee, U. Z. Ijaz, K. Y. Kim, and B. Y. Choi, "Sensitivity Map Generation in Electrical Capacitance Tomography using Mixed Normalization Models," *Measurement Science and Technology*, vol. 18, no. 7, pp. 2092–2102, 2007.

[160] Z. Guo, F. Shao, and D. Lv, "Sensitivity Matrix Construction for Electrical Capacitance Tomography Based on The Difference Model," *Flow Measurement and Instrumentation*, vol. 20, no. 3, pp. 95–102, 2009.

[161] T. Dyakowski, L. F. C. Jeanmeure, and A. J. Jaworski, "Applications of Electrical Tomography for Gas–Solids and Liquid–Solids Flows — A review," *Powder Technology*, vol. 112, no. 3, pp. 174–192, 2000.

[162] M. H. Fazalul Rahiman and R. Abdul Rahim, "A Novel Hybrid Binary Reconstruction Algorithm for Ultrasonic Tomography," *Sensors & Transducer*, vol. 89, no. 3, pp. 93–100, 2008.

[163] Z. Wang, A. C. Bovik, H. R. Sheikh, and E. P. Simmoncelli, "Image Quality Assessment: From Error Visibility to Structural Similarity," *IEEE Transactions on Image Processing*, vol. 13, no. 4, pp. 600–612, 2004.

[164] Z. Wang, A. C. Bovik, and L. Lu, "Why is Image Quality Assessment So Difficult?," in *Proceedings of the 2002 IEEE International Conference on Acoustics Speech and Signal Processing*, May 13-17, 2002, Florida, USA,

2002, vol. 303, pp. 3313–3316.

[165] Z. Wang and A. C. Bovik, “Error : Love It or Leave It ?,” *IEEE Signal Processing Magazine*, vol. 26, no. January, pp. 98–117, 2009.

[166] C. G. Xie, S. M. Huang, C. P. Lenn, A. L. Stott, and M. S. Beck, “Experimental Evaluation of Capacitance Tomographic Flow Imaging Systems using Physical Models,” in *IEE Proceedings- Circuits, Devices and Systems*, 1994, vol. 141, no. 5, pp. 357–368.

[167] R. Abdul Rahim and M. H. Fazalul Rahiman, *Ultrasonic Tomography Non-Invasive Techniques for Flow Measurement*. Johor Bharu, Malaysia: Penerbit UTM Press, 2012.

[168] R. C. Gonzalez and R. E. Woods, *Digital Image Processing*, 2nd. ed. New Jersey: Prentice Hall, 2010.

[169] I. L. S. Mei, I. B. Ismail, A. Bawadi, and A. Shafquet, “Evaluation of Electrical Capacitance Tomography Thresholding Techniques for Void Fraction Measurement of Gas-Liquid System,” *Applied Mechanics and Materials*, vol. 625, pp. 439–443, 2014.

[170] C. H. Radewan, “Digital Image Processing with Pseudo-Color,” *Acquisition and Analysis of Pictorial Data*, vol. 48, p. 50, 1975.

[171] L. Riordan, “Programming the AD9833/AD9834,” in *An-1070 Application Note*, USA: Analog Device, 2010, pp. 1–4.

[172] R. L. Boylestad and L. Nashelsky, “Operational Amplifiers,” in *Electronic Devices and Circuit Theory*, 9th. ed., United State of America: Pearson, 2006, pp. 608–611.

[173] G. King, “Ask the Applications Engineer-Capacitive Loads on Op Amps,” *Analog Dialogue*, vol. 31, no. 2, pp. 19–20, 1997.

[174] R. L. Boylestad and L. Nashelsky, “Op-Amp Applications,” in *Electronic Devices and Circuit Theory*, 9th. ed., United State of America: Pearson, 2006, p. 640.

[175] M. A. Shayib, *Applied Statistics*, 1st. ed. London: Bookboon, 2013.

[176] J. Sauro and J. R. Lewis, “Six Enduring Controversies in Measurement and Statistics,” in *Quantifying the User Experience Practical Statistics for User Research*, 2nd. ed., Cambridge: Elsevier Inc., 2012, pp. 241–267.

[177] X. Liu and X. Xu, “A New Generalized P-Value Approach for Testing The Homogeneity of Variances,” *Statistics & Probability Letters*, vol. 80, no. 19–

20, pp. 1486–1491, 2010.

[178] S. M. Ross, *Introduction to Probability and Statistics for Engineers and Scientists*, 4rd. ed. Canada: Elsevier Academic Press, 2009.

[179] J. Sauro and J. R. Lewis, “Did We Meet or Exceed Our Goal?,” in *Quantifying the User Experience Practical Statistics for User Research*, 2nd. ed., Cambridge: Elsevier Inc., 2012, pp. 41–62.

# APPENDIX A

# PUBLICATIONS

**1) Publications Related to The Thesis**

**i) Journals**

1. **Y. Abdul Wahab**, R. Abdul Rahim, M.H. Fazalul Rahiman, S. Ridzuan Aw, F.R. Mohd Yunus, C.L. Goh, *et al.*, Non-invasive process tomography in chemical mixtures – A review, *Sensors Actuators B Chemical*, vol. 210, pp. 602–617. 2015. (Published, ISI IF 4.758: ,Q1)

2. **Y. Abdul Wahab**, R. Abdul Rahim, M.H. Fazalul Rahiman, L. Pei Ling, S. Ridzuan Aw, F.R. Mohd Yunus, *et al.*, Compatible Study on Utilizing Frequency for Non-Invasive Electrical Resistance Tomography using COMSOL Multiphysics, *Jurnal Teknologi*, vol. 73:6, pp. 65–70, 2015. (Published, SCOPUS, Q3)

3. **Y. Abdul Wahab**, R. Abdul Rahim, M.H. Fazalul Rahiman, L. Pei Ling, S. Ridzuan Aw, F.R. Mohd Yunus, *et al.*, Simulation Study on Non-Homogenous System of Non-Invasive ERT using COMSOL Multiphysics, *Jurnal Teknologi*, vol. 77:17, pp. 43–48, 2015. (Published, SCOPUS, Q3)

**ii) Conference proceedings**

**Y. Abdul Wahab**, R. Abdul Rahim, M.H. Fazalul Rahiman, L. Pei Ling, S. Ridzuan Aw, F.R. Mohd Yunus, *et al.*, Simulation Study on Non-Homogenous System of Non-Invasive ERT using COMSOL Multiphysics, in *Proceedings of*

*the International Workshop on Computed Tomography and Imaging Technology (IWMyCT),* June 1-2, 2015, Perlis, 2015. (Published)

**2) Other Publications Related to The Research Field**

**i) <u>Journals</u>**

1. **Y. Abdul Wahab**, R. Abdul Rahim, M.H. Fazalul Rahiman, H. Abdul Rahim, S. Ridzuan Aw, N.S. Mohd Fadzil, *et al.*, A Review of Process Tomography Application in Inspection System, *Jurnal Teknologi*, vol. 70:3, pp. 35–39, 2014. (Published, SCOPUS, Q3)

2. M. H. Fazalul Rahiman, R. Abdul Rahim, H. Abdul Rahim, Z. Zakaria, M.J. Pusppanathan, G.C. Loon, N. Ahmad., **Y. Abdul Wahab,** Gas Holdup Profiles Determination By Means Of Ultrasonic Transducer, *Jurnal Teknologi*, vol. 69:8, pp. 81-84, 2014. (Published, SCOPUS, Q3)

3. S. Ridzuan Aw, R.Abdul Rahim, M. H.Fazalul Rahiman , F. R. Mohd Yunus ,N. S. Fadzil , M. Z. Zawahir , M. F. Jumaah , M. J. Pusppanathan , N.M. Nor Ayub , **Y. Abdul Wahab** , S. Bunyamin, Application Study On Bubble Detection In A Metallic Bubble Column Using Electrical Resistance Tomography, *Jurnal Teknologi*, vol. 69:8, pp. 19-25, 2014. (Published, SCOPUS, Q3)

4. L. E. Hong, R. Abdul Rahim, A. Ahmad, M. Amri, K. Hamimah, L. Pei Ling, H. Wahid, N. Ahmad, M. F. Abd Shaib, **Y. Abdul Wahab**, S. Ridzuan Aw, H. Fazalul Rahiman, and Z. Zakaria, “Fundamental Sensor Development in Electrical Resistance Tomography,” *Jurnal Teknologi*, vol. 6, pp. 117–124, 2015. (Published, SCOPUS, Q3)

5. F. R. Mohd Yunus, R. Abdul Rahim, L. Pei Ling, N. M. Nor Ayob, **Y. Abdul Wahab**, S. Ridzuan Aw, N. Ahmad, and M. H. Fazalul Rahiman, “Simulation of Electrode for Dual- Electrical Resistance and Ultrasonic Transmission Tomography for Imaging Two-Phase Liquid and Gas,” *Jurnal Teknologi*, vol. 17, pp. 55–61, 2015.(Published, SCOPUS, Q3)

6. S. Ridzuan Aw, R. Abdul Rahim, F. R. Mohd Yunus, M. H. Fazalul Rahiman, **Y. Abdul Wahab**, M. B. Nor Shah, J. Pusppanathan, and E. J. Mohamed, "Sensitivity Map Generation for Conducting Strategy in Electrical Resistance Tomography," *Jurnal Teknologi*, vol. 17, pp. 91–97, 2015. (Published, SCOPUS, Q3)

7. E.J. Mohamad, R.A. Rahim, M.H.F. Rahiman, H.L.M. Ameran, **Y.A. Wahab**, O.M.F. Marwah, Analysis of crude palm oil composition in a chemical process conveyor using Electrical Capacitance Tomography, *Flow Measurement and Instrumentation*, vol. 50, 57–64, 2016.
(Published, ISI IF 1.152: ,Q2)

8. Goh Chiew Loon, Ruzairi Abdul Rahima, Hafiz Fazalul Rahiman, Tee Zhen Cong, **Yasmin Abdul Wahab**, Simulation and experimental study of the sensor emitting frequency for ultrasonic tomography system in a conducting pipe, *Flow Measurement and Instrumentation*, vol. 54, pp. 158-171, 2017. (Published, ISI IF 1.152: ,Q2)


**ii) <u>Book Chapter</u>**


1. Ismail Mohd Khairuddin, Ruzairi Abdul Rahim, **Yasmin Abdul Wahab**, Biometrics. *Progress in Process Tomography & Instrumentation System – Series 23*. Malaysia: Malaysia: Pusat Pengurusan Penyelidikan (RMC) & Penerbit UTM Press, pp. 14-36, 2016. ISBN: 978-967-354-215-4. (Published)

2. Ibrahim Albool, Ruzairi Abdul Rahim,, Khaled, Alsaih, Abdulrahman Zaroug, Osama Mazhar, **Yasmin Abdul Wahab**, Suzzana Ridzuan Aw, Mohd Hafiz Fazalul Rahiman, Anita Ahmad, Electrical Resistance Tomography (ERT). *Progress in Process Tomography & Instrumentation System – Series 20*. Malaysia: Pusat Pengurusan Penyelidikan (RMC) & Penerbit UTM Press, pp. 38-39, 2016. ISBN: 978-967-354-202-4. (Published)

3. Khaled Alsaih , Ruzairi Abdul Rahim, Anita Ahmad, Ibrahim Albool, Abdulrahman Zaroug, Osama Mazhar, Seriaznita Mat Said, Mohd. Amri Md. Yusus, Mohamad Hafis Izran Ishak, **Yasmin Abdul Wahab**, Temperature Sensors for Steel Melting, *Progress in Process Tomography & Instrumentation System – Series 23.* Malaysia: Pusat Pengurusan Penyelidikan (RMC) & Penerbit UTM Press, pp. 9-21, 2016. ISBN: 978-967-354-202-4. (Published)

# APPENDIX B

## PROGRAMMING CODE FOR WAVEFORM GENERATOR

```c
#include <18F4580.h> //This both defines the chip, and includes everything.
#fuses HS,NOWDT,NOPROTECT,NOLVP,NODEBUG

#use delay(clock=20000000)
#use spi(SPI1, MODE=2, ENABLE=PIN_E2, STREAM=AD9833)

#define RESET 0x0100  //initialize reset bit D8=1
#define WRITE_FREQ0 0x2000 //initialize LSB & MSB write consecutively, D13=1
#define RUN 0          //intialize give output after reset off
#define PHASE0_ZERO 0xC000  //initalize PHASE0 use
#define spi_14(x) spi_xfer(AD9833,(x & 0x3FFF) | 0x4000,16)
//0x4000 is the register for FREQ0

void write_val_freq0(int32 divisor)
{
   //Do the maths to send 28bits to freg - more reliable than DIY
   spi_14(divisor); //send 14 LSb's
   spi_14((divisor>>14)); //then the next 14 bits
}

void main()
{
   setup_adc_ports(NO_ANALOGS); //E2 is an analog pin - make sure this
   //is setup to digital.
   while(TRUE)
   {
     // activate control register; both LSB & MSB FREQ write consecutively
     // enable reset
     spi_xfer(AD9833, RESET | WRITE_FREQ0, 16);

     //on FREQ0 for generate 2MHz if using MCLK=20MHz same as PIC clock
     //26843545 in decimal
     write_val_freq0(26843545); //setup FREQ0

     //on PHASE0 with zero phase shift
     spi_xfer(AD9833, PHASE0_ZERO, 16);

     //activate control register
     //disable reset; enable sinewaveform signal
     spi_xfer(AD9833, RUN, 16);

     //generally you don't want to keep sending data to chips 'non stop'...
     //with your existing code, only a few uSec after getting here, the chip
     //would be programmed back to RESET, so the waveform would stop
     //since the waveform doesn't start till 8 clocks after the RESET
     //goes off, there would be almost nothing on the output.....
     delay_ms(300); //output the waveform for a 300ms
   }
}
```

# APPENDIX C

## PART OF PROGRAMMING CODES FOR DSPIC30F6010A

```
/////////////////////* main coding *///////////////////////////////////////////////

int main (void)
{
    TRISD=0;                    //Port D as output
    TRISCbits.TRISC15 = 0;          //Port C15,C14,C13,C3 and C1 as output
    TRISCbits.TRISC14 = 0;
    TRISCbits.TRISC13 = 0;
    TRISCbits.TRISC3 = 0;
    TRISCbits.TRISC1 = 0;

    intial_adc();
    initial_uart();

    while(1)
    {

wait:
      while(!DataRdyUART1());
      Rx_data = ReadUART1();

      if (Rx_data != 'a')
         goto wait;
      Rx_data = 0;

/************************ TX1 ***************************************************/
    Sw1=1;          //Ch1 as Tx
        Sw2=0;          //Ch2 as Rx and the rest of channel as Rx (except Ch1)
        Sw3=0;
        Sw4=0;
        Sw5=0;
        Sw6=0;
        Sw7=0;
        Sw8=0;
        Sw9=0;
        Sw10=0;
        Sw11=0;
        Sw12=0;
        Sw13=0;
        Sw14=0;
        Sw15=0;
        Sw16=0;

    SwA3=0;         //trigger sine wave on ch 1
    SwA2=0;
    SwA1=0;
    SwA0=0;
    En=1;

    __delay_us(100); //stabilize the switching pins

      Sample_adc();    // ADC sample and send to pc
```

# APPENDIX D

## PART OF PROGRAMMING CODES FOR MATLAB

i) LBP algorithm

```
% --- Executes on button press in Read_select.
function Read_select_Callback(hObject, eventdata, handles)
global s
global Vref
global Vmeas
global Stop_Button
global DispMap
global normDispMap
Stop_Button=0;
%----load normalized pair projection e1 till e16
    NormEpairProj=load('NormalizedEpair.mat');
    NormEpair=NormEpairProj.N;  %SP=single projection

while Stop_Button == 0 % Do for real time

%% -------------------- LINEAR BACK PROJECTION(LBP)-----------------------
    axes(handles.image_axes);
    disp('Displaying Tomogram...');
    Resolution = 136;  % --- IMAGE PIXEL SIZE

    load1 = load ('Vhomo.mat');  % load the Vhomo.mat file that run from GUI
    Vref = load1.Vref;  %select variable Vref in Vhomo.mat file

tic % Start stopwatch timer when matlab start acquire ADC signal
    %%%%% Read for non homogenous data %%%%
    fprintf(s,'a');    % Write text to the device; show what inside the data read form uc
    y1= fread (s); % Read binary data from the device
    Vmeas=reshape(y1,[16,16]); % single column multiple rows into 16x16 arrays

    save ('Vnonhomo.mat','Vmeas');  % save the non homogenous value in Vnonhomo.mat file

    Attenuate_xy=(Vref-Vmeas)./Vref;  % Get the sensor loss value
```

```
for i=1:16 %eliminate NAN values in Attenuate_xy
    for j=1:16
    e=Attenuate_xy(i,j);
    d=isnan(e);
    e(d)=0;
    Attenuate_xy(i,j)=e;
    end
end
   save ('Attenuate_xy.mat','Attenuate_xy');

DispMap = zeros(Resolution); %view = 1;

            for Tx = 1:16
                for Rx = 1:16

                    DispMap = DispMap + (Attenuate_xy(Rx,Tx) * NormEpair(Rx, Tx));  %%% coding for getting LBP

                end
            end

% to eliminate NaN and limit start at 0 value
   for i=1:Resolution
       for j=1:Resolution
            e=DispMap(i,j);
            d=isnan(e);
            e(d)=0;
            DispMap(i,j)=e;
        end
   end

 save ('ImageB4Norm.mat','DispMap');  % save tomogram before normalized as .mat file for analysis
```

```
%%-------Fixed scale 0 to 1------
normDispMap=DispMap; % rename display image
a = min(normDispMap(:));
b = max(normDispMap(:));

for Tx = 1:Resolution;
   for Rx = 1:Resolution;

       normDispMap(Tx,Rx) = ((normDispMap(Tx,Rx)-a)./ (b-a))*1;
       %%%eliminate NaN value at norm DispMap ; if not matlab cant plot
       %%%image
       e=normDispMap(Tx,Rx);
       d=isnan(e);
       e(d)=0;
       normDispMap(Tx,Rx)=e;
   end
end

save ('ImageNorm.mat','normDispMap');  % save tomogram before normalized as .mat file for analysis
%% ----- DISPLAY TOMOGRAM RESULT---------------------------------------------
           imagesc(normDispMap, 'Parent',handles.image_axes); set(gca,'YDir','normal');
           set(handles.image_axes, 'CLim', [0,1]);
           imageCenter=[68.5,68.5];
           viscircles(imageCenter,64,'EdgeColor','w','LineWidth',1); %  % k=black,b=blue,w=white
           colormap (jet)               % change color map to jet colour
           colorbar                     % Display colorbar

           axis off                     % off the axis x and y number
```

```
toc % Read elapsed time from stopwatch after draw tomogram
elapsedTime = toc;
frame=1/elapsedTime; % To get how many frame in 1 s
answ_frame= num2str(frame);% need to convert the answer back into String type to display it
set(handles.display_frame,'String',answ_frame); %display frame/s


           pause (0.05)  % update figure in 50ms

end


% update data
guidata(hObject,handles);
```

ii) LBP + Threshold

```
%%%%%-------------------threshold image------------------------------%%%%%%%
loadThres = load ('Pth.mat');  % load the threshold value from slider
Pth = loadThres.Pth;  %select variable Pth


for m = 1:Resolution;
   for n = 1:Resolution;

    if normDispMap(m,n)<Pth;normDispMap(m,n)=0;end
    if normDispMap(m,n)>=Pth;normDispMap(m,n)=1;end

   end
end

save ('ImageThres.mat','normDispMap');
```